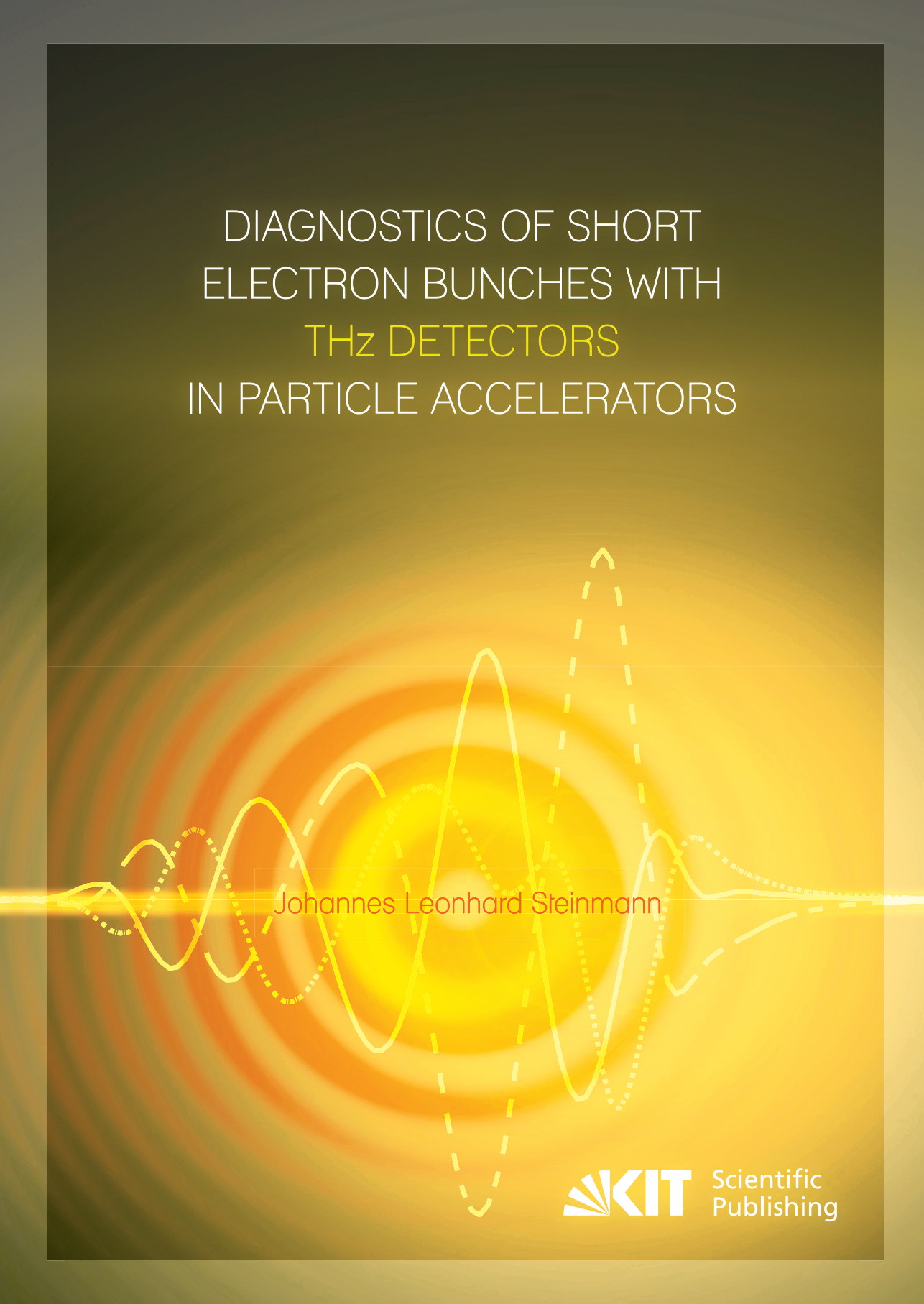


DIAGNOSTICS OF SHORT ELECTRON BUNCHES WITH THz DETECTORS IN PARTICLE ACCELERATORS



Johannes Leonhard Steinmann

Johannes Leonhard Steinmann

Diagnostics of Short Electron Bunches with THz Detectors in Particle Accelerators

Diagnostics of Short Electron Bunches with THz Detectors in Particle Accelerators

by

Johannes Leonhard Steinmann

Karlsruher Institut für Technologie
Institut für Beschleunigerphysik und Technologie

Diagnostics of Short Electron Bunches with THz Detectors in Particle Accelerators

Zur Erlangung des akademischen Grades eines Doktor-Ingenieurs
von der KIT-Fakultät für Elektrotechnik und Informationstechnik des
Karlsruher Instituts für Technologie (KIT) genehmigte Dissertation
von M.Eng. Johannes Leonhard Steinmann, geboren in Rauenberg

Tag der mündlichen Prüfung: 11. Dezember 2018
Hauptreferent: Prof. Dr. Michael Siegel
Korreferent: Prof. Dr. Anke-Susanne Müller

Impressum



Karlsruher Institut für Technologie (KIT)
KIT Scientific Publishing
Straße am Forum 2
D-76131 Karlsruhe

KIT Scientific Publishing is a registered trademark
of Karlsruhe Institute of Technology.
Reprint using the book cover is not allowed.

www.ksp.kit.edu

This document – excluding the cover, pictures and graphs – is licensed
under a Creative Commons Attribution-Share Alike 4.0 International License
(CC BY-SA 4.0): <https://creativecommons.org/licenses/by-sa/4.0/deed.en>

The cover page is licensed under a Creative Commons
Attribution-No Derivatives 4.0 International License (CC BY-ND 4.0):
<https://creativecommons.org/licenses/by-nd/4.0/deed.en>

Print on Demand 2019 – Gedruckt auf FSC-zertifiziertem Papier

ISBN 978-3-7315-0889-2
DOI 10.5445/KSP/1000090017

Zusammenfassung

Beschleunigerbasierte Synchrotronstrahlung wird seit vielen Jahren als wissenschaftliche Lichtquelle genutzt. Sie zeichnet sich durch hohe Brillanz und ein breitbandiges Spektrum aus, welches von Millimeterwellen bis zu harter Röntgenstrahlung reicht. Diese Eigenschaften werden bisher von keiner anderen künstlichen Apparatur erreicht. Die Beschleuniger zur Erzeugung dieser einzigartigen Strahlung werden deshalb kontinuierlich weiterentwickelt. Nachdem die Synchrotronstrahlung in der ersten Generation noch parasitär an Beschleunigern für die Teilchenphysik genutzt wurde, sind Lichtquellen der zweiten Generation speziell zur Erzeugung von Synchrotronstrahlung konstruiert worden. Sie sind als Speicherringe konzipiert, bei denen die Teilchenenergie konstant hoch gehalten wird und die Strahlstabilität an erster Stelle steht. Zusätzlich bieten sie tangential abgehende Strahlrohre, in denen dauerhafte Experimente für Wellenlängen von Infrarot bis Röntgenstrahlung installiert sind. In der dritten Generation wurden lange gerade Strecken in den Ringbeschleuniger eingefügt, um dort mittels Wigglern und Undulatoren die Strahlintensität zu vervielfachen.

In der aktuellen Generation von Lichtquellen, die gerade in Betrieb gehen, wird zusätzlich transversal beugungslimitierte Strahlung emittiert. Das wird durch eine transversale Komprimierung der Elektronenpakete unter die Wellenlänge der emittierten Strahlung erreicht. Dadurch werden die Strahlqualität um mehrere Größenordnung verbessert und neuartige Experimente ermöglicht.

Die nächste signifikante Verbesserung der Lichtqualität könnte entweder durch einen deutlich erhöhten Strahlstrom oder eine deutlich reduzierte Elektronenpaketelänge oder der Kombination aus Beidem erreicht werden. Zwar wären beide Verfahren sehr anspruchsvoll, würden aber eine weitere Steigerung der Lichtintensität um mehrere Größenordnungen ermöglichen. Pulslängen, welche kleiner sind als die Wellenlänge der beobachteten Strahlung, führen unter anderem zu einer kohärenten Verstärkung und damit zu einer Intensitätssteigerung in der Größenordnung der Anzahl der beteiligten Elektronen, welche im Bereich von 10^8 bis 10^{11} liegt. Außerdem würden

dann Einzelzyklenpulse emittiert, die wiederum neuartige Experimente ermöglichen würden.

Die verbesserten Eigenschaften von ultrakurzen Pulsen im Femtosekundenbereich werden bereits an Freie-Elektronen-Lasern (FEL), Linearbeschleunigern wie dem LCLS II in Kalifornien oder dem europäischen XFEL in Hamburg, genutzt. Dort ermöglichen sie vor allem zeitaufgelöste Messungen mit hochenergetischen Röntgenstrahlen. Im Gegensatz zu Kreisbeschleunigern sind diese aber in der Pulswiederholrate und der Anzahl der gleichzeitigen Nutzer stark limitiert und können die weltweite Nachfrage nicht decken. Zudem bieten diese Einzelschussmessungen noch nicht die Stabilität, die Nutzer an Synchrotron-Speicherringen schätzen. Kreisbeschleuniger können dadurch also nicht ersetzt werden und sind als komplementäre Messstationen anzusehen. Deshalb wird die Forschung hin zu ultrakurzen Elektronenpaketen in Kreisbeschleunigern intensiviert.

Aufgrund von Instabilitäten ist eine Kombination aus kürzeren Pulsen und höheren Strahlströmen in Kreisbeschleunigern allerdings begrenzt. Momentan werden Pulslängen von etwa einer Pikosekunde erreicht, bevor Mikrostrukturen auf den sonst Gaußförmigen Elektronenpaketen zu einer unkontrollierten Emission von Terahertzstrahlung führen und das Elektronenpaket wieder aufblähen. Diese Strahlung zeichnet sich jedoch durch hohe Brillanz aus und wird deshalb auch für Nutzerexperimente verwendet. Für die Maschinendiagnose stellt die Analyse der abgestrahlten THz-Leistung während des Auftretens der Instabilität ein wertvolles Instrument dar, um Rückschlüsse auf die Art der Instabilität ziehen zu können und eine Beeinflussung zu messen. Die Beschleunigerdiagnostik mit Synchrotronstrahlung im Terahertzbereich ist im Vergleich zu konventionellen Methoden noch ein relativ junger Bereich, da für diesen Spektralbereich zwischen den Millimeterwellen und der Infrarotstrahlung lange Zeit weder geeignete Quellen noch Detektoren verfügbar waren. Allerdings wurden hier in den letzten Jahren große Fortschritte erzielt, sodass einfache THz-Diagnostik mittlerweile an vielen Beschleunigern im Einsatz ist.

In dieser Dissertation werden neue Methoden im Bereich der Strahlanalyse durch Terahertzstrahlung erforscht und demonstriert. Eine verbesserte Diagnose ist wichtig, um die Instabilitäten charakterisieren und später kontrollieren zu können. In der Zukunft könnten dadurch der Wissenschaft noch kürzere, intensivere Lichtpulse, welche zu kohärenter Synchrotronstrahlung führen, zur Verfügung gestellt werden. Dafür wird zuerst kurz auf die Grundlagen der Teilchenbeschleunigung und Synchrotron-

strahlungsquellen eingegangen, um dann die Theorie zur limitierenden Instabilität zu erläutern. Diese ist eng verknüpft mit der Erzeugung von Synchrotronstrahlung, die zusammen mit der Auskopplung an die Experimentierstationen untersucht wird.

Ausgehend vom Stand der Technik zur THz Spektralanalyse, der FourierTransform-Infrarotspektrometrie, wird ein balanciertes Martin-Puplett Interferometer mit ultraschnellen THz-Detektoren in Betrieb genommen. Durch eigene Messungen werden die technologisch bedingten Limitierungen in der Auslesegeschwindigkeit und der Frequenzauflösung aufgezeigt. Für beide Limitierungen werden im Laufe der Dissertation Lösungen erarbeitet und am Beschleuniger KARA des Karlsruher Instituts für Technologie eingesetzt.

Die Diagnostik mittels ultra-schneller THz-Detektoren wird zuerst im Zeitbereich demonstriert. Dabei werden grundlegende Eigenschaften der limitierenden Instabilität diskutiert und erste Möglichkeiten zur Beeinflussung aufgezeigt. Im folgenden Kapitel wird ein Prototyp für ein Einzelschuss-Spektrometer vorgestellt. Es basiert auf vier schmalbandigen, schnellen Detektoren welche mit einer Wiederholrate von 500 MHz kontinuierlich ausgelesen werden.

Dieser weltweit einmalige Aufbau erlaubt gleichzeitig die Beobachtung von allen Elektronenpaketen im Synchrotron, die in einem Abstand von zwei Nanosekunden mit annähernd Lichtgeschwindigkeit durch den 110 m langen Beschleunigerring fliegen. Die Beobachtung eines Paketes über viele Umläufe hinweg gibt Einblick in die Veränderung der Elektronenpaketform und die umlaufaufgelöste Entwicklung der Instabilitäten.

Zum Ende der Arbeit wird ein Experimentaufbau vorgestellt, der mittels heterodynener Detektion eine Frequenzauflösung des Terahertzspektrums von einem Hertz ermöglicht. Dadurch wird der kohärente Frequenzkamm sichtbar, der vom Beschleuniger emittiert wird. Erstmals wird dafür die Abhängigkeit des Synchrotronstrahlungsspektrums von der Füllstruktur des Beschleunigers hochauflösen untersucht und eine einfach anzuwendende Formel entwickelt. Zusätzlich wird demonstriert, wie durch unterschiedliche Einstellungen am Beschleuniger der Frequenzkamm beeinflusst werden kann, sodass Probenuntersuchungen im Terahertzbereich mit einer Frequenzauflösung von einem Hertz durchgeführt werden können.

Contents

1	Introduction	1
1.1	Outline	1
1.2	Conventions	4
1.2.1	Citations	4
1.2.2	Units	5
1.2.3	Ultra-fast	5
1.2.4	Terahertz	5
1.2.5	Fourier Transformation	5
1.2.6	Coordinate System	6
1.3	Synchronous Particle	8
1.4	Ultra-Relativistic Approximations	9
1.5	Particle Acceleration and Storage Rings	9
1.5.1	Acceleration of Charged Particles	10
1.5.2	Radiation of Charged, Relativistic Particles	11
1.5.3	Longitudinal Beam Dynamics	13
1.5.4	Natural Energy Spread and Natural Bunch Length	18
1.6	KARA Storage Ring: The KIT Synchrotron	19
1.7	Short Bunch Length Operation at KARA	21
2	Beam Impedances, Wake Potentials and the Micro-Bunching Instability	23
2.1	Beam Impedances in a Storage Ring	23
2.1.1	Synchrotron Radiation Impedance in a Rectangular Pipe	25
2.1.2	Synchrotron Radiation Impedance between Parallel Plates	29
2.1.3	Synchrotron Radiation Impedance in Free Space	30
2.1.4	Impedance at the Edges of Bending Magnets	33
2.1.5	Longitudinal Space-Charge Impedance	34
2.1.6	Resistive Wall Impedance	35
2.1.7	Discussion on Impedances	37

2.2	Bunch Deformation by Self-Interaction	38
2.2.1	Hamiltonian of Phase Space System	41
2.2.2	Vlasov-Fokker-Planck Equation	41
2.2.3	Häissinski Distribution	43
2.3	Micro-Bunching Instability Threshold Current	45
2.4	Bursting Radiation above the Threshold Current	48
3	Synchrotron Radiation	51
3.1	Emitted Synchrotron Radiation Power	51
3.2	Edge Radiation	58
3.3	Angular Distribution	60
3.4	Comparison of Constant Field Radiation and Edge Radiation	61
3.5	Extraction of Synchrotron Radiation at Beamlines	62
3.6	The KARA Infrared Beamlines	67
4	Equipment and Machine Parameters	73
4.1	THz Detectors	73
4.2	THz Optics and Transport	78
4.3	Determination of Machine Parameters	78
4.3.1	Beam Energy	78
4.3.2	Beam Energy Spread	80
4.3.3	Beam Current	81
4.3.4	Filling Pattern and Individual Bunch Current	82
4.3.5	Bunch Length	83
4.3.6	Bunch Sub-Structure	83
4.3.7	Synchrotron Frequency	84
4.3.8	RF Voltage	85
5	Fourier Transform Infrared Spectrometry	87
5.1	Michelson Interferometer	87
5.1.1	Normalization	88
5.1.2	Incoherent Spectrum	90
5.1.3	Coherent Spectrum	92
5.2	Balanced Martin-Puplett Interferometer	94
5.2.1	Balanced Detection	94
5.3	Limitations of FTIR	98

6 Time Domain Measurements with ultra-fast THz-Detectors	99
6.1 Pulse Amplitude Measurements	99
6.2 Bursting Spectrogram as an Accelerator Fingerprint	103
6.3 Behavior at High Bunch Currents and Low Shielding Factors	105
6.4 Weak Instability	107
6.5 Snapshot Measurements and Parameter Scans	110
6.6 Influence of RF Phase Modulation	111
6.7 Summary of Time Domain Measurements	116
7 High Repetition Rate Single Shot Spectrometer	119
7.1 Four-Channel Spectrometer Setup	120
7.2 Current Decay	122
7.2.1 Measurement	122
7.2.2 Inovesa Simulation	125
7.3 Sawtooth Bursting Regime	129
7.4 Bursts at Medium Bunch Current	132
7.5 Regular Bursting Regime	134
7.6 Summary and Outlook	137
8 Heterodyne THz-Spectroscopy	139
8.1 The Heterodyne Detection Principle	140
8.2 RF Mixers	142
8.3 Frequency Comb by Repeated Emission	144
8.4 Heterodyne Measurement Setup	146
8.5 Direct Observation of Synchrotron Motion Sidebands in CSR	149
8.6 Comparison between Diode and Mixer Power	154
8.7 Multi Bunch Filling Patterns	156
8.7.1 Bunch Trains	157
8.7.2 Bunch Current Variations	160
8.7.3 Bunch Spacing	162
8.7.4 Broadband Data Evaluation	164
8.8 Summary of Heterodyne Measurements	166
9 Summary and Outlook	169

Appendix	173
A Synchrotron Motion	173
B Readout Systems	175
B.1 Oscilloscopes	175
B.2 Single-Shot Realtime Mode	176
B.3 Segmented Mode	177
B.4 Peak Detect Mode	178
B.5 Spectrum Analyzer	179
B.6 Lock-In Amplifier	180
B.7 Data Acquisition	181
B.8 KAPTURE	182
C THz Filters	185
C.1 Lowpass	185
C.2 Highpass	186
C.3 Bandpass	186
C.4 Beam Splitters	187
Publications	189
Bibliography	199

List of Acronyms and Symbols

Acronyms

ADC	analog to digital converter
APD	avalanche photo diode
BBB	bunch-by-bunch feedback
BPM	beam position monitor
BW	bandwidth
CBS	Compton backscattering
CFR	constant field radiation
CSR	coherent synchrotron radiation
DC	direct current
DFT	discrete Fourier transformation
DSB	double side band
EM	electromagnetic
EOSD	electro-optical spectral decoding
ER	edge radiation
FFT	fast Fourier transformation
FIR	far infrared
FS	free space
FT	Fourier transformation
FTIR	Fourier transform infrared spectrometry
HEB	hot electron bolometer
HiSLIP	high speed LAN instrument protocol
IBPT	Institute for Beam Physics and Technology
IF	intermediate frequency
IMS	Institute of Micro- and Nanoelectric Systems
Inovesa	Inovesa numerical optimized Vlasov equation solver application
IPE	Institute for Data Processing and Electronics

IR	infrared
ISR	incoherent synchrotron radiation
KAPTURE	Karlsruhe Pulse Taking Ultra-Fast Readout Electronics
KARA	Karlsruhe research accelerator
KIT	Karlsruhe Institute of Technology
LAS	Laboratory for Applications of Synchrotron Radiation
LIA	lock-in amplifier
LLRF	low-level RF
LO	local oscillator
LSB	lower side band
LSC	longitudinal space charge
MBI	micro-bunching instability
MPI	Martin-Puplett interferometer
NEP	noise equivalent power
PP	parallel plates
PSD	power spectral density
RBW	resolution bandwidth
RF	radio frequency
RMS	root mean square
RW	resistive wall
SA	spectrum analyzer
SBD	Schottky barrier diodes
SNR	signal-to-noise ratio
SR	synchrotron radiation
SRW	synchrotron radiation workshop
STD	standard deviation
TBP	time-bandwidth product
TCSPC	time-correlated single photon counting
TDS	time-domain spectrometer
USB	upper side band
VBW	video bandwidth
VDI	Virginia Diodes
VFP	Vlasov-Fokker-Planck
VISA	virtual instrument software architecture
YBCO	$\text{YBa}_2\text{C}_3\text{O}_{7-\text{x}}$

Symbols

\vec{B}	magnetic field strength	[T]
β	fraction of lightspeed ($\beta = v/c$)	
$\sigma_{z,s}$	longitudinal rms bunch length	[m]
$\sigma_{z,t}$	longitudinal rms bunch duration	[s]
$\sigma_{z,0}$	zero current bunch length	[m]
$\rho(t)$	longitudinal bunch current	[A]
$\rho(q)$	bunch current in normalized longitudinal coordinate q	[C/m]
$\varrho(f)$	spectral density of longitudinal bunch current $\rho(t)$	[A/Hz]
*	convolution operator, Eq. (2.33)	
S_{CSR}	CSR strength parameter, Eq. (2.49)	[m·s]
\mathcal{J}_E	damping partition number (≈ 2)	
DFT	discrete Fourier transform, Eq. (8.18)	
\vec{E}	electric field strength	[V/m]
E	total particle energy	[eV]
E_0	energy of the reference particle	[eV]
ΔE	energy offset to the reference particle ($E - E_0$)	[eV]
δE	energy change per turn ($E_2 - E_1$)	[eV]
σ_E	energy spread (rms), Eq. (1.33)	[eV]
$\sigma_{E,0}$	natural energy spread (rms)	[eV]
σ_δ	normalized energy spread (rms) (σ_E/E_0)	
$\sigma_{\delta,0}$	normalized natural energy spread (rms), Eq. (1.38)	
$\wp(f)$	form factor: FT of p_d , Eq. (3.7)	
f_{RF}	accelerating frequency, (hf_0)	[Hz]
f_0	revolution frequency of the reference particle	[Hz]
T_0	accelerator revolution period	[s]
ΔT	revolution period offset to the reference particle, Eq. (1.7)	[s]
T_{RF}	RF period	[s]
f_s	synchrotron oscillation frequency	[Hz]
T_s	synchrotron oscillation period ($T_s = 1/f_s$)	[s]
γ	Lorentz factor Eq. (1.11)	
h	harmonic number of the storage ring, Eq. (1.23)	
\mathcal{H}	phase space Hamiltonian Eqs. (2.34) and (2.37)	
h_c	height of the vacuum chamber	[m]
I_B	beam current, Eq. (4.2)	[A]

I_b	integrated bunch current	[A]
$I_{b,\text{th}}$	bunch current at MBI threshold, Eq. (2.51)	[A]
$i(t)$	bunch current, Eq. (3.2)	[A]
$I(f)$	spectrum of bunch current signal $i(t)$	[A/Hz]
$I^*(f)$	conjugate complex of bunch current spectrum $I(f)$	[A/Hz]
L	orbit length	[m]
L_0	orbit length of reference particle	[m]
ΔL	orbit length relative to reference particle Eq. (1.7)	[m]
m_0	particle mass at rest	[kg]
α_c	momentum compaction factor, Eq. (1.24)	
N_e	number of electrons	
$P(f)$	power spectrum, Eq. (3.1)	[W/Hz]
p_d	electron probability density function: normalized profile $\rho(t)$	
Q	electrical charge	[C]
R	radius of curvature of an electron inside the bending magnet	[m]
ψ	particles arriving phase of the RF voltage	[deg]
ψ_0	reference particle arriving phase of the RF voltage	[deg]
$\Delta\psi$	RF phase offset to reference particle Eq. (1.7)	[deg]
III	Shah distribution, Eq. (8.7)	
Π	shielding factor Eq. (2.48)	
$s_F(t)$	filling pattern signal	
$s_p(t)$	single pulse electric field	[V/m]
$S_p(f)$	spectrum of single pulse signal	[Vs/m]
τ_s	synchrotron oscillation amplitude	[s]
τ_d	longitudinal damping time, Eq. (1.28)	[s]
v	particle speed. In the ultra-relativistic limit $v = c$	[m/s]
V_k	intensity of a bunch in the filling pattern signal $s_F(t)$, Eq. (8.16)	
β_d	normalized damping time, Eq. (2.39)	
θ	normalized time coordinate, Eq. (2.36)	
p	normalized energy coordinate, Eq. (2.36)	
q	normalized longitudinal coordinate, Eq. (2.36)	
V_{RF}	RF voltage amplitude	[V]
$V_{\text{RF,eff}}$	effective accelerating voltage per turn	[V]
W	energy loss per turn, Eq. (1.20)	[eV]
W_0	energy loss per turn of reference particle	[eV]
$W(t)$	wake function, Eq. (2.1b)	[Ω/s]

V_w	wake potential, Eq. (2.32)	[V]
w_c	width of the vacuum chamber	[m]
z	longitudinal coordinate, see Chap. 1.2.6 and Eq. (2.35)	[m]
$Z(f)$	impedance spectrum, Eq. (2.1a)	[Ω]

Constants

c	speed of light in vacuum ($2.997\,924\,58 \times 10^8$)	[m/s]
C_q	radiation constant (3.84×10^{-13})	[m]
e	electric charge unit ($1.602\,176\,53 \times 10^{-19}$)	[C]
μ_0	vacuum permeability ($4\pi \times 10^{-7}$)	[Vs/Am]
Z_0	free space impedance ($Z_0 = \mu_0 c \approx 119.92\pi$)	[Ω]
ε_0	vacuum permittivity ($8.854\,187\,817 \times 10^{-12}$)	[F/m]
$m_e c^2$	electron energy at rest ($510.998\,18 \times 10^3$)	[eV]

1 Introduction

*“Begin at the beginning,” the King said gravely,
“and go on till you come to the end: then stop.”*

— Lewis Carroll, Alice in Wonderland

1.1 Outline

Although the emission of energy by accelerated particles had already been proposed in 1912 [1], it took until 1945, to detect this radiation [2], and until 1947 before the first visible light was observed in an electron synchrotron [3]. This emitted radiation was therefore called *synchrotron light* and has since then experienced a rapid growth in its scientific use. Special accelerators, dedicated to the production of synchrotron radiation, were built and are still continuously developed further, because of the superior properties of this radiation, like an ultra-broadband spectrum and high beam-collimation. Often, the history of light sources is grouped into four generations [4].

The first generation were parasitic users of circular electron synchrotrons. In the second generation, from 1968 on, special electron storage rings were built, exclusively for the use of synchrotron radiation. The third generation of light sources, whose first machines came online around 1992, had special long straight sections in the ring for the installation of so-called insertion devices to increase the radiation output. Additionally, these rings had reduced electron beam emittance to achieve a smaller and more collimated light beam. The fourth generation of light sources, recently going into operation, have such a small emittance that the light source-point becomes diffraction-limited even for X-ray radiation. Further reduction of the transverse electron beam dimensions would therefore not have any additional gain.

The next significant improvement of brilliance could be achieved by either much higher peak current or much shorter bunch length, or a combination of both. Both

tasks would be very challenging, yet they have the potential to increase the intensity and quality of the synchrotron radiation by many orders of magnitude. A bunch length which is shorter than or equal to the wavelength of the observed radiation leads to the emission of coherent synchrotron radiation. The power of coherent radiation is proportional to the number of the involved electrons squared, whereas the power of incoherent radiation is only linearly proportional to the number of electrons involved. Therefore, coherent radiation leads to an increase of the emitted power in the range of 1×10^8 to 1×10^{11} , which corresponds to the number of electrons per bunch in a synchrotron. Furthermore, single cycle light pulses would be emitted, which would enable new kinds of experiments.

These improved features of ultra-short bunches of femtosecond length are already used by X-ray Free Electron Lasers (FEL), linear accelerators like the LCLS II in California or the European XFEL in Hamburg (Germany). They are used especially for time-resolved pump-probe experiments with hard X-rays. However, in comparison to a synchrotron, the linear accelerators are limited in pulse repetition rate, number of parallel users, and the stability of the light quality. Therefore, circular light sources cannot be replaced by linear accelerators and have to be considered as complementary measurement stations. For this reason, research of ultra-short electron bunches in storage rings is being intensified.

Due to instabilities, the combination of shorter pulses and higher beam currents is limited in synchrotrons. Currently, bunch lengths of about a picosecond are achieved, before micro-structures on the usually Gaussian shaped bunches lead to the uncontrolled emission of THz radiation and blow up the bunch length. Although the responsible micro-bunching instability (MBI) was predicted, simulated, and experimentally verified already in 2002 [5; 6; 7], the bunch dynamics above the threshold are still not completely understood. The outbursts of THz radiation by this instability have already been observed at various facilities, i.e. Bessy II [10; 9; 8], SURF II [11] and III [12], ANKA [13], NSLS VUV [15; 14], ALS [7], UVSOR-II [16; 17], MAX I [18], Diamond [19; 20], MLS [21], Soleil [22], MIT-Bates [23], Elettra [24], CLS [25]. Yet, no practical cure to the instability has been found¹.

¹ A solution was presented by Nodwick & Saxon in 1954 by suppressing the radiation with the vacuum chamber walls, whose distance has to be in the order of the bunch length. However, for bunches shorter than a millimeter, this is no longer practical. This is discussed in more detail in Chapter 3.1.

By analyzing the emitted THz radiation during the instability, conclusions can be drawn about their nature, and options to influence them can be quantified. The accelerator diagnostic with synchrotron radiation in the THz regime still is a relatively young field compared to conventional methods, because for a long time neither sources nor detectors were available for this spectral range between millimeter waves and infrared radiation. However, great progress has been achieved in the past years, so that simple THz diagnostic is now being used at many accelerators.

This dissertation investigates and demonstrates new methods of beam diagnostics in the THz regime. An improved diagnostic is important in order to characterize the instabilities, so that in future times they can be controlled. This might lead to shorter and more intense coherent light pulses for scientific use. The thesis starts with a small introduction into the context and the workplace along with some basics of synchrotron storage rings and the short bunch operation. Chapter 2 introduces the concept of electron beam impedances and how they affect the bunch shape and size, and finally lead to the micro-bunching instability. Furthermore, recent theoretical developments describing the instabilities are presented and our in-house numerical simulation tool is introduced. The emission of coherent and incoherent synchrotron radiation is presented in Chapter 3 with a special focus on the extraction of radiation of the comparably long wavelengths of the THz radiation to the experimental stations. In Chapter 4, the used experimental equipment, like THz optics and detectors, and the corresponding readout devices are discussed.

The following experimental chapters start with state-of-the-art Fourier transform infrared spectrometry (FTIR) measurements in Chapter 5. Beginning with a commercial Michelson interferometer, a self-made Martin-Puplett interferometer is set up with ultra-fast THz detectors in a balanced detection mode. Although interferometers provide a good compromise between spectral resolution and repetition rate, they are limited in both because the time-bandwidth product is a constant. Therefore, the best spectral resolution and the highest repetition rate cannot be achieved at the same time. The work in hand presents two complementary setups to achieve each of them individually in the subsequent chapters.

Single-shot measurements with ultra-fast THz detectors are presented in Chapter 6. Basic characteristics of the micro-bunching instability are shown experimentally. Bursting spectrograms are introduced as a fingerprint of the instability, and measurements of the weak and strong micro-bunching instability are analyzed. In the end of

the chapter, first results in controlling the instability by RF phase modulations are presented.

In Chapter 7, the currently fastest THz spectrometer setup, continuous streaming of 500 million single-shot spectra per second, is presented and its potential demonstrated by first measurements. The bunch-to-bunch measurements are compared to simulation, and some characteristic bunch currents are evaluated in greater detail.

Chapter 8 focuses on heterodyne measurements, allowing resolution bandwidths better than 1 Hz at 0.27 THz. With this setup, the emitted frequency comb of the storage ring is revealed. The established theory of the emitted high resolution spectrum focuses on signals observed by electrical pickup electrodes in the micro-wave region and is therefore extended for synchrotron radiation in the THz range. For the first time, the dependence of the filling pattern in the storage ring on the emitted spectrum is systematically analyzed and the experimental results are compared to the developed theory.

A summary and an outlook in Chapter 9 complete the work.

1.2 Conventions

I have spent most of the day putting in a comma and the rest of the day taking it out.

— Oscar Wilde

1.2.1 Citations

There are three different kinds of citations used in this thesis. External citations are given in numeric style and sorted by their first occurrence. My own publications are given in a separate list with the first three letters of the main author followed by the year of publication. The same style is used for the last type of citations of supervised theses.

1.2.2 Units

In particle physics and especially in the USA, the Gaussian centimetre–gram–second system of units (CGS) and Lorentz–Heaviside CGS unit systems are very popular and have support from theorists. Throughout this thesis, however, SI units are used consequently. If the cited formula was in Gaussian units, it has been converted according to Ref. [26]. An exception from the strict SI units is done to quantify the energy of accelerated particles in the unit of electron volts (eV) rather than Joule. An elementary charge e experiencing the field of 1 V gains an energy of $1 \text{ eV} \approx 1.602\,18 \times 10^{-19} \text{ J}$.

1.2.3 Ultra-fast

In the following, the term *ultra-fast* is applied for an equipment that is able to resolve at least two adjacent light pulses without pile-up. In practice that applies to time constants faster than 500 ps or analog bandwidths higher than 2 GHz.

1.2.4 Terahertz

The frequency range between millimeter waves and infrared radiation is named *terahertz*. This term is used in this thesis to describe frequencies between 300 GHz and 3 THz or wavelengths between 1 mm and 100 μm , respectively.

1.2.5 Fourier Transformation

The Fourier Transformation (FT) connects time and frequency domain. The general form can be written as [27, eqn. 15-16]

$$F(f) = \sqrt{\frac{|b|}{(2\pi)^{1-a}}} \int_{-\infty}^{\infty} f(t) e^{-jbft} dt, \quad (1.1)$$

$$f(t) = \sqrt{\frac{|b|}{(2\pi)^{1+a}}} \int_{-\infty}^{\infty} F(f) e^{jbft} df, \quad (1.2)$$

where in literature various values of a and b are used. When working with angular frequencies $\omega = 2\pi f$, the preferred choice is $a = 0, b = 1$. The often used $a = 1, b = 1$ has the disadvantage of different pre-factors so that Parseval's theorem is no longer a

unitary transformation. In this thesis, the engineering convention of $a = 0, b = 2\pi$ is used leading to

$$F(f) = \int_{-\infty}^{\infty} f(t)e^{-j2\pi ft} dt, \quad (1.3)$$

$$f(t) = \int_{-\infty}^{\infty} F(f)e^{j2\pi ft} df. \quad (1.4)$$

Wherever applicable, capital letters are used in frequency domain, while small letters refer to the time domain.

A simple Gaussian $e^{-t^2/(2\sigma_t^2)}$ with a root mean square (RMS) width of σ_t transforms to another Gaussian $\sqrt{2\pi\sigma_t^2}e^{-2\pi\sigma_t^2 f^2}$, which leads to an RMS width of $\sigma_f = \sqrt{(4\pi\sigma_t^2)^{-1}}$ [28, pp. 105–106]. The so-called *time-bandwidth product (TBP)* is then $\sigma_t\sigma_f = \sqrt{(4\pi)^{-1}}$. Such a pulse is called *Fourier limited*.

Deviations from a Gaussian pulse lead to higher TBPs. As a rule of thumb, a TBP of one is used. Therefore, a pulse with a length of 1 ps covers at least a spectral bandwidth of 1 THz. On the other hand, to achieve a frequency resolution of 10 Hz, a signal has to be observed for at least 100 ms.

1.2.6 Coordinate System

The position of the particles can be described by a Frenet–Serret type coordinate system [29, p. 22]. This is a Cartesian coordinate system which moves with the particle bunch. Therefore, an ideal beam path s through the accelerator is defined, which is the path of a *reference particle*. In the longitudinal axis, it is also called the *synchronous particle*, as it is synchronous to the radio frequency (RF) system and always arrives at the same RF phase. So every particle has x , y and z coordinates relative to the synchronous particle. The s axis is along the particle's trajectory, while the z axis is orthogonal to x and y and therefore tangential to the beam path. For very small distances, s equals z . This coordinate system is sketched in Fig. 1.1.

As the bunch is moving with relativistic speed, a direct observation to measure the length or profile is usually not practical, and therefore, longitudinal diagnostics are mostly done in time-domain measurements like an oscilloscope trace, given in units of time. For ultra-relativistic electrons, the z axis, given in units of length (z_s), can be converted to an axis in units of time (z_t) by the speed of light c

$$z_s = -cz_t. \quad (1.5)$$

The minus sign accounts for different axis conventions. While the position in length is relative to the synchronous particle and positive values account for positions in front, the time axis is given in the laboratory frame, where particles ahead arrive earlier (negative time). Thus, the axis is in accordance to what a stationary observer would see on an oscilloscope trace.

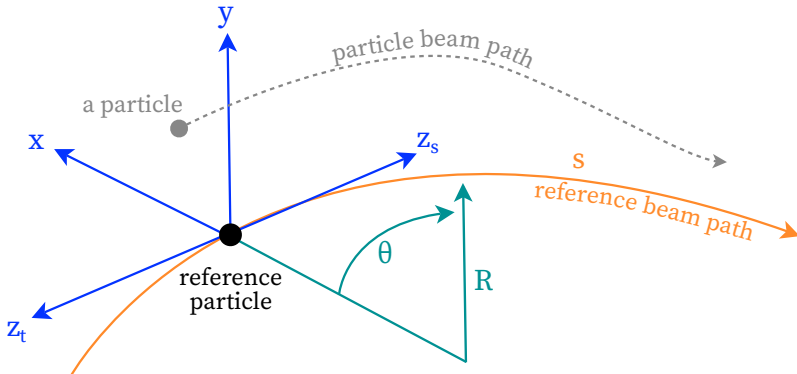


Figure 1.1: Frenet-Serret coordinate system (adapted from [30]).

To summarize: A bunch density profile $\rho(t)$ as depicted in Fig. 1.2 can be given in units of length or time depending on the context. While for theory the axis in length is preferred, experiments use the measured value of time. Often, a dimensionless axis in units of the natural bunch length is used. Especially then special care has to be taken of the different sign convention. In this thesis, wherever applicable, the head of the bunch is to the right.

On the other hand, as RMS values are not affected by the sign conventions, the bunch length $\sigma_{z,s}$ and the bunch duration $\sigma_{z,t}$ are directly connected by the speed of light:

$$\sigma_{z,s} = c\sigma_{z,t} \quad (1.6)$$

In this thesis, the expression *bunch length* is also used to describe a *bunch duration*, as it has become common in the accelerator community.

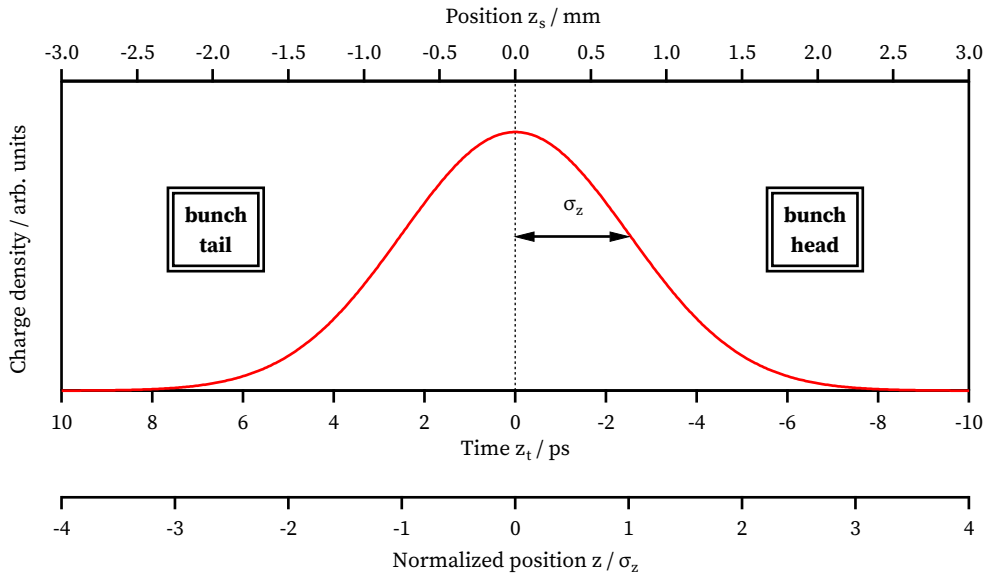


Figure 1.2: Longitudinal line density profile of a bunch. The time axis is defined like an oscilloscope trace, where the time is negative at the bunch front, as it arrives before the tail of the bunch. The position is relative to the synchronous particle, where particles ahead have positive distances.

1.3 Synchronous Particle

The *synchronous particle* described above is used as a reference not only for the spatial coordinates but also for values like particle energy E , revolution time T , path length L or arrival time phase ψ . The quantities can be expressed relatively to the reference, where the subscript 0 denotes the synchronous particle

$$\Delta E = E - E_0, \quad (1.7)$$

$$\Delta L = L - L_0, \quad (1.8)$$

$$\Delta \psi = \psi - \psi_0, \quad (1.9)$$

$$\Delta T = T - T_0. \quad (1.10)$$

1.4 Ultra-Relativistic Approximations

This work has been done in the context of an electron storage ring, where the electrons are accelerated close to the speed of light. At relativistic speeds, the velocity v is often given as a fraction of the speed of light c : $\beta = \frac{v}{c}$. Very close to the speed of light, it is more convenient to scale with the Lorentz factor

$$\gamma = \frac{1}{\sqrt{1 - \beta^2}} = \frac{E}{E_{\text{rest}}}. \quad (1.11)$$

where E is the particle's total energy and E_{rest} its energy at rest. The relation to the particle's momentum p is $E = \sqrt{p^2 c^2 + E_{\text{rest}}^2}$. For all studied particle energies, $E \gg E_{\text{rest}}$ and therefore, the following approximations are used in the following

$$\beta \approx 1, \quad (1.12)$$

$$v \approx c, \quad (1.13)$$

$$E \approx pc. \quad (1.14)$$

1.5 Particle Acceleration and Storage Rings

Nothing happens until something moves.

— Albert Einstein

Until the early 1930s, radioactive sources had been used in experiments as a source of fast, high energetic particles. This changed when John D. Cockcroft and Ernest Walton at the Cavendish Laboratory in Cambridge, England, used a 200 kV transformer to accelerate protons down a straight discharge tube [31]. Using capacitors, connected by rectifying diodes as switches, they managed to increase the accelerating voltage to 800 kV. The accelerated protons were shot onto a lithium target that disintegrated into two alpha particles [32]. This was not only the first artificial splitting of a nucleus, but also the first transmutation using artificially accelerated particles. They also observed a loss in the total mass of the nuclei. This reaction was the first experimental proof of Einstein's $E = mc^2$. Cockcroft and Walton were awarded the Nobel Prize in physics in 1951 “for their pioneer work on the transmutation of atomic nuclei by artificially accelerated atomic particles” [33].

1.5.1 Acceleration of Charged Particles

Dr Livingston has asked me to advise you that he has obtained 1,100,000 volt protons.

He also suggested that I add ‘Whoopee’!

— Secretary of the Department, Telegram to E.O. Lawrence, 1931

In order to accelerate particles, a force needs to be applied. Technically feasible is the use of electromagnetic fields on charged particles Q , described by the Lorentz force \vec{F}_L

$$\vec{F}_L = Q(\vec{E} + \vec{v} \times \vec{B}). \quad (1.15)$$

In the same equation (1.15), due to the cross-product, only perpendicular components of the magnetic field \vec{B} and the particle's velocity \vec{v} are considered. As a result, a magnetic field does not change the particle's energy, but rather its direction. It should be mentioned here, that the direction can also be changed by electric fields \vec{E} . However, for ultra-relativistic particles ($v \approx c$), as used in this work, a 1 T magnet achieves the same deflection as an unrealistic high electric field of 300 MV/m would do. Therefore, in general, electric fields are used to accelerate the beam, while magnetic fields are used for steering and focusing. The magnetic fields guide the particles on a path, where the deflection angle R can be determined by the equilibrium of Lorentz and centripetal force, which is for transverse magnetic fields by using the approximation of Eq. (1.14)

$$R = \frac{E}{BQc}, \quad (1.16)$$

with the particle energy E and the particles charge Q . Particles with a higher energy are less deflected, while a higher magnetic field deflects stronger. Due to the saturation of iron, the field limit for a normal conducting magnet is around 1.5 T. Therefore, in order to store a 2.5 GeV electron, a minimum radius of 5.556 m is needed. For smaller radii, superconducting magnets, providing higher fields would be necessary.

An energy change of the particles can only be done with electric fields. Electro-static fields as used in cathode ray tubes are limited by the break down voltage. For further acceleration, time-varying fields are needed. In 1928 Rolf Widerøe described a method to accelerate particles repeatedly by switching the polarity of the accelerating field while the particle is in a shielded environment [34]. This method, however, needed a long vacuum tube that couldn't be built at that time but later led to the development of the betatron [35]. Inspired by the work of Widerøe, Ernest O. Lawrence and M. Stanley

Livingston built the first cyclotron in Berkeley, USA [36]. This device forces the particles on a circular orbit by an external magnetic field. An accelerating structure was used to transfer 1800 eV to the particles at every turn. As the magnetic field stayed constant, the orbit of the particles increased with their energy and limited the device to 80 keV.

In 1944, V. I. Veksler proposed “A New Method of the Acceleration of Relativistic Particles” in several publications [37; 38; 39] where both, the accelerating electric field and the magnetic field are changed synchronously to the particle energy to keep the particle orbit constant. This was the invention of the synchrotron, a circular accelerator with the ability to create highest particle energies, limited by the maximum magnetic field, defining the radius of curvature in the bending magnets. A special case of a synchrotron is a storage ring, where the accelerating structures just equalize the losses of the particles, keeping the energy constant. Until today, this principle is used in colliders, accumulation rings, or synchrotron radiation sources.

1.5.2 Radiation of Charged, Relativistic Particles

The following sections review only the basics of the radiation of charged relativistic particles. The interested reader can find a detailed discourse of Jackson [40] and Hofmann [41].

The Coulomb field of the accelerated particles has to follow the particles’ path. In 1864, James Clerk Maxwell published first versions of the later called *Maxwell equations* about the creation and interaction of electric and magnetic fields. Alfred-Marie Liénard in 1898 [42] and independently Emil Wiechert in 1900 [43] derived the theory of retarded potentials which leads to the far-fields of moving charge carriers. Following on that work, Joseph Larmor found out that a part of the coulomb field can not follow the acceleration and is radiated off [44].

In the non-relativistic case the emitted power of a particle with momentum $\vec{p} = m_0 \vec{v}$ and the charge Q is

$$P = \frac{\mu_0 Q^2}{6\pi c} \left(\frac{d\vec{p}}{dt} \right)^2, \quad (1.17)$$

where $\mu_0 = (\epsilon_0 c^2)^{-1}$ is the magnetic constant and c the speed of light in vacuum. Obviously a particle without momentum change does not radiate. Even with changes, in the classical model the emitted radiation is negligible. However, for relativistic

momenta, as they happen in an accelerator, the Lorentz-invariant form has to be considered. For electrons $Q = e$ in the following equation [45]:

$$P = \frac{e^2 c}{6\pi\varepsilon_0(m_0 c^2)^2} \left[\left(\frac{d\vec{p}}{dt} \right)^2 - \frac{1}{c^2} \left(\frac{dE}{dt} \right)^2 \right]. \quad (1.18)$$

The emitted energy is highly dependent on the direction of acceleration. A linear acceleration, even with today's highest achievable field gradients of up to 150 MeV/m, would result in $P \approx 4 \cdot 10^{-16}$ W. Considering that the radiation only occurs during the acceleration process, this energy loss can be neglected. On the other hand, centripetal acceleration ($\frac{d\vec{p}}{dt} = d\omega = d\frac{v}{R}$) as it happens in circular accelerators, leads to a much higher energy loss. The emitted power by an electron on a circular orbit R simplifies with the approximation $v \approx c$ to

$$P = \frac{e^2 c}{6\pi\varepsilon_0(m_0 c^2)^4} \frac{E^4}{R^2} = \text{const.} \cdot \frac{\gamma^4}{R^2} \quad (1.19)$$

In 1898, long before this radiation had been named synchrotron radiation, Liénard developed Eq. (1.19) and found the radiation to depend on the fourth power of the ratio of energy at rest to total energy, and to the radius squared [42]. To get the highest synchrotron radiation power, electrons are the preferred source particles as they have the lowest rest mass of charged particles².

The total energy emitted by a single particle over one turn is

$$W = \oint P dt = P \frac{2\pi R}{c} = \frac{e^2}{3\pi\varepsilon_0(m_0 c^2)^4} \frac{E^4}{R} = \frac{e^2}{3\pi\varepsilon_0 R} \gamma^4. \quad (1.20)$$

with $m_e c^2 = 510.998\,18$ keV. The energy loss per turn of a single electron in the Karlsruhe research accelerator (KARA) is shown for different energies in Tab. 1.1. The emitted energy of a bunch of particles and the angular distribution are discussed in more detail in Chapter 3.

² The same properties apply for positrons. However, their production is much more complex and costly.

Table 1.1: Energy loss per turn of a single electron in KARA

Particle energy	γ	Energy loss per turn	
[GeV]		[J]	[keV]
0.5	979	1.6×10^{-16}	1
1.3	2545	7.3×10^{-15}	46
2.5	4893	1×10^{-13}	623

1.5.3 Longitudinal Beam Dynamics

The following derivation of the synchrotron motion is based on Chapter 5.6 of Ref. [45] with the difference, that I distinguish between the absolute energy offset to the synchronous particle ΔE and the change in energy offset δE .

In a storage ring, the emitted energy has to be fed back into the bunch so that the average particle energy stays the same. This is achieved by using a radio frequency (RF) station which drives a cavity resonator. The cavity is mounted into the storage ring so that an alternating electric field in longitudinal direction is built up. A passing electron gains energy equal to the electric field inside the cavity at the time of transit

$$V_{\text{RF,eff}} = V_{\text{RF}} \sin \psi, \quad (1.21)$$

the RF field-change during the passage being neglected. An equilibrium particle energy is reached, when the energy gained in the cavity compensates the losses around the ring

$$eV_{\text{RF}} \sin \psi_0 = W_0. \quad (1.22)$$

In the case of an equilibrium, the energy loss per turn is constant and thus is the correct RF phase. Consequently, the revolution frequency has to be an integer multiple of the RF frequency. This is called the *harmonic number* h

$$f_{\text{RF}} = h f_0, \quad (1.23)$$

with $h = 184$ at KARA.

A particle with a slightly higher energy than the synchronous particle ($\Delta E > 0$) experiences a larger bending radius and therefore, covers a longer path ΔL around

the accelerator. However, due to the higher energy, the velocity of the off-momentum particle is increased, too. These effects are summarized in the *momentum compaction factor* α_c , that accounts for the proportionality between a length ΔL offset over one turn due to an energy offset ΔE . With the approximation of ultra-relativistic particles, the length offset directly corresponds to a revolution time offset

$$\frac{\Delta L}{L_0} \approx \frac{\Delta T}{T_0} \approx \alpha_c \frac{\Delta E}{E_0}. \quad (1.24)$$

The momentum compaction factor is influenced by the magnet optics and given in first order by the integral of the dispersion $D(s)$ in the bending sections $R(s)$ around the ring

$$\alpha_c = \frac{1}{L_0} \oint \frac{D(s)}{R(s)} ds. \quad (1.25)$$

As a consequence, with a positive momentum compaction factor, particles with a lower momentum arrive earlier. Stable operation happens when the particles hit the falling slope of the accelerating RF where the earlier particles gain more energy than the late ones. This leads to a longitudinal focusing, called *phase focusing*. In summary, particles orbiting in a storage ring perform longitudinal oscillations with having a periodic phase and energy shift. This is described by the longitudinal equation of motion³

$$\Delta \ddot{E} + \frac{2}{\tau_d} \Delta \dot{E} + \omega_s^2 \Delta E = 0, \quad (1.26)$$

with the *synchrotron frequency* f_s

$$f_s = \frac{\omega_s}{2\pi} = f_0 \sqrt{-\frac{\alpha_c h e V_{RF} \cos \psi_0}{2\pi E}}, \quad (1.27)$$

and the longitudinal *damping time* τ_d

$$\frac{1}{\tau_d} = \frac{1}{2T_0} \frac{W_0}{E_0} \mathcal{J}_E, \quad (1.28)$$

with \mathcal{J}_E being the damping partition number, which is $\mathcal{J}_E \approx 2$ for most storage rings. As a rule of thumb, the damping time is the time a particle would need to radiate away its total energy [46, p. 102].

³ A detailed derivation of the equation of motion can be found in App. A

This is illustrated in Fig. 1.3 which shows the longitudinal phase space of energy deviation and phase offset (or arrival time). The synchronous particle is defined to be in the center. A particle with less energy, for example due to spontaneous synchrotron radiation, experiences a stronger deflection in the magnets and, with a positive momentum compaction factor, the particle arrives earlier at the next cavity. There it gains more energy than the synchronous particle and the energy offset shrinks. However, the energy is still reduced and the phase offset increases further, leading to an even higher effective voltage at the cavity. At some point, the energy is the same again as that of the synchronous particle, but the position differs, and the particle still gains more energy in the cavities. Having a positive energy offset with respect to the synchronous particle, the deflection is less in the magnets, and the time offset shrinks. To make a long story short, the particle oscillates harmonically around the synchronous particle, where the oscillation is damped with the longitudinal damping time τ_d .

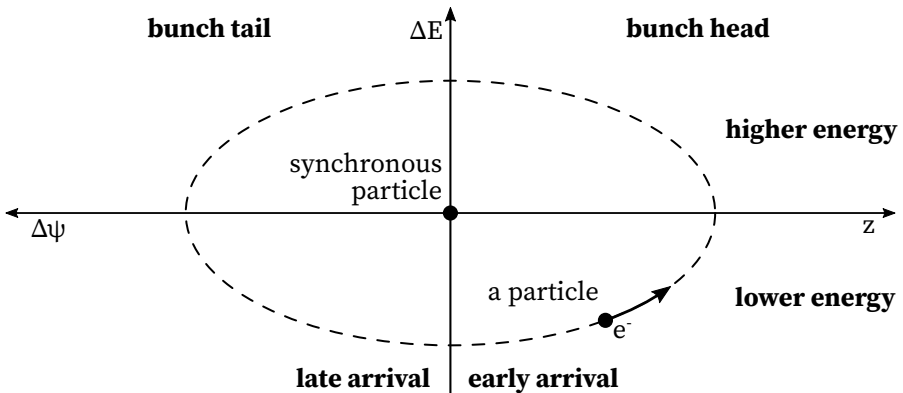


Figure 1.3: Longitudinal phase space: A particle having less energy than the synchronous particle arrives earlier at the cavity and thus gains more energy. This phase focusing effect leads to a harmonic oscillation around the synchronous particle, whose amplitude is damped with the longitudinal damping time τ_d .

One distinguishes between *incoherent* synchrotron motion, which describes the motion of individual particles and *coherent* synchrotron motion, which a whole bunch of particles performs. While the incoherent motion of a stable bunch, with a sufficiently high number of particles inside, can hardly be measured, the oscillation of a whole bunch around the stable phase is observed on the longitudinal profile and position, i.e. arrival time. The bunch can perform several modes of oscillation in the phase space, due to different instabilities. A more detailed discourse can be found in Ref. [47]. Figure

1.4 illustrates different modes of oscillation. A bunch with an energy offset oscillates around the synchronous phase with the synchrotron frequency, performing a *dipole* oscillation. A *quadrupole* oscillation leads to periodic bunch length fluctuations with twice the synchrotron frequency. Sextupole and octupole modes are not discussed here but lead to the observation of higher synchrotron frequency harmonics.

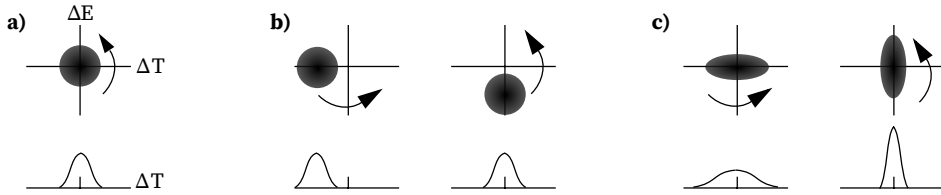


Figure 1.4: Longitudinal phase space modes. For a stationary distribution (a), where all particles oscillate harmonically around the stationary synchronous particle, the projection stays constant. However, when the bunches' center of mass oscillates back and forth (b), an oscillation with the synchrotron frequency is observed in the longitudinal plane whereas a quadrupole motion (c) leads to a bunch length modulation with twice the synchrotron frequency. The time difference between the pictures in (b) and (c) is a quarter of a synchrotron period. Like [11], modified.

The beam position monitoring system at the storage ring measures the center of mass of the bunch and can therefore determine the coherent oscillation frequency. Especially at high beam currents, the coherent motion and the incoherent motion can happen with slightly different frequencies, where the incoherent motion is usually a bit slower. This depends on the imaginary part of the beam impedance, discussed in more detail in Chapter 2. Moreover, this is a possible source of errors between the simulations, which is introduced in Chapter 2.4 and the measurements. While the coherent oscillation frequency is measured, the simulation needs the incoherent frequency as input parameter.

Bunch length

The bunch length is the projection of all particles in the phase space onto the phase axis and is determined by the amplitude of the incoherent synchrotron motion. In dependence of the phase offset it is

$$\sigma_{z,s} = \frac{c}{2\pi f_{RF}} \hat{\psi}. \quad (1.29)$$

In Eq. (1.26) was shown, that the phase performs an harmonic oscillation with the synchrotron frequency

$$\psi(t) = \hat{\psi} \sin(2\pi f_s t + \phi), \quad (1.30)$$

$$\dot{\psi}(t) = 2\pi f_s \hat{\psi} \cos(2\pi f_s t + \phi). \quad (1.31)$$

The amplitude of the phase-change oscillation ($2\pi f_s \hat{\psi}$) equals Eq. (A.2) at the maximum energy deviation $\Delta \hat{E}$, which leads to a maximum RF angle of

$$\hat{\psi} = \frac{f_0 h \alpha_c}{f_s} \frac{\Delta \hat{E}}{E_0}. \quad (1.32)$$

A bunch length is only defined for a bunch of particles, all having a different energy deviation. A RMS energy spread over all particles is defined as

$$\sigma_E = \sqrt{\langle (E - E_0)^2 \rangle}, \quad (1.33)$$

which, by inserting (1.32) into (1.29), leads to a RMS bunch length of

$$\sigma_{z,s} = \frac{\alpha_c c}{2\pi f_s} \frac{\sigma_E}{E_0}. \quad (1.34)$$

Often, the relative energy spread is used

$$\sigma_\delta = \frac{\sigma_E}{E_0}. \quad (1.35)$$

By inserting the synchrotron frequency of Eq. 1.27, the bunch length reads

$$\sigma_{z,s} = \frac{c}{2\pi f_0} \sqrt{-\frac{2\pi \alpha_c E}{e h V_{RF} \cos \psi_0}} \sigma_\delta, \quad (1.36)$$

where $c/(2\pi f_0)$ equals the average bending radius $\langle R \rangle = L_0/(2\pi)$ of the storage ring. The bunch length at a given Energy E is therefore dependent on the RF amplitude V_{RF} and the momentum compaction factor α_c

$$\sigma_{z,s} \propto \sqrt{\frac{\alpha_c}{V_{RF}}}. \quad (1.37)$$

One has to keep in mind, that Eq. 1.36 is only valid without additional forces, i.e. the potential of nearby electrons. Therefore, the calculated bunch length is that of a

hypothetical zero-current bunch and called *zero-current bunch length* $\sigma_{z,0}$. Chapter 2.2 discusses current-dependent bunch deformations, which usually leads to increased RMS bunch lengths.

1.5.4 Natural Energy Spread and Natural Bunch Length

The longitudinal damping calculated above leads to a shrinking of the energy spread and therefore a reduction in bunch length. However, the emission of synchrotron radiation photons of a single electron is a statistical process. On average, every electron with the same energy emits the same amount of radiation. But the exact time and position differ. Consider two identical particles, one emitting a photon at the beginning of a bending magnet and the other particle emitting an equal photon at the end. After the bending magnet, the energy of both electrons is the same again, but their position differs, because the particle which has emitted the photon at the beginning of the magnet experienced a slightly stronger deflection due to its reduced energy. This horizontal position offset is transformed into an energy offset on the pathway through the accelerator. Therefore, the discrete emission of energy leads to an increase of the energy spread. Both mechanisms, the statistical emission and the radiation damping, result in an equilibrium, called the *natural energy spread* $\sigma_{\delta,0}$ and can be calculated according to Ref. [29, p. 301 ff.]

$$\sigma_{\delta,0} = \frac{\sigma_{E,0}}{E_0} = \sqrt{C_q \frac{\gamma^2 \langle R^2 \rangle}{J_z \langle R^3 \rangle}}, \quad (1.38)$$

with $C_q = 3.84 \times 10^{-13}$ m being the radiation constant and $J_z \approx 2$ being the longitudinal partition number. The natural energy spread is therefore defined by the beam energy and the bending radius, similar to the emitted synchrotron radiation power. At a beam energy of 1.3 GeV at KARA, it is 0.47×10^{-3} . This natural energy spread is only reached at zero bunch current, as current-dependent effects, like the micro-bunching instability discussed in Chapter 2.3, increase the energy spread. The minimum bunch length, reached at the natural energy spread, is therefore called *zero-current bunch length* or *natural bunch length* $\sigma_{z,0}$.

1.6 KARA Storage Ring: The KIT Synchrotron

The Karlsruhe research accelerator (KARA) is a storage ring with a circumference of 110.4 m. It is operated by the Institute for Beam Physics and Technology (IBPT) of the Karlsruhe Institute of Technology (KIT), Germany, while the beamlines, using synchrotron radiation are being operated by other Karlsruhe Institute of Technology (KIT) institutes. Beside from providing high intensity synchrotron radiation to the beam lines, the mission of the IBPT involves the development and testing of new beam and acceleration technologies, pooling research of new accelerator concepts, and development of novel diagnostic methods. This is done in close cooperation with the Laboratory for Applications of Synchrotron Radiation (LAS), being associated with the university campus of KIT.

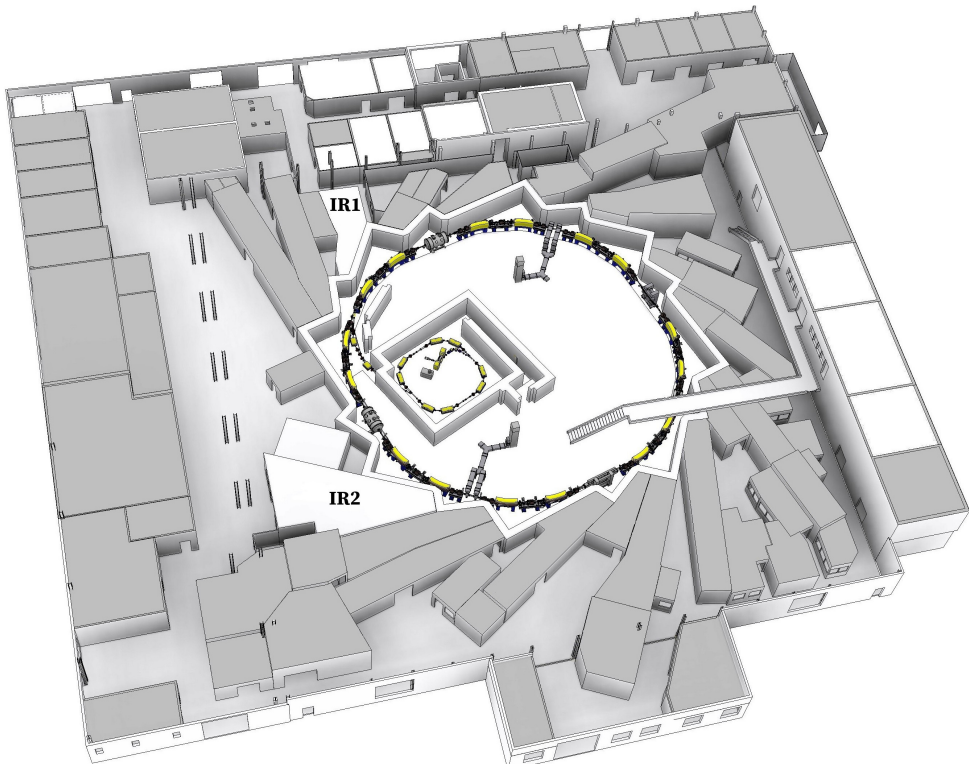


Figure 1.5: Overview of the KIT synchrotron radiation facility. Around the 110m long storage ring KARA, several beam lines are located. The two infrared beam lines (IR1 and IR2) are located in the south and west of the hall. The pre-accelerators are located inside the storage ring. Courtesy of IBPT-CAD

KARA consists of 16 bending magnets and 16 connecting straight sections of different length. Currently, five so-called insertion devices are installed in the longer straight sections serving synchrotron radiation to the attached beamlines. In order to generate the high relativistic electrons, low energy electrons are released from a hot cathode, then accelerated in pre-accelerators up to 500 MeV and inserted into the storage ring. There, the energy of the electrons can be varied in a range from 0.5 GeV to 2.5 GeV. The usual user operation for serving hard X-ray radiation is done at 2.5 GeV, while the short pulse length mode that is used in this work is mainly done at 1.3 GeV. The reason for this is investigated more deeply in Chapter 3, which focuses on the properties of the emitted radiation. Figure 1.5 shows a ground plan of KARA, the beam lines and corresponding laboratories.

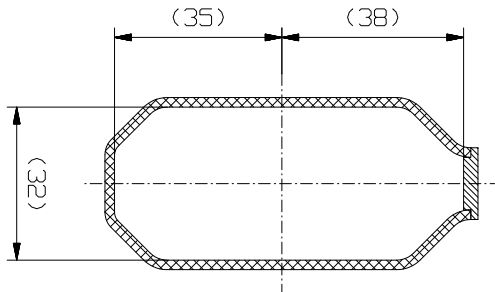


Figure 1.6: Cross section of the KARA beam pipe. The outer side has a water cooled synchrotron radiation absorber which leads to a small deviation of the symmetric geometry. Courtesy of IBPT-CAD.

At KARA, with an accelerating frequency of approx. 500 MHz, a bunch of particles can be accelerated every 600 mm. This makes up to 184 electron bunches over the whole 110.4 m long storage ring. The particles are guided by magnetic fields inside a vacuum chamber. This chamber is being evacuated in order to minimize the collision rate of the electrons with heavy residual gas particles. A cross section of the beam pipe is shown in Fig. 1.6. The asymmetry is due to a water cooled absorber for unwanted synchrotron radiation which placed on the outside. The height is 32 mm in the center and the width 75 mm+3 mm. The desired position of the electron beam is in the center of the beam pipe.

To accumulate electrons in the storage ring, the newly injected particles must have the same energy as the already stored ones. Due to the limited maximum energy of the pre-accelerators, this is only possible at the injection energy of 500 MeV. A usual operation cycle starts with the accumulation of electrons at injection energy

and then the storage ring is ramped up to the desired energy. Electrons lost during the experiment can not be replaced. Because of several effects, like the scattering at residual gas molecules or beam instabilities, the stored electrons get lost. As a rough estimate, one electron gets lost per turn, resulting in several hours of good experimental conditions. However, the bunch charge is continuously decreasing. This is called *beam decay*. In this thesis charge dependent effects are being investigated. Most of them have been recorded during such a beam decay, where every ten seconds a dataset was taken, while the bunch charge slowly decreased. When the bunch charge becomes too low for the experiments, the leftover electrons are kicked out and the magnets are cycled to the injection energy again.

1.7 Short Bunch Length Operation at KARA

Equation (1.37) shows that the zero current bunch length (see Chap. 1.5.3) can be decreased by reducing the energy, by increasing the RF voltage, or by reducing the momentum compaction factor. The short bunch length operation at KARA is established at 1.3 GeV beam energy, which is below the nominal user operation energy of 2.5 GeV but above some beam instability regions [48]. The RF voltage can be tuned between ≈ 100 kV (the lowest value before the beam is lost) and 1.6 MV, which is currently the limit of the klystrons providing the accelerating voltage.

Table 1.2: KARA bunch lengths for different machine settings.

Setting	E / GeV	V _{RF} / kV	f _s / kHz	α _c	σ _{z,0} / ps
Injection	0.5	328	35	8.6×10^{-3}	7.1
Unsqueezed	1.3	732	32	8.4×10^{-3}	19.4
Short bunch operation	1.3	732	7.5	4.6×10^{-4}	4.5
Fully squeezed	1.3	1500	6.3	1.6×10^{-4}	1.9
User operation	2.5	1288	30.5	1×10^{-2}	45

The momentum compaction factor $α_c$ is the integral over the dispersion of the ring (see Eq. (1.25)). By changing the beam optics to achieve a negative dispersion at some regions of the ring, the integral is stepwise reduced to $< 2 \times 10^{-4}$. This leads to a minimum achievable zero-current bunch length of under 2 ps. Bunch lengths for

different machine settings are summarized in Tab. 1.2. Please note, that the given values are subject to change. In contrast to other light sources, where the beam optics are kept stable for years, at the test facility KARA the optics are often adjusted to meet special requirements [Pap18]. This can be the installation of new insertion devices and diagnostics as well as continuous optimization of the beam parameters. Therefore, I explicitly state the used operation settings for every experiment.

2 Beam Impedances, Wake Potentials and the Micro-Bunching Instability

Nature is written in mathematical language
— Galileo Galilei, 1564-1642

In the first part of this chapter the concept of beam impedances is introduced. This concept was invented to describe how the electron beam is effected by the vacuum chamber and external magnetic or electric fields. It also allows to depict the emission of synchrotron radiation, which is the central part of this thesis and will be discussed in more detail in Chapter 3.

In the second part of this chapter, the actual effects of different impedances are characterized by the Haïssinski distribution as a stable solution of the Vlasov-Fokker-Planck equation. Then the micro-bunching instability is introduced and its threshold analyzed.

2.1 Beam Impedances in a Storage Ring

Forces and subsequent changes to the electron bunch can be described with an effective impedance analogously to the impedance in an electrical network which influences the moving charges in a conductor. Consequently, every part of the accelerator is described with its specific impedance, and from that the power loss and its influence to the bunch shape can be studied. This has first been done at CERN in 1966 by V.G. Vaccaro and named "beam coupling impedance" [49].

The electric field of an ultra-relativistic, point-like charge acts like a Dirac δ -impulse to the impedance and thus triggers its impulse response which is called *wake field* in analogy to a ship sailing in the wake emitted by another one. Nearby particles will,

depending on their position relative to the source particle, exhibit the integrated wake field on their path named the *wake function*.

The impedance $Z(f)$ and the wake function $W(t)$ are connected by their Fourier transform (for conventions see Chapter 1.2.5):

$$Z(f) = \int_{-\infty}^{\infty} W(t) e^{-j2\pi ft} dt \quad (2.1a)$$

$$W(t) = \int_{-\infty}^{\infty} Z(f) e^{j2\pi ft} df \quad (2.1b)$$

Since the impedance is in the familiar units of Ohm, the wake function has units of $[\Omega/s] = [V/C]$, which one can think of as a charge-normalized potential. Several different types of impedances are known today. *Geometrical impedances* describe the surrounding of the electron beam, where the impedance is given by the geometry and conductivity of nearby structures. Since the charge travels nearly with the speed of light, the geometric wake can not reach particles ahead, thus $W(t) \equiv 0$ for $t < 0$. Note that the front of the bunch passes the structure at time $t < 0$ (cf. Chapter 1.2.6).

A completely different type of impedance is due to the emittance of synchrotron radiation of the particle itself. As introduced in Chapter 1.5.2, the bunch emits energy when moving on an arc. This energy loss can also be modeled as an impedance which is named *synchrotron radiation impedance* (SR-impedance). The radiation is emitted in a cone in forward direction while the bunch travels on an arc, so that, in contrast to the geometric impedance, the SR-impedance acts on particles ahead. In the case of free space, without scattering and reflections, there is no SR-wake behind the particle $W(t) \equiv 0$ for $t > 0$. However, in a real environment, reflections at the boundaries will lead to a rich interaction of the whole electron bunch with its own emitted field, which will be analyzed in more details in Chapter 2.2.

Some properties of the beam impedances have been found to be [50]

a) $Z^*(f) = Z(-f)$

b) $\int_0^{\infty} \frac{\text{Im}\{Z(f)\}}{f} df = 0$

c) $\text{Re}\{Z(0)\} = 0$

d) $\text{Re}\{Z\} = \pi^{-1} \text{P.V.} \int_{-\infty}^{\infty} df' \frac{\text{Im}\{Z(f')\}}{f-f'}$

e) $\text{Im}\{Z\} = -\pi^{-1} \text{P.V.} \int_{-\infty}^{\infty} df' \frac{\text{Re}\{Z(f')\}}{f-f'}$

where P.V. denotes the principal value of the integral. a) is due to the fact that the impedance is the Fourier transform of the purely real wake function, and thus the real part of the impedance is even and the imaginary part is odd. The other items are due to causality. As described above, the geometric wake field cannot overtake the particles moving with the speed of light, while the radiation impedances lead to a wake field which is in front of the emitting particle. However, in the case of boundaries – like vacuum chamber walls – where reflections and scattering can occur, this is not applicable and the given properties may not be valid.

The calculation of beam impedances due to synchrotron radiation became an emerging research field in the early nineties, when several boundary conditions were analyzed. In one of the first and simplest models (*free-space model*), the beam was treated as a line charge in free space, neglecting the transverse beam dimensions as well as the surrounding vacuum chamber and was limited to low frequencies [51]. Back then, the authors realized that the result is only applicable for bunches that are long compared to the radius of the beam pipe. Yet it is extremely valuable for crude and quick estimates. A model taking into account the shielding by perfectly conducting parallel plates below and above the electron orbit (*parallel-plates model*), was developed by Murphy, Krinsky and Gluckstern [52]. More sophisticated geometries like toroidal beam chambers were analyzed by Warnock and Morton [53] and Ng [54]. All these impedances were restricted to a circular beam path as it is the case in storage rings. An important next step was done by Saldin, Schneidmiller and Yurkov [55] as well as Dohlus and Limberg [56] who extended the model with straight paths between the bending magnets and enabled the investigation of short bending sections to study the bunch compressors in modern X-ray free electron lasers, too. Recently, Stupakov and Zhou developed an analytical solution for arbitrary beam paths [57].

In this thesis, I will limit myself to the impedances needed for understanding the micro-bunching instability and the generation of intense THz radiation.

2.1.1 Synchrotron Radiation Impedance in a Rectangular Pipe

We will start with the impedance in a rectangular pipe as described by Agoh [58; 59] and then follow his calculations to treat the special cases of parallel plates and free-space impedance. It will be shown that the rectangular pipe model can be approximated

by parallel plates, whereas the free space model is too simple. To develop the theory described in the following, T. Agoh has made the following assumptions [59]:

- The dipole magnet is infinitely long, the reference axis has a constant curvature radius ($c/R = f_0$).
- The beam pipe is perfectly conducting and has a cross section of width w_c and height h_c . The pipe cross section is uniform along the orbit.
- The frequency of the field satisfies $f \gg c/(2 * \min(w_c, h_c, R))$, where $c/(2w_c)$ and $c/(2h_c)$ are the transverse cutoff wave numbers of the straight rectangular waveguide. This is called the “paraxial approximation”.
- The bunch consists of relativistic electrons ($\gamma \gg 1$) all having the same and constant energy and velocity $\beta = v/c$.
- The charge distribution of the bunch is rigid and has no internal correlation. The bunch has no transverse dimension.

He finds the impedance per unit length L of the rectangular chamber to be [59, Eq. (69)]

$$\frac{Z(f)}{L} \Big|_{RC} = Z_0 \frac{2\pi}{\beta h_c} \left(\frac{2f_0}{f} \right)^{1/3} \sum_{p=0}^{\infty} (\hat{G}_x + \beta_p^2 \hat{G}_y), \quad (2.2)$$

with

$$\beta_p = \frac{\frac{\pi}{h_c}(2p+1)}{\left[\frac{2}{R} \left(\frac{2\pi f}{c} \right)^2 \right]^{1/3}}, \quad (2.3)$$

where the boundary condition on the upper-lower walls constrains the vertical Fourier mode into $n = 2p + 1$ ($p = 0, 1, 2, 3, \dots$), and only odd modes can propagate in the chamber. \hat{G}_x and \hat{G}_y describe the horizontal and vertical electric fields and depend on the distance to the beam of the inner (x_a) and outer (x_b) sidewalls

$$\hat{G}_x = \frac{\hat{s}(v_p, w_p) \hat{s}(w_p, u_p)}{\hat{s}(v_p, u_p)}, \quad (2.4)$$

$$\hat{G}_y = \frac{\hat{p}(v_p, w_p) \hat{p}(w_p, u_p)}{\hat{p}(v_p, u_p)}, \quad (2.5)$$

with

$$u_p = w_p - \left(2 \frac{f^2}{f_0^2}\right)^{1/3} \frac{x_a}{R} \quad (2.6)$$

$$v_p = w_p - \left(2 \frac{f^2}{f_0^2}\right)^{1/3} \frac{x_b}{R} \quad (2.7)$$

$$w_p = \beta_p^2 + \left(2 \frac{f^2}{f_0^2}\right)^{1/3} \frac{1}{2\gamma^2} \quad (2.8)$$

and a set of Airy functions

$$\hat{p}(x, y) = \text{Ai}(x) \text{Ci}(y) - \text{Ci}(x) \text{Ai}(y), \quad (2.9)$$

$$\hat{q}(x, y) = \text{Ai}(x) \text{Ci}'(y) - \text{Ci}(x) \text{Ai}'(y), \quad (2.10)$$

$$\hat{r}(x, y) = \text{Ai}'(x) \text{Ci}(y) - \text{Ci}'(x) \text{Ai}(y), \quad (2.11)$$

$$\hat{s}(x, y) = \text{Ai}'(x) \text{Ci}'(y) - \text{Ci}'(x) \text{Ai}'(y), \quad (2.12)$$

and $\text{Ci}(r) = \text{Ai}(r) - j \text{Bi}(r)$. The Airy functions with their derivatives and integrals are shown in Fig. (2.1). Only positive parameters are used in the calculations presented here. The Airy function Ai starts at $\text{Ai}(0) = (3^{3/2}\Gamma(2/3))^{-1} \approx 0.355$ and converges to zero for high values. Its integral reaches the constant value of $1/3$ at high values. Note that the derivative is inverted in the plot. The Airy function of second kind Bi has its origin at $\text{Bi}(0) = \sqrt[6]{3}\Gamma(2/3) \approx 0.61$, but is tending to infinity for high values as does its derivative and integral.

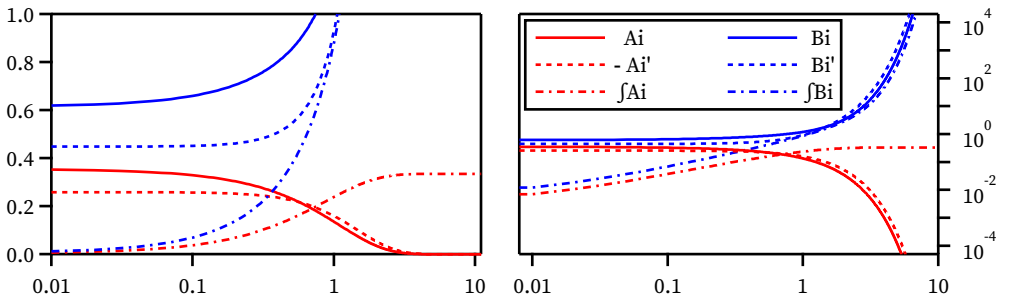


Figure 2.1: Airy functions with their derivatives and integrals in linear (left) and logarithmic scale (right). Please note that the derivative of Ai is inverted.

The impedance appears imaginary. However, the real part of the rectangular beam pipe impedance is located at the resonance points of the imaginary singularities [59].

They have been calculated in [58], but this complicated solution is by-passed here, as it can well be approximated by the following models. In the next step, Eq. (2.2) is simplified by moving the inner wall to infinite distance. The impedance per unit length of this *pillbox model* is [59, Eq. (71)]

$$\left. \frac{Z(f)}{L} \right|_{PB} = Z_0 \frac{2\pi}{\beta h_c} \left(\frac{2f_0}{f} \right)^{1/3} \sum_{p=0}^{\infty} F_1(\beta_p), \quad (2.13)$$

where F_1 is given by:

$$F_1(\beta_p) = \frac{\text{Ai}'(w_p)}{\text{Ai}'(v_p)} \hat{s}(v_p, w_p) + \beta_p^2 \frac{\text{Ai}(w_p)}{\text{Ai}(v_p)} \hat{p}(v_p, w_p). \quad (2.14)$$

Here too, the real part of the impedance is concealed in the resonance points. As shown in Refs [60; 59], when the aspect ratio of the curved chamber w_c/h_c is larger than 2, the shielding of the side walls can be neglected, and the parallel plates model is a good approximation for a long bending magnet. However, an additional effect has to be taken into account: The side walls in this model are perfectly conducting and therefore reflect all radiation. If the bunch length is long enough, the reflected radiation from the front of the bunch can interfere with the back, leading to additional disturbances [51]. This results in an additional dependence on the bunch length, which has to be shorter than

$$\sigma_z \ll \frac{2}{3} \sqrt{\frac{w_c^3}{R}}, \quad (2.15)$$

which at KARA corresponds to a bunch length of 5.3 mm or 19.7 ps. Otherwise the interference will lead to narrow resonance peaks in the impedance spaced by [61]

$$\Delta f = \frac{3c}{2} \sqrt{\frac{R}{w_c^3}}. \quad (2.16)$$

The condition $w_c/h_c = 73 \text{ mm}/32 \text{ mm} > 2$ is fulfilled, but the bunch length can be critical. At KARA, the RMS bunch length of a fully compressed bunch is below 2 ps, whereas the uncompressed size is in the order of 35 ps. However, the next chapter will show, that the intensity of its emitted radiation can be neglected, although the bunch length is long enough so that the sidewall reflections hit the bunch again. Therefore, the *parallel plates (PP)* impedance will be used in this thesis instead of the much more complicated and time consuming calculation of the rectangular or pillbox chamber.

2.1.2 Synchrotron Radiation Impedance between Parallel Plates

By additionally removing the outer wall from Eq. (2.13), Agoh arrives at the impedance for parallel plates (PP) [59, Eq. (76)]

$$\frac{Z(f)}{L} \Big|_{PP} = Z_0 \frac{2\pi}{\beta h_c} \left(\frac{2f_0}{f} \right)^{1/3} \sum_{p=0}^{\infty} F_0(\beta_p), \quad (2.17)$$

where F_0 is given by:

$$F_0(\beta_p) = \text{Ai}'(w_p) \text{Ci}'(w_p) + \beta_p^2 \text{Ai}(w_p) \text{Ci}(w_p). \quad (2.18)$$

This solution is connected to the solution found by Warnock and Morton [53; 62] via asymptotic expansion for the Bessel functions. The electric field generated by a bunch moving parallel to perfectly conducting infinite plates has first been found by Faltens and Laslett [63].

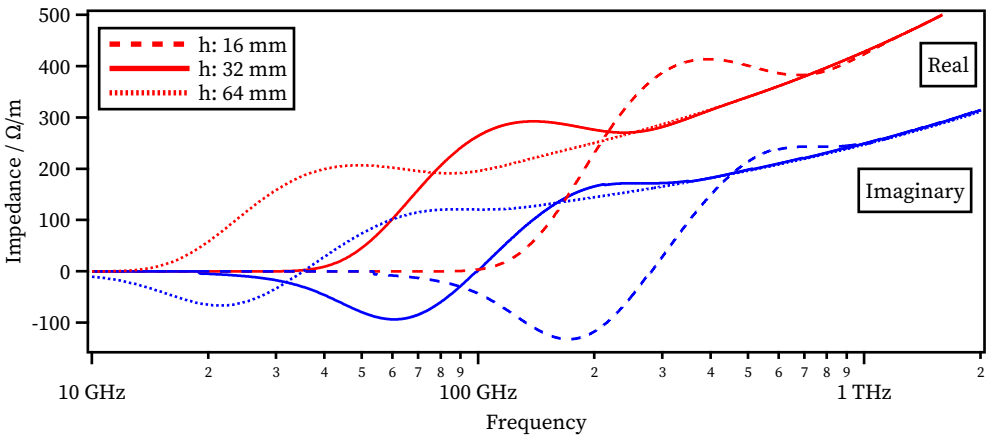


Figure 2.2: PP-impedance according to Eq. (2.17) for a gap height of 16, 32 and 64 mm, respectively. The radiation of low frequencies is suppressed and their components shifted to higher frequencies. The standard KARA vacuum chamber has a gap height of 32 mm.

Figure 2.2 depicts the influence of the parallel plates distance for different gap heights at low frequencies. Long wavelengths cannot propagate in the vacuum chamber and are suppressed. This effect is named *shielding* by parallel plates. Several different definitions and discrepancies in literature are examined in detail in [64]. As an ap-

proximation, the cutoff frequency is dependent on the gap height h_c and curvature radius R [65]

$$f_{cutoff} = \sqrt{\frac{\pi}{6}} c \sqrt{\frac{R}{h_c^3}}. \quad (2.19)$$

At KARA, with a gap of 32 mm in the standard vacuum chamber, this results in a cut-off frequency of 89 GHz. Below the cutoff frequency, the real part of the impedance is exponentially suppressed, whereas the imaginary part has negative components. At approximately four times the cut-off frequency, both the real and the imaginary part approach the free space model described in the next section. Higher frequencies do not exhibit any shielding and can thus be treated by using the free space impedance model.

At first glance it looks counterintuitive that a pair of parallel plates can even suppress synchrotron radiation for wavelengths that are much shorter than the waveguide cutoff of the same dimension. Sagan et al. brought up an heuristic shielding argument to visualize this [66]: When a bunch enters a magnet, the synchrotron radiation is built up over a distance of $R^{2/3} \lambda^{1/3}$ known as the *formation length* [67]. Provided, that the magnet length exceeds the formation length, the radiation becomes fully formed and can be approximated by the steady-state PP solution. The opening angle of the radiation can be approximated by $\Delta\Theta = (\lambda/R)^{1/3}$. Therefore, the width w_r and height h_r of the radiation cone that builds up during the formation length is given by $w_r \approx h_r \approx R(\lambda/R)^{2/3}$. Wavelengths that hit the chamber wall during this build up process are distorted. A more sophisticated analysis leads to the Eq. (2.19). As a result, radiation at wavelengths much shorter than the chamber dimensions is suppressed.

2.1.3 Synchrotron Radiation Impedance in Free Space

Above the shielding cutoff, the chamber walls can be neglected. Hence the calculation for low frequencies of ultra-relativistic beams ($\gamma = \infty$) simplifies drastically, as the sum in Eq. (2.17) turns into an integral which can be calculated exactly. Finally one obtains [59, Eq. (79)]

$$\left. \frac{Z(f)}{L} \right|_{FS} \xrightarrow{\gamma=\infty} Z_0 \frac{\Gamma(2/3)}{2\pi} \left(j \frac{2\pi f}{3R^2 c} \right)^{1/3}, \quad (2.20)$$

which agrees well with the impedance found by Murphy, Krinsky and Gluckstern [52].

The differences of parallel plates and free space impedances are shown in Fig. 2.3. Low frequencies are shielded by the vacuum chamber, approximated by perfectly conducting parallel plates with distance 32 mm. In contrast to the free space approximation, the parallel plates reactance is inductive at lower frequencies which leads to a different influence on the bunch profile. This influence will be discussed in more detail in Chapter 2.2.

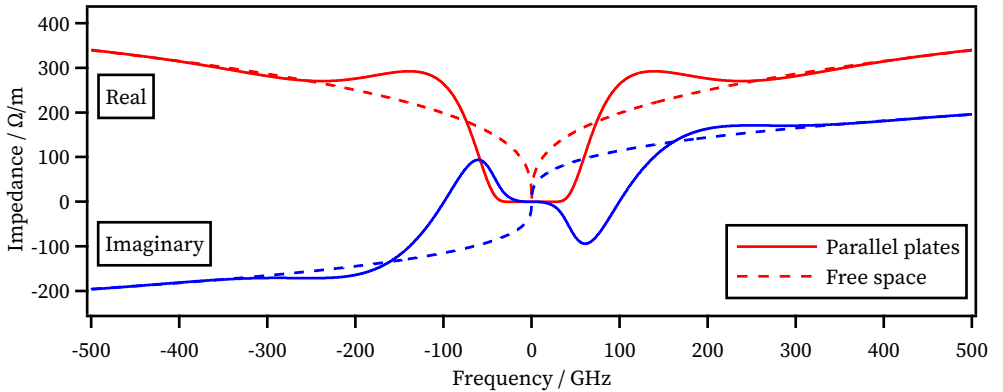


Figure 2.3: Free space impedance and shielding by parallel plates for the KARA parameters.

For non-ultrarelativistic beams, Schwinger found the solution for the emitted power and thus the real part of the impedance [68]. The imaginary part, however, contains singularities that are understood to reflect local space-charge interaction [69]. A different approximation has been found by Li and Tsai for both, the real and the imaginary part [69]¹

$$\text{Re } \frac{Z(f)}{L} \Big|_{FS} = \frac{Z_0}{2} \left[-\left(\frac{2\pi f}{cR^2} \right)^{1/3} \text{Ai}'(\mu) + \frac{\pi f}{c\gamma^2} \left(\int_0^\mu \text{Ai}(\xi) d\xi - \frac{1}{3} \right) \right], \quad (2.21)$$

$$\text{Im } \frac{Z(f)}{L} \Big|_{FS} = \frac{Z_0}{2} \left(\frac{2\pi f}{cR^2} \right)^{1/3} \left[\frac{1}{3} \text{Bi}'(\mu) + \int_0^\mu \text{Ai}'(\mu) \text{Bi}(\xi) - \text{Ai}(\xi) \text{Bi}'(\mu) d\xi \right], \quad (2.22)$$

$$\mu = \gamma^{-2} (2\pi f R/c)^{2/3}. \quad (2.23)$$

¹The imaginary part of the equation by Agoh seems to tend to infinity at high frequencies, whereas the solution found by Li and Tsai approaches zero as expected. However, this can also be due to problems in numerical accuracy in my calculation. The multiplication of the Airy functions where Bi tends to infinity, while Ai approaches zero can be numerically challenging. At low frequencies and for the real part, both solutions agree very well.

To improve numerical stability in the calculations I have used the fact that

$$\frac{1}{3} - \int_0^\mu \text{Ai} = \int_\mu^\infty \text{Ai}, \text{ which leads to}$$

$$\text{Im} \left. \frac{Z(f)}{L} \right|_{FS} = \frac{Z_0}{2} \left(\frac{2\pi f}{cR^2} \right)^{1/3} \left(\text{Ai}'(\mu) \int_0^\mu \text{Bi}(\xi) d\xi + \text{Bi}'(\mu) \int_\mu^\infty \text{Ai}(\xi) d\xi \right). \quad (2.24)$$

Figure 2.4 shows the influence of different beam energies on the impedance spectrum. The impedance in the low frequency regime is the same for all energies and can well be approximated by Eq. (2.20).

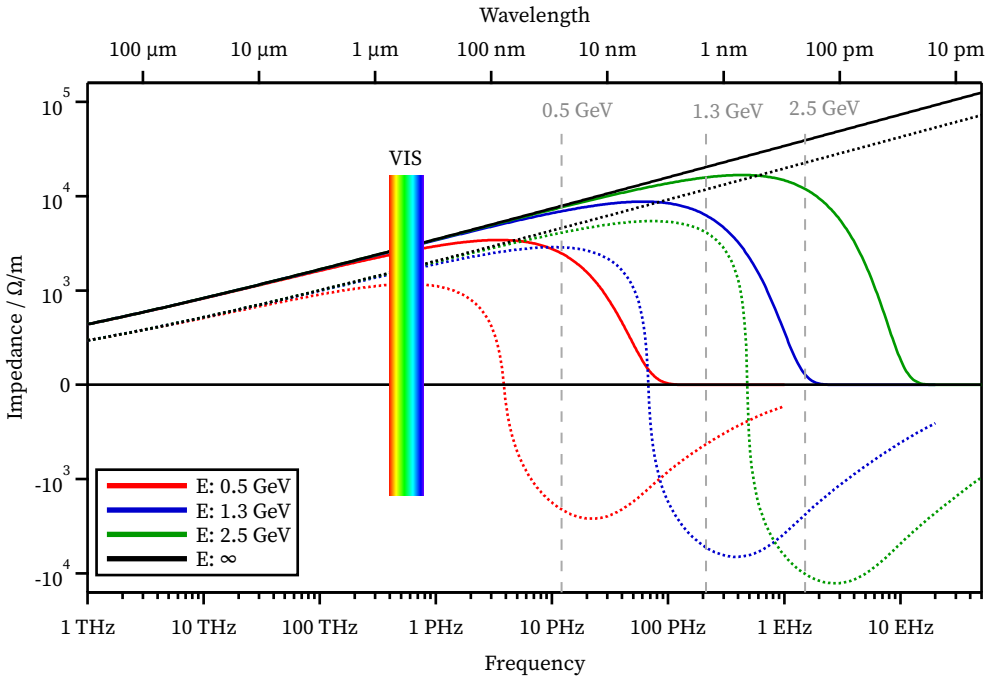


Figure 2.4: Free space impedance with finite γ (Eqns. (2.21) and (2.24)), and the low-frequency approximation with $\gamma = \infty$ (Eq. (2.20)). The visible light range is shown as a rainbow as a guideline. The vertical dashed lines denote the critical frequencies (Eq. (2.25)) for 0.5, 1.3 and 2.5 GeV. The maximum magnitude is in the soft and hard X-ray region for higher beam energies, while the low frequencies can be well approximated by the energy independent approximation. Note the two-sided log-axis where impedances below 100Ω were treated as zero.

Schwinger has also defined a so-called critical frequency

$$f_c = \frac{3c}{4\pi R} \gamma^3 \quad (2.25)$$

whose definition is that half of the total resistivity is reached at that frequency²

$$\int_0^{f_c} \operatorname{Re}(Z(f)|_{FS}) df = \int_{f_c}^{\infty} \operatorname{Re}(Z(f)|_{FS}) df = \frac{1}{2} \int_0^{\infty} \operatorname{Re}(Z(f)|_{FS}) df. \quad (2.26)$$

While the total impedance increases by γ^4 , the critical frequency scales by γ^3 . It is shown as vertical gray lines in Fig. 2.4 for the three different energies. The critical frequency corresponds to $\mu = (3/2)^{2/3}$ while the zero-crossing of the imaginary part happens³ at $\mu = (3/(2\pi))^{2/3}$ and is by a factor of pi lower in frequency.

2.1.4 Impedance at the Edges of Bending Magnets

A real *synchrotron storage ring* is not a perfect ring, but the individual bending magnets are connected by straight lines, where among others, diagnostics, RF power stations and insertion devices are located. At the edges of the magnets, the particles encounter a step in the surrounding magnetic field which leads to so-called *edge radiation (ER)*. The ER impedance can be obtained from the emitted power. However, this only returns the real part of the impedance, which is responsible for the energy loss (this will be discussed in more detail in the following chapter).

The intensity and spatial distribution has first been calculated by Bosch [70]. He found out that edge radiation occurs when the dimension of the fringe field d , i.e. the building up of the magnetic field, is short compared to the observed frequency $f \ll \gamma^2 c/d$. Therefore, it vanishes at high frequencies but can be rather strong at the lower ones. A far field model can be used to describe the emitted radiation. For $\gamma \gg 1$ one obtains the real part of the impedance per magnet edge N_{Edge}

$$\operatorname{Re} \left. \frac{Z(f)}{N_{\text{Edge}}} \right|_{\text{ER}} = Z_0 \frac{\ln(2\gamma) - 1}{2\pi^2}, \quad (2.27)$$

which leads to 125Ω , 144Ω and 156Ω for 0.5 GeV , 1.3 GeV and 2.5 GeV respectively. If the magnet is much longer than the formation time of the radiation, the wake field becomes the steady state solution of the bending magnets described above, and the impedance of the magnet entrance edge becomes negligible [71].

² Originally, Schwinger defined the critical frequency to be at half of the emitted incoherent power, which will be treated in the next section.

³ numerically evaluated

A special case is the impedance at the exit edge of a magnet, since the power emitted at the exit travels with the bunch and slowly overtakes it. The interaction therefore needs to be considered until an equilibrium is reached. An approximation for the integrated impedance downstream of a magnet for a drift length L_d is given by [72]

$$\int \text{Re} \left. \frac{Z(f)}{N_{\text{Edge}}} \right|_{\text{EER}} = Z_0 \frac{1}{2\pi} \ln \left(\frac{\min(L_d, \gamma^2 c/(2\pi f))}{R^{2/3} (c/f)^{1/3}} \right). \quad (2.28)$$

The magnet edge impedance is similar to bremsstrahlung of a suddenly decelerated (or accelerated) particle. In fact it can be seen as the transition from one medium to the other. That's also the reason why the entrance and exit edges do not have exactly the same behavior, since at the entrance the transition is from zero to high magnetic field and vice versa at the exit [73].

2.1.5 Longitudinal Space-Charge Impedance

Especially for low particle momentum or high intensity beams, the compelling electric fields of the individual particles act as a force and change the bunch shape. Its impedance is purely imaginary and therefore does not lead to an energy loss. The longitudinal space charge (LSC) impedance in free space is [74; 75]

$$\left. \frac{Z(f)}{L} \right|_{\text{LSC}} = j Z_0 \frac{c}{2\pi^2 f r_b^2} \left[1 - \frac{2\pi f r_b}{c\gamma} K_1 \left(\frac{2\pi f r_b}{c\gamma} \right) \right] \quad (2.29)$$

with K_1 being the modified Bessel function and r_b the transverse bunch radius. In general the LSC-impedance is highly dependent on the 3D bunch shape. Here, a Gaussian bunch profile in the transverse dimensions with RMS sizes of σ_x and σ_y is assumed, so that the LSC can be approximated by the effective radius $r_b = 0.85(\sigma_x + \sigma_y)$ in Eq. (2.29).

Figure 2.5 shows the imaginary part of the longitudinal space charge. Different beam energies for $r_b = 1$ mm are color coded and different effective radii at 1.3 GeV shown in different line styles. At very high frequencies, the impedance is dominated by the transverse size of the bunch, whereas for low frequencies the beam energy becomes dominant. The integrated impedance decreases with γ^{-2} and therefore can be neglected in the ultra-relativistic limit. More complicated geometries have been analyzed in Ref. [74], however, the more appropriate parallel plates model results in even lower impedances and is therefore neglected here.

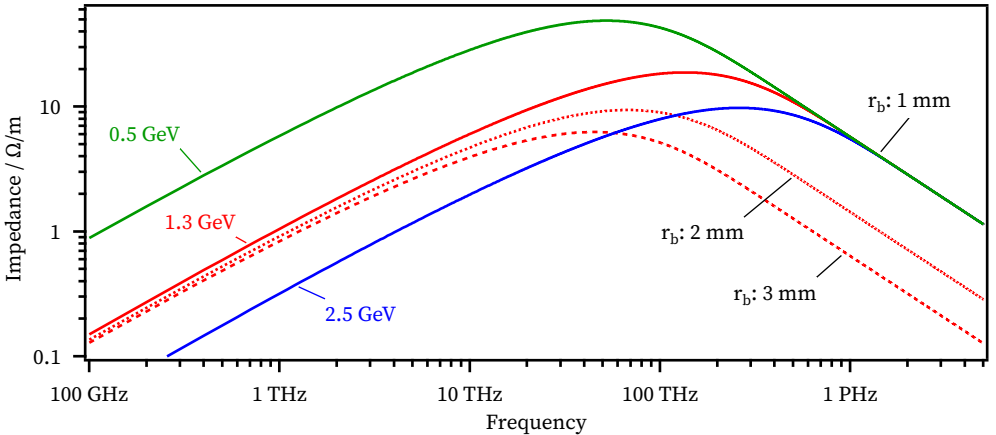


Figure 2.5: Longitudinal space charge impedance for different effective radii and particle energies.

2.1.6 Resistive Wall Impedance

The resistive wall (RW) impedance accounts for the fact, that the vacuum chamber has a finite conductivity and hence leads to losses. An approximation, which neglects the very high and very low frequencies of the impedance per unit length of a round vacuum chamber with a radius a , is given in Ref. [76, Eq. (7)] and is converted to SI units as

$$\frac{Z(f)}{L} \Big|_{RW} = \frac{Z_0}{2\pi a} \left(\frac{\xi c}{2\pi f} - j \frac{\pi f a}{c} \right)^{-1}, \quad \xi = (j + \text{sign}(f)) \sqrt{Z_0 \sigma_c(f) \pi |f| / c}, \quad (2.30)$$

with σ_c being the conductivity of the material. The KARA beam pipe is made out of Remanit 4429 (DIN: X2 CrNiMoN 17 13 3) which has an electrical resistivity of $0.75 \Omega \text{ mm}^2/\text{m}$ at 20°C (EN 10088) which leads to a direct current (DC) conductivity of $\sigma_{c,\text{DC}} = 1.33 \times 10^6 \text{ S/m}$. Taking into account that the conductivity is not constant at all frequencies, the Drude-Sommerfeld free-electron model of conductivity yields the alternating current (AC) conductivity

$$\sigma_c(f) = \frac{\sigma_{c,\text{DC}}}{1 - j 2\pi f \tau_r} \quad (2.31)$$

where τ_r is the relaxation time. Unfortunately the relaxation time of Remanit or other stainless steels is not known [77]. Table 2.1 lists common materials with their known values from Ref. [78].

Table 2.1: Conductivity and Relaxation Times

Material	Conductivity	Relaxation Time
Silver	5.93×10^7 S/m	37.6 fs
Copper	5.88×10^7 S/m	24.6 fs
Aluminum	3.54×10^7 S/m	7.1 fs
Iron	1.1×10^7 S/m	2.3 fs
Remanit 4429	0.133×10^7 S/m	unknown

The shorter the relaxation time, the better is the DC approximation. Figure 2.6 shows the comparison between different materials and the influence of the relaxation time. The KARA beam pipe dimensions are approximately 32 mm \times 70 mm while the formula is for a round beam pipe. Since a smaller beam pipe has a higher impedance, a radius of 16 mm is taken as worst case in the following. Furthermore, a relaxation time of 20 fs is assumed.

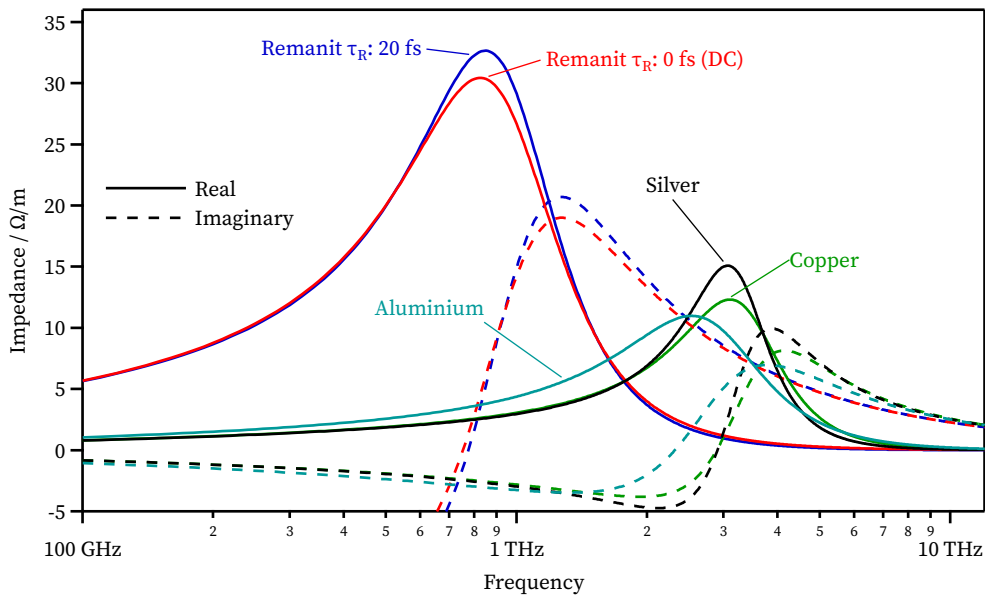


Figure 2.6: Resistive wall impedance for different materials. Solid lines denote the real part, while the dashed lines denote the imaginary part. The actual relaxation time of Remanit is unknown.

2.1.7 Discussion on Impedances

The influence of the surrounding vacuum chamber, the charge of the electrons itself and the emitted electric field on the particle distribution can be modeled by impedances. The strength of the individual impedances varies with various parameters like the surrounding geometry, beam energy, bunch charge or beam path. Furthermore, the impedances have a strong dependence on the frequency. The total impedance a particle observes in one revolution is the sum of all individual impedances integrated over one turn. However, this is only valid if all wake fields have decayed during the turn. Long range wake fields, which last longer than one revolution, are not considered in this thesis. In fact, the impedances described above (except pillbox and rectangular chamber) decay even before the next bunch arrives after 2 ns. Therefore, the above described impedances can not be used to describe bunch-to-bunch interaction.

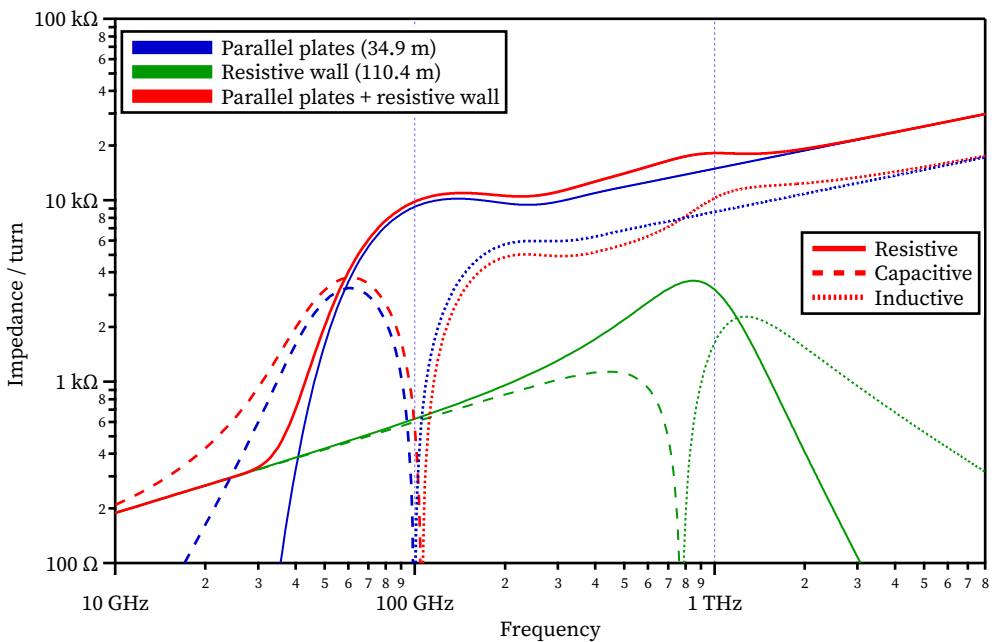


Figure 2.7: PP and RW impedance of a complete KARA turn. Solid lines show the real part, dashed lines the capacitance (negative imaginary part), and dotted lines denote the inductance (positive imaginary part). The PP impedance is clearly dominating, however, if the bunch spectrum interferes with the maximum of the RW impedance around 900 GHz, its contribution should not be neglected. Additionally, at low frequencies where the synchrotron radiation is shielded, the resistive wall impedance becomes dominant for both, the real and the imaginary part.

Depending on the frequency range of interest, some impedances are dominant, while others can be neglected. Figure 2.7 compares the RW and PP impedance in the THz range. At the frequencies shielded by the vacuum chamber, the resistive wall impedance is dominant, however, its total energy loss is still low compared to the PP-Impedance. The influence of the impedances on the particle bunch will be discussed in the next chapter. It will show, that the region of interest is between 0.1 THz to 3 THz. In that region the space charge impedance at 1.3 GeV is negligible. The resistive wall impedance is dominant below the synchrotron radiation (SR) shielding cutoff and has minor influences at its maximum. The resonance frequencies of most geometric impedances are well below the THz range and not considered in this thesis. However, in the future, it might be possible to build special structures with impedances, designed for resonances in the THz regime. Good candidates for this are for example periodic structures [79] like corrugated pipes as described in [81; 80].

For a rough estimation, the dominating impedance is parallel plates. For now, the differences with a pillbox, rectangular, or even the real vacuum chamber wall model do not justify the much more complicated calculations. Depending on the needed accuracy, other impedances should be added first, starting with resistive wall, space charge and further geometric impedances. However, most impedances are constant for an accelerator and need to be calculated only once. For a better accelerator model this should be done in the future.

2.2 Bunch Deformation by Self-Interaction

*For every problem there is a solution
which is simple, clean and wrong.*

— Henry Louis Mencken

This section focuses on the bunch deformation due to impedances and the corresponding wake fields. The wake function $W(t)$ described above is caused by a single particle and expressed as charge normalized voltage. Therefore, the total potential V_w another particle observes at a given position is the convolution of the wake function $W(t)$ with the electron bunch profile $\rho(t)$. It is called *wake potential* and can also be expressed in terms of the impedance $Z(f)$ which is the Fourier transformation (FT) of the wake function.

The FT also transforms the convolution into a multiplication, so that it reads

$$V_w(t) = \int_{-\infty}^{\infty} W(t - \tau)\rho(\tau)d\tau = W(t) * \rho(t), \quad (2.32a)$$

$$V_w(t) = \int_{-\infty}^{\infty} \varrho(f)Z(f)e^{j2\pi ft}df, \quad (2.32b)$$

where $\varrho(f)$ is the Fourier transformation of the longitudinal line density profile $\rho(t)$ and $*$ denotes the convolution

$$(f * g)(t) \equiv \int_{-\infty}^{\infty} f(\tau)g(t - \tau)d\tau. \quad (2.33)$$

Consequently, the wake potential is expressed in units of Volt and results in an additional accelerating or decelerating potential a particle observes due to the impedance. The wake potential is emitted by the bunch, therefore, a positive value is due to energy loss of the bunch and a negative due to an energy gain. This can be seen as a distortion of the potential well which is created by the accelerating cavities and called *potential-well distortion* [82; 83].

Figure 2.8 shows the resulting wake potentials of the PP-impedance and free space (FS)-impedance on a Gaussian shaped $Q = 1 \text{ pC}$, $\sigma_{z,t} = 5 \text{ ps}$ bunch according to Eq. (2.32b). Please note, that the bunch head is to the right, at negative times, according to the definition in Chapter 1.2.6. While the free space wake function quickly drops to zero after the particle and the causality discussed at the beginning of the chapter is valid, the wake function also influences particles behind due to the parallel plates model. This can be seen in the shown wake potential, where in the free space case the influence to the bunch tail is negligible, whereas the parallel plates impedance significantly influences the back of the bunch, too.

Because of the multiplication of the spectrum of the longitudinal bunch profile $\varrho(f)$ with the impedance, the bunch profile is the crucial and changing part. While the impedance is determined by the accelerator geometry and settings and is constant in a storage ring, the bunch profile changes. Not only the charge of the bunch changes, but also its shape. The dependence of the bunch shape on the emitted energy will be discussed in more detail in the next chapter. Figure 2.9 shows the influence of the width of a Gaussian shaped bunch. A small bunch deviation can lead to a change in the wake potential of several hundred volts. If the bunch length is longer than the

cutoff wavelength of the parallel plates impedance, the wake potential is negligible, since there is almost no overlap of the bunch spectrum and the impedance.

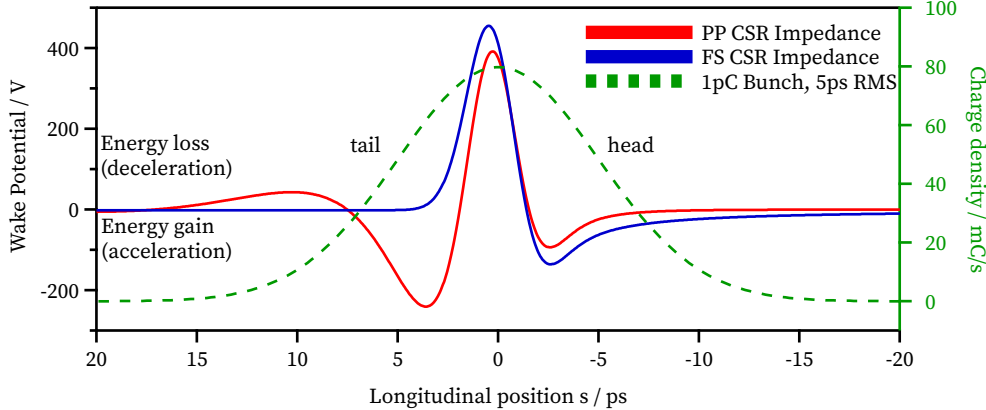


Figure 2.8: Calculated wake potentials by PP-impedance and FS-impedance for a $Q = 1 \text{ pC}$, $\sigma_{z,t} = 5 \text{ ps}$ Gaussian shaped bunch.

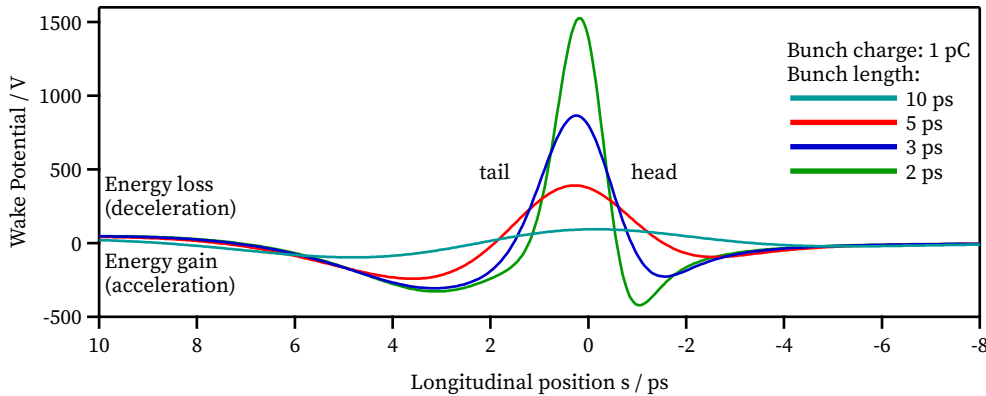


Figure 2.9: Calculated wake potentials with parallel plates impedance for different bunch lengths of Gaussian shape.

While the potential well due to the RF system leads to an equilibrium with a Gaussian bunch shape, the additional wake potential disturbs the potential well and leads to changes in the bunch shape. This changed bunch shape itself has influence on the wake potential, as can be seen when comparing different bunch lengths. To investigate this further, the longitudinal equation of motion has to be studied with this additional distortion. A convenient way is to look at its Hamiltonian.

2.2.1 Hamiltonian of Phase Space System

The Hamiltonian of the phase space system discussed in Chapter 1.5.3 can be written as [84, Eq. 2.40]

$$\mathcal{H} = \pi h f_0 \alpha_c \sigma_\delta^2 + \frac{1}{2} \frac{e V_{\text{RF}} f_0}{E_0} \Delta\psi^2, \quad (2.34)$$

where the phase axis can be converted to a position axis by

$$z = \frac{c}{2\pi f_{\text{RF}}} \Delta\psi. \quad (2.35)$$

It can be expressed by a set of dimensionless, generalized coordinates [85]

$$q := \frac{z}{\sigma_{z,0}} \quad , \quad p := \frac{\Delta E}{\sigma_{E,0}} \quad \text{and} \quad \theta := \frac{t}{T_s} \quad (2.36)$$

where p, q and θ account for the energy, longitudinal, and time axis, respectively. Assuming, that the transverse dimensions of the bunch can be neglected, the Hamiltonian is simplified to

$$\mathcal{H} = \frac{1}{2}(p^2 + q^2). \quad (2.37)$$

In this case, the Hamiltonian is assumed to be linear, however, higher order terms of α_c and V_{RF} , as they occur in a real accelerator, can be included.

2.2.2 Vlasov-Fokker-Planck Equation

The particle density distribution $\Psi(q, p)$ in a conservative system ($d\Psi(q, p, \theta)/dt = 0$) is constant and can be described by the Vlasov equation [86] (cited from [87, p. 48]):

$$\frac{d\Psi}{d\theta} = \frac{\partial\Psi}{\partial\theta} + \frac{\partial\mathcal{H}}{\partial p} \frac{\partial\psi}{\partial q} - \frac{\partial\mathcal{H}}{\partial q} \frac{\partial\psi}{\partial p} = 0. \quad (2.38)$$

However, the emission of synchrotron radiation leads to diffusion and damping and is therefore not conservative. This is considered in the Vlasov-Fokker-Planck (VFP) equation. It was first developed for the particle distribution inside a plasma, however, the concept was adapted to particle accelerators.

Two additional assumptions are made:

- Constant radiation: The quantum excitation nature is not considered.
- All particles emit the same amount of incoherent synchrotron radiation, i.e. $P \propto E^4$ is not considered for small ΔE .

Then, the VFP equation reads (notation as [88]):

$$\frac{d\Psi}{d\theta} = \frac{\partial\Psi}{\partial\theta} + \frac{\partial\mathcal{H}}{\partial p} \frac{\partial\Psi}{\partial q} - \frac{\partial\mathcal{H}}{\partial q} \frac{\partial\Psi}{\partial p} = \beta_d \frac{\partial}{\partial p} \left(p\Psi + \frac{\partial\Psi}{\partial p} \right), \quad (2.39)$$

with the dimensionless parameter $\beta_d = T_s/\tau_d$ for the longitudinal damping time per synchrotron period.

A perturbation to the system due to the corresponding impedances described above, can be modeled as an additional term in the Hamiltonian for the collective effects

$$\mathcal{H}(q, p, \theta) = \underbrace{\mathcal{H}_e(q, p, \theta)}_{\text{external fields}} + \underbrace{\mathcal{H}_c(q, p\theta)}_{\text{collective effects}}, \quad (2.40)$$

$$\mathcal{H} = \frac{1}{2}(p^2 + q^2) + \text{sign}(\alpha_c) \frac{ef_0}{\sigma_E f_s} \int_q^\infty V_w(q', \theta) dq'. \quad (2.41)$$

The perturbation is expressed by the wake potential V_w integrated over one turn. By the multiplication with the revolution frequency it gets normalized to a unit time, and by multiplication with the elementary charge it becomes an energy. Then it is normalized by the energy spread and synchrotron frequency like the other parts of the Hamiltonian. In terms of the impedance, the Hamiltonian is

$$\mathcal{H} = \frac{1}{2}(p^2 + q^2) + \text{sign}(\alpha_c) \frac{ef_0}{\sigma_E f_s} \int_q^\infty \int_{-\infty}^\infty \varrho(f) Z(f) e^{j2\pi f q'} df dq'. \quad (2.42)$$

It is noteworthy, that the wake potential is only position dependent (q) but not energy dependent (p). In an equilibrium case, a stationary solution is reached. In this case, the distribution in q can be expanded in p to the full phase space density as

$$\Psi(q, p) = \frac{1}{\sqrt{2\pi}} e^{-p^2/2} \rho(q), \quad (2.43)$$

since the equilibrium solution of the Vlasov equation is a Gaussian when the external force is independent of p .

2.2.3 Haïssinski Distribution

A known equilibrium solution of the Vlasov equation is the Haïssinski distribution [83], which provides a stable bunch shape. It is determined by

$$\rho(q) = \kappa e^{-\mathcal{H}(q,\rho)} \quad (2.44)$$

where κ has to be chosen so that $\int_{-\infty}^{\infty} \rho(q) dq \stackrel{!}{=} eN_e$ equals the bunch charge.

By inserting Eq. (2.40) it reads

$$\rho(q) = \kappa \exp \left[-\frac{q^2}{2} + \frac{\text{sign}(\alpha_c) e f_0}{\sigma_E f_s} \int_q^{\infty} \int_{-\infty}^{\infty} \varrho(f) Z(f) e^{j 2\pi f q'} df dq' \right]. \quad (2.45)$$

It can be easily verified, that for a zero bunch charge, the perturbation vanishes and the bunch shape is Gaussian. In general, the Haïssinski distribution can be solved by Newton iteration. However, for some impedances like the simple free space model, analytic solutions exist, too [89]. To study the potential well distortion of different impedances, a *Haïssinski solver* was implemented, following the algorithm by Warnock and Ellison [85] and the improvements by Warnock and Bane [90].

Figure 2.10 (left) shows the effect, if a pure resistive impedance is present. A positive resistance accounts to energy losses, while a negative refers to energy gain. Due to the convolution of the longitudinal bunch profile with the static impedance, the parts of the bunch with a high density will be affected stronger than sections with low density. In this example with a Gaussian bunch shape, the center of the bunch will lose or gain the most energy, depending on a positive or negative impedance. To compensate for that additional energy change, the particles arrive in the cavity either earlier or later. This leads to a leaning forward or backward of the bunch and consequently to a bunch asymmetry. That effect is the opposite, if the sign of the momentum compaction factor α_c changes. Note, that the *longitudinal position* axis only has the same number as the *normalized longitudinal position* axis, since the initial zero-current bunch length was chosen to be 1 ps.

A different scenario is shown in Fig. 2.10 (right) which has a purely reactive impedance. The imaginary part of the impedance affects the bunch length. Like an electrical network, where an inductive impedance is a lowpass filter, the rise time of the electron current is limited and the bunch is lengthened for an inductive impedance. The bunch shape itself stays stable. To conclude: A constant, purely inductive impedance

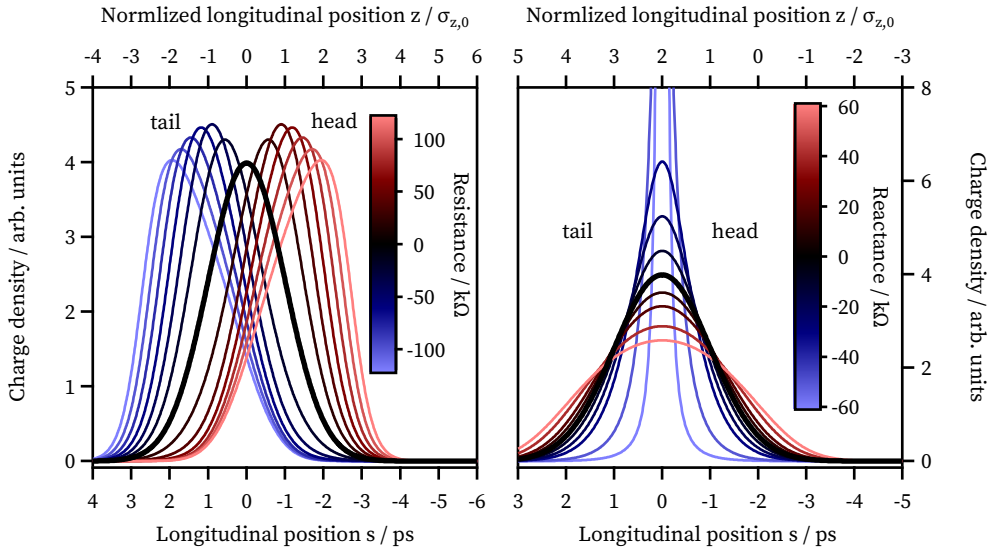


Figure 2.10: Potential well distortion due to a purely resistive (left) or reactive (right) impedance. A positive resistance leads to additional energy loss. To compensate this loss, the particles have to arrive earlier at the cavity to gain more energy in the equilibrium solution. Negative resistance results in an additional energy gain. A positive reactance (inductive) leads to bunch lengthening, while a negative reactance (conductive) leads to a shortening of the bunch length, keeping the symmetry.

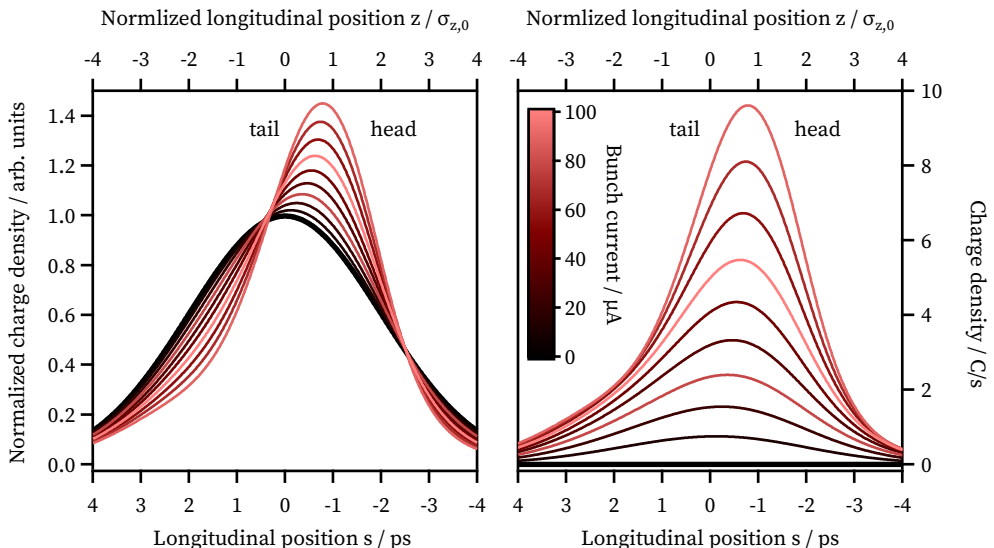


Figure 2.11: Haïssinski solution for different bunch currents in the KARA storage ring with normalized (left) and absolute (right) bunch charge. Due to the higher energy loss for higher bunch charges, the bunch profile leans forward. At even higher bunch charges, Eq. (2.45) does not converge.

lengthens the bunch while maintaining more or less a head-tail symmetry. A constant, purely resistive impedance does not alter the bunch length, but tends to cause a head-tail asymmetry [91]. However, the parallel plates impedance due to synchrotron radiation is neither purely resistive or inductive, nor has a constant value. Therefore, the impact of the impedance on the bunch shape is a mixture of the above described effects and additionally stronger dependent on the bunch spectrum.

The effect of the more realistic PP-impedance is shown in Fig. 2.11 for different bunch currents. The parameters are chosen to match the KARA storage ring with a synchrotron frequency of 10 kHz and a zero-current bunch length of 2 ps. For even higher bunch currents than displayed, Eq. (2.45) does not converge to a stable solution.

2.3 Micro-Bunching Instability Threshold Current

How wonderful that we have met with a paradox.

Now we have some hope of making progress.

— Niels Bohr

Above a given bunch charge, Eq. (2.45) does not converge. Indeed, no charge distribution exists, which would lead to an equilibrium between the disturbance due to the additional impedance and the diffusion and damping term. The key parameter to the instability is the nonlinear increase of the wake potential for small disturbances due to the nonlinear impedance. In general, the system is critical since a small disturbance leads to an even higher wake potential and amplifies itself. While the damping as a repelling force is a single particle effect and independent of the number of particles, the wake potential increases quadratically with the current. Therefore, above a threshold current, the build up of the instability can no longer be controlled by the radiation damping.

The threshold has a strong dependence on the zero-current bunch length. To illustrate that, one has to keep in mind, that the disturbing wake potential is quantified by the multiplication of the bunch spectrum and the impedance. The dominating parallel plates impedance is negligible for low frequencies, and therefore has only minor overlap with long bunches. For shorter bunches, it leads to potential well distortion. Above the threshold, the wake potential becomes so big that the kick, which the bunch encounters, leads to an uncontrolled blowup of the bunch. During that blowup, the

additional wake potential drops, because the bunch broadens and its spectrum shrinks. The positive feedback is stopped and the radiation damping takes over. If the energy acceptance of the storage ring is big enough, all particles of the blown-up bunch can be collected and damped down again. Therefore, no direct particle loss is observed. However, during that procedure strong THz radiation is emitted. This is discussed in more detail in the next chapter.

To summarize, the instability threshold depends on the initial bunch spectrum (determined by the size and charge of the bunch) and on the affecting impedance. While the zero-current bunch profile is Gaussian and its length can be calculated from the machine settings, the impedances as described above are more complicated. There have been several attempts to characterize these instabilities. It began with impedances of proton beams where the gamma factor is too low for significant SR impedances. Therefore, resistive wall, space charge or other geometric impedances are dominating. Starting from the Keil-Schnell criterion [92] for infinite bunch length (coasting beam), Boussard developed a criterion for long bunches [93]. At the same time, Sacherer introduced an integral equation which gives a threshold for a longitudinal mode-coupling instability [94]. Based on that work, Chao and Gareyte found a scaling law [95] which states, that if an impedance scales like $Z(f) \propto f^a$, the bunch length $\sigma_{z,t}$ scales like

$$\sigma_{z,t} \propto \xi^{(2+a)^{-1}} \quad (2.46)$$

with the scaling parameter

$$\xi = \frac{\alpha_c I_b}{f_s^2 E_0}. \quad (2.47)$$

In the case of the low frequency approximation of the FS-impedance, which scales with $Z(f) \propto f^{1/3}$, that would lead to an increase of bunch length of $\sigma_{z,t} \propto \xi^{3/7}$ above the threshold. In fact, a similar behavior has been observed in the KARA storage ring [96].

Krinsky and Wang [97] included non-Gaussian bunch shapes and short bunches in their studies. However, all of them focus on specific dominant impedances and can not be directly applied to the PP-impedance, which has no simple frequency dependence in the range of interest. Until today, no analytic solution exists to describe the microwave instability due to the PP-impedance. Therefore, the above described Haïssinski equation is solved numerically to estimate the threshold. Bane, Stupakov and Cai [88] implemented a VFP solver to iteratively compute the above equations

based on the work of Oide and Yokoya [98] and Heifets [99] with an algorithm written by Warnock and Ellison [85]. By introducing two dimensionless parameters, a *shielding factor* Π

$$\Pi = \frac{\sigma_{z,0}}{(h_c/2)} \sqrt{\frac{R}{h_c/2}}, \quad (2.48)$$

and a *CSR strength*⁴ S_{CSR}

$$S_{\text{CSR}} = \frac{Z_0}{4\pi} \frac{I_b e}{\alpha_c \sigma_\delta^2 E} \left(\frac{R}{\sigma_{z,0}} \right)^{1/3}, \quad (2.49)$$

they found an almost straight line for the instability threshold in vicinity of the PP-impedance [88]

$$S_{\text{CSR,th}} = 0.5 + 0.12\Pi. \quad (2.50)$$

For a given set of machine parameters, the threshold bunch current $I_{b,\text{th}}$ is therefore given as

$$I_{b,\text{th}} = \frac{4\pi}{Z_0} \frac{E}{e} \sigma_\delta^2 \alpha_c \left(\frac{\sigma_{z,0}}{R} \right)^{1/3} \left(0.5 + 0.34 \frac{\sigma_{z,0}}{h_c} \sqrt{\frac{R}{h_c}} \right), \quad (2.51)$$

where the bunch current is calculated for an isomagnetic ring. However, as the momentum compaction factor α_c scales the same way as the bunch current for a ring with straight sections, they effectively cancel out each other. Since the vacuum gap height h_c , the bending radius R and the particle energy E_0 are kept constant, the threshold current depends on α_c and the zero-current bunch length $\sigma_{z,0}$. α_c can be determined by the zero-current bunch length $\sigma_{z,0}$ and the RF voltage V_{RF} (cf. Eq. (1.36)). The bunch length itself depends on the synchrotron frequency f_s and the RF voltage. Therefore, by measuring V_{RF} and f_s , the threshold current can be determined. Figure 2.12 shows the scaling law of $I_{b,\text{th}}$ for typical KARA parameters.

Besides from the almost linear threshold of Eq. (2.50), a second instability was found around a shielding factor of $\Pi \approx 0.8$. It is attributed to a weak instability and, in contrast to the strong instability, dependent on the damping time β_d , too. A measurement of this weak instability will be discussed in Chapter 6.4.

⁴ CSR stands for coherent synchrotron radiation and will be discussed in detail in the following chapter

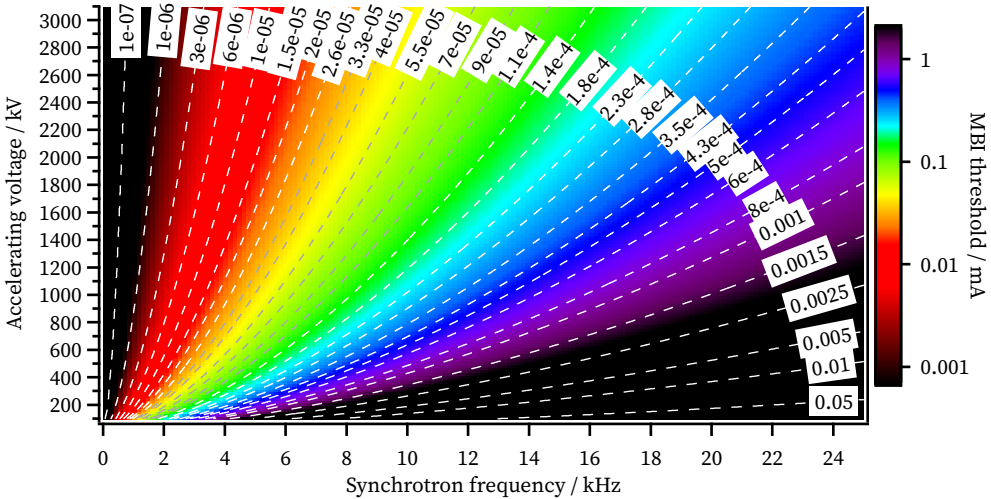


Figure 2.12: Bursting threshold calculated by Eq. (2.51) for KARA parameters at 1.3 GeV. The MBI threshold current is expressed by only two measurable parameters, the RF amplitude and the synchrotron frequency.

In addition to the PP-impedance described above, Y. Cai also analyzed the threshold for a rectangular chamber and developed a scaling law, too [100]. He found out, that a rectangular chamber decreases the instability threshold. Above an aspect ratio of two, where the rectangular chamber impedance approaches the parallel plates impedance, their instability thresholds agree.

2.4 Bursting Radiation above the Threshold Current

Above the instability threshold current, there is no stable solution for the Haïssinski distribution. Therefore, the bunch profile and consequently the emitted coherent synchrotron radiation (CSR) are constantly changing. Beyond the strong instability threshold current, sub-structures on the bunch shape evolve, leading to an even increased wake potential and the emittance of intense THz radiation. Therefore, this instability is called the *micro-bunching instability (MBI)*. The high wake potential drives the sub-structures and leads to a blow-up of the energy spread. When the bunch's electron density becomes too low, the effective wake potential drops and the damping and diffusion takes over. The bunch shape becomes smoothens and shrinks, until the threshold is reached again. Thus, bursts of radiation are observed in the emitted THz radiation.

The first evidence that the monitored bursts [12] were due to a micro-bunching instability driven by the emission of synchrotron radiation in the bunch was presented in Ref. [7]. Then M. Venturini and R. Warnock described a dynamic model for the CSR bursts due to the micro-bunching instability [6].

To simulate the phase space evolution, the VFP equation has to be solved numerically in an iterative process. Patrik Schönfeldt developed *Inovesa numerical optimized Vlasov equation solver application (Inovesa)*. It is a software toolbox, which uses modern parallelization to do this computation on a conventional desktop PC [84]. It currently has built-in impedances of parallel plates, free space and resistive wall, and additionally supports arbitrary impedances as an optional input file. It calculates the phase space distribution according to the VFP equation and extracts the longitudinal bunch profile, from which the emitted radiation and the wake potential for the next time step are calculated. A crucial parameter is the starting distribution. When simulating a beam decay, a blown-up bunch with the highest simulated current is used first and then slowly damped down. The first simulated data are considered to be a rather long initializing phase and are thus neglected.. Then the simulation is started with the found distribution. All the following current steps are performed with the last calculated phase space of the previous simulation run, only changing the total bunch charge.

A detailed explanation of the working principle was also published in [Sch17c]. Time domain measurements, showing the real bursting behavior in time domain can be found in Chapter 6. A comparison with Inovesa simulations is presented in Chapter 7.

3 Synchrotron Radiation

*Physicists like to think that all you have to do is to say,
these are the conditions, now what happens next?*
— Richard Feynman

Based on the impedances which were described in the previous chapter, this chapter shows how the emitted synchrotron radiation is calculated. Coherent and incoherent radiation are introduced and the effect of sub-structures on the bunch profile is analyzed. Then the special case of edge radiation is treated and the angular distribution of the different radiation types investigated. Finally, the extraction of the radiation from the storage ring to the experimental stations is discussed.

3.1 Emitted Synchrotron Radiation Power

A particle experiencing an impedance loses energy according to its real part. Some losses like the resistive wall are dissipated as heat in the chamber walls. Assuming perfectly conducting plates, the losses of the SR-impedance are emitted as electromagnetic (EM) waves. This intense and broadband EM wave is known as synchrotron radiation (SR). By Joule's first law, the power P is proportional to the product of the impedance Z and the current $i(t)$ squared. Expressed in the frequency domain with the Fourier transform of the current $I(f)$, it reads

$$P = \int_{-\infty}^{\infty} P(f) df = \int_{-\infty}^{\infty} I(f) I^*(f) Z(f) df = 2 \int_0^{\infty} I(f) I^*(f) \operatorname{Re}(Z(f)) df, \quad (3.1)$$

where the superscripted star denotes the complex conjugate for the square of the complex current spectrum. Since the imaginary part of the impedance is an odd function, the integral of the reactance is zero (cf. a) in Sec. 2), and thus only the real

part of the impedance accounts to the power losses. Considering that the real part is symmetric, it's convenient to only integrate two times the positive part.

In time domain, a single point-like charge is described by a Dirac δ -function. So the total current is the sum of all N particles, each with unit charge e

$$i(t) = e \sum_{k=1}^N \delta(t - t_k). \quad (3.2)$$

The corresponding spectrum is determined by the Fourier transformation

$$I(f) = e \int_{-\infty}^{\infty} i(t) e^{-j2\pi f t} dt = e \sum_{k=1}^N e^{-j2\pi f t_k}. \quad (3.3)$$

If the particle distribution is smooth enough it can be assumed that micro-bunching effects, as discussed in the previous chapter, are only driven by the structure of the distribution and therefore, the particles are uncorrelated. This assumption leads to [101]

$$I(f)I^*(f) = e^2 \sum_{k,l}^N e^{-j2\pi f t_k} e^{j2\pi f t_l} = Ne^2 + e^2 \sum_{k \neq l}^N e^{-j2\pi f(t_k - t_l)}. \quad (3.4)$$

Since the number of particles is very high ($N \approx 10^8 - 10^{12}$) and their absolute position is constantly changing, an average distribution can be defined given that the probabilities p_d for charges at arrival time t are independent¹ and identical for all particles [102]:

$$\langle I(f)I^*(f) \rangle = Ne^2 + e^2 \sum_{k \neq l}^N \iint e^{-j2\pi f(t_k - t_l)} p_d(t_k) p_d(t_l) dt_k dt_l. \quad (3.5)$$

By introducing the *form factor* $\wp(f)$, which is defined as the magnitude squared of the Fourier transform of the probability density function p_d , one arrives at the well known notation of the CSR formula, first found by Nodvick and Saxon [103]

$$\langle I(f)I^*(f) \rangle = Ne^2 + e^2(N^2 - N)\wp(f). \quad (3.6)$$

The probability density function p_d can be retrieved from the normalized linear line density profile $\rho(t)$ of the bunch (compare Fig. 1.2). It can be measured with a streak

¹ Note that this may not be valid for seeded particle distributions as they may happen for example in a Free-Electron-Laser

camera or by electro-optical spectral decoding (EOSD) (cf. Chapters 4.3.5 and 4.3.6). The form factor reads

$$\wp(f) = \left| \int_{-\infty}^{\infty} p_d(t) e^{-j2\pi f t} dt \right|^2 = \frac{1}{N^2 e^2} \left| \int_{-\infty}^{\infty} \rho(t) e^{-j2\pi f t} dt \right|^2 = \frac{1}{N^2 e^2} |\varrho(f)|^2, \quad (3.7)$$

where $\varrho(f)$ denotes the Fourier transformation of the linear line density profile $\rho(t)$. Figure 3.1 shows the form factors of two bunch profiles which are depicted in the small inlet. You see a bunch profile, as it has been measured in the KARA storage ring by electro optical spectral decoding (EOSD) [30], and for comparison, a Gaussian bunch profile with an RMS width of 5 ps.

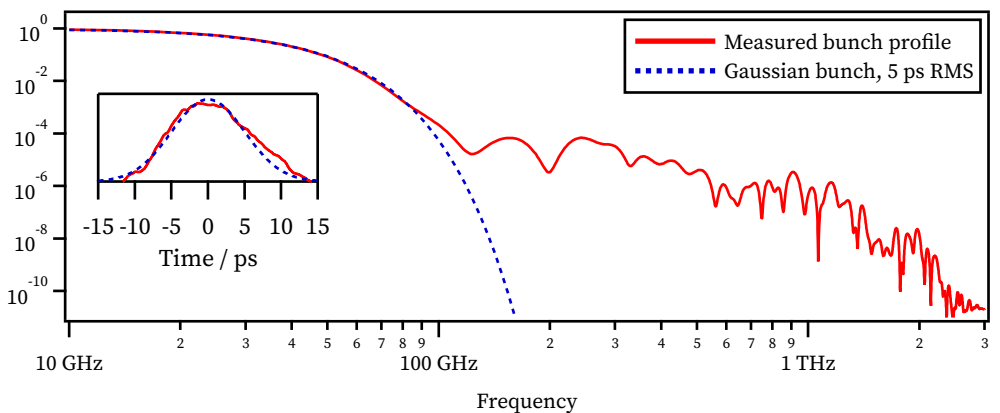


Figure 3.1: Form factor of two bunch profiles. In dashed a Gaussian profile with an RMS width of 5 ps and in solid a real bunch profile measured in the KARA storage ring within the micro-bunching regime. The form factor approaches unity at low frequencies and zero at high frequencies. In-between it is determined by the form of the bunch profile. Even small disturbances can lead to an increase of several orders of magnitude compared to the smooth distribution at the corresponding frequencies.

At low frequencies, the form factor always is unity and, according to the bunch profile, decreases to zero for wavelengths smaller than the structures on the bunch profile. Sub-structures on the bunch, as it is the case for the measured profile, can have a significant influence on the form factor and thus the emitted frequency spectrum. Figure 3.1 shows the form factor for both, the measured profile with sub-structures and the purely Gaussian profile. Considering the high number of particles and that the form factor is multiplied by the number of particles squared, even small disturbances can lead to a significant increase in the power of SR by several orders of magnitude at the corresponding frequencies.

Inserting (3.6) into (3.1) leads to the total emitted power

$$P(f) = e^2 [N + N(N - 1)\wp(f)] Z_{s(f)}, \quad (3.8)$$

where $Z_s(f)$ is the integrated impedance each electron encounters in a unit time. Since the impedances in a ring recur each turn, it is possible to use $Z_s(f) = f_0 Z_{\text{turn}}(f)$, with f_0 being the revolution frequency and $Z_{\text{turn}}(f)$ the integrated impedance per turn.

The emitted energy per turn W can be expressed by the revolution time $T_0 = 1/f_0$ and the emitted power. So the total energy a bunch loses in one turn is

$$W = e^2 \int_{-\infty}^{\infty} [N + N(N - 1)\wp(f)] Z_{(f),\text{turn}} df. \quad (3.9)$$

Two contributions can be identified: The first, linearly proportional to the number of electrons in the bunch, is called the *incoherent synchrotron radiation (ISR)*. It's independent of the bunch shape and size and determined only by the impedance which in the case of bending magnet radiation is dependent on the bending radius and particle energy. The second contribution is additionally dependent on the form factor, taking into account the longitudinal position of the electrons, but scaled by the number of electrons squared. It is therefore called *coherent synchrotron radiation (CSR)*. The coherent radiation is not only many orders of magnitude more intense than incoherent radiation, but it also provides single-cycle fields, since the length of the emitting electron bunch is shorter than the wavelength of the emitted light. One of the first documented observations of coherent synchrotron radiation was made in 1989 in the Tohoku 300-MeV Linac using a 2.4 mm short bunch [104].

The form factor limits the maximum frequency of CSR in most light sources well below the critical frequency f_c (Eqn. 2.25), so that the low-frequency approximation, which is independent of the energy, can be used. Thus the coherent power only depends on the bunch shape and the number of electrons.

The impedances discussed above are either given per length, e.g., the resistive wall and bending magnet impedances, or per occurrence, e.g., impedance of a bending magnet edge. Keeping in mind that in a storage ring each impedance recurs after a complete revolution, all impedances are normalized to one turn and then scaled by the number of turns per second leading to the total integrated impedance per second

of the electron bunch. That is to say, the resistive wall impedance is integrated over the whole length of the beam pipe (110.4 m), while the parallel plates impedance is integrated over the length of the dipoles (34.9 m), and the bending edge radiation is scaled by the number of bending edges per turn (16 entrances and 16 exits). In the following, to distinguish between different sources of synchrotron radiation (SR), the radiation emitted from a constant magnetic field inside a bending magnet is called *constant field radiation (CFR)* and the radiation emitted at the edge of a magnetic field is named *edge radiation (ER)*. If not explicitly stated, SR refers to the constant field radiation.

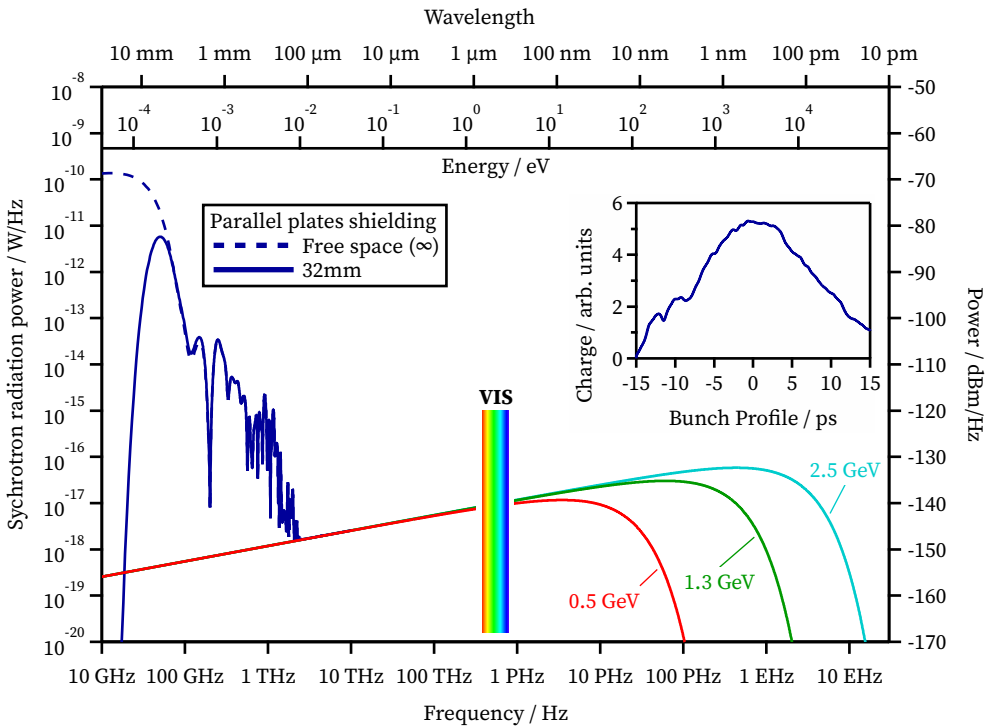


Figure 3.2: Power radiated by a single electron of different energies in the KARA storage ring. The coherent radiation is calculated based on the measured, unstable bunch profile shown in the inlet.

Figure 3.2 shows the emitted power for a bunch current of 250 μA ($\approx 5.7 \times 10^8$ electrons) with different electron energies. On the horizontal axis is frequency, wavelength and photon energy, typical units used in the range covered by synchrotron radiation. The visible light range is indicated by a rainbow. Low frequencies are independent of the particle energy, while above the visible light range the influence can be seen.

According to Eqn. (1.19), the total integrated power rises by the fourth power of the particle energy. The inlet shows a measured bunch density profile. The coherent enhancement is shown with and without shielding by parallel plates. It is up to the number of particles of 5.7×10^8 . The total integrated power of the incoherent radiation at 1.3 GeV adds up to 11.4 W, whereas the coherent radiation amounts to 0.16 W. When only considering the radiation below 10 THz, the ratio changes: While the coherent power stays the same, the incoherent radiation in that range is only 20 μ W.

Table 3.1: Emitted SR of a single bunch with stable form factor according to the inlet in Fig. 3.2

Bunch current: 250 μ A			
Particle energy	Incoherent (W)	Coherent (W)	Ratio
0.5 GeV	0.25		0.64
1.3 GeV	11.4	0.16	0.014
2.5 GeV	155		0.001
Bunch current: 500 μ A			
Energy	Incoherent (W)	Coherent (W)	Ratio
0.5 GeV	0.5		1.26
1.3 GeV	23	0.63	0.027
2.5 GeV	310		0.002
Bunch current: 1 mA			
Energy	Incoherent (W)	Coherent (W)	Ratio
0.5 GeV	1		2.5
1.3 GeV	46	2.5	0.05
2.5 GeV	620		0,004
Bunch current: 250 μ A, < 10 THz			
Energy	Incoherent (W)	Coherent (W)	Ratio
0.5 / 1.3 / 2.5 GeV	2×10^{-5}	0.16	8000

Table 3.1 summarizes the emitted SR for the discussed example. Note that the coherent power emitted by a bunch is strongly dependent on the longitudinal bunch density

profile. The sub-structures as depicted in Fig. 3.2 are not stable in a real accelerator, and its resulting radiation, with the discussed intensity, will only be observed for a short time frame. Furthermore, in a real accelerator, increasing the bunch current will change the form factor due to current-dependent effects like the potential well distortion discussed in Chapter 2.2.

In Chapter 1.5.3, the dependence of the particle motion in the longitudinal phase space due to the emitted radiation per turn has been shown. The above example makes clear, that a change in bunch shape or size and therefore a change in emitted coherent radiation effects the whole bunch motion, because the energy loss per turn changes. Especially at relatively low beam energy, where the ratio of coherent to incoherent radiation is higher, this can have a significant impact. Due to the micro-bunching instability (MBI) discussed in the previous chapter, a short bunch can be significantly lengthened in a few hundred turns, so that the coherent radiation almost vanishes. On the other hand, sub-structures on the bunch profile, resulting in an increased form factor, can also be formed in a few turns due to the same instability.

In his early studies of the Saturnian model of an atom in 1912, George A. Schott already considered the effects of coherent radiation [1]. The model presumed that a large number of electrons move simultaneously in a closed orbit, similar to a circular particle accelerator. Later on, Leonard I. Schiff [105], Julian S. Schwinger [68] and John S. Nodvick & David S. Saxon [103] investigated more deeply into that issue when it became important for accelerators. As they wanted to accelerate to highest possible energies, their focus was on suppressing the extra energy loss from coherent emission. They concluded that parallel plates can sufficiently suppress CSR for long bunches.

The attention to this problem came back in 1982, when F.C. Michel described possible applications in a storage ring [106], and especially, when accelerators became capable of compressing bunches down to the order of the beam pipe radius. Today, bunches are being shortened on purpose to serve users with intense CSR radiation in the THz regime. The spectrum of coherent emission, being dependent on the bunch structure, has also been found to serve as a diagnostic tool, e.g. to determine the bunch length [107].

Even though the shielding by parallel plates was first introduced as a solution to suppress CSR emission, the real part of the integral of the free space impedance equals the parallel plates impedance. Shielding does not suppress the emission of incoherent radiation power, but shifts the components to higher frequencies, which are increased

accordingly. This feature, as well as the theory itself has been experimentally proven by Kato, et. al. in 1993 in a dedicated experiment with a bending magnet of variable gap size [108; 109]. The radiation of coherent power, through its dependence on the bunch profile, however, can be suppressed by parallel plates shielding if the bunch profile does not have spectral components at frequencies above the shielding cutoff. Figure 3.3 summarizes the dependencies on the various accelerator properties of the emitted spectrum.

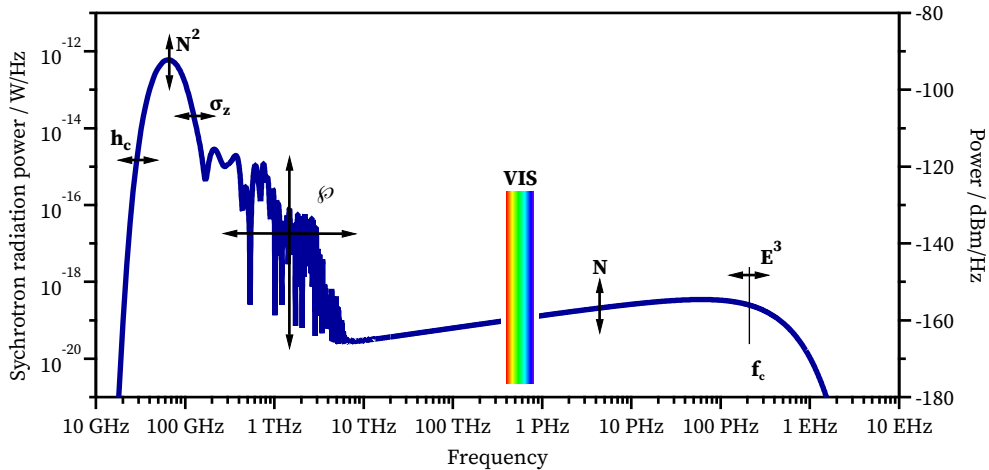


Figure 3.3: Synchrotron radiation spectrum and its main dependencies in the KARA storage ring with a fixed radius of curvature of $R = 5.556$ m and a total accelerator length of $L_0 = 110.4$ m. The parameters of the shown trace are the same as in Fig. 3.2, 1.3 GeV. While coherent radiation scales with the number of particles squared (N^2), the incoherent radiation has a linear dependence (N). The cutoff of the coherent radiation is determined by the bunch length σ_z , while the transition from coherent to incoherent is determined by the form factor $\phi(f)$, i.e. the bunch profile. The vacuum chamber height h_c accounts for the shielding at the very low frequencies, while the high frequency cutoff is determined by the particle energy E where the critical frequency scales with the third power of the energy (E^3).

3.2 Edge Radiation

A real storage ring does not only consist of bending magnets. For several reasons, straight sections are needed. At the edges of the bending magnets there is a steep change in the magnetic field. However, that change is not instantaneous, but accompanied by so-called fringe fields where the magnetic field extends over the mechanical length of the bending magnet. In these fringe fields, where the deflection of the electrons changes, radiation is emitted. Similar to constant field radiation, the low

frequencies are suppressed by the apertures. Furthermore, the edge radiation (ER) is suppressed at very high frequencies, because a finite distance is required to deflect the electron in the fringe field and emit radiation. Therefore edge radiation only occurs for wavelengths that are long in comparison to the fringe field dimension and short in comparison to the vacuum chamber dimension. The total emitted power of coherent edge radiation can be calculated by the impedance in Eq. (2.27), which considers a zero-length edge, valid only at low frequencies.

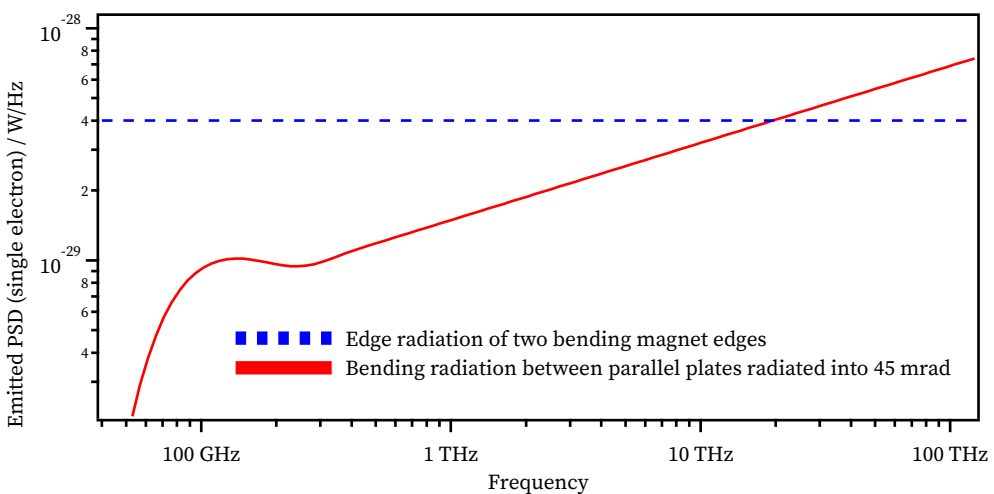


Figure 3.4: Comparison of the emitted synchrotron radiation power due to a constant magnetic field and due to a magnetic field edge. Here, the constant field radiation is limited to an opening angle of 45 mrad.

On total, the constant field radiation (CFR) exceeds the ER by a great amount. However, when considering a single beamline, things change due to the finite aperture. At the beamline discussed in Chapter 3.5 it will be shown that the horizontal beamline acceptance is 45 mrad. A simplified comparison of the emitted CFR into 45 mrad with the power of two edges is shown in Fig. 3.4. Note, that there is always radiation from two concurrent edges, because the radiation emitted at the exit of a bending magnet is overlapped by the radiation emitted at the entrance edge of the following magnet.

At the low frequencies, even in this rough estimation, the ER emits more power than the corresponding CFR. This effect becomes stronger, when a vertical aperture is taken into account, too. For a better understanding of the radiation and its transport through the beamline, the angular distribution needs to be investigated.

3.3 Angular Distribution

Many textbooks state, that the opening angle of SR scales with $1/\gamma$. However, in the case of radiation emitted in a constant field (CFR), the exact definition is that at an opening angle of $\Theta = 1/\gamma$ the intensity is only $1/8$ of the main direction [45]. Therefore, most of the energy is confined inside that angle. But that result is misleading as it is only valid when integrating over the full spectral range. The angular distribution, i.e. the natural vertical divergence, of the radiation at a given frequency is independent of the electron energy and is given by [110]

$$\Theta_{\text{vert}} \approx 1.66 \text{ rad} \left(\frac{c}{fR} \right)^{1/3}. \quad (3.10)$$

The γ -dependent opening angle of the integrated radiation is therefore due to the higher frequencies which are additionally emitted at higher beam energy and have a significantly smaller divergence. For the infrared and THz frequencies, there is no benefit of having higher beam energies, because the additionally emitted X-rays are unwanted and absorbed². It is a big challenge to extract the low frequency radiation with its broader divergence, which will be discussed in more detail in Chapter 3.5.

At the IR beamlines with a vertical acceptance of 14 mrad, the radiation is cut for frequencies smaller than 90 THz according to Eqn. (3.10). At 1 THz the vertical divergence would already be 63 mrad. Therefore a big part of the CFR will be transmitted through the beamline.

For ER at angles $\Theta \ll 1 \text{ rad}$ the photon flux per unit solid angle can be approximated by [70]

$$\frac{dF}{d\Omega_{\text{edge}}} \approx \Theta \frac{\Delta\omega}{\omega} \frac{I}{e\pi^2} \frac{\gamma^4 \Theta^2}{(1 + \gamma^2 \Theta^2)^2}. \quad (3.11)$$

In accordance to the impedance, the flux density is independent of the frequency. Additionally, it is zero at the direction of motion ($\Theta = 0$) and has a peak at the observer angle $\Theta = 1/\gamma$. In a storage ring, you will not observe the radiation of a single edge, since it is always superimposed by the radiation of the preceding exit edge. On the straight line between the magnets, the exit edge radiation travels approximately with

² This assumption is only true for a point-like particle. When considering a broad electron bunch, the transverse dimensions of the bunch have to be taken into account, and these can change with energy.

the same speed as the electron bunch and interferes with the radiation from the next entrance edge. The resulting flux density can be described by [70]

$$\frac{dF}{d\Omega} = \frac{dF}{d\Omega_{\text{edge}}} 4 \sin^2 \left(\frac{\pi L f}{2c\gamma^2} (1 + \gamma^2 \Theta^2) \right), \quad (3.12)$$

with L being the distance between the magnets. The intensity peaks again at $\Theta = 1/\gamma$ but has an additional oscillating term leading to a frequency dependent, ring-like pattern. Therefore, the effective transmission through the beamline becomes frequency dependent, too. Furthermore, the collimation of the radiation is dependent on the distance between the two edges. With higher distance, the radiation becomes more collimated [111].

3.4 Comparison of Constant Field Radiation and Edge Radiation

Numerical simulations of the radiation have been carried out with synchrotron radiation workshop (SRW) [112; 113]. Two scenarios were investigated: First, an electron in a constant magnetic field with the length of two KARA dipoles. And second, the real layout, where the two bending magnets are separated by a straight section of approx. 4.8 m. The longitudinal path of the electron and its horizontal displacement is shown in Fig. 3.5.

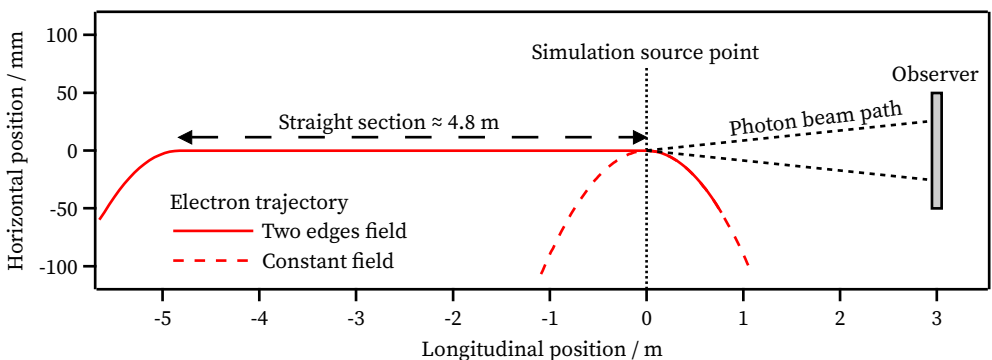


Figure 3.5: Setup for the SRW simulations. Longitudinal and horizontal position of the electron path for a constant magnetic field (dashed) and a real configuration (solid line) with a straight section between the bending magnets. The observer screen is located 3 m behind the entrance edge of the second magnet. Note the different scaling for horizontal and longitudinal position.

The electron path is from left to right. The source point of the simulation is chosen to be the entrance edge of the second bending magnet. The observer screen is located 3 m behind and has a size of 180 mm horizontal and 200 mm vertical, resulting in an acceptance of 30 mrad horizontal and 33.3 mrad vertical. The image on the screen for three different frequencies is shown in Fig. 3.6. The left images show the radiation emitted in the constant field and the right images the radiation emitted when the bending magnets are separated by a straight section. The rightmost panel shows the averaged vertical power for the three cases. The maximum peak intensity is always higher in the edge radiation case. Furthermore, most of the intensity is confined in a cone significantly smaller than the CFR. While the integrated overall intensity is the same for all frequencies, the peak intensity drops, and it becomes obvious that a small aperture will cut the low frequencies first.

The intensity differences will become more pronounced, when the horizontal acceptance is reduced, because the edge radiation is confined in a small cone, while the CFR is almost equally distributed. Small deviations in the CFR result from the fact, that the radiation emitted at the beginning of the magnet has a slightly longer path and thus seen more divergence than the radiation emitted at the end of the magnet. Therefore, the detected intensity slightly drops at the outside. The polarization of the beam is another property to be mentioned. Edge radiation is radially polarized. Yet, the CFR is mainly linearly polarized in the orbit plane. The polarization is indicated by white arrows in the last image of Fig. 3.6.

The transfer of the radiation through a beamline to the experimental stations will be discussed in Chapter 3.5 and measurements of the real beam profile at the end of the beamline are presented in Chapter 3.6.

3.5 Extraction of Synchrotron Radiation at Beamlines

In order to use the SR for experiments, the emitted photons have to be separated from the electrons and the desired frequencies have to be guided to the experiment. The KIT synchrotron has two infrared beamlines, *IR1* and *IR2*, which are designed for the use of radiation with a wavelength between 2.5 mm and 1 μm (0.12 THz to 3000 THz) [114; 13]. Although they are optimized for the infrared range, the nearby ranges of THz and visible light are also partially transmitted. Due to the above mentioned advantages of ER, the optics of the infrared beamlines have been designed to image the entrance

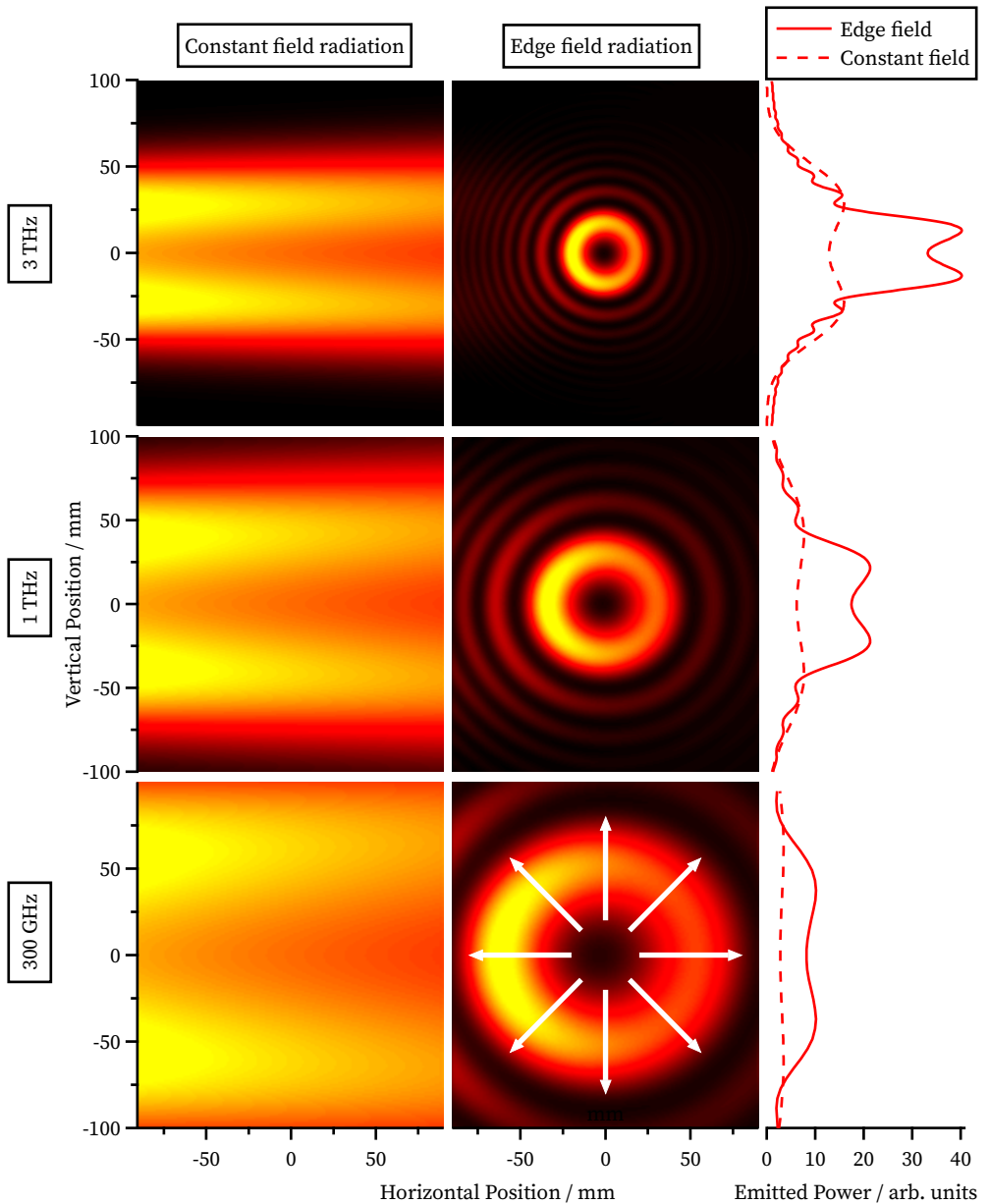


Figure 3.6: Synchrotron radiation workshop (SRW) simulations of synchrotron radiation emitted in a constant magnetic field and from two edges 3 m behind the source (cf. Fig. 3.5). For better visibility, the color scales are normalized to the individual maximum. The right panel shows the averaged vertical power, the white arrows indicate the polarization direction.

edge of the bending magnet. The IR1 beamline was one of the first beamlines in the world dedicated to edge radiation. Due to the great success, the IR2 beamline has been designed to use the intense edge radiation, too. Therefore, the zero degree port of the bending magnet is used to extract the synchrotron light from the storage ring.

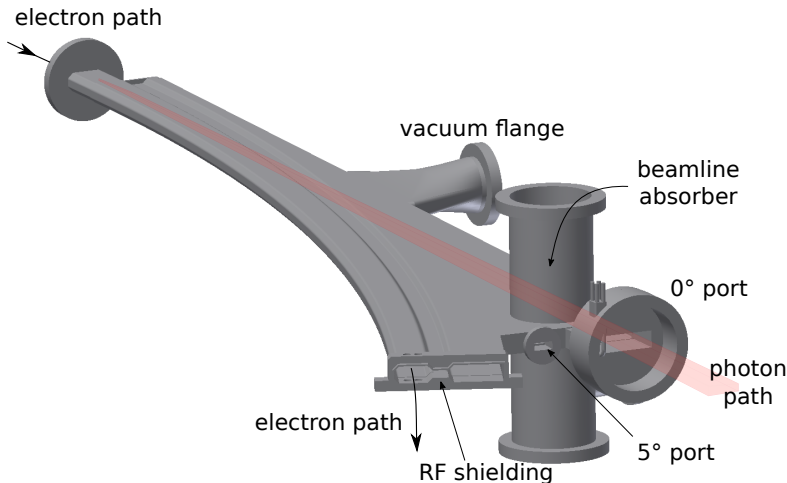


Figure 3.7: Top: 3D CAD model of the vacuum chamber in front of the IR2 beamline. While the electron path is bent by 22.5°, the synchrotron light is coupled out at the enlarged 0° port. The standard size 5° port is currently not being used. Courtesy of IBPT-CAD, modified.

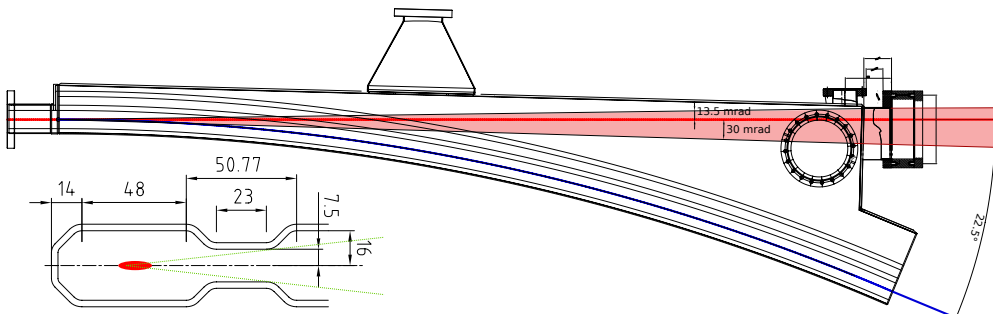


Figure 3.8: CAD drawing of the IR2 extraction chamber. The drawing in the bottom left shows a cross section of the beam pipe. The photon feed-through limits the height to 15 mm. Afterwards the chamber expands to 32 mm again. Together with the next absorber (A2), this limits the vertical beam divergence to 15 mrad and the horizontal to approx. 45 mrad. Courtesy of IBPT-CAD, modified.

Figure 3.7 shows a 3D model of the vacuum chamber inside the bending magnet. The electrons travel on the curved path and are deflected by 22.5°. This chamber

has two photon outputs, the 0° and 5° port. The 0° port for edge radiation has larger apertures to enhance the transmission of long wavelengths compared to the standard port used for X-rays. To protect the surrounding, a special water cooled X-ray absorber is installed. However it limits the horizontal acceptance. A CAD drawing of the dipole chamber is shown in Fig. 3.8. Additionally, the photon beam path along with the limiting apertures and mirrors is summarized in Fig 3.9.

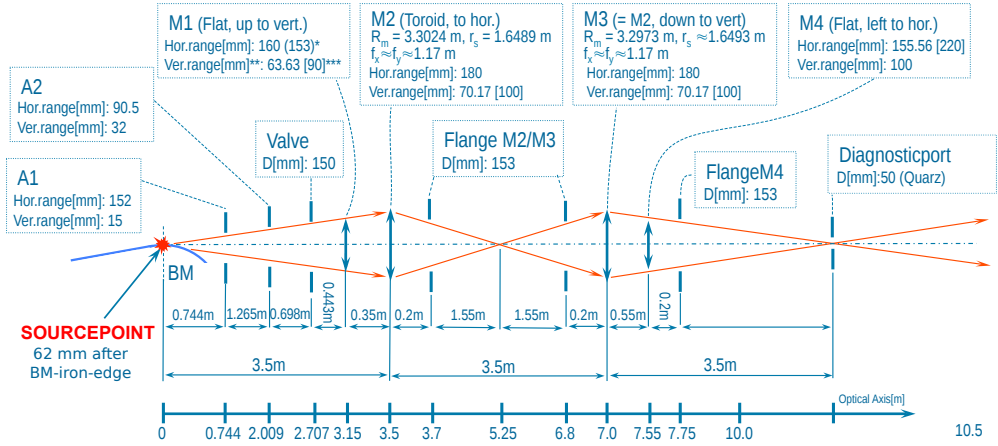


Figure 3.9: Optical beam path profile of the IR2 beamline. The radiation source point is the entrance edge of the bending magnet (BM). The limiting apertures (A) restrict the effective opening angle of the radiation. With a set of four mirrors (M), the light is coupled out of the storage ring into the experimental hutch. Adapted from IR2 documentation, courtesy of Yves-Laurent Mathis and Peter Rieger.

To keep the geometric impedance of the chamber walls as low as possible, the photon feed-through is usually just 5 mm in height, but was enlarged to 15 mm (A1) for the IR beamlines. However, this still limits the vertical acceptance to ± 7.5 mrad. Then the chamber expands to 32 mm again. The second aperture (A2) is due to an X-ray absorber with an opening width of 90.5 mm. To improve the radiation transport, the whole vacuum chamber has a small tilt, which shifts the center of the absorber 15 mm from the straight path towards the ring. Seen from the source point, the horizontal acceptance is approximately $+15/-30$ mrad. Between the storage ring vacuum chamber and the beamline frontend is a vacuum valve with a diameter of 150 mm, sufficient to let all the radiation pass. The first mirror of the beamline is a flat beryllium mirror that reflects the wanted radiation upwards, but is transparent and partially absorbing for X-rays which are dumped into an X-ray absorber afterwards. Considering the 45 degree mounting, the effective dimensions of the mirror is 160 mm horizontal and 63.63 mm vertical.

This is sufficient to transport most of the infrared light to the experiments with a minimum of loss due to scattering, diffraction and absorption. The long wavelengths in the THz range, however, are cut off. It's noteworthy, that the energy density per solid angle is much higher at the high frequencies, whereas the total emitted power is constant over frequency. Since a lot more of the low frequencies are cut off and scattered by apertures, the power transfer through the beamline is much more efficient for the high frequencies.

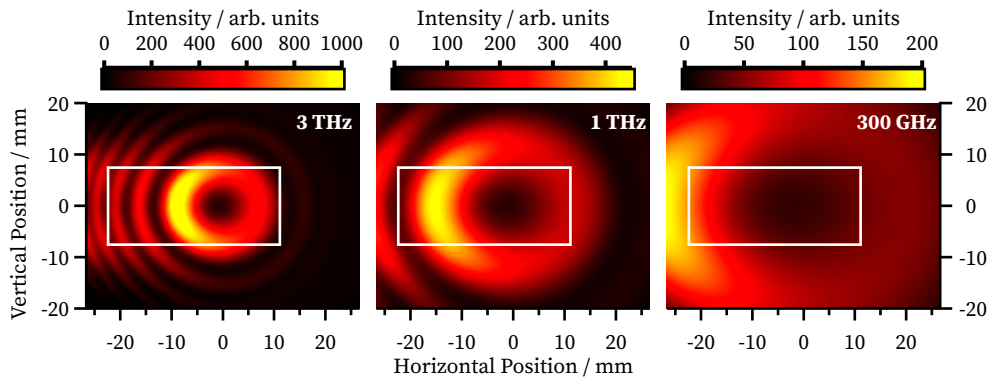


Figure 3.10: SRW simulation of the intensity distribution at A1 for different frequencies. The white rectangles indicate the apertures. The horizontal restriction is due to A1, the vertical is a projection from A2.

Figure 3.10 shows SRW simulations of different frequencies at the position of the first aperture A1. The projection of the second aperture A2 results in the horizontal limitation. Since it is arranged slightly off-center, the high intensity part of the left half ring is transmitted for frequencies above 1 THz. Also note the much higher power density which is transmitted through the beamline.

At 300 GHz and below, the natural edge radiation shape is not transmitted to the beamline, and a lot of scattering and reflections happens. Due to the cut-off of the upper and lower part, mainly the horizontally polarized radiation is transmitted. Therefore, the measured radiation at the beamline is mainly horizontally polarized. The amount of other polarization directions increases for higher frequencies, until in the mid-IR range the whole radially polarized beam is transmitted.

3.6 The KARA Infrared Beamlines

The frontend of the two infrared beamlines is almost identical. The main difference is the size of the vacuum components and the position, where the separation of the beamline vacuum system and the storage ring vacuum system is done. At IR1, a diamond window is placed at the position of the first intermediate focus to separate the two vacuum systems. Since this small aperture has been found to be too small, leading to diffraction at the low frequencies, this transition was moved to a later point in the beam path at the IR2 beamline.

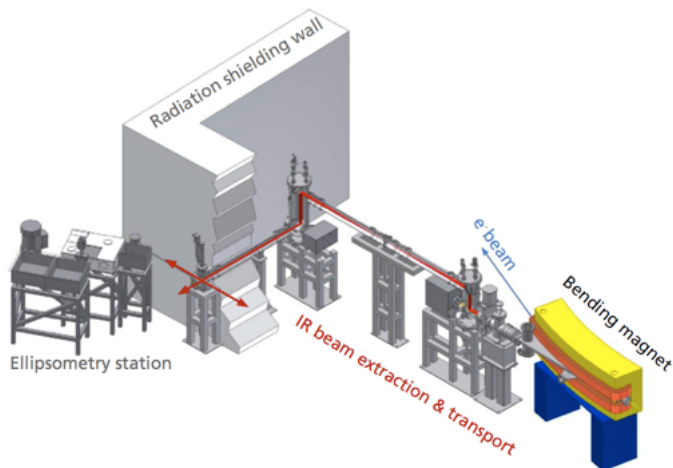


Figure 3.11: IR1 beamline frontend and experimental stations. With four mirrors, the radiation is first reflected upwards above an X-ray absorber, then focused onto a 20 mm diamond window and afterwards reflected down again. With a 90° angle, the radiation is fed through the radiation shielding wall into the beamline hutch. The beamline is equipped with an FTIR spectrometer and an ellipsometry station. Additionally, a free space experiment can be carried out at the straight diagnostic port. Image is courtesy of the IBPT-CAD group.

Inside the hutch, the two beamlines differ in more details, as different kinds of experiments are performed. At the IR1, as depicted in Fig. 3.11, a mirror can either reflect the radiation to the ellipsometry station or to an available non-permanent station. Or the mirror is removed to let the radiation pass straight. The straight port has a z-Cut quartz window and is referred to as the *diagnostic port*. The ellipsometry station is equipped with an FTIR spectrometer which is used in Chapter 5. All other experiments at IR1 have been done at the diagnostic port.

A CAD model of the IR2 beamline is shown in Fig. 3.12. Behind the radiation shielding wall, a window changer is installed, so that different vacuum windows can be used. The windows are necessary to separate the storage ring vacuum system ($<1 \times 10^{-7}$ Pa) from the beamline system ($<1 \times 10^{-3}$ Pa). Each window is optimized for a different frequency range. For the THz range, a z-Cut quartz window and a diamond window can be chosen. Another option is the diagnostic port which is straight through a z-Cut quartz window similar to the IR1 beamline.

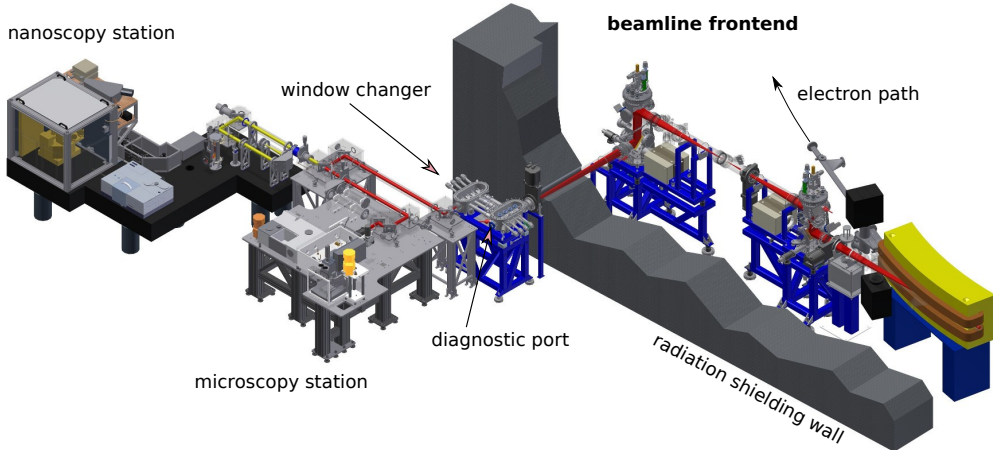


Figure 3.12: IR2 beamline frontend and experimental stations. In comparison to the IR1 beamline, some improvements have been made. First, the vacuum window between mirror one and two has been moved to the inside of the hutch and replaced by a window changer, where one out of four windows can be chosen for the optimum of the experiment. The windows are located at a 1:1 focus position. The diagnostic port is straight through the window changer passing a z-Cut quartz window. Toroidal mirrors come after the window changer to adjust the beam shape to be more rectangular and collimated. Then, a fast feedback system for beam stabilization follows as well as a beam path changer to guide the radiation either to the nanoscopy or microscopy station. Image is courtesy of the IBPT-CAD group.

The rest of the beam line consists of two toroidal mirrors, whose purpose is to increase its transverse size and to make the beam more homogeneous and collimated. The following mirrors are all flat, until the beam is focused onto the experiment. A feed-back system can be used to stabilize the beam by piezo driven mirrors. A switching mirror can send the radiation either to the microscopy or nanoscopy station. Both are equipped with a Bruker Vertex 80v FTIR, which is used for the experiments described in Chapter 5. All other experiments have been done directly at the diagnostic port.

Peter Rieger performed a simulation for 1 THz with SRW and with a code with additional own improvements [115]. Figure 3.13 shows the simulated beam profile at

the position of the z-Cut quartz window as well as 375 mm behind. The propagation through the beamline has led to major distortions of the beam profile due to diffraction and scattering. At the diagnostic window, the profile is vertically symmetric with spots on both sides. Horizontally, additional spots with different intensities can be identified. At the second position, the profile has homogenized, so that in horizontal position only a single peak is left, but now the position of the maximum intensity is above the vertical zero position. The simulation uses approximations which are not valid below 1 THz, therefore, this was the lowest simulated frequency.

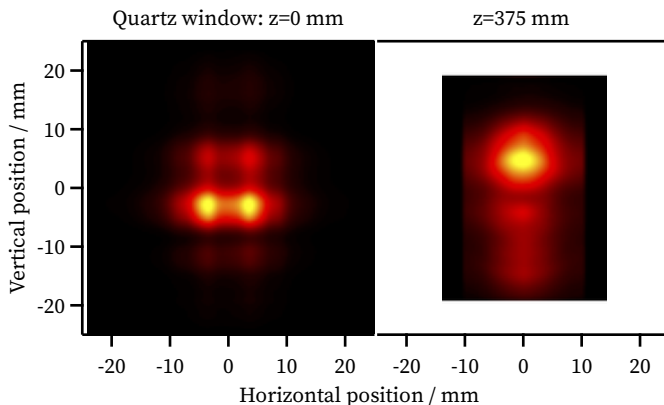


Figure 3.13: Simulated beam profile at 1 THz at the position of the z-Cut quartz window as well as 375 mm behind. Simulation done by Peter Rieger.

Measurements of the radiation between 90 GHz to 500 GHz were done in the framework of the Bachelor thesis by Carl Sax [Sax17] and shown in Fig. 3.14. The used detectors are sensitive in a specified frequency range and will be introduced in detail in Chapter 4.1. The nearest measurement distance to the window was 86 mm. The visible light spot has been chosen as the origin of the axis. Note that the THz and optical spot positions match vertically, while the THz radiation is systematically shifted horizontally. The low frequencies show an almost Gaussian profile, but with different transverse widths, which also change over distance. This is an indication that the aperture is too small and acts as a virtual source point in the beam path. At the highest measured frequency, the simulated shape at the window position is reproduced better. At a later position, the two horizontal spots combine similar to the simulation. In contrast to the simulation, however, the spot with higher intensity is below the other.

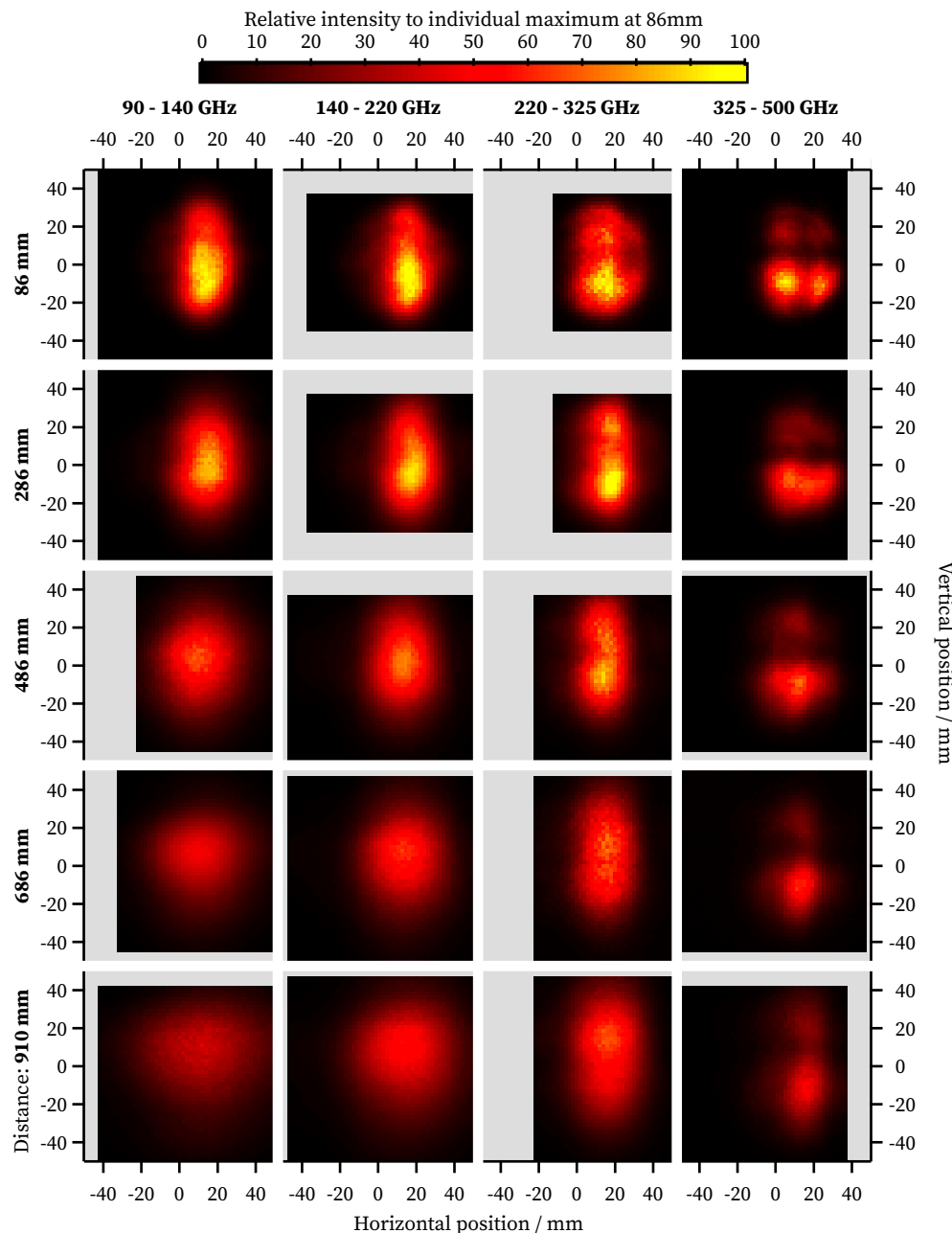


Figure 3.14: Beam profile measurements at several distances behind the IR2 diagnostic port. The center of the visible radiation is chosen to be the origin of the coordinate system. Grey areas have not been scanned. By a coarse scan at the beginning, it was verified that no bigger parts of the radiation have been missed. Data is taken from [Sax17]. For more information, see text and Ref. [Sax17].

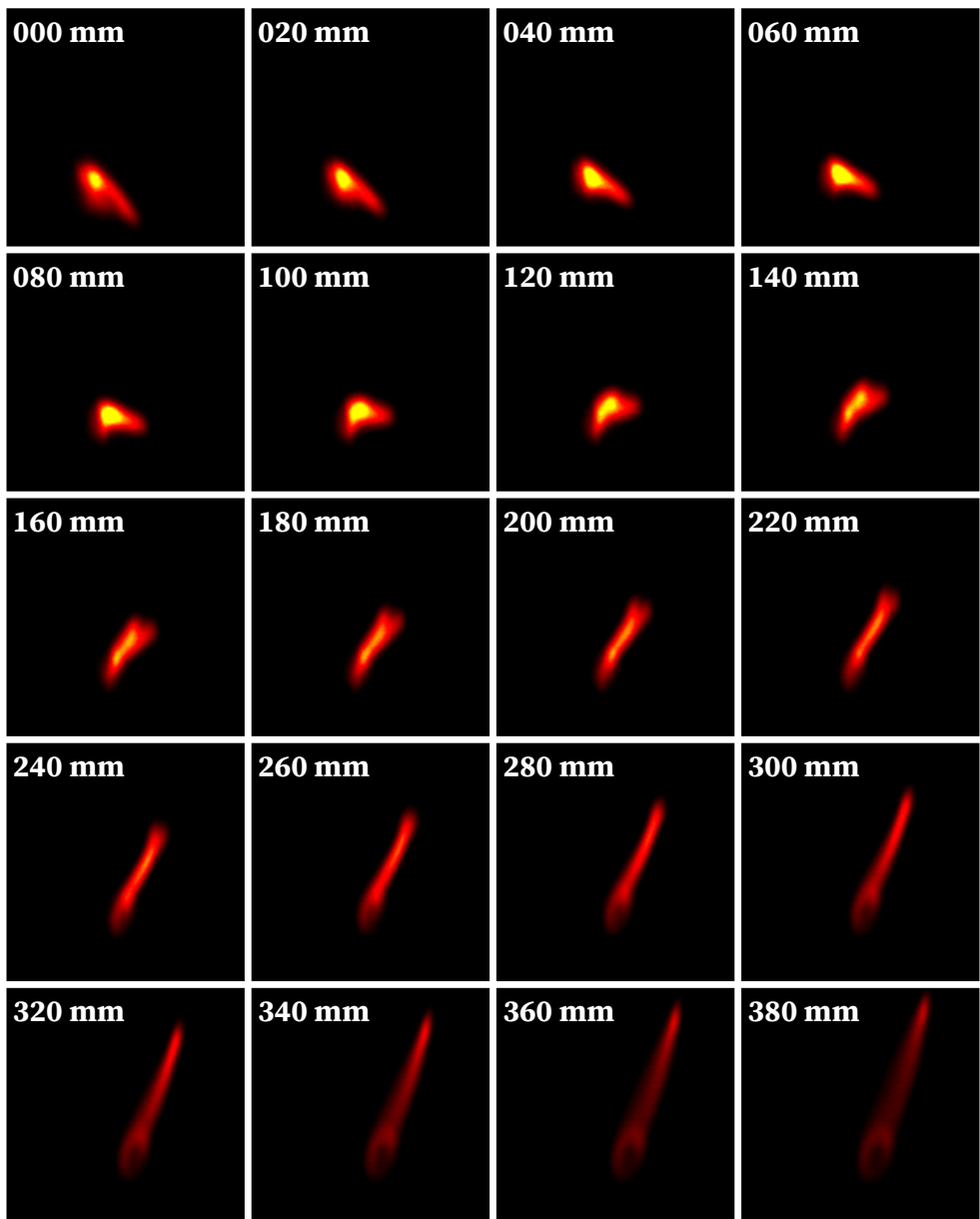


Figure 3.15: Beam profile measurement with a mid-IR camera at different distances from the IR2 diagnostic port. The constant field radiation, compared to the edge radiation, is much stronger at the mid-IR than in the THz range. Especially at distances further away, the separation of the edge and constant field radiation can be seen due to the different radiation source points.

The case is different at the higher frequencies of the mid-infrared region. There, the transmitted bending magnet radiation is much stronger so that the difference in intensity to the ER is not that severe. Besides, the initial opening angle is small enough to transport the radiation to the experiment with much less diffraction. Therefore, not only the ER spot is visible, but also the CFR tail. This is nicely illustrated by the profile measurements at different distances from the diagnostic port at higher frequencies, shown in Fig. 3.15. They were measured with a commercial *Pyrocam IV* camera which is equipped with a Germanium window (PY-IV-W-GE-8-12), transparent from 8 μm to 12 μm (25 THz to 37 THz).

4 Equipment and Machine Parameters

During an intense period of lab work, the outside world vanishes and the obsession is total.

Sleep is when you can curl up on the accelerator floor for an hour.

— In Leon Lederman and Dick Teresi, The God Particle:
If the Universe is the Answer, What is the Question, p14-15., 1993

Every experimental Chapter in the following has a dedicated setup, which will be explained in detail in the corresponding chapter. Here, common tools used for all experiments are described, like the available THz detectors and the determination of machine parameters. Additional information about the different readout schemes which have been used can be found in App. B.

4.1 THz Detectors

The fastest oscilloscope to date is limited in readout bandwidth to around 100 GHz. For that reason, sub-THz electromagnetic waves can not be observed directly. However, several detectors measuring the power of the fields exist and the ones available at KARA will be described in the following. Detectors that only detect the power of the radiation but not the phase and the amplitude are called *direct* detectors. These can be categorized into three types [116].

First, *thermal detectors*, which absorb the incoming radiation and produce heat that can be detected. Examples for these detectors are bolometers which detect the change in electrical resistance, pyroelectric detectors where an internal electrical charge alters with temperature, or the Golay cell detector where the expansion of a gas-filled cell is measured with an optical system. The speed of these detectors depends on the detected thermal effects. While the Golay cell response time is in the range of seconds, some superconducting and semiconducting bolometers can be very fast,

reaching some hundred picoseconds. Furthermore, the absorption of radiation can be very broadband and is – in the ideal case – independent of frequency. But this mostly applies to the infrared range and breaks down in the THz region.

The second type are *photo detectors* which rely on the photoelectric effect where the absorbed energy corresponds to the energy gap between the valence and conduction band. Due to the small photon energy in the THz range, these detectors are used mainly above 10 THz and are not taken into account for the studies discussed in this thesis.

Rectifying detectors are the third type. These are high speed versions of the commonly used electrical rectifying circuits to measure the RF power. Schottky diodes are well known to function as such a device due to their nonlinear current-voltage dependence. In this thesis, zero-biased Schottky barrier diodes (SBD) are used. In general, they are made as planar detectors from InGaAs or InP, where the low barrier allows for zero bias operation [117; 118]. Usually they are flip-chip mounted and bonded to an antenna [119]. Figure 4.1 shows a scanning probe micrograph and the corresponding current-voltage characteristic of a Virginia Diodes (VDI) WR-10 SBD [120].

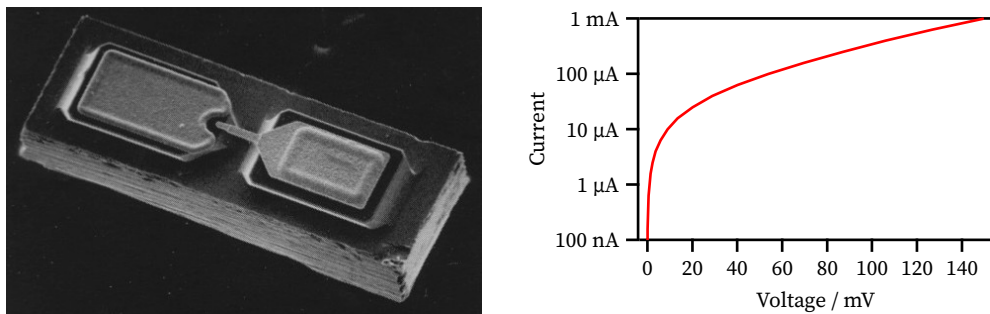


Figure 4.1: Scanning probe micrograph of a planar Schottky barrier diodes (left) [120]. Chip dimensions are approximately 180x180x40 μm . The measured current-voltage characteristic of the used zero-bias flip-chip WR3.4R7 3-24 Schottky detector diode (right). Figure and data provided courtesy of Jeffrey Hesler, Virginia Diodes Inc., Charlottesville, VA, USA.

Two different types of Diodes have been used: First, broadband quasi optical detectors, where the radiation is focused by a silicon lens onto a log-spiral antenna [121]. Second, waveguide-coupled diodes, where the radiation is coupled with a horn antenna into a waveguide which results in narrowband detectors where the bandwidth is determined by the waveguide dimensions. These room temperature detectors are easy to maintain and are used at several accelerators for monitoring THz signals [122].

Table 4.1 presents the THz detectors available at KARA. It starts with quasi optical detectors from ACST GmbH (Hanau, Germany) and waveguide coupled detectors from VDI (Virginia Diodes Inc., Charlottesville, VA, USA). Besides, a Tydex (St. Petersburg, Russia) Golay cell detector is available. Since its rise-time is rather slow, it has only been used for some characterizing offline measurements that are not described here. All detectors described above work at room temperature. In addition, there are two high temperature super-conducting (SC) detectors based on $\text{YBa}_2\text{C}_3\text{O}_{7-x}$ (YBCO) developed at the Institute of Micro- and Nanoelectric Systems (IMS) of the KIT as well as two low temperature super-conducting hot electron bolometer (HEB)s operated in a liquid helium cryostat. The most sensitive detectors available are the two SI bolometers operated at 4.2 K and 1.8 K bath temperature, respectively.

Table 4.1: THz detectors available at KARA. Values according to datasheets

Detector	Manufacturer	Optical BW (GHz)	Analog BW	NEP (pW/Hz ^{1/2})
SBD-2DL	ACST	50 - 1'000 ^a	10 MHz - 4 GHz	70-1000
SBD-WR8.0 2-01	VDI	90 - 140	DC - 14 GHz	1.6
SBD-WR5.1R6 4-04	VDI	140 - 220	DC - 22 GHz	2
SBD-WR3.4R7 3-13	VDI	220 - 325	DC - 32 GHz	2.7
SBD-WR2.2R8 1-13	VDI	325 - 500	DC - 40 GHz	3.2
SBD-WR1.5R8 2-19	VDI	500 - 750	DC - 40 GHz	5.1
Golay Cell GC-1T	Tydex	30 - 300'000	30 Hz	100
KIT-YBCO	KIT-IMS	100 - 2'000	50 kHz - 65 GHz	100
2x KIT-HEB	DLR / KIT-IMS	200 - 6'000	100 MHz - 4 GHz	0.3
2x 1.8K SI Bolometer	IRlabs	<6'000, <3'000 ^b	30 Hz	0.004
2x 4.2K SI Bolometer	IRlabs	<30'000, < 3'000	500 Hz	0.115

^a The 3 dB bandwidth is approx. 50 GHz to 200 GHz

^b Two different input low-pass filters are provided to prevent the detector from saturation due to background radiation and they limit the heat deposition onto the cold plate.

In principle, the noise equivalent power (NEP) gives the optical power which is necessary to be equivalent to the noise in 1 Hz bandwidth. However, ultra short pulses are typically shorter than the time constant of the detector, therefore, the response is mostly dominated by the quality of the RF readout path and not the responsivity and noise of the detector element like in the DC case. This can be illustrated by a test

measurement with two of the WR3.4 diodes. The first one was specified having a DC sensitivity two times higher than the second one which was optimized for a broadband RF readout. Despite the lower responsivity, the measured output voltage on an oscilloscope was more than twice as high for the RF improved version. However, there is no parameter in the data sheets accounting for the fast pulse response. In fact, to date there does not exist an accepted method to specify the sensitivity on fast pulses which is comparable between detectors. This is also due to the fact, that short pulses have a very broad spectrum and most detectors don't have a flat frequency response, which makes calibration very complicated. So, special care has to be taken into account when comparing detectors directly. First measurements at the synchrotron radiation source DELTA in Dortmund, Germany, were done [Mai18]. This storage ring can be operated in a mode which produced tunable, narrowband pulses in the sub-THz and THz range. Due to the promising first results, further measurements are planned.

Figure 4.2 shows the measured DC-responsivity of the different SBD detectors. The used WRx diodes are the RF improved versions. As stated above, the absolute value of the responsivity is only an estimate for the pulse sensitivity. However, the relative values of the responsivity provide valuable information on the frequency response of a single detector.

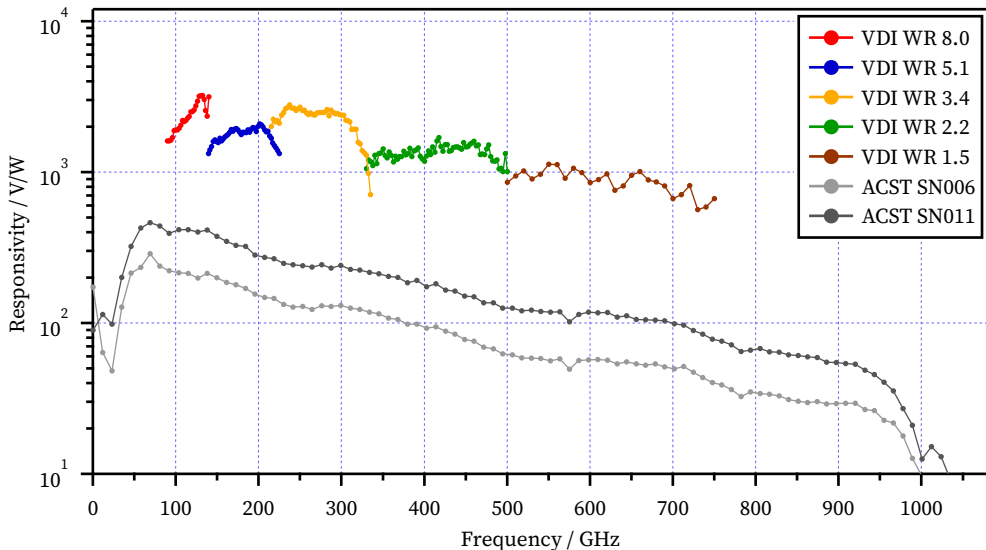


Figure 4.2: DC-responsivity of different SBD detectors. Data of the WRx detectors courtesy of Virginia Diodes Inc. and for the broadband diodes courtesy of ACST GmbH.

The impulse response of the three different types of ultra-fast THz detectors is shown in Fig. 4.3. It was measured with short pulses from the KARA accelerator. The pulses RMS length was measured by a streak camera to be below 10 ps and is considered to act as a δ -impulse to the detector. The ACST SBD has an internal 4 GHz amplifier which limits the impulse response and leads to ringing. The VDI WR3.4 diode was operated without amplifier and shows a negative peak. Usually it is operated with an inverting amplifier. The small reflection after 450 ps is reproducible and not visible on the other detectors. A zero-bias operation was chosen for the YBCO detector. Then, its detection mechanism differs from that of a bolometer but leads to a much faster response time and becomes sensitive to the electrical field [Raa15a; 123]. However, the sensitivity is reduced, too.

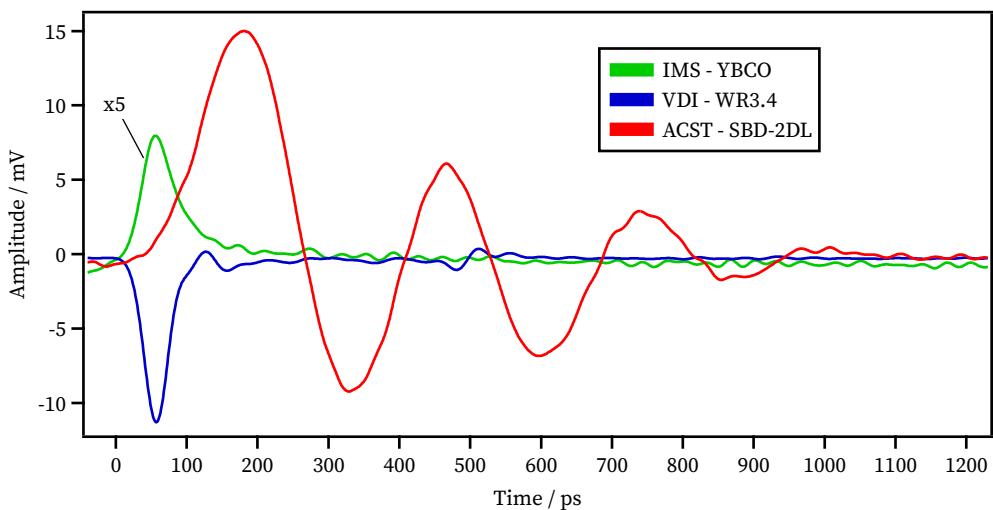


Figure 4.3: Impulse response to a < 10 ps pulse of three different ultra-fast THz detectors. The traces have not been taken at the same time and the same input power and can therefore not be compared quantitatively. The ACST SBD is limited by a 4 GHz amplifier. The WR3.4 diode and the YBCO detector are limited by the bandwidth of the connected cables and the readout oscilloscope. The YBCO detector was operated in zero-bias mode without amplifier. It only looks more noisy, because its trace is scaled by a factor of 5 for better visibility.

Mixers are a completely different type of detectors, which do not use a direct process but have the potential to detect amplitude and phase. These will be discussed in more detail in Chapter 8.

An important value of the ultra-fast detectors is the response time. It is given by the analog output bandwidth of the detector. Usually, the response time is limited

by the detection process, i.e., the diffusion of the created charge carriers. However, some ultra-fast detectors like the YBCO elements intrinsically have a faster response time and are limited by the bandwidth of the electrical readout line. The electrical output bandwidth can not be higher than the optical input bandwidth in which the detector is sensitive. Therefore, a detector with a 10 GHz analog bandwidth covers at least an optical range of 10 GHz. Since all these values are connected by the Fourier transform, also the different case is true: In order to get a frequency resolution of 1 Hz, an observation time of at least 1 s is needed.

4.2 THz Optics and Transport

The synchrotron radiation emitted by the electrons in the accelerator has to be guided to the experiments. To ensure minimal losses and beam waist deformations on the way, special optics are needed. These are often called *quasi-optics*, since the spatial extend of these optics is only a few times the wavelength of the radiation [124]. Therefore, quasi-optical systems are dominated by scattering effects and can be described by Gaussian wave optics. A Gaussian beam keeps it's Gaussian distribution along the propagation direction while focusing or defocusing only changes it's size, not the character [125]. Planar mirrors are used to guide the beam to the experiment and off-axis paraboloid mirrors focus it down to the detector element. Used quasi-optical filters and beam splitters are described in more detail in App. C.

4.3 Determination of Machine Parameters

An accelerator itself is a complex machine and the validity and reproducibility of experiments with synchrotron radiation depends on the knowledge and precision of various machine properties. Moreover, the accuracy of simulations depends on the exact knowledge of the accelerator properties. In the following, the most important values, their determination and errors are discussed.

4.3.1 Beam Energy

In most operation modes of the accelerator, it's not necessary to know the beam energy precisely. Yet it is important to keep it constant, since many parameters like

the critical frequency change with energy. As shown in Chapter 2.1.3, also the low frequencies of the synchrotron radiation are not affected by the energy, however, many other parameters depend on the particle energy, becoming especially important in the short bunch length mode. Not only the MBI threshold current (Eq. (2.51)), but also the synchrotron frequency (Eq. (1.27)), longitudinal damping time (Eq. (1.28)), and the bunch length itself (Eq. (1.36)) depend on the energy.

The particle energy is determined via the magnetic field inside the bending magnets in combination with the RF voltage. If the magnetic field is increased, the particles' path is bent stronger and the revolution time decreases. This is compensated by the RF system by transferring more energy to the bunch. After reaching an equilibrium again, the electrons travel on the same orbit as before, but with higher energy. Changing the RF frequency also changes the energy, but shifts the orbit at the same time. This has several side effects which can reduce the beam lifetime. For example, the electron bunch passes the quadrupoles and sextupoles off-center, resulting in further distortion of the beam orbit and, in addition, to a change of transverse tunes. Changing the RF frequency too much leads to beam loss, latest when the orbit does no longer meet the physical dimensions of the beam pipe.

Therefore, a rough value of the beam energy is determined by measuring the current of the bending magnets from which the magnetic field is applied. At 2.5 GeV, a current of 650 A is flowing in the KARA bending magnets creating a saturated magnetic field of 1.5 T. However, the field is not perfectly constant, and especially at the magnet edges, so-called fringe fields lead to uncertainties in the real integrated magnetic field the particles observe. For exact measurements of the beam energy, the electrons themselves have to be observed. Two non-destructive methods are commonly used and were both realized at KARA: Resonant spin depolarization [126] and Compton backscattering (CBS) [127]. At KARA, resonant spin depolarization is only applicable above 2 GeV. Therefore CBS has been used to determine the energy at a set value of 1.3 GeV and will be described in the following.

The basic principle of CBS is the collision of a photon with an electron. After the collision, the energy of a backscattered photon depends on the initial energies of the electron and the photon as well as the collision angle. By using a stable, well characterized laser and shooting onto the electron beam with a well defined angle, the electron energy can be determined by measuring the maximum energy of the backscattered photons with a relative uncertainty of 1×10^{-4} [Cha14; Cha15; 127]. The

width of the Compton edge determines the energy spread of the laser and the electron beam.

The exact beam energy at 1.3 GeV operation was determined to be 1.2883(2) GeV [127, p. 99]. The parameters defining the electron beam energy can be considered to be constant during a decay and as reproducible as the magnet current is. Therefore, a continuous measurement is not needed. Instead, the gained results are used as calibration for other measurements like the RF voltage, the momentum compaction factor and simulation parameters.

4.3.2 Beam Energy Spread

The natural energy spread as given in Eq. (1.38) only depends on the particle energy and the bending radius. This is due to its underlying dependency on the emitted synchrotron radiation. In the bursting regime, the emitted synchrotron radiation is not stable, and neither is the energy spread. A direct, time-resolved and non-destructive measurement of the bunch energy spread is not possible to date. An indirect method has been implemented at KARA by measuring the horizontal bunch shape in a dispersive section [Keh17; 128]. The concept behind this is, that in a dispersive element, like a bending magnet, electrons with higher energy are deflected less than electrons with lower energy. Therefore, an energy spread increases the horizontal bunch size σ_x . Given the horizontal dispersion D_x , horizontal emittance ϵ_x and beta function β_x at the radiation source point, the energy spread σ_E is given by [29, p. 307ff]:

$$\sigma_E = \frac{1}{D_x} \sqrt{\sigma_x^2 - \beta_x \epsilon_x}. \quad (4.1)$$

As the dispersion and the beta function are assumed to be constant in time, the energy spread is proportional to the measured horizontal bunch size. Furthermore, by a good knowledge of the static parameters, they can be taken into account to determine the absolute energy spread. At the optical diagnostic beam line at KARA, a fast-gated-camera setup is used to get single shot images of the horizontal bunch profile [130; 129]. This setup is one of the experiments that can be triggered synchronously.

4.3.3 Beam Current

The beam current is the basic quantity of an accelerated beam, besides the energy. The beam current I_B at a given position is the number of charges Q per unit time. In a circular accelerator it is expressed by

$$I_B = \frac{dQ}{dt} = N_e e f_0, \quad (4.2)$$

with the number of stored electrons N_e , the charge of a single electron e and the revolution frequency f_0 . A non-destructive way to measure this current is by a DC current transformer (DCCT) similar to a current probe for an electrical wire. At this transformer, the electron beam is used as the primary winding, and the measurement is done at the secondary winding. It therefore measures the magnetic field of the beam, which, by the Biot-Savart law is given for a cylindrical symmetry by [131]

$$\vec{B} = \mu_0 \frac{I_B}{2\pi r} \vec{e}_\phi, \quad (4.3)$$

with $\mu_0 = 4\pi \times 10^{-7} \text{ Vs A}^{-1} \text{ m}$ being the permeability of the vacuum, r the distance between the center of the beam and the observation point, and \vec{e}_ϕ the unitary vector ($\vec{B} \parallel \vec{e}_\phi$). A beam current of 1 mA at 10 cm distance results in a magnetic field of 2 μT . Considering that the earth magnetic field has a value of about 50 μT , it becomes evident, how sensitive the measurement of the beam current is. Figure 4.4 shows the scheme of a beam current transformer.

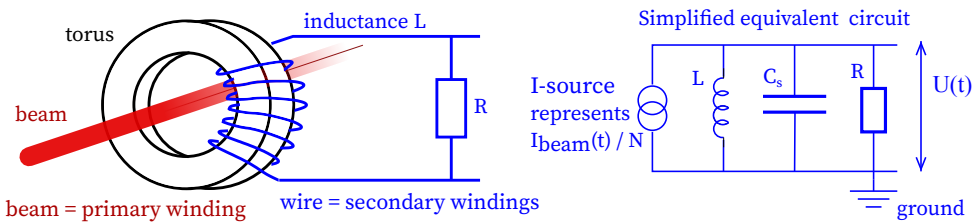


Figure 4.4: Scheme of a current transformer (from [131], modified)

Today, sensitive current transformers are commercially available. At KARA, a parametric current transformer (PCT) from Bergoz is installed. It can measure up to 600 mA with a resolution of $< 0.5 \mu\text{A}$ for 1 s of integration time. The KARA control system

reads out a value every 0.7 s, so that an uncertainty of $0.6 \mu\text{A}$ is expected. In fact, measurements have shown that even for very low currents of 0.1 mA , an uncertainty of $0.55 \mu\text{A}$ is reached [Sax17]. This error will be used for all beam current measurements in the following.

For the decay measurements (cf. Chapter 1.6), where measurements are taken while the beam decays, a double exponential fit of the beam current is used to increase the accuracy and ensure a monotonic current over time behaviour. Figure 4.5 shows the measurement of the beam current during a decay, the double exponential fit and the error of the fit function.

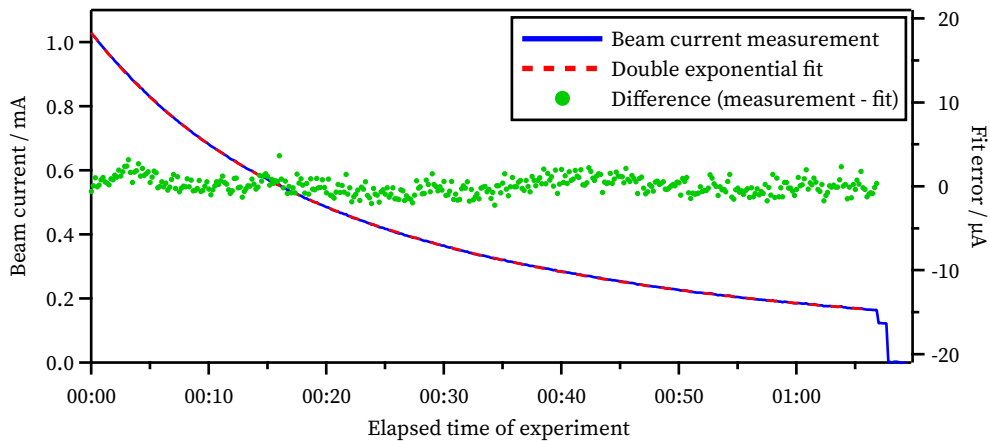


Figure 4.5: Beam current of a single bunch during a decay measurement. A double exponential fit is used in the following data evaluation.

4.3.4 Filling Pattern and Individual Bunch Current

The beam current measurement described above is not fast enough to distinguish different bunches and therefore only measures the total number of electrons in the storage ring. To determine the individual bunch currents, relative methods are used and then scaled by the total beam current. At KARA, this is done via time-correlated single photon counting (TCSPC) [132; Keh18a]. For this method, the visible synchrotron light is dimmed, so that –on average– less than one photon per turn reaches the detector. The used avalanche photo diode can detect single photons and triggers a counting unit, which measures the time between the absorption of the photon until

the next revolution clock. Therefore, the position of the detected photon relative to the revolution clock is measured. The events per bunch are counted for a given time, usually 30 s, and the relative intensity per bunch can be determined by statistical methods. A measurement time of about 30 s leads to an accuracy of $< 1 \times 10^{-4}$ in the resulting filling pattern. A scaling by the known total current of the beam current measurement leads to the current per bunch.

4.3.5 Bunch Length

The overall bunch length at KARA is measured by using a commercial streak camera (C5680 by Hamamatsu). Basically, a streak camera transforms the time variation of an incoming optical pulse into a spatial profile at a detector. Therefore, the incoming light is transferred into photoelectrons by a photocathode, having the same time distribution as the initial light pulse. Then the photo-electrons are spatially separated by a fast changing deflection voltage (fast sweep), similar to an analog oscilloscope, and directed onto a fluorescent screen. This leads to a *streak* of light on the screen that is read out with a CCD camera. With a slow sweep, the recurring light pulses can be swept over the CCD screen so that a bunch can be observed over time and its position and size tracked. The streak camera has a point spread function of 3.35(15) ps and therefore can't resolve the bunch sub-structures [133].

4.3.6 Bunch Sub-Structure

In order to resolve the sub-structures on top of a picosecond short bunch, a resolution in the sub-picosecond regime is needed. Additionally, the measurement has to be single-shot, since the sub-structures are unstable. Currently, that is not possible by a streak camera for intensity reasons. In linear accelerators, a technique based on an electro-optic (EO) effect has been developed to determine the bunch shape and length of subpicosecond long bunches [134].

The basic principle relies on the Pockels effect of an electro-optical crystal. The EO crystal is placed near the electron beam path inside the vacuum pipe. The Coulomb field of a passing electron bunch induces a birefringence inside the crystal, which can be probed by a laser pulse. The bunch profile, being proportional to its Coulomb field is thus modulated onto the laser pulse. This modulation has the same time dependency as the bunch and can not be read out by electronics directly.

Two methods have been used at KARA: In the first setup, now permanently installed at KARA, a method called electro-optical spectral decoding (EOSD) is used: A short femtosecond laser pulse is stretched in a way, that a linear chirp is created. By that, the laser pulse has a clear relation between time and frequency. After the modulation at the crystal, the pulse is read out by a spectrometer and from that, the original electron bunch profile is calculated. The spectrometer is made out of a grating in combination with an ultra-fast line array. The currently used setup at KARA has a resolution of 300 fs and a repetition rate of 2.7 MHz [135; Hil14b; Hil14a; 30]. The readout is done by KALYPSO which is a readout electronic for line-arrays, sharing the same technology as Karlsruhe Pulse Taking Ultra-Fast Readout Electronics (KAPTURE) and is an in-house development of the Institute for Data Processing and Electronics (IPE) at KIT, too. Second, in a collaboration with colleagues from the University of Lille, France, a time-stretch method was installed. It uses the same laser setup as the previously described, but the readout is different. In this method, the modulated laser pulse is stretched by a 2 km long fiber and then read out by a 40 GHz photodiode in the time domain [137; 136; Rou15a; Szw17; Bie17]. The readout speed and observation time is limited by the oscilloscope and does not reach the properties of KALYPSO. However, it provides balanced detection and good signal-to-noise ratio (SNR).

4.3.7 Synchrotron Frequency

The synchrotron frequency is another very important beam parameter especially in low-alpha mode. When changing the optics to reduce the momentum compaction factor, the synchrotron frequency changes accordingly. Furthermore, by measuring the synchrotron frequency and the RF voltage, the zero-current bunch length can be calculated. The synchrotron frequency can be obtained from the signal of a beam position monitor (BPM). A BPM consists of four electrodes at the beam pipe. Depending on the beam position, a different voltage is induced when the bunch passes by. The synchrotron oscillation leads to a harmonic change in the arrival time and therefore modulates the beam signal. In the frequency domain, this modulation can be detected as sidebands of the revolution signal. A mathematical description can be found in App. A. Additionally, a useful and lengthy discussion on the beam signals that are obtained by a BPM can be found in [138; 139].

When observing the BPM signal with a spectrum analyzer, a good signal-to-noise ratio and frequency accuracy can be achieved, although the signals of all bunches

are overlapped. To avoid this, the KARA bunch-by-bunch feedback (BBB) system [140; 141] reads the signal of each bunch individually and does a sorting according to the revolution frequency, similar to KAPTURE. Consequently, the transverse and longitudinal position of a bunch can be tracked for a given number of turns. A Fourier transformation (FT) of that signal provides the bunch motion in each plane. Based on that information, a feedback can be applied to the beam. Even if no feedback is given to the beam, the analysis is available in the control system and the frequencies can be continuously read out. The number of the observed turns is limited by the memory of the BBB system, and so is the frequency resolution.

4.3.8 RF Voltage

The RF voltage is needed to first accelerate the particles and then, in the storage ring, feed back the lost energy, to keep the particles' momentum constant. Due to phase focusing described in Chapter 1.5.3, the particles always shift to the synchronous phase where the losses get compensated by the RF voltage. The slope of the RF voltage $\dot{V}_{\text{RF,eff}}$ can be changed by setting the total RF voltage V_{RF} , although the effective voltage $V_{\text{RF,eff}}$ transferred to the beam stays constant. A precise knowledge of that slope is important, especially in the short bunch operation, since it directly effects the synchrotron frequency and thus the bunch length as well as the MBI threshold discussed in Chapter 2.3.

The accelerating voltage is created by a klystron and then fed to the cavity with rectangular waveguides. The transmitted and reflected RF power, measured with directional couplers, and a diagnostic output port of a cavity are analyzed by the low-level RF (LLRF) system which controls the RF path. The effective RF amplitude can be directly read from the Dimtel, Inc. LLRF system, used at KARA. It takes into account small phase offsets between the cavities and was calibrated by CBS energy measurements.

5 Fourier Transform Infrared Spectrometry

The way to get started is to quit talking and begin doing.

— Walt Disney

For many years, the standard device for spectral measurements in the far infrared (FIR) or terahertz range has been Fourier transform infrared spectrometry (FTIR). It's based on a Michelson-Morley interferometer, and state-of-the-art devices are now commercially available. Each of the two infrared beamlines of IBPT is equipped with an evacuable Vertex 80v from Bruker Optics which are used in the following measurements. In this thesis, I will limit myself to a very brief introduction into FTIR, however, the interested reader can find a complete discourse for example in reference [142].

In this chapter, state-of-the-art Fourier transform infrared spectrometry (FTIR) measurements will be discussed. Both, a Michelson interferometer and a Martin-Puplett interferometer will be described and own measurements analyzed. In the end, its limitations are discussed which lead to the motivation of the following chapters.

5.1 Michelson Interferometer

A Michelson interferometer splits an incoming beam into two equal parts and recombines them again with a phase offset. The working principle is sketched in Fig. 5.1. One of the two split beams is reflected by a stationary flat mirror, while the other one is reflected by a movable mirror. The two partial beams are overlapped again in the beam splitter, leading to an interference between them. This interference depends on the path difference which is introduced by the moving mirror. The effective power of

the output beam is measured and by scanning all positions, a so-called *interferogram* is recorded. The Fourier transform of that interferogram is connected to the spectrum of the incoming light.

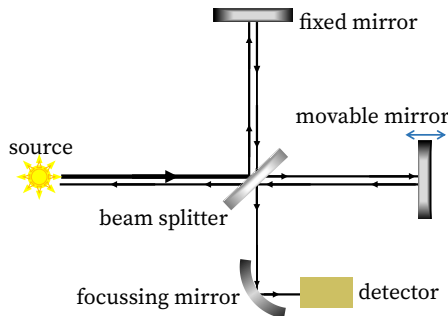


Figure 5.1: Working principle of FTIR. An incoming beam is split into two equal parts. A movable mirror introduces a path difference in one path and the recombined light is an interference depending on the mirror position. Recording the power at every position leads to an interferogram, which is connected by the Fourier transform to the incoming light spectrum.

Therefore, the spectral resolution is a function of the length of the interferometer arms, and the highest observable frequency is determined by the step size of the mirror displacement. Moreover, the spectral coverage is not only determined by the detector, but also by the frequency-dependent efficiency of the beam splitter. The efficiency drops if radiation is absorbed by the beam splitter or if the beams are not split and recombined in equal parts. Figure 5.2 summarizes the available beam splitter for the Bruker devices. While there is a good coverage in the near- and mid-infrared region, the FIR and THz range is challenging. The available beam splitters (in the THz regime, Mylar foils are used) only work in a limited frequency band.

5.1.1 Normalization

Usually, infrared spectroscopy is done via relative measurements. In the first place, a background sample is measured. This can be an empty substrate, a specified gas, ambient air, or an evacuated sample chamber. Then the sample is measured and both spectra are compared to determine the transmission, absorption, or reflection of the sample according to the experimental setup. But if the synchrotron radiation itself is the sample, as it is in the present work, other normalization techniques have to be used.

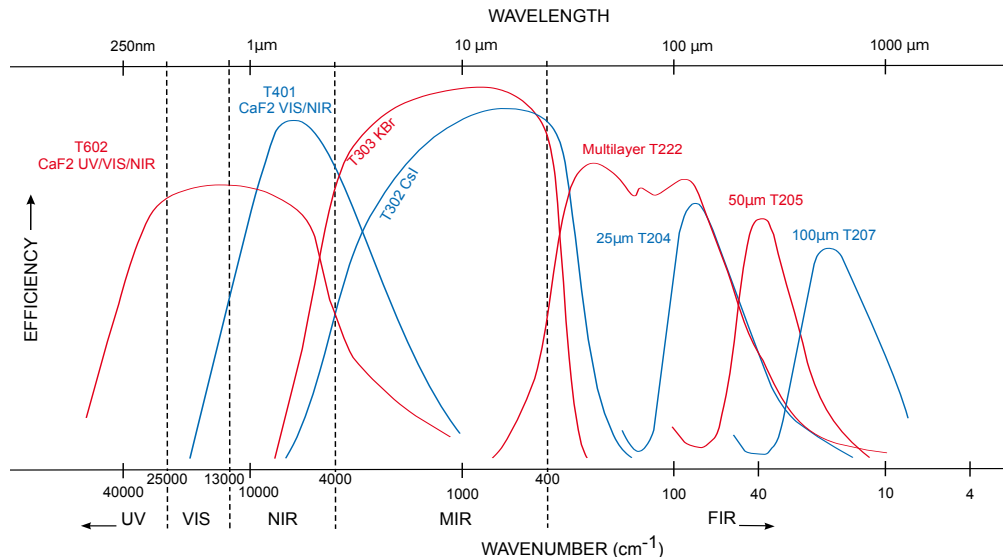


Figure 5.2: Available beam splitters for Bruker spectrometers (from [143]). In the FIR or THz range, the choice is limited as well as the working bandwidth and the efficiency. Note that 30 wavenumbers correspond to 1 THz and $10 \text{ cm}^{-1} = 300 \text{ GHz}$.

If the transmission properties of all components of the beamline and spectrometer were known, they could be subtracted out and the emitted spectrum could be measured directly with a quantitative scale. But unfortunately, they are not known. The best solution would be a comparison with an independent, well known calibrated light source. However, until now there are no traceable standard sources in the THz range. In fact, the calibration standard used by the PTB is a synchrotron radiation source specially designed for this purpose [144]. So, except of doing no normalization at all, there are basically three options: First, an additional internal or external light source connected directly to the spectrometer. Second, if the detectors are sensitive enough, the surrounding black body radiation, for example emitted by the closed beamline absorber. Third, when analyzing coherent synchrotron radiation (CSR), a previously detected incoherent spectrum.

All of these possibilities have advantages and disadvantages. The internal sources at the spectrometer are well known but don't have a flat frequency response. Besides, they don't regard the beamline transmission. The black body radiation of the surrounding, for example, a closed beamline absorber, has the advantage, that it takes the beamline into account, however with a different source point position. Furthermore, even if water-cooled, the temperature is dependent on the deposited heat load and therefore

on the beam current. Moreover, the used detector has to be sensitive enough to detect 300 K black body radiation in the THz regime while having enough dynamic range to not being saturated by high intensity CSR. Of all the available detectors (see Chapter 4.1), this requirement is only fulfilled by the silicon bolometers.

The incoherent radiation as a background measurement is dependent on the beam current. However, the incoherent synchrotron radiation (ISR) has a linear dependence on the beam current and is independent of the bunch shape, so that it can be normalized to the beam current. Therefore, it seemed to me to be the best choice.

However, some aspects have to be considered. First, this method is obviously only applicable if the detector is sensitive enough to measure the incoherent radiation. Second, a background measurement can only be done before switching into the short-bunch mode, since at KARA, the reduction of the momentum compaction factor is a one-way procedure and the coherent radiation can not be turned off for additional reference measurements. Furthermore, the bunch length reduction procedure can change the orbit and thus the source point of the radiation. Especially at the THz range of interest, this can lead to significant side effects. The strong dependence of the beam orbit on the measured FTIR spectra at KARA has been shown by Jan Christoph Heip [145]. Last but not least, the incoherent radiation itself can not be characterized. At the mid-IR frequencies this is unproblematic, since the expected radiation can be well calculated (cf. Chapter 3). However, at the THz frequencies, the radiation spectrum reaching the detector is not only limited by the shielding properties of the source point but also distorted by diffraction and scattering of the beam transport line (cf. Chapter 3.5). Therefore, only the amplification of the coherent radiation with respect to the incoherent radiation can be determined.

So, in order to determine the incoherent radiation, sensitive bolometers were used, the water-cooled radiation absorber of the beamline was closed, and the black body radiation (\approx 300 K) was taken as a background.

5.1.2 Incoherent Spectrum

Measurements were done with two 4.2K bolometers at IR1 and IR2 at the same time to observe an identical machine status. The first measurement was done in a multi-bunch environment with 160 mA. Then the bolometers were swapped between the beamlines and the measurement was repeated with a beam current of 140 mA. The

internal averaging of the spectrometer was set to 16, the scanner velocity to 1.6 kHz and the low-pass filter to 16 kHz.

Fig. 5.3 shows both measurements together with the reference measurements of the closed absorbers and their corresponding ratios. A different behavior of both detectors can be seen, however the differences in the transmission properties of the two beamlines are far more significant. The fact, that detector 1 seems to be more sensitive at IR1 and less at IR2 can be due to slightly different alignment when changing the detectors or due to the beam current normalization where the same current has been assumed for the background and SR measurement. The ratio in the bottom panel illustrates the effect of the beam splitter. At the minimum around 1.93 THz and below 400 GHz the measurement can not be trusted.

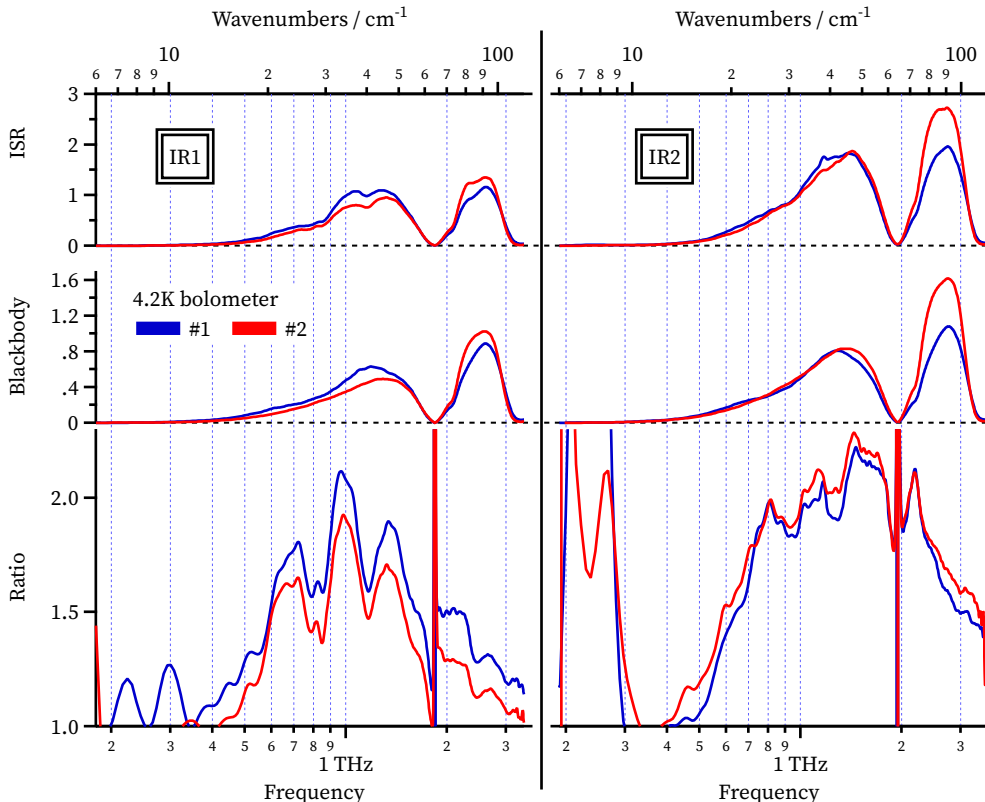


Figure 5.3: Measurement of ISR compared to the absorber black body radiation at the IR1 and IR2 beamline. The bolometers' lowpass filter blocks radiation above 3 THz. Below 400 GHz, the beam splitter efficiency is so low, that the normalization leads to unphysical results. At 1.93 THz, a minimum of the beam splitter efficiency can be seen, too.

This means that for the use as a reference measurement, the signal to noise ratio needs to be improved at THz frequencies. A higher amplification saturates the detector due to unwanted high intensity IR radiation. Therefore a low-pass filter like the Zitex foil (see App. C.1) needs to be used.

5.1.3 Coherent Spectrum

The coherent spectrum has been measured with the two 4.2K bolometers and one 1.8K bolometer. Again, the background is the black body radiation but with different amplifier settings due to saturation with CSR. The measurements with the 4.2K bolometers have been taken at the same time in IR1 and IR2. The measurements with the 1.8K bolometer, however, have been done sequentially, because there was only a single 1.8K bolometer available. Thus the beam current changed between the measurements. This has not been corrected, since the CSR power has neither a strict linear nor a quadratic dependence on the beam current. Figure 5.4 shows the measured spectra with the bolometers. For better visibility, the data have been interpolated. The original resolution was 30 GHz.

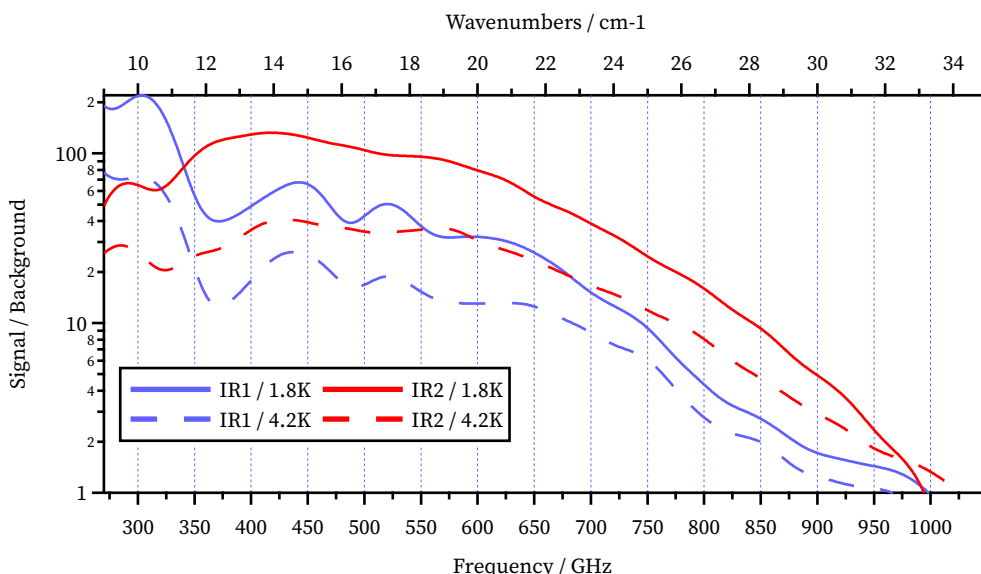


Figure 5.4: CSR Spectrum measured with the 4.2K and 1.8K bolometer at both beamlines. The data are interpolated, the original resolution of the measurement being 30 GHz. The IR2 beamline has a higher overall transmittance, however, the lower frequencies are attenuated stronger. The measurements have been done at different beam currents and can not be compared quantitatively

In general, the measured CSR intensity in IR2 is higher than in IR1 which can be explained by the improved beamline design which is more suited for THz radiation. The frequencies below 350 GHz, however, are attenuated stronger. The reason for this has to be investigated. Probably the small mirrors of the beam stabilization system cut the low frequencies. In combination with the long beam path which is approximately 5 m longer than at IR1, this leads to an increased highpass cutoff frequency.

For the use of FTIR as an accelerator diagnostic tool, the following conclusions are drawn:

Beam splitter: The bottle neck is the beam splitter. It should be exchanged with a more broadband one, like silicon or better a wire grid.

Beamlines: The IR2 beamline in general has a higher transmission. However, the current alignment cuts the relevant frequencies in the THz range. A measurement at the IR2 diagnostic port, and thus in front of the beamline stabilization system should provide the highest intensities.

Detectors: The two 4.2K bolometers are sufficiently equal, but not as sensitive in the THz range as the 1.8K one. However, balanced detection is not possible as only one is available. The bolometers are not fast enough to observe bunch-by-bunch or turn-by-turn dynamics.

Operation during the MBI: While for ISR the measured interferogram is stable and the signal-to-noise can be increased by averaging, the situation becomes more difficult during the MBI. There, the emitted spectrum changes continuously. In order to get a valid interferogram, one has to be sure that each point of that interferogram is sufficiently averaged.

Scan speed: Sometimes the scanning frequency interferes with the bursting repetition rate, so that for some settings no reliable interferograms can be measured. For a whole beam decay, where the bursting frequency changes much, an automated adaption of the scanning parameters is not feasible. A different scanning technique, like step-scan mode should be used in combination with a reliable averaging method. This could be achieved by balanced detection.

Operation mode: To analyze bursting regimes, a single bunch operation mode is necessary, since the device can not distinguish between bunches, and not all bunches have the same current and thus the same bursting regime.

5.2 Balanced Martin-Puplett Interferometer

A way to avoid some of the above-mentioned limitations is the use of a *Michelson-polarizing* or *Martin-Puplett* interferometer (MPI) developed by D.H. Martin and E. Puplett in 1970 [146]. The main difference to a pure Michelson-Morley interferometer is that it uses linearly polarized light at the input and a polarizer as a beam splitter. This has several advantages. First, the beam splitter can be much more broadband and can cover the range from around 0.06 THz to 60 THz at once. Second, splitting and recombining the beam by its polarization is more efficient than the conventional beam splitters where half of the signal power is sent back to the source. Third, it easily allows balanced detection when detecting both output polarizations independently. The described setup is sketched in Fig. 5.5. This chapter is partially based on the work done in [Mal15] and [Geg15].

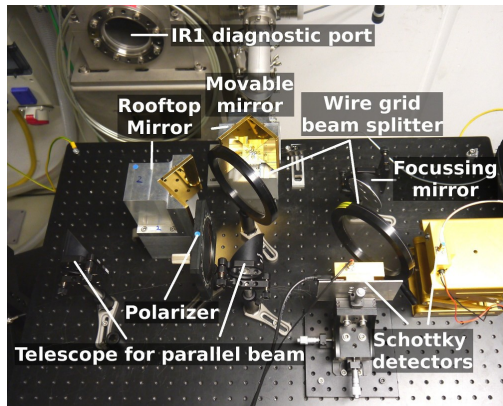
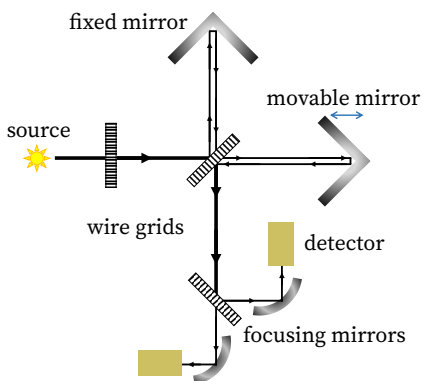


Figure 5.5: Working principle of a Martin-Puplett interferometer (MPI). In contrast to a pure Michelson interferometer as described above, a MPI makes use of the linear polarization of an input beam. The beam is split by a polarizing wire grid into two equal parts. By roof mirrors instead of flat ones, the polarization is turned. This way, no power is lost at the beam splitter. Additionally, the recombined beam can be split again into two polarizations and read out independently. This leads to two complementary interferograms and allows balanced detection.

5.2.1 Balanced Detection

The MPI provides two cross-polarized beams at different outputs that can be recorded simultaneously, thus giving two complementary interferograms, which can be used for balancing. By calculating the difference-interferogram of the horizontally I_H and

vertically I_V polarized signals and normalizing by the sum, small fluctuations can be damped and the signal-to-noise ratio improved [147]:

$$I_B = \frac{I_H - I_V}{I_H + I_V}. \quad (5.1)$$

Afterwards, the same filtering and processing of the data can be applied as for the Michelson FTIR. In the following measurements, two ACST quasi optical SBD detectors have been used (cf. Chapter 4.1) and read out with the Anfatec Lock-In Amplifier (cf. App. B.6) simultaneously. These ultra-fast detectors allow the recording of turn-by-turn data, however, they are neither sensitive enough to detect 300 K black body radiation nor no detect ISR, so they can not be used for the normalization procedures described above (cf. Chapter 5.1.1). Instead, the detector sensitivity curve will be used, as the beam splitter function of the polarizer is assumed to be linear.

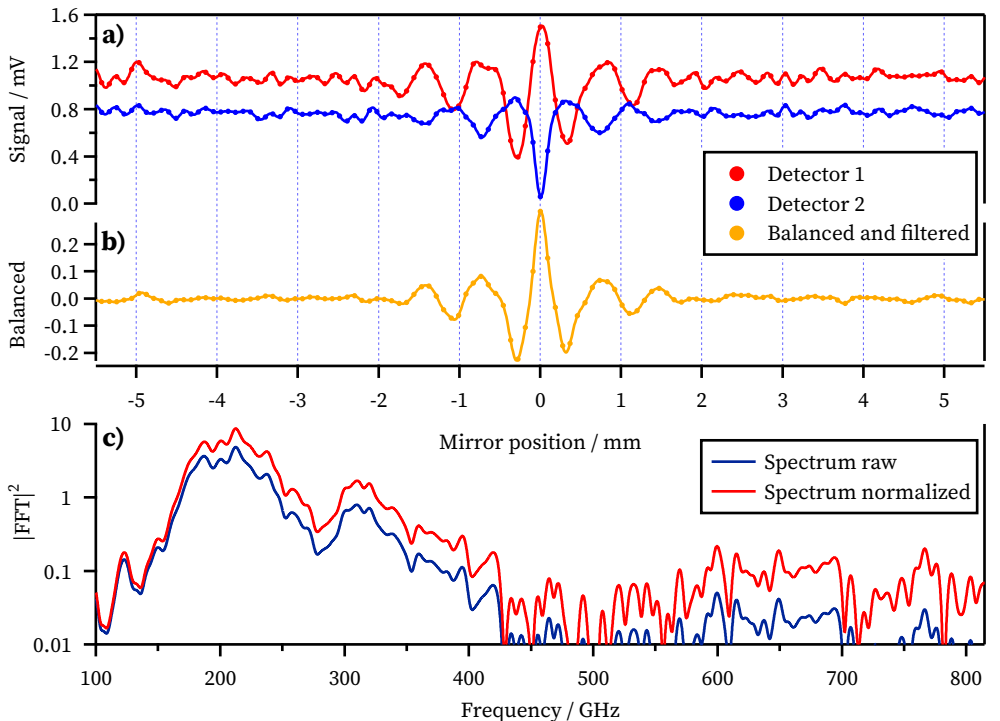


Figure 5.6: Procedure of balanced detection measurements. Two detector signals (a) of the orthogonal polarizations at the output of the MPI are balanced (b) according to Eq. (5.1). Then the interferogram is filtered, scaled and the spectrum is calculated by performing a fast Fourier transformation (FFT) (c). The normalized curve is obtained by dividing by the responsivity curve of the detectors. For details see text.

The process and the impact of the balanced detection is shown by an example measurement in Fig. 5.6. The two orthogonal detector signals do not only have inverted signals due to the different polarizations, but also differ in responsivity and noise due to the individual detectors and alignment errors. After applying Eq. (5.1), an optimized interferogram is obtained. The noise is reduced and intensity fluctuations are canceled out. The resulting spectrum, however, is dependent on the responsivity of the used detectors. One method to improve the situation is to normalize the spectrum with the measured responsivity of the detector. Figure 5.6 also shows a comparison of the directly obtained spectrum and a normalization with the responsivity curve provided by the manufacturer (see Chapter 4.1 and Fig. 4.2). The responsivity curve has been interpolated by a sinc function in order to get the same frequency bins as the raw spectrum.

Admittedly, the differences are not too large, and one has to keep in mind that the responsivity in the frequency range of 100 GHz to 800 GHz only differs by a factor of three while the measured spectrum spans three orders of magnitude. However, noise increases at low signal levels. Therefore, this technique has to be applied with care. To minimize the disturbance by the bursting radiation, a step-scan mode can be used: the movable mirror is stopped and the signal at each mirror position is averaged until a stable signal is observed. Then the next mirror step is done. This increases the measurement time, but also increases the accuracy, as the bursting frequency does not interfere with the scan speed. While this method provides a deviation to each point in the interferogram, it does not provide the deviation for the spectral components. This would be achieved by taking several spectra with the same settings. Due to the decaying bunch current, this is not applicable.

A feature of the balancing by Eq. (5.1) is that the intensity of the source is normalized. But then it is impossible to compare the absolute intensity of different spectra. For incoherent radiation, the total intensity can be scaled linearly with the beam current, but for coherent radiation, especially above the bursting threshold, there is no simple dependency between beam current and THz power. This dependency will be analyzed later in more detail (cf. Fig. 6.5). Therefore, the balanced interferogram is scaled by the peak-to-peak intensity at the zero-path difference of the two detectors. Figure 5.7 shows such a spectrogram. As expected, noise at the position of low intensity is seen as well as a spectrum reducing in intensity with decreasing bunch current. Interestingly, the prominent frequencies do not move as one would expect for a lengthening bunch.

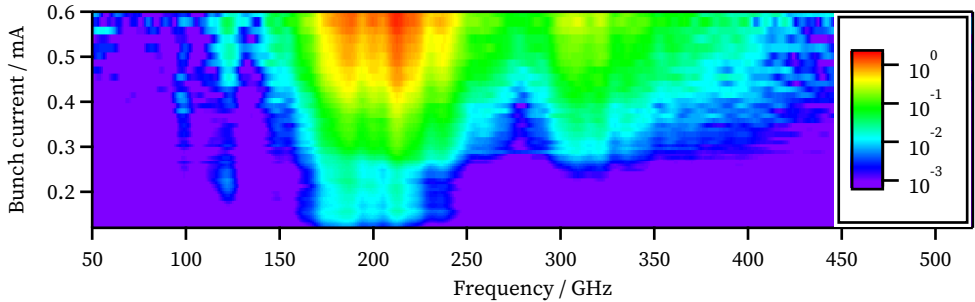


Figure 5.7: CSR Spectra measured at different bunch currents.

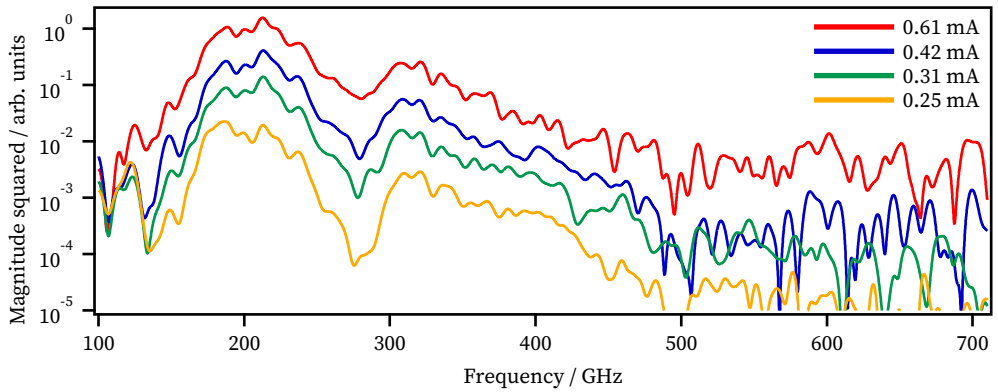


Figure 5.8: Spectra at four different bunch currents of Fig. 5.7.

A closer look at specific bunch currents is given in Fig. 5.8. It shows that the signal-to-noise ratio of the chosen setup is limited to approximately three orders of magnitude. Therefore, only the signals between 100 GHz to 500 GHz have significant amplitudes. In this measurement the form of the spectrum does not change, but rather its total intensity. However, the MBI leads to different average bunch lengths and bursting behaviour for different currents and therefore, a changing spectrum would be expected. This discrepancy could be due to the fact that the setup only measures averaged spectra or that beamline effects determining the spectra are dominant. Another uncertainty is the behavior of the ultra-fast detectors to the even shorter synchrotron radiation pulses. The FTIR principle relies on the interference of the two split beams. However, if the delay between the two paths is longer than the pulse length, the pulses do not physically overlap. This overlap happens when the pulses are absorbed by the detector. The first pulse leads to molecular vibration according to its spectrum and the second pulse interferes with that vibration. This happens much faster than the slow detector

readout. The ultra-fast detectors, however, are able to resolve both pulses individually and an interference does not happen. For that reason, the obtained spectra should be taken with a grain of salt. To analyze the bursting dynamics of the instability, faster methods than the standard FTIR need to be used.

5.3 Limitations of FTIR

Because of the need of the mechanical moving mirror, Fourier transform infrared spectrometry has several limitations, especially in terms of resolution and speed. While the speed of the moving mirror directly affects the measurement time, the total travel range of the mirror limits the frequency resolution. Several techniques to improve the scanning speed have been proposed in literature and have already been realized, like rotating interferometers, which achieve repetition rates up to 2 kHz [148], or birefringence interferometers that can acquire up to 140 000 spectra per second [149]. Recent developments of a multi-channel FTIR spectrometer [150] can record an interferogram in a single shot, and therefore the acquisition time is only limited by the speed of the array detector, the signal-to-noise ratio still being better than that of a grating spectrometer. The frequency resolution, however, is limited to 300 GHz. Moreover, the above mentioned solutions have only been demonstrated in the mid-IR range and can not directly be implemented in the THz range. A special THz single shot interferometer for bunch length measurements is available from RadiaBeam Technologies [151], but it is not sensitive enough to detect the KARA pulses, and it is also limited to 10 kHz repetition rate.

6 Time Domain Measurements with ultra-fast THz-Detectors

It doesn't matter how beautiful your guess is or how smart you are or what your name is.

If it disagrees with experiment, it's wrong. That's all there is to it.

— Richard Feynman

The observer at a beamline receives radiation from every bunch in a storage ring at each turn. The radiation consists of coherent and incoherent synchrotron radiation (cf. Chapter 3). The incoherent radiation is linearly dependent on the bunch current and appreciated for its stability. The coherent radiation is dependent on the size and shape of the bunch which can change within a few turns. To investigate the changing coherent radiation, fast THz detectors are needed. For bunch-to-bunch analysis the response time has to be shorter than the bunch separation time of 2 ns. The following chapter will present the time evolution of measured pulse amplitudes. First, measurements of the pulse amplitudes at different bunch currents are compared and their Fourier transforms are investigated, in order to extract basic properties of the micro-bunching instability (MBI). Then an analysis method is introduced using spectrograms which can work as a fingerprint of the machine settings. Two special cases, the weak instability and a high current regime for very low shielding factors, are analyzed in more detail. Furthermore, first attempts to influence the bursting pattern by RF modulations are presented.

6.1 Pulse Amplitude Measurements

The measurements have been performed directly at the diagnostic ports of the infrared beamlines. In the most simple setup, the radiation is focused onto the detector by an off-axis parabolic mirror, which is placed just behind the diagnostic port. Then

the analog detector output is amplified and read out, either by an oscilloscope or by KAPTURE. With either method, the output pulse amplitude of the pulse over the turns is measured and saved. As an example, measurements at four different bunch currents with a broadband Schottky barrier diodes (SBD) detector are shown in Fig. 6.1. The RF voltage was set to 800 kV resulting in a synchrotron frequency of 8.3 kHz. From this, the zero-current bunch length and the momentum compaction factor are calculated to be $\sigma_{z,0} = 4.6 \text{ ps}$ and $\alpha_c = 5 \times 10^{-4}$, respectively. According to the scaling law of Eq. (2.51), the MBI threshold is expected at 0.2 mA bunch current. The shown measurements were performed slightly below (at 0.18 mA) and above (at 0.22 mA) the MBI threshold as well as two different bursting regimes with higher currents at 0.48 mA and 1.6 mA.

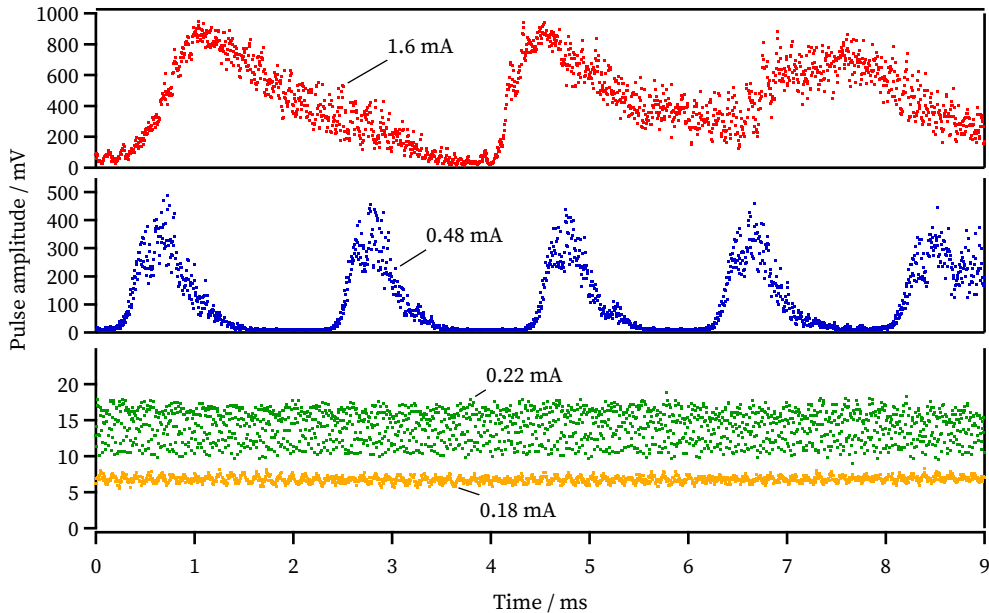


Figure 6.1: Measured pulse amplitudes with a broadband SBD detector for four different bunch currents. The bursting threshold is at 0.2 mA. Therefore, the lowest current is slightly below the threshold, while the next is slightly above. The average pulse amplitude is doubled, although the current only increased by 20 %. At higher currents, big outbursts of radiation are observed.

A few characteristics of the MBI, especially a clear bunch-current dependency and different behaviors, can be seen immediately. Below the threshold, at 0.18 mA, the pulse amplitude is more or less stable with small modulations mainly due to the synchrotron motion. This is likely due to a dipole oscillation of the bunch, modulating the bunch length at the turning points and therefore the CSR emission (cf. Fig. 1.4).

Slightly above the threshold current, at 0.22 mA, the amplitude deviation as well as the average intensity have increased. The average pulse amplitude almost doubled, while the current only increased by 20 %. This is due to the formation of sub-structures, which emit additional coherent radiation in the detector's spectral range.

At even higher currents, distinct outbursts of radiation can be observed, followed by a damping phase. Assuming that the detector is in its linear region, where the output voltage is proportional to the optical input power, the power during a burst is about 10 times higher than in between. The bursts themselves look similar at a given current and repeat regularly, although not two of them are identical. In summary, the intensity, length, and distance of the bursts change with current.

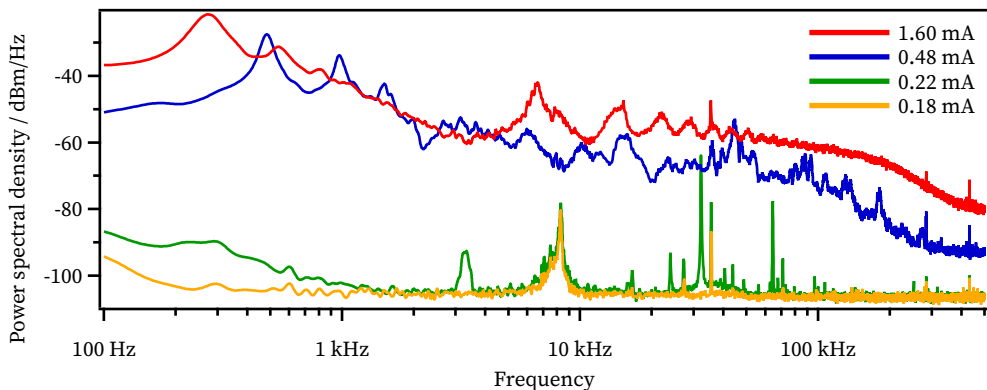


Figure 6.2: Spectra of the time domain signals of Fig. 6.1. The bursting threshold is at 0.21 mA. Therefore, the yellow line is below the threshold and only fluctuates with the synchrotron frequency at 8.3 kHz. For a detailed discussion see text.

Recurring events lead to corresponding patterns in the frequency domain. Therefore, a Fourier transformation (FT) of the pulse amplitude evolution signal is performed to identify significant frequency patterns. Figure 6.2 shows the magnitude squared¹ of the FT of the pulse amplitude signal. The pulse-amplitude of every 3rd turn was measured for half a second. To smoothen the data, a segmented FFT algorithm is used, with each segment overlapped by half its length. Frequencies below 10 kHz have been

¹ Some authors prefer to plot the magnitude of the time domain signal, because the detector voltage is already proportional to the optical power. However, in this thesis, the magnitude squared as being proportional to the detectors output power is used to be comparable to the data, where the detector is read out directly with a spectrum analyzer. Note that in the logarithmic dB scale, this different definitions lead to a difference of a factor of two.

calculated with 3 segments of length 250 ms, leading to a frequency resolution of 4 Hz. Above 10 kHz, a segment length of 10 ms and above 100 kHz, a length of 1 ms was used to improve the visibility of the spectrum, leading to a frequency resolution of 100 Hz and 1 kHz, respectively. Afterwards, a box filter with a width of 200 Hz was applied to smoothen the data. While the height and position of the peaks are not affected by that procedure, the width increases. In the following, such a spectrum is called the *bursting spectrum*.

The spectrum at 0.18 mA has three significant peaks: A relatively broad one at 8.3 kHz which is the synchrotron frequency and two very narrowband frequencies at 27.3 kHz and 35.5 kHz. They are electrical interferences from the internal amplifier since they are visible, even without optical signal. Additionally, some high frequency components above 200 kHz are attributed to the interference of nearby switched power supplies. Above the bursting threshold, the average intensity increases. But distinct frequencies arise, too, a prominent one at 32.1 kHz, which is slightly below four times the synchrotron frequency. A more detailed analysis of the frequencies directly at the MBI threshold will be done in Chapter 7.5.

A significant change in the spectrum can be seen at the higher bunch currents. The displayed average noise level increases, because the 8 bit readout oscilloscope has only about 50 dB dynamic range. The dynamic range is continuously being adjusted by the control software, so that the full burst amplitude fits to the ADC range. At the highest bunch currents, there is something to be seen that looks like white noise, but is above the oscilloscope's noise floor. This is actually a real signal and is attributed to the chaotic behavior during the bursts. Therefore, not two of the bursts are really identical, because the amount of randomness is so high.

The low frequency peak at the high currents is due to the repeating of the bursts, and the harmonics are due to the shape of a burst. At 1.6 mA, the spectrum can be separated into two regions. Firstly, the low frequency, contributing to the repetition rate of the bursts and secondly, the harmonics of the sub-structures rotation in phase space. Usually, the fundamental frequency of this rotation is near the coherent synchrotron frequency. This regime is called *sawtooth* bursting, because in time domain the fast rise of the instability and the decay afterwards until the next burst starts, looks like a sawtooth (cf. the high currents in Fig. 6.1).

As the discussed spectral contributions are below 100 kHz, this frequency is also used as a low pass filter to smoothen the time domain data. If one is only interested in

the spectrum of the bursting behaviour, it is sufficient to store every 10th turn only, resulting in a maximum observable frequency of 270 kHz while reducing the memory needs by a factor of 10. If applicable, for example when measuring with KAPTURE, the available oversampling is used to smoothen the data as described above.

6.2 Bursting Spectrogram as an Accelerator Fingerprint

*To me, what makes physics physics is that experiment is intimately connected to theory.
It's one whole. Physics is about questioning, studying, probing nature.
You probe, and, if you're lucky, you get strange clues.*
— Lene Hau, 2007, In: The Boston Globe

The measured spectrum at a specific bunch current is reproducible for a given set of machine parameters, whereas it differs for other machine settings. Therefore, a set of spectra, one for each bunch current, can be put together into a spectrogram which is a fingerprint of the machine settings. This so-called *bursting spectrograms* have proven to be an excellent tool to analyze the bursting dynamics [152; 20; 22; 21]. In practice, a spectrogram is measured by recording the bursting spectrum at each current during a current decay. Such a *bursting spectrogram* is shown in Fig. 6.3 and Fig. 6.4 with logarithmic and linear frequency axis, respectively. They have been measured with a broadband ACST THz detector (cf. Table 4.1) and read out by KAPTURE. While the lower frequencies representing the repetition rate of the bursts are better visible in the logarithmic plot, the linear plot highlights the fast oscillations. The threshold is located, where the first additional frequencies rise.

A more reliable method to determine the threshold is the use of the standard deviation (STD) of the THz signal. While the average power is the zero bin of the spectrogram, the power in all others represents the fluctuations and therefore the STD. Figure 6.5 shows the average pulse amplitude and the STD of the amplitude for the measurement presented above. The bursting threshold at 0.21 mA can be determined by the kink in the STD. It's interesting to see, that the THz power around the threshold increases stronger than a quadratic behavior. This is due to emerging sub-structures which coherently emit THz radiation in higher frequency ranges than the stable bunch. This characteristic is found even below the threshold and is due to the potential well distortion (cf. Chapter 2.2), which changes the bunch shape and increases the form

factor. Note that the shown characteristic is a signature of the machine settings and is not a global property.

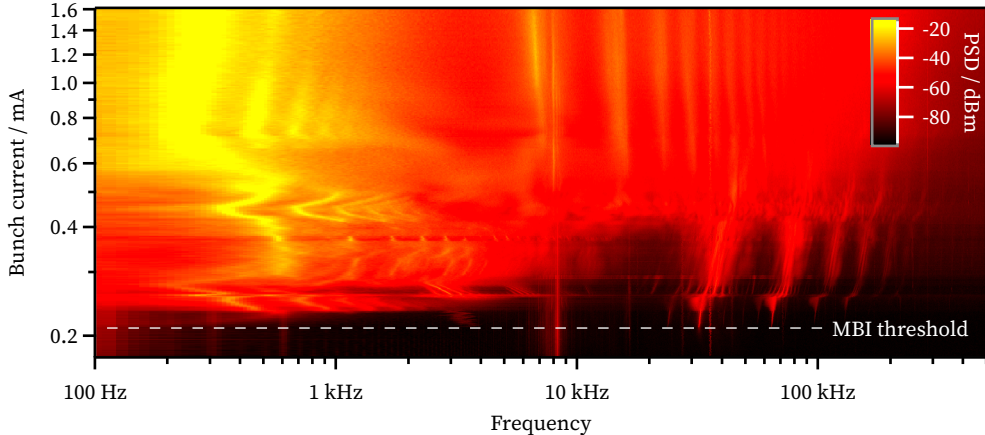


Figure 6.3: Example of a spectrogram with logarithmic frequency axis, highlighting the low frequencies, which account for the occurrence of big bursts. Measured with a broadband ACST THz-detector readout with KAPTURE

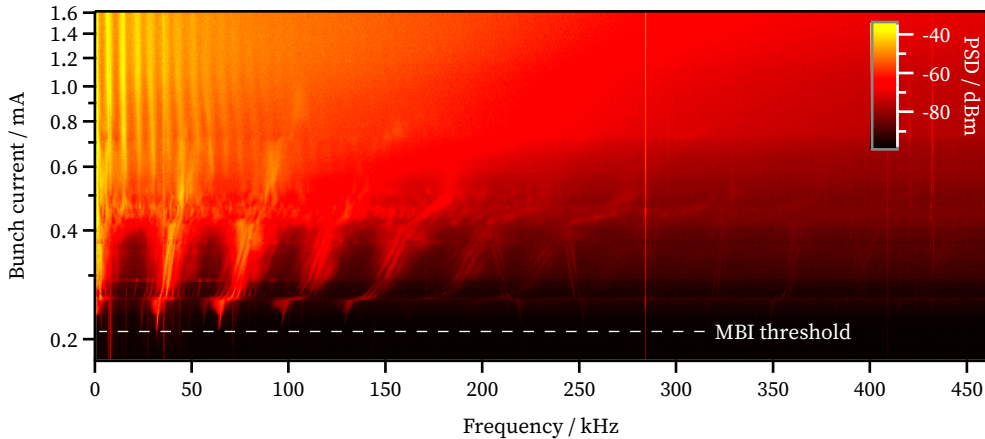


Figure 6.4: Same measured Spectrogram as 6.3, here with a linear frequency axis. Now the higher bursting frequencies become more pronounced. Measured with a broadband ACST THz-detector readout with KAPTURE

Additionally, purely incoherent radiation was measured at the same time by an avalanche photo diode, sensitive in the visible frequency range. It is also shown in Fig. 6.5 for comparison. The avalanche photo diode (APD)' signal is not affected

by the bunch shape modulations as it's sensitivity range does not cover the coherent radiation. Consequently, its average pulse amplitude is linear to the bunch current.

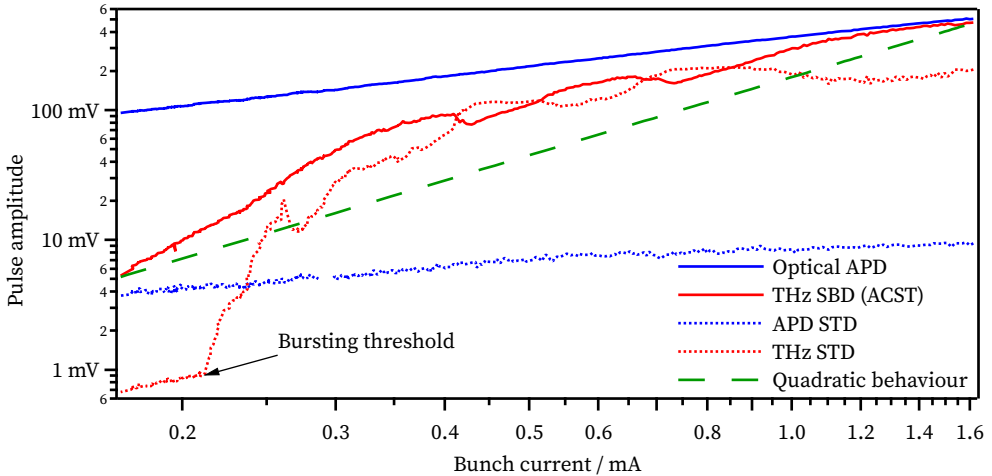


Figure 6.5: Average amplitude and standard deviation (STD) of a broadband THz-SBD detector and an APD sensitive in the visible spectral range. While the APD only detects incoherent radiation, the THz detector measures CSR, affected by the bunch shape modulations. The bursting threshold is determined at the current, where the STD of the THz signal starts to rise (here 0.21 mA). The green dashed line is a pure quadratic behavior to guide the eye. A quadratic power increase would be assumed if a stable bunch profile emits coherently.

6.3 Behavior at High Bunch Currents and Low Shielding Factors

When analyzing samples, a stable source is necessary, especially for spectroscopy. The outbursts of radiation contribute as noise to the experiment and lead to long averaging times. Therefore, a bunch current below the MBI threshold is often chosen as a stable operation point. However, below the threshold, not only the overall intensity is lower but also the sub-structures on the bunch profile are missing, which are responsible for the higher frequency components. For high bunch currents, far above the MBI threshold and short zero-current bunch lengths, another option for more stable conditions becomes available. At these low shielding factors at high currents, the bursts vanish and only high frequency oscillations remain. Consequently, the pulse amplitudes have a much lower deviation and can therefore be averaged out more easily.

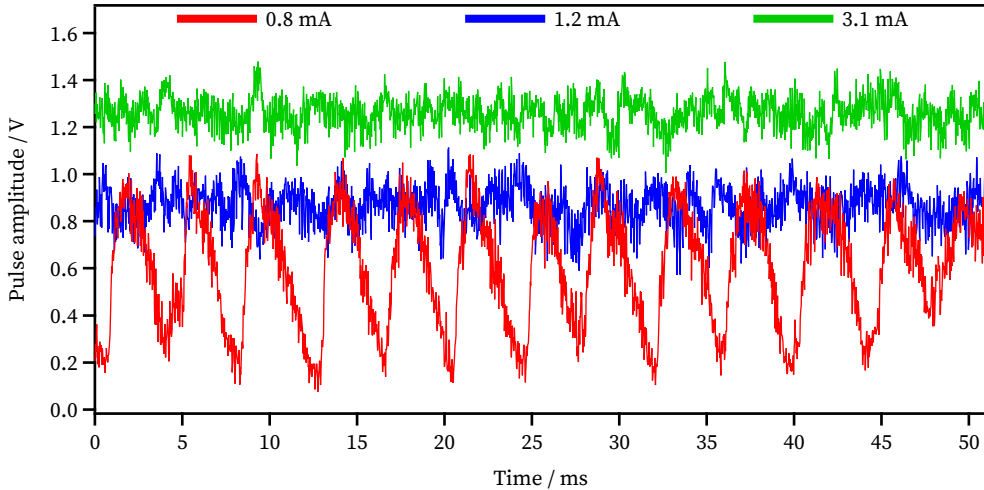


Figure 6.6: Three example bunch currents well above the MBI threshold (0.05 mA). The 0.8 mA trace is in the sawtooth bursting regime with the characteristic bursts. At higher currents, the bursts are gone and only fast, but small oscillations remain.

As an example, measurements with a shielding factor $\Pi = 0.71$ and a threshold current of $I_{b,\text{th}} = 0.05 \text{ mA}$ are shown in Fig. 6.6. While at 0.8 mA, the sawtooth bursts are clearly visible, they vanish at even higher bunch currents. Thus, the spectrum in Fig. 6.7 (left) shows the same high frequency behavior at both currents. But the low frequency peak, corresponding to the repetition rate of the bursts, is only present at the lower bunch current.

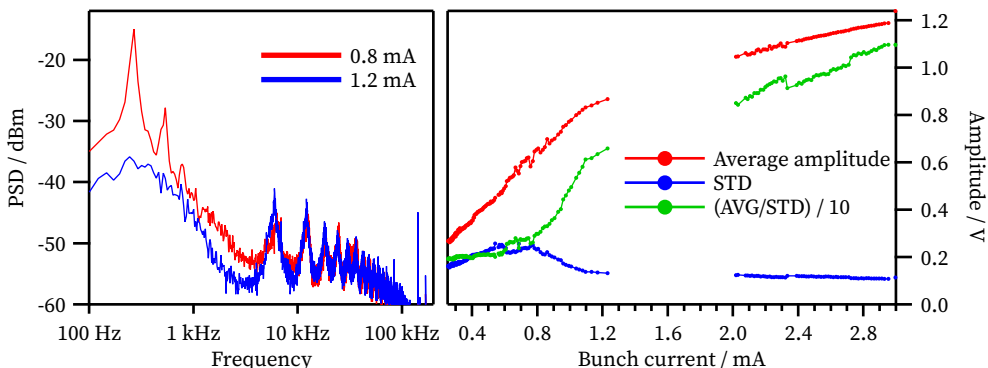


Figure 6.7: Spectra of the pulse amplitude evolution at two different bunch currents (left) and statistical properties of the bunch current decay (right). The ratio of average pulse amplitude and STD is used as a signal-to-noise ratio (SNR). Due to a partial beam loss, between 2 mA to 1.2 mA, no data is available in that range. At high bunch currents, no repetitive outbursts of radiation are observed in the diodes' frequency range as they are characteristic in the sawtooth bursting regime.

In Fig 6.7 (right), the transition from the sawtooth behavior to the more stable emission at higher current is visible. Above 0.8 mA, the STD is reduced until 0.95 mA, where the big bursts do no longer appear. As a measure for the signal-to-noise ratio (SNR), the average pulse amplitude divided by the STD is shown, too. At these high beam currents, the measured pulse amplitude becomes more stable. That does not imply, that the bunches phase space itself becomes less fluctuating, but rather that the phase space projection to the time axis is more stable. To be more precise, the form factor $\wp(f)$ (cf. Chapter 3.1) in the frequency range of the detector remains steady.

Further investigation into this regime needs to be done in order to find the best working point. Unfortunately, this working point cannot be kept stable at KARA, since the accelerator does not have a full-energy injector (cf. Chapter 1.6). Therefore, this interesting high current regime only lasts for a couple of minutes before the beam current decays into the next bursting regime. However, if the beam lifetime could be increased or a re-injection directly at the full energy were possible, this would seem to be the best regime in terms of SNR.

6.4 Weak Instability

A completely different regime is the weak instability, briefly introduced in Chapter 2.3. It exists for very short bunches with a low current, i.e. at a low shielding factor $\Pi < 0.8$. It additionally depends on the damping time and does not lead to the big outbursts of radiation like observed at high bunch currents. In the following, a measurement at a shielding factor of $\Pi = 0.73$ is presented. This low shielding factor was achieved by reducing the momentum compaction factor down to 2×10^{-4} and increasing the RF voltage to 1498 kV. This resulted in a synchrotron frequency of 7.1 kHz and a zero-current bunch length of 2.1 ps.

The measured spectrogram is shown in Fig. 6.8. It was recorded in peak detect mode (cf. App. B.4) with a small-band SBD, sensitive in a range between 140 GHz to 220 GHz (cf. Chapter 4.1). The weak instability occurs, in this example, at currents lower than the micro-bunching instability. In this measurement, they are well separated with a stable region in-between. Both instabilities may overlap for even lower shielding factors. The strong instability threshold is still around the current predicted by the scaling law (Eq. (2.51)). The power at the low frequencies is less than during the strong instability, indicating that it does not lead to big outbursts of radiation.

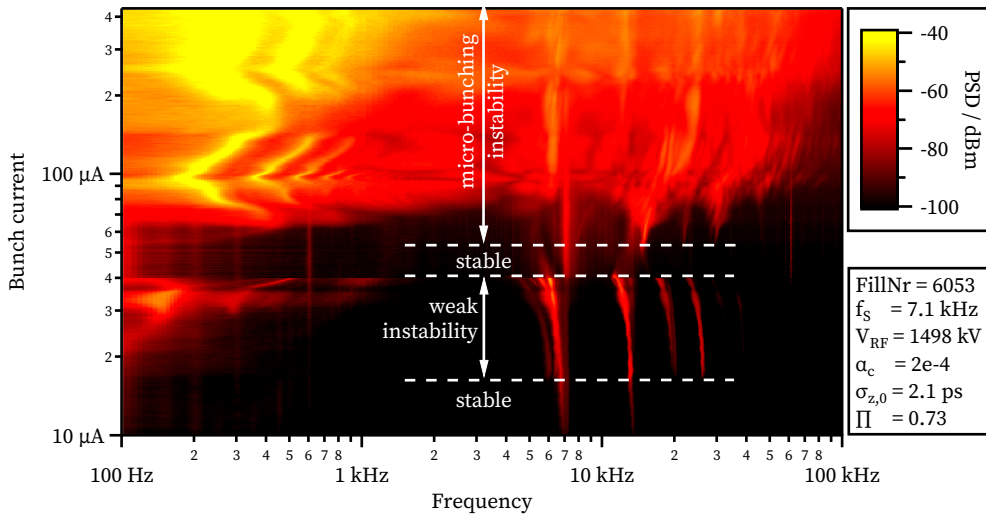


Figure 6.8: Measured spectrogram at a shielding factor of $\Pi = 0.73$ with the occurrence of the weak instability for low bunch currents.

The average pulse amplitudes and their STD for the same current range are shown in Fig. 6.9. During the weak instability, the STD rises significantly because of the disturbances. In contrast to the strong instability, it does not lead to an increased amount of emitted THz radiation. This is a sign, that the created sub-structures are broader than during the strong instability and do not lead to the emission of higher frequencies. However, the overall bunch length is increased, therefore, leading to less detected CSR power above the lower threshold.

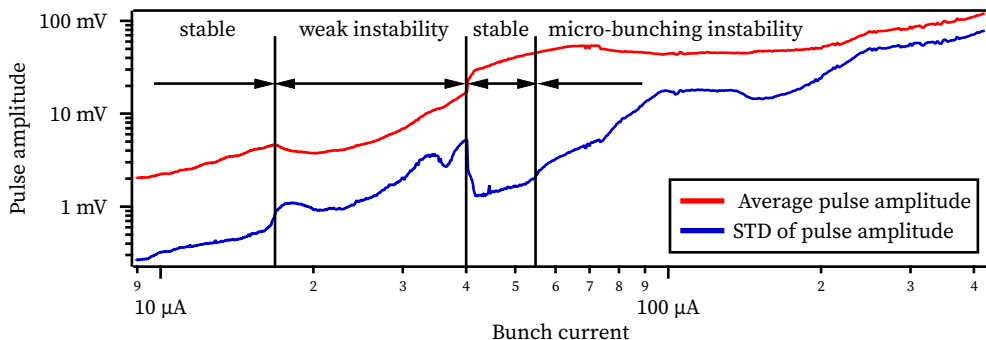


Figure 6.9: Average pulse amplitude and its STD thereof. In contrast to the strong instability, during the weak instability no significant sub-structures are formed which would emit intense THz radiation. Instead, only the average bunch length is increased, resulting in less coherent radiation in the frequency range of the used detector (140 GHz to 220 GHz).

Figure 6.10 shows time domain data of selected currents around the instability thresholds of the weak instability. At 16 μA the bunch is stable only undertaking synchrotron motion. Just 1 μA higher, the bunch shows a significant increase of its oscillations, while the average amplitude stays almost the same. At the upper threshold, the difference is more visible. At 40 μA , the bunch oscillates strongly with a frequency below the coherent synchrotron frequency², however, this is subject of ongoing investigation. The higher harmonics seen in the spectrogram (cf. Fig. 6.8) indicate, that this oscillation is not purely harmonic. Additionally, the beating with the coherent synchrotron frequency is visible. At a slightly higher current (around 42 μA), the bunch becomes stable again with a significantly increased average amplitude.

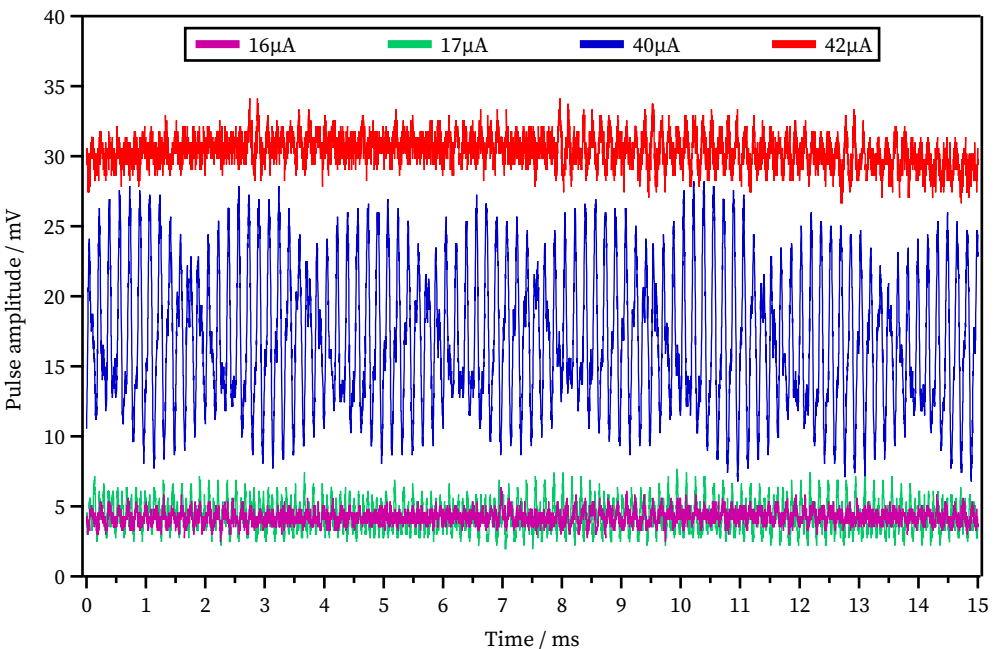


Figure 6.10: Time domain signal of selected currents around the weak instability thresholds. At the lower threshold, the standard deviation increases while the average power stays the same. However, at the upper threshold between 40 μA to 42 μA , a significant change in the dynamics is visible. The fact, that the beam is more stable at a higher bunch current, is very unusual in particle accelerators.

² Similar to the synchrotron radiation, one distinguishes between an *incoherent oscillation*, which is a single particle effect and describes how each electron oscillates in phase space, and a *coherent oscillation* which is a multi-particle effect of the whole bunch performing synchrotron motion.

In the range of the strong micro-bunching instability, the average pulse amplitude stays more or less constant between 70 μ A to 210 μ A, even though the bunch current tribled. The reason for this is the limited optical bandwidth of the detector in combination with the different bursting regimes. With a zero-current bunch length of only 2 ps, the diode mainly detects coherent radiation due to the already low overall bunch length, while the sub-structures account for an increase of the emitted power at even higher frequencies, which are not covered by the used diode (140 GHz to 220 GHz). With the onset of the MBI, the average bunch length increases, thus reducing the average power detected by the diode. In combination, the average power stays almost constant up to 270 μ A. In Chapter 7 it will be investigated, how the average power behaves at different frequency bands.

6.5 Snapshot Measurements and Parameter Scans

As discussed above, the MBI threshold can be identified by an increase of the pulse amplitudes STD. However, to analyze the thresholds of weak and strong instability, a spectrogram for each different machine setting would be needed. Taken into account, that the recording of just one spectrogram takes three to six hours, depending on the beam lifetime, this is a challenging task, as beam time is very limited.

Therefore, a snapshot technique was developed at KIT (see also [Bro16b]). It is based on the fast readout of KAPTURE (cf. App. B.8) together with the ability of the BBB system to adjust the bunch charge and create a tailored filling pattern: First of all, a filling pattern is created, with each bunch having a different charge, covering all the currents needed for a spectrogram. Then, with the KAPTURE readout system, all bunches in a multi-bunch environment can be observed simultaneously. In this way, a low-resolution spectrogram is recorded within a single KAPTURE dataset. Usually, one second of data of each bunch is recorded and then analyzed. Although the current resolution in the spectrogram is pretty poor compared to a conventional decay, the thresholds can be identified within a reasonable uncertainty. Bunch-to-bunch effects which could interfere with the measurement have also to be taken into account. However, Miriam Brosi has shown in her analysis, that these effects, at least for the investigated cases, are below the measurement uncertainty described before [Bro17]. To summarize, this method allows the determination of the bursting thresholds by recording just one second of data. With this method, many different machine settings have been scanned.

The resulting thresholds are shown in Fig. 6.11, where the scaling law (Eq. (2.51)) is drawn as a theoretical prediction line, which corresponds well with the measured data. The lower weak instability threshold seems to not depend on the shielding factor, while the upper threshold does. Shielding factors below 0.62 could not be measured with the current machine optics.

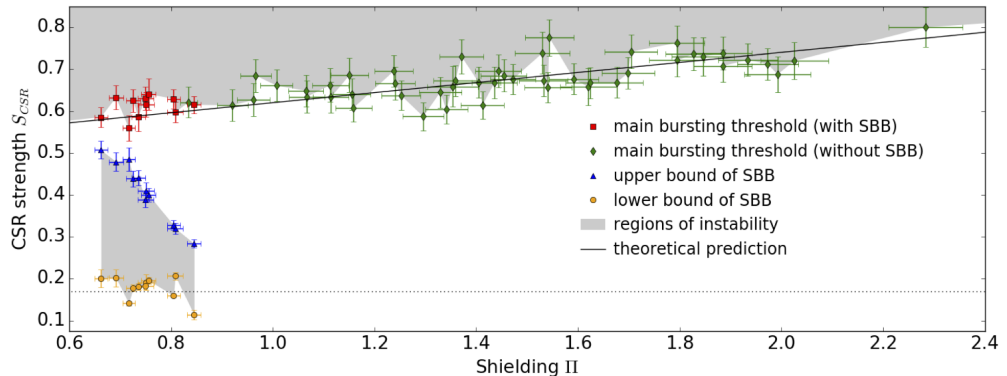


Figure 6.11: Measured instability thresholds vs shielding factor II (cf. Chapter 2.3). SBB denotes the weak instability. The threshold for measurements where no weak instability was observed is shown with green diamonds. The MBI threshold where a weak instability was observed is shown with red squares, while the upper and lower bound of the weak instability are shown with blue triangles and yellow dots, respectively. The theoretical prediction line is the MBI scaling law (cf. Chapter 2.3). Courtesy Miriam Brosi, published in [Bro16a] and [Bro19].

6.6 Influence of RF Phase Modulation

The potential well can be influenced by a change of the RF potential. The RF phase is controlled by the LLRF system, which can also modulate it. This leads to a nonlinear phase space and has been studied intensively in the early 1990s [156; 155; 154; 153]. It has been shown, that a modulation of the RF phase can lead to several stable operation points, called *islands of stability* [157]. All stable islands get populated by electrons, leading to several small bunches, called *bunchlets*. This method is used in several accelerators to increase the bunch length [158], to increase the beam life time [160; 159], or to damp instabilities [161].

To study the effect of a modulation on the MBI, I modulated the RF phase with twice the synchrotron frequency as described in [162]. Without modulation, all electrons are

gathered in a single island. The modulation frequency f_m and amplitude A_m define the number of islands during the modulation [162]

$$\frac{f_m}{f_s} > \left(2 - \frac{A_m}{2} \tan(\pi - \psi_0) \right) \mapsto 2 \text{ islands}, \quad (6.1)$$

$$\frac{f_m}{f_s} < \left(2 - \frac{A_m}{2} \tan(\pi - \psi_0) \right) \mapsto 3 \text{ islands}. \quad (6.2)$$

In the following experiment, $f_m/f_s = 2$ is chosen with a phase modulation amplitude of two degrees, which ensures a two island operation. Consequently, the RF potential is shifted periodically by 11.1 ps. The machine parameters are summarized in Tab. 6.1.

Table 6.1: Machine parameters during RF phase modulation experiment

Beam energy	E	1.287 GeV
Bunch current	I_b	0.38 mA
RF amplitude	V_{RF}	755 kV
Synchrotron frequency	f_s	7.5 kHz
Calc. MBI threshold	$I_{b,th}$	0.2 mA
Calc. momentum compaction	α_c	4.8×10^{-4}
Calc. zero-current bunch length (RMS)	$\sigma_{z,0}$	4.6 ps
Average bunch length (unmodulated, RMS)	$\sigma_{z,t}$	16.52(174) ps

Longitudinal bunch profile measurements made with a streak camera (cf. Chapter 4.3.5) are shown in Fig. 6.12. In this bursting regime, the unmodulated bunch has a measured average RMS size of (16.52 ± 1.74) ps due to bunch-lengthening. In this measurement the bunch hardly performs any coherent synchrotron motion. However, with a $2f_s$ -modulation, two bunchlets are observed, performing large amplitude oscillations around the former stable phase.

In order to analyze the effect of the modulation in the THz signal, two measurements were set up. The first was set up in the IR1 beamline: An optical APD and a small band SBD sensitive between 140 GHz to 220 GHz were read out synchronously by an oscilloscope in segmented mode. The second measurement was carried out at the IR2 beamline, where a broadband detector was read out by KAPTURE. The two

experiments were synchronized, so that the same bunch could be observed. Both readout devices were triggered by a common trigger. The LLRF system, activating the phase modulation was triggered 1 ms afterwards. With this synchronized set up, it is possible to observe the effect on different detectors at different positions at the same time. The APD is sensitive in the optical range and therefore only to ISR while the THz detectors comprise a small-band waveguide-coupled detector and a broadband quasi-optical detector sensitive to the emitted CSR.

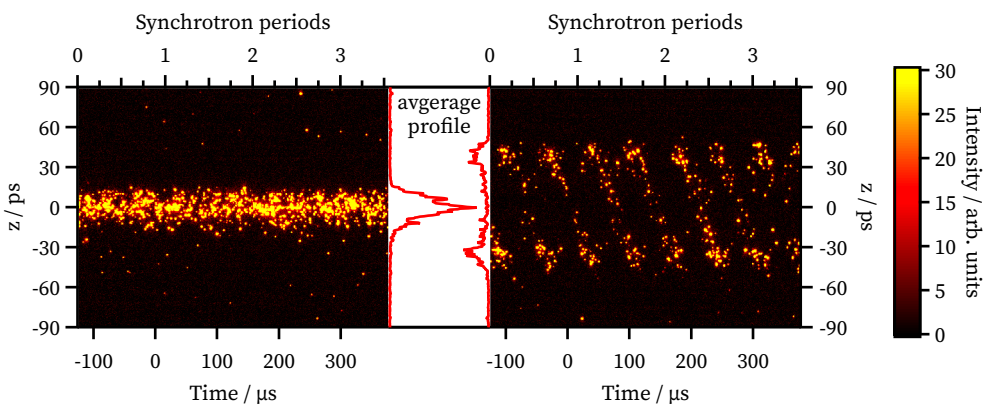


Figure 6.12: Streak camera measurements of a stable (left) and a modulated (right) single bunch. In the case of a modulated beam, two bunchlets can be seen, oscillating with almost the stable synchrotron oscillation frequency around the center. The peak-to-peak amplitude of the oscillation is around 70 ps while the phase modulation is 2° (11.1 ps). Due to dispersion, the two bunchlets also orbit each other in the horizontal plane, leading to periodic out-of-focus images of reduced intensity. The single random light spots are artifacts of the measurement: single stray photons detected by the fluorescence screen. (courtesy of Patrik Schönfeldt)

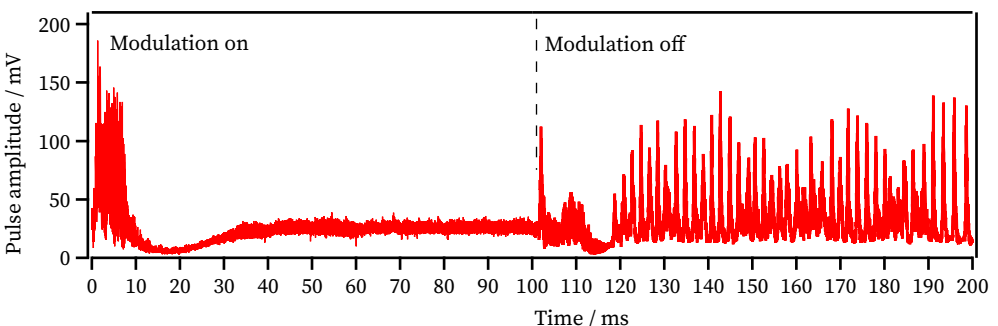


Figure 6.13: Influence of $2f_s$ RF phase modulation on the bursting behavior. Pulse amplitude of a broadband THz detector read out by KAPTURE at the IR2 beamline. The modulation is turned on 1 ms after the start of the measurement and turned off 100 ms later. The width of the line is caused by high frequency oscillations, which cannot be resolved in the shown time scale.

In a first experiment, the modulation is turned on and off repeatedly by the LLRF system. Figure 6.13 shows the pulse amplitude of the broadband detector measured at the IR2 beamline by KAPTURE. After the modulation is turned on, a burst, lasting approximately 7 ms with high frequency oscillation, follows. Afterwards, the amplitude drops to almost zero before it recovers to an almost stable, low intensity. When turning off the modulation, a short burst is emitted shortly after, followed by some modulation and a small region of low intensity, before the normal bursting behavior restarts at around 120 ms.

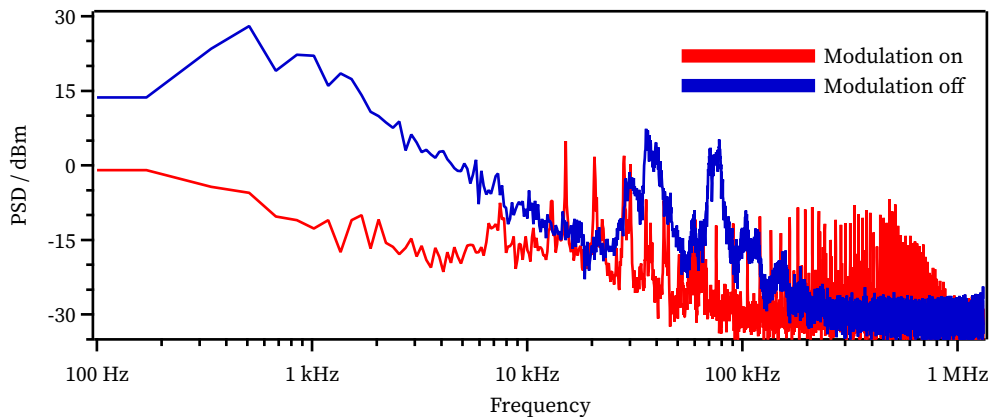


Figure 6.14: Spectra of the pulse amplitude evolution with (red) and without (blue) modulation. The spectra have been calculated by a FFT for the time ranges 40 ms to 100 ms and 140 ms to 200 ms of Fig. 6.13.

The spectra of the emitted pulse amplitudes between 40 ms to 100 ms and 140 ms to 200 ms are shown in Fig. 6.14. Without modulation, the observed spectrum is the expected spectrum of the MBI for that bunch current. After applying the $2f_s$ -modulation, the characteristic bursting frequencies are gone and the spectrum mainly consists of two frequencies and their harmonics. The coherent synchrotron frequency was identified to be 7.5 kHz. Therefore a 15 kHz modulation was applied. This frequency and its many harmonics are very prominent in the spectrum. A frequency slightly below the applied 15 kHz can also be identified and is probably the incoherent synchrotron frequency. Although the modulated spectrum looks stable, despite of the modulation frequency, one can not directly conclude, that the modulation suppresses the MBI. One has to keep in mind, that each of the created bunchlets has only half of the initial bunch current and therefore in the observed case, the bunchlet current is below the MBI threshold of 0.2 mA.

The transition from the modulated to the unmodulated signal and vice versa described above changes with bunch current. But nevertheless, it is reproducible for a given current. Fig. 6.15 shows three transitions from the unmodulated to the modulated state, the time between the measurements being 20 s. This time, the data is taken at the IR1 beamline with the small-band detector, sensitive between 140 GHz to 220 GHz. The behavior is quite similar taking into account the different frequency response of the detectors. This shows, that the effect is not a local phenomenon at IR2 but is also observed in the ring later on. Such a phenomena could be due to the fact, that the IR2 beamline is located directly at the straight section after an RF cavity, which applies the modulation (cf. Fig. 1.5) and for example be a local orbit distortion. So it can be concluded, that the changes in the longitudinal phase space between the location of the two beamlines are negligible.

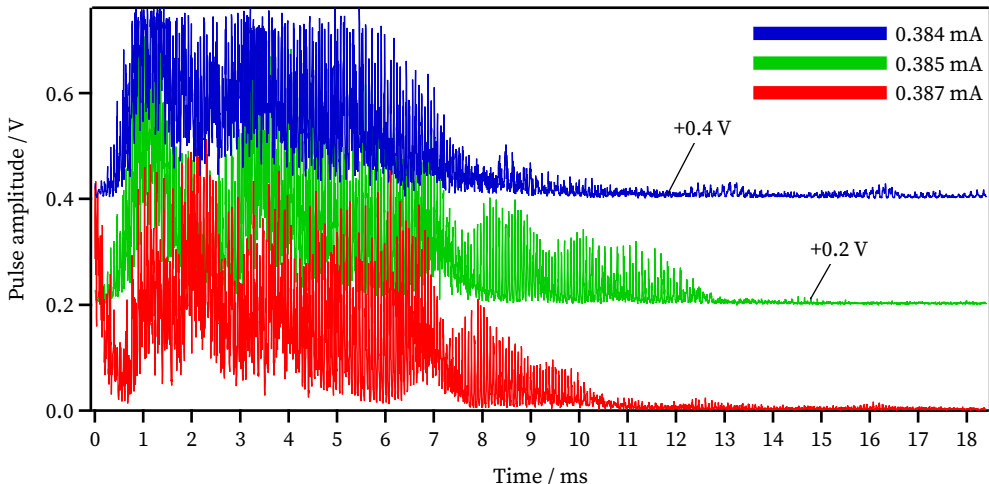


Figure 6.15: Pulse amplitude evolution of a narrowband SBD detector after a $2f_s$ -modulation is applied. The time difference between the measurements is 20 s, so that the bunch current has only slightly decreased. The response to the onset of the modulation is similar in all measurements, independent of the bursting phase the bunch had before. The response is therefore triggered by the onset of the modulation. The visible saturation of the pulse amplitude during the outburst is due to the oscilloscope's setting and a limitation of the dynamic range.

The modulation, starting after 1 ms, leads to high frequency oscillations of the THz amplitude for all observed cases, independent of the bursting phase the bunch did before. After 10 ms, which coincides with the longitudinal damping time τ_d , the THz radiation is almost gone. The increase afterwards as seen in Fig. 6.13 happens after 20 ms. The other case, the transition from modulated to unmodulated, is shown in

Fig. 6.16. At around 2 ms, the THz radiation has an outburst, followed by a characteristic tail until the radiation almost vanishes around 12 ms. Approximately 6 ms after the radiation vanished, the bursting starts again, where the MBI leads to the expected outbursts.

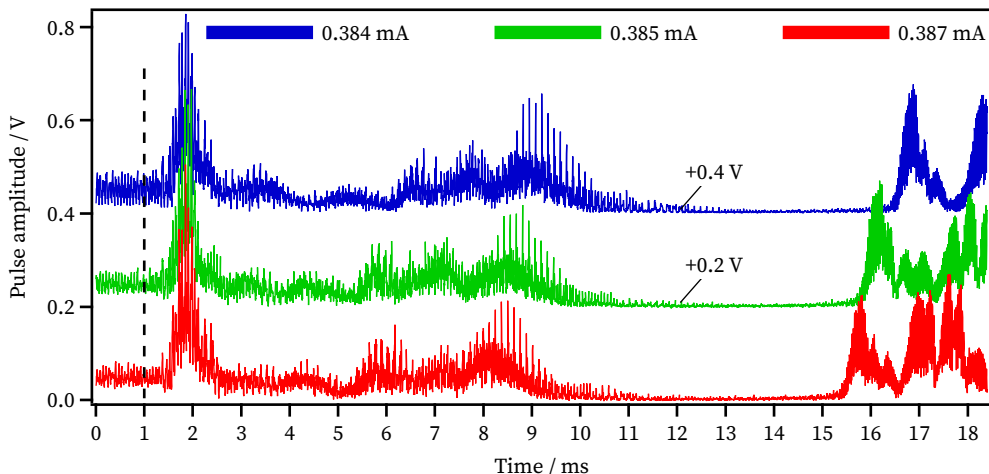


Figure 6.16: Same conditions as Fig. 6.15, but the modulation is turned off at 1 ms. A similar response is triggered every time. After a small phase of reduced emission, the typical bursting behavior restarts.

6.7 Summary of Time Domain Measurements

The basic properties of the micro-bunching instability were analyzed with a simple experimental setup, just focusing the emitted THz radiation onto a fast detector and measuring the pulse amplitude. Firstly, the intensity and fluctuations of the pulse amplitudes over time were investigated at some specific bunch currents and then the spectrum of that fluctuation signal discussed in more detail. They show typical characteristics of the MBI. It was shown, that the measured intensity of the THz pulses above the MBI threshold starts to oscillate and its average increases. In the spectrum, the frequency of the oscillation could be identified to be slightly below four times the synchrotron frequency. A characteristic for the machine settings used in this measurement. Then a spectrogram was introduced as a powerful representation to visualize the effect of micro-bunching instability. To verify the threshold current seen in the spectrogram, statistical methods were presented and the threshold current

defined as the current, where the standard deviation of the pulse amplitudes rises significantly.

Two special cases at low shielding factors, i.e. short zero-current bunch lengths were analyzed in greater detail. First, the bursting behavior at high bunch currents, where the radiation intensity in the observed frequency range does not drop between the outburst. Second, the occurrence of an additional weak instability at low bunch currents.

It was shown that the use of the KAPTURE readout system in combination with a tailored filling pattern enables snapshot measurements, where a rough spectrogram can be recorded in a single one-second long measurement. This setup allows the fast scan of machine parameters and their influence for example on the bursting threshold current. The found results coincide well with the scaling law presented in Chapter 2.3.

In the end of the Chapter, first experiments to influence the micro-bunching instability deterministically were discussed. The applied RF phase modulation leads to a splitting of the bunch in two bunchlets and greatly affects the bursting behavior. In the observed cases, shortly after having applying the modulation, an outburst of THz radiation is measured before the THz intensity vanishes, and then stabilizes on a low intensity.

This could be of potential interest for setups like FTIR spectrometry, which rely on a stable signal rather than on unpredictable high intensity bursts. The presented method of changing the RF phase with a frequency of two times the synchrotron oscillation can provide the needed stabilization during short-bunch operation. However, one has to keep in mind that the observed stabilization could be due to the fact, that the individual bunchlet-current is below the MBI threshold. This has to be investigated in future systematic studies.

To achieve the maximum average THz peak power, a faster frequency of starting and stopping the modulation could provide high intensity THz radiation because the first radiation outburst after applying the modulation has shown to be reproducible. This can be used to seed a bursting behaviour in future experiments, which are synchronized to the LLRF system providing the modulation.

7 High Repetition Rate Single Shot Spectrometer

An expert is a person who has found out by his own painful experience all the mistakes that one can make in a very narrow field.

— Niels Bohr

Fourier transform (far-)infrared spectroscopy, as presented in Chapter 5, provides good resolution and a high dynamic range. Although the measurement time of recent devices has improved a lot, they can not resolve bursting dynamics. This chapter focuses on a single shot spectrometer, that continuously measures spectra with 500 MHz repetition rate, therefore being able to measure spectral components of every bunch at each turn. Here, a prototype is presented, which uses the four input channels of KAPTURE (cf. App. B.8), and a setup of four Schottky barrier diodes (SBD) (cf. Chapter 4.1). First measurements with this setup are presented and the results compared to Inovesa simulations. Due to the success of this prototype, further development is ongoing and will be briefly introduced at the end.

A great step forward to completely understand the micro-bunching instability (MBI) would be a reconstruction of the longitudinal phase space during the MBI. A starting point is the reconstruction of the longitudinal bunch profile. However, the used THz detectors only measure the emitted power of the synchrotron radiation while the phase information is lost. Unfortunately, a unique reconstruction of a signal only from the magnitude of its Fourier transform is mathematically impossible [163]. Workarounds like a Kramers-Kronig dispersion relation give impressive results for known bunch shapes like a single Gaussian or cosine half wave [164]. However, they fail for spikes in the profile and, especially, many small sub-structures as they happen for bunch charges above the MBI threshold current as it is being investigated here. Therefore, *Inovesa* (cf. Chapter 2.4) was used to simulate the phase space, extract the emitted power spectrum and compare this to the spectroscopic measurements. A

comparison of the four spectral bands gives much more evidence about the validity of the simulation than the previous comparison to a single detector which integrates all the emitted radiation. A match between the simulation and all the detectors is a good indication that the simulated phase space represents the real bunch dynamics.

The main results presented in this chapter have also been published in [Ste17; Ste18b]. Additional work and planned future projects, only briefly discussed here, can also be found in [Raa15b; Raa16; Sch16b; Sch17a]. A similar experiment was set up at the Diamond light source by Finn et al. [165; 166], where spatial segregation is used to record different frequencies simultaneously. In their current readout setup, the power and frequency components are analyzed in the frequency domain, dropping the phase relation between the different frequencies. While their array consists of eight channels, the readout is limited to turn-by-turn data and does not provide single bunch resolution.

7.1 Four-Channel Spectrometer Setup

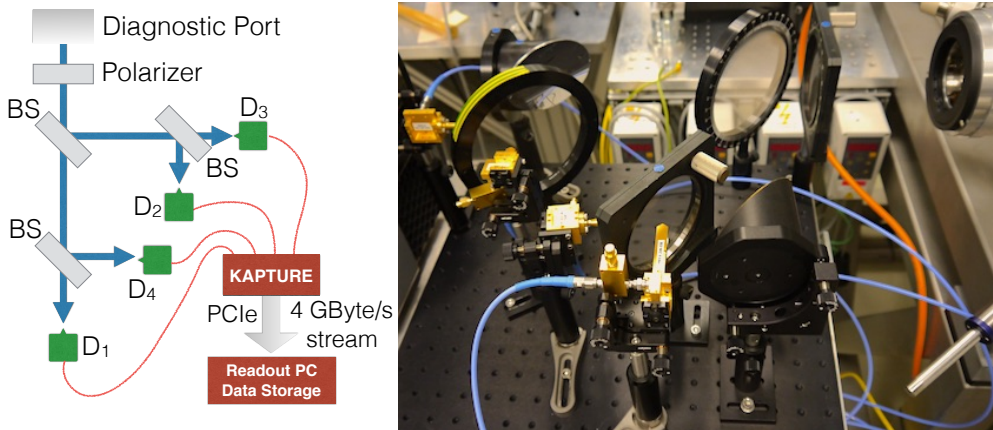


Figure 7.1: Experimental setup: The synchrotron radiation emitted at the diagnostic port is first polarized and then divided into four beams by three wire-grid beam splitters (BS). The split beams are focused onto four detectors, each one sensitive in a different frequency band (see Table 7.1 and Fig. 7.8 for details). The single-shot measurements are sampled and read out by the KAPTURE system.

The prototype setup, sketched in Fig. 7.1, has been installed at the IR2 beamline (cf. Chapter 3.5). The radiation was coupled out through a Z-cut quartz window at the diagnostic port and directly fed into the setup. To ensure a purely linear polarization

of the incoming CSR, the beam is pre-polarized and afterwards, with a set of three additional wire-grid polarizers, split into four partial beams of nearly equal power, each focused to a wave guide coupled SBD detector (cf. Chapter 4.1). The detectors used in this prototype spectrometer are summarized in Tab. 7.1. Each detector is sensitive in a different frequency band. The same bands are used in the corresponding simulations. To easily distinguish between them they will be labeled as D_1 (90 GHz to 140 GHz), D_2 (140 GHz to 220 GHz), D_3 (220 GHz to 325 GHz) and D_4 (325 GHz to 500 GHz) throughout this chapter. Each detector signal was simultaneously read out with one of KAPTURE's four input channels.

Table 7.1: Schottky barrier diode detectors used in spectrometer [167]

Label	Band (GHz)	VDI Model	DC responsivity (V/W)
D_1	90-140	WR8.0ZBD	2000
D_2	140-220	WR5.1ZBD	2000
D_3	220-325	WR3.4ZBD	1500
D_4	325-500	WR2.2ZBD	1250

In the first measurements, KAPTURE was programmed to store datasets with a length of 100 ms, recorded in intervals of 10 seconds. Thus, each bunch has been tracked continuously for more than 2.7×10^5 consecutive turns. To improve the used ADC range, three of the SBD detectors (D_2 , D_3 and D_4) were amplified using a 15 dB amplifier with 18 GHz bandwidth.

The storage ring was filled with a maximum initial bunch current just above 2 mA. Then, measurements were performed during a beam current decay (cf. Chapter 1.6) for bunch currents between 2 mA and 0.18 mA. During that time, all other machine parameters were kept constant. They are summarized in Table 7.2.

In the following, an overview of the measurements will be presented by analyzing the spectrograms of all detectors and investigating the statistical properties like average power and standard deviation which are compared to Inovesa simulations. After that, three different bunch currents are analyzed in more detail. The highest analyzed bunch current is in the sawtooth bursting regime, the second one in an intermediate regime and the third one is directly above the MBI threshold. These regimes have been described in Chapter 6.

Table 7.2: Machine parameters during spectrometer measurements

Beam energy	E	1.287 GeV
Bunch current	I_b	2 mA to 0.18 mA
RF amplitude	V_{RF}	799.2 kV
Synchrotron frequency	f_s	8.2 kHz
Shielding factor		1.53
Calculated MBI threshold	$I_{b,\text{th}}$	0.2 mA
Calculated momentum compaction	α_c	5×10^{-4}
Calculated zero-current bunch length (RMS)	$\sigma_{z,0}$	4.5 ps

7.2 Current Decay

This section compares the measurements during the current decay (cf. Chapter 1.6) and the Inovesa simulations.

7.2.1 Measurement

First of all, similar analyses of the four channels are carried out as described in Chapter 6 for a single detector. To determine the MBI threshold at the given machine setting, the standard deviation of the detectors' amplitude is analyzed and shown in Fig. 7.2. Below the threshold current, only two diodes (D_1, D_2) detect fluctuations in the pulse intensity, because no CSR is emitted at the higher frequencies (D_3, D_4). The fluctuations below the threshold are in accordance with a dipole motion model of the synchrotron oscillation that modulates the bunch length. The slope increases significantly at the threshold current, where additional sub-structures influence the emitted radiation.

The determined MBI threshold at 0.214(2) mA is in agreement with the threshold calculated by the scaling law (Eq. 2.51, 0.20(1) mA) and the one simulated by Inovesa (0.225(5) mA). Uncertainties of the measured input parameters account for the error in scaling law value, but have not been considered in the VFP simulation. The uncertainty of the Inovesa simulation originate from the simulated bunch current steps. The scaling law is known to be slightly below the simulated values for most shielding

factors, especially for $\Pi < 4$. Additionally, the snapshot measurements show a slightly higher threshold than the scaling law, too (cf. Chapter 6.5 and Fig. 6.11).

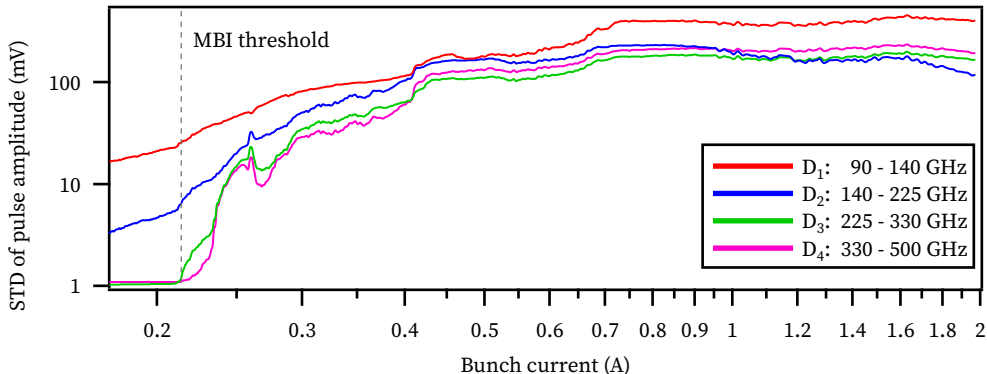


Figure 7.2: Measured standard deviation (STD) of the pulse intensity in the different diode frequency bands. Above the determined MBI threshold of 0.214(2) mA (vertical dashed line), the fluctuations increase significantly.

Above the threshold, the standard deviation increases until it remains at a high level, which is even above the average amplitude. This is due to the outbursts of radiation followed by relatively low power during the shrinking of the bunch. Consequently, long averaging times are needed in this regime, if one intends to do conventional spectroscopy with typically slower (in comparison to these measurements) data acquisition systems.

Bursting spectrograms as introduced in Chapter 6.2 are excellent tools to analyze the bursting dynamics. Such a spectrogram, showing specific modulation frequencies of the THz power, is reproducible and depends on machine parameters like the momentum compaction factor, the accelerating voltage and the impedance of the storage ring. As mentioned in the previous chapters, it is a fingerprint of the accelerator in its current state. Figure 7.3 shows the spectrogram for each of the four detectors. Different current-dependent bursting regimes can be identified.

Above the bursting threshold at 0.214(2) mA, the instabilities start with high frequency modulations around 32 kHz. With increasing current, low frequencies arise, too, which indicate the occurrence of periodical bursts. The repetition rate of the bursts is below 1 kHz and is hardly visible in the plots. After an intermediate stage with more complex structures above 0.7 mA, the spectrum changes to a regular pattern of harmonics near the synchrotron frequency. With increasing bunch current, the

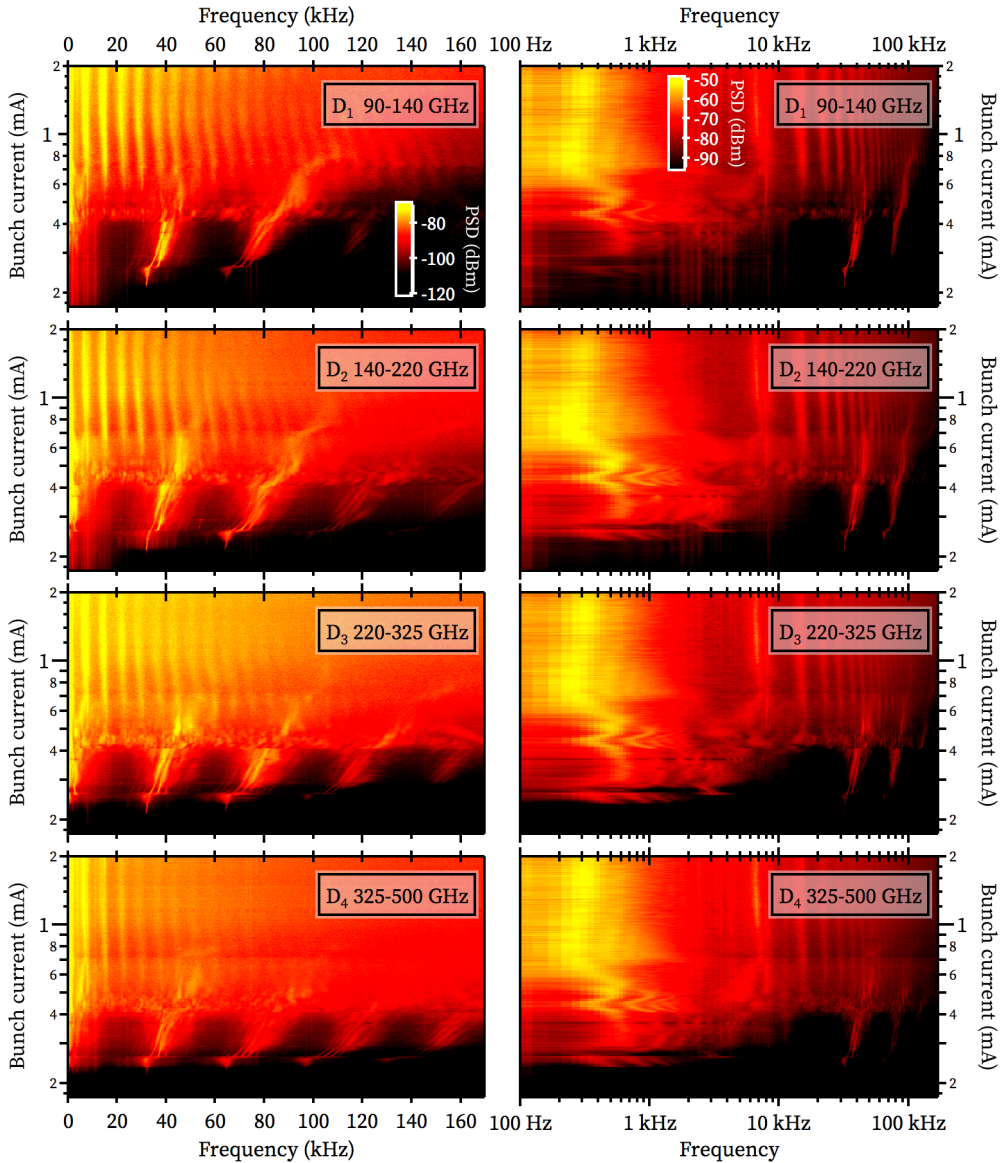


Figure 7.3: Measured bursting spectrograms of each detector with linear (left) and logarithmic (right) frequency axis. The main features are visible in all spectrograms, albeit with different contrast. The color scale is a logarithmic scale of the detector output power into 50 Ohms and should not be compared quantitatively between the diodes due to different frequency bandwidth, responsivity and RF readout efficiency of the diodes. Also note, that detector D₁ was operated without amplifier, whereas all other diodes were amplified by 15 dB.

amount of white noise also rises. Since the ADC pre-amplifier has not been changed, these are not digitization-induced fluctuation effects, but account for a high amount of randomness in the bursting behavior. As a consequence, none of the bursts are identical, even though the form of them is similar and their appearance repeats.

Furthermore, it can be seen that the main features of the spectrogram are the same, although the different diodes span different frequency ranges from 90 GHz to 500 GHz. Differences in the spectrogram are caused by the relative intensities of some features, the amount of random noise and the number of visible harmonic structures.

7.2.2 Inovesa Simulation

In order to classify the measurements and to identify and distinguish artifacts from physical results, simulations using the same machine parameters have been carried out with Inovesa v0.14 (cf. Chapter 2.4). Inovesa simulates the longitudinal phase space in the vicinity of a disturbance, which is modeled by an impedance. The simulations presented in the following, use the CSR impedance with shielding by parallel plates (cf. Chapter 2.1.2). Projecting the simulated longitudinal phase space onto the time axis provides the bunch profile. Therefore, the form factor and subsequently the emitted coherent radiation is calculated (cf. Chapter 3). One has to keep in mind that this is the energy the bunch radiates due to the parallel plates impedance, which is not exactly the radiation emitted into the beamline. Effects like edge radiation, polarization, and the beamline transport system are neglected in this simulation.

The simulation uses the bending radius (5.559 m) and beam pipe height (32 mm) of the KARA storage ring. All “non-static” properties, like synchrotron frequency and RF voltage, have been chosen to fit to the measurements presented in the following (see Table 7.2 for measurement parameters).

The simulated emission spectrogram in Fig. 7.4 shows the average emitted spectrum for different bunch currents. The MBI threshold in this simulation is located between 0.22 mA to 0.23 mA, the simulated current steps being 10 μ A. The average emitted spectrum below the threshold is dominated by bunch-lengthening and above the threshold by the duration, intensity, and repetition rate of the bursts due to the bunch sub-structures. At a hypothetical zero current, the bunch is shortest and has a Gaussian shape without any sub-structures. With increasing current, the bunch form changes due to potential-well distortion. This leads to a decrease of the intensity of the first

frequency peak around 50 GHz when compared to the quadratic current-dependency expected for constant bunch shapes. On the one hand this results in an increased RMS bunch length, on the other hand in a leaning forward of the bunch (cf. Fig. 2.11 in Chapter 2.2.3). Therefore, the intensity of the first frequency peak below is decreased, even though the bunch current increases. Above the bursting threshold, additional sub-structures form, and even higher frequency components arise.

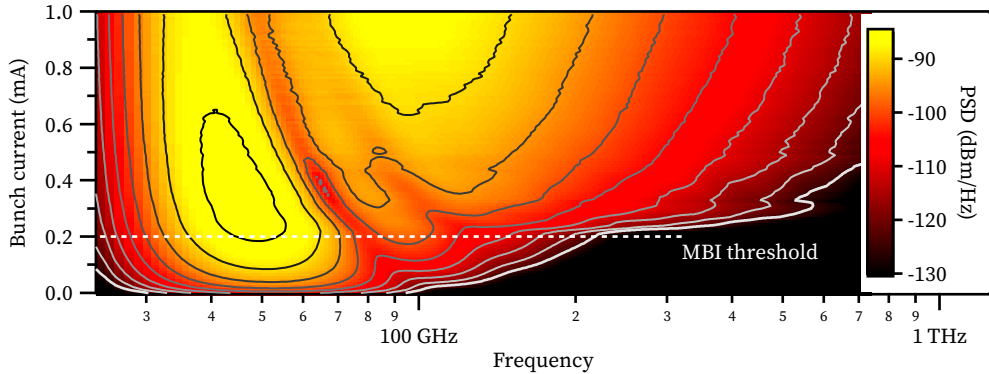


Figure 7.4: Inovesa simulation: Average emitted power spectral density (PSD) of the emitted SR for different bunch currents. The contour lines are in 5 dB distance between -85 dBm and -130 dBm .

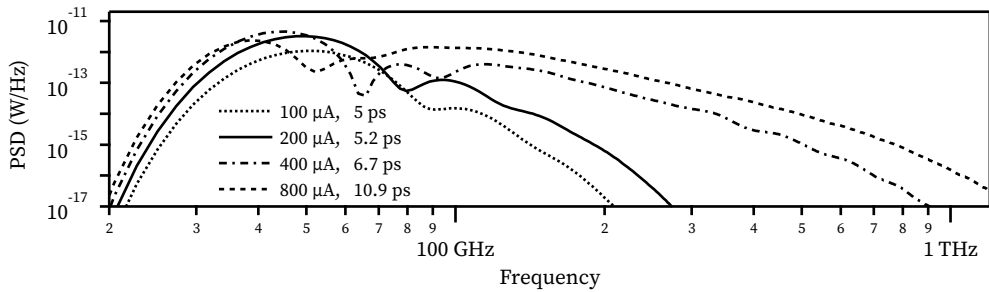


Figure 7.5: Inovesa simulation: Slices for selected bunch currents and average RMS bunch durations of the emitted CSR spectrum in Fig. 7.4.

This can be seen even better in Fig 7.5, which shows in greater detail four specific averaged spectra at 0.1 mA , 0.2 mA , 0.4 mA and 0.8 mA with an average rms bunch length of 5.0 ps , 5.2 ps , 6.7 ps and 10.9 ps , respectively. The spectral components below $\approx 30 \text{ GHz}$ increase quadratically with the bunch current, since the form factor is always one at these bunch lengths. However, these frequencies are shielded by the beamline

geometry and cannot be observed. The frequencies slightly above are dominated by the overall bunch length, and therefore, higher currents can lead to less power due to the bunch lengthening effect. Above 100 GHz, the sub-structures become dominant and the spectral intensity increases stronger than quadratic with the bunch current at some frequencies.

To cross-check the simulation with the measurement, averaged values are compared. The average simulated emitted power is shown in Fig. 7.6 and the average measured pulse amplitude of the four detectors is shown for comparison in Fig. 7.7. Note that the electrical output voltage of the SBD detectors is proportional to the optical input power in its linear regime. The simulated power and the derived average pulse amplitude show good agreement around the MBI threshold. While almost no change is observed at the two lower frequency bands (D_1 and D_2), the emerging sub-structures lead to a significant rise in emitted power at the higher frequencies (D_3 and D_4).

The MBI threshold in the measurements (Fig. 7.7) can be identified at 0.214(2) mA, while in the simulation (Fig. 7.6) it is slightly higher, at 0.225(5) mA. Noteworthy is the different behavior of the diodes' signal at this threshold value. The forming of sub-structures above the MBI threshold has only a minor effect at the D_1 frequency band between 90 GHz to 140 GHz. This is attributed to the already high amount of coherence from the bunch as a whole, so that the forming sub-structures mostly affect higher frequency components. The latter is evident in the data obtained in the two highest frequency bands. Without sub-structures, these diodes hardly detect any radiation while they are not sufficiently sensitive for incoherent radiation in this setup. Note that the sudden drop of detected power, seen for the two diodes D_2 and D_3 above 0.4 mA, and for D_2 , D_3 and D_4 around 0.7 mA (cf. Fig. 7.7) is due to a change of the bursting behavior. These sudden drops in the average values correlate with distinct features in the spectrograms (Fig. 7.3), i.e. these average traces are highly reproducible and sudden drops are connected to the underlying electron density dynamics. For the simulation, D_3 and D_4 show a similar drop at about 0.35 mA. There are two possible explanations for this small discrepancy. First, the simple parallel plates model does probably not fully reproduce the beam dynamics. Secondly, we assumed a flat spectral sensitivity for the simulation, while in the measurement the exact frequency of an emission peak is important (cf. Fig. 7.4).

If we assume a stable bunch shape, a quadratic increase of CSR with current is expected (see Fig. 7.7). This can be seen for the two lowest frequency bands, however, the bunch

is not short enough for coherent radiation at the higher frequencies. Around the MBI threshold, with the starting potential well distortion resulting in an asymmetric bunch shape and formation of sub-structures, the power at the higher frequencies increases stronger than quadratic as shown in the simulations (cf. Figs. 7.4 and 7.5).

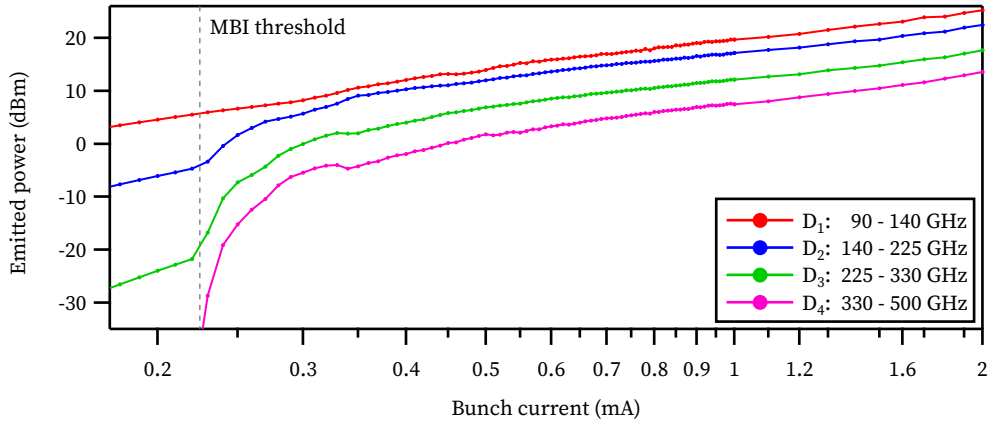


Figure 7.6: Inovesa simulation: Average integrated CSR power emitted in each frequency range of the measurement. The connecting line between the simulation steps is a guide to the eye. The vertical dashed line denotes the bursting threshold at 0.225(5) mA. This is the average simulated power emitted by the bunch over the whole turn. For details see text.

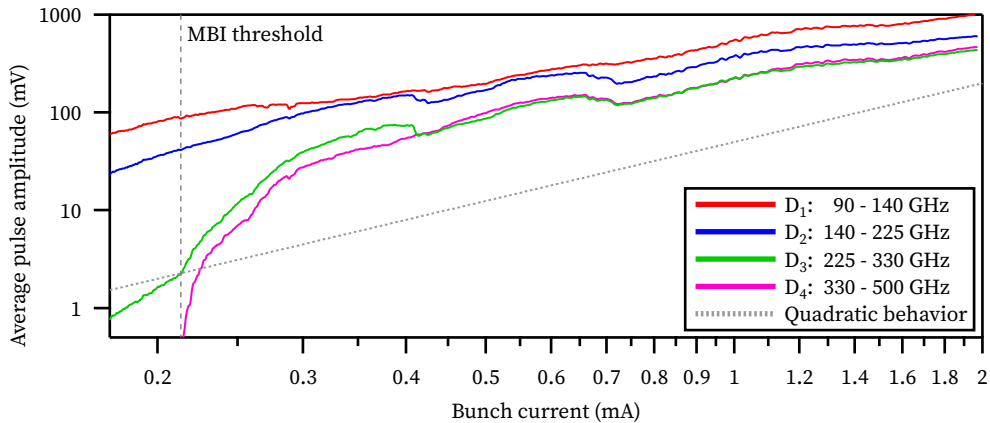


Figure 7.7: Measured average amplitude of the single pulse signal over the bunch current corresponding to the average optical power emitted in each frequency band. For a stable bunch profile, a quadratic dependency would be expected. To guide the eye, the dotted line shows such a behavior. The bursting threshold appears at 0.214(2) mA (vertical dashed line).

Above the threshold, the total emitted CSR power is stronger influenced by the changing form factor due to the sub-structures than by the number of the overall electrons. Subsequently, a larger power increase can be observed for a small current range at higher frequencies in comparison to the quadratic behavior (cf. Fig. 7.7). This saturates quickly. Above 0.7 mA, in the regime of the resonant bursts described before, the average power is determined by the length and repetition rate of the bursts. With increasing current, a slight repetition-rate decrease of the bursts is observed, counteracting the increased number of electrons and resulting in an almost stable average current between 1.2 mA to 1.6 mA. This sawtooth bursting regime is analyzed in more detail in the next section.

7.3 Sawtooth Bursting Regime

In the following, a simulated time-domain dataset for a bunch current of 0.8 mA is investigated and compared to the measurements. This current is about four times the bursting threshold and in the regime of large periodic bursts. Due to bunch lengthening, the average bunch length is about 60 % longer than the calculated zero-current bunch length. This limits the amount of stable coherent radiation. Nevertheless, the strong instability with many small sub-structures in the electron density leads to periodic bursts of high amplitude THz radiation, more than an order of magnitude more intense than the power emitted by stable bunches.

Figure 7.8 presents simulated data. The changing instantaneous CSR spectrum over time is calculated from the simulated bunch profiles. For comparison to slower data acquisition systems and spectrometers, the average spectrum of all spectra, which are emitted within 50 ms is displayed. Most of the emitted spectra are below the average, because the high frequencies and high intensities are emitted only for a short time during a burst. The fact that the coherent enhancement increases the emitted power by many orders of magnitude, leads to an average above the median spectrum. Figure 7.8 additionally shows the emitted THz intensity in these four spectral bands and the rms bunch length at that time. The small, but fast, bunch-length modulation between the radiation outbursts can be modeled by a quadrupole motion (cf. Fig. 1.4), which leads to a periodicity with twice the synchrotron frequency. On the longer timescales, the rms bunch length decreases due to radiation damping, until the threshold is reached. Then, the strong MBI drives sub-structures and blows up the bunch. This

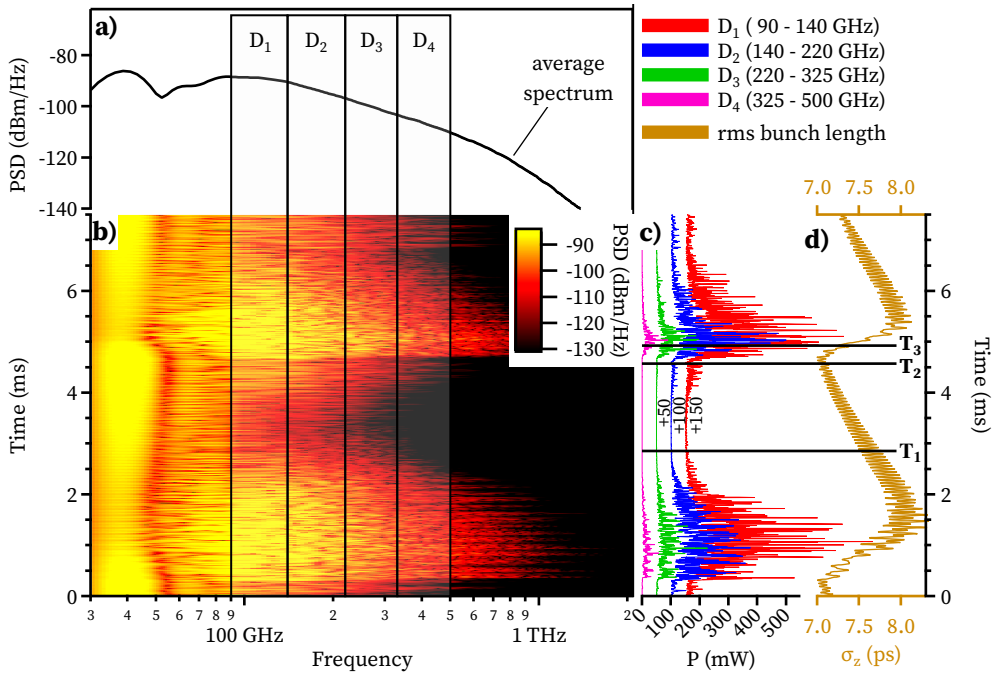


Figure 7.8: Inovesa simulation: Bursts at 0.8 mA. a) shows the average emitted spectrum on a logarithmic scale. The image in b) shows the instantaneous emitted coherent radiation due to the changing bunch profile over time. The expected integrated power P in the marked frequency bands of the used Schottky diodes are shown in c) and the corresponding RMS bunch length σ_z in d) for the same time axis. For better visibility, the signals of D_1 , D_2 and D_3 , are shifted by 150, 100 and 50 mW, respectively. For selected times T_1 , T_2 and T_3 see details in Fig. 7.9.

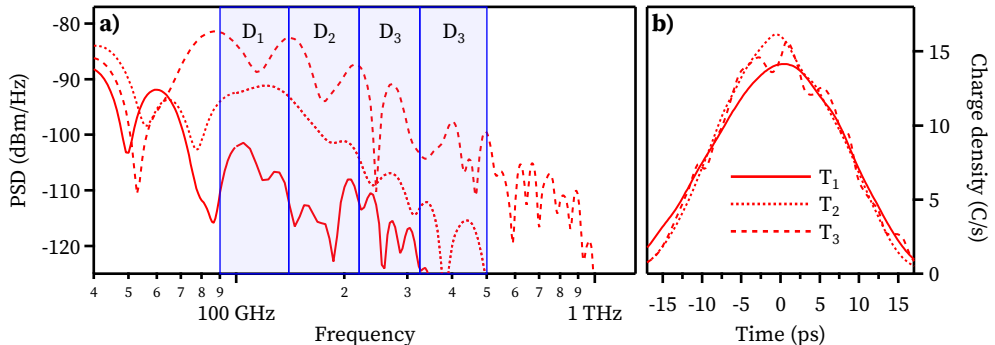


Figure 7.9: Calculated emitted spectra a) and bunch profile b) at selected times T_1 , T_2 and T_3 of Fig. 7.8 as a function of spectral frequency and time, respectively. The high frequencies are very unstable and only emitted for a short time during a burst. However, the intensities emitted by the sub-structures are many orders of magnitude higher due to the coherent enhancement. The indicated bands (shaded blue) correspond to the bandwidth of the detectors. For details see Fig. 7.8 and the text.

blow-up in combination with diffusion and damping in phase space homogenizes the bunch shape and the sub-structures vanish. Accordingly, the bunch length and the energy spread fluctuation show the same periodicity as the bursting behavior (see also [Keh17]). Because the emitted spectrum is sub-structure dominated and only the spectral intensity is measured (i.e. the phase is lost), a direct reconstruction of the bunch profile is not possible.

Three points in time (T_1 , T_2 and T_3) are shown in more detail in Fig. 7.9 with their spectra and bunch profile. T_1 lies between two outbursts (cf. Fig. 7.8(d)): the shape is smooth since the sub-structures have already decayed, and the bunch is further shortening. At the high frequencies of D_3 and D_4 , very low power is emitted. At time T_2 , the shortened bunch implies an increased wake potential, which leads to a bunch deformation, visible in the bunch profile (cf. Fig. 7.9(b), trace B) and drives the MBI. This results in more radiation, seen first at lower frequencies (cf. Fig. 7.9(a)), and also increases the intensity of the wake potential. At T_3 , the sub-structures, now clearly visible on the bunch profile, have the highest amplitude and shortest size leading to the outburst of radiation as seen at all frequency bands. The high wake potential blows up the bunch quickly, which, due to diffusion and damping, becomes stable again and shrinks until the next burst occurs. This described process takes a few milliseconds, only.

Turn-by-turn data of the four detectors are shown in Fig. 7.10. In agreement with the simulations (compare to Fig. 7.8), the pulse amplitudes of the D_1 and D_2 diodes are on an almost constant and low level before the burst. They are mainly modulated with twice the synchrotron frequency in accordance with the quadrupole motion model (not visible in the plots). When the burst starts, as seen in the zoom-in, the observed modulation changes (in this case) to twelve times the synchrotron frequency, which is due to the forming sub-structures rotating in phase space. The diodes, sensitive at a higher frequency band, do not measure notable coherent radiation until the burst starts. Additionally, the burst's observation occurs later compared to the lower frequencies bands.

In contrast to the simulation, the bursts' shape looks more sawtooth-like with a steep rise at the beginning and a slow decay, whereas the simulation predicted a more triangular shape of the bursts. This discrepancy can be due to a different synchrotron frequency as input parameter to the simulation or to additional effects, which are not covered by the simple parallel plates impedance used in the simulation. Many effects,

like a synchrotron tune shift or beam loading, depend on the bunch current. Therefore the discrepancy is expected to rise at higher currents. However, indications that the coherent synchrotron frequency, measured by the BBB system, does not exactly fit in with the incoherent synchrotron frequency used in the simulation are also found at lower currents.

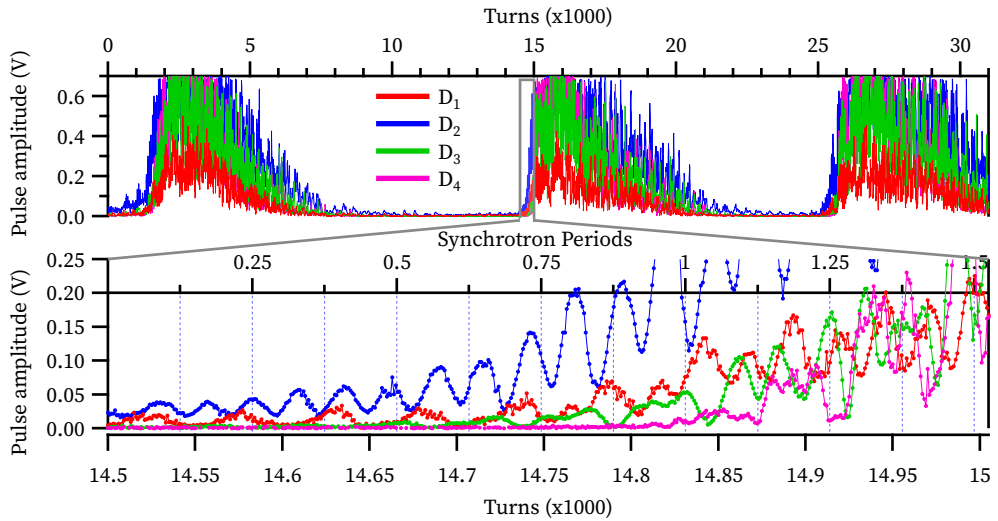


Figure 7.10: Measured turn-by-turn amplitudes of the four different diodes (1000 turns ≈ 0.368 ms ≈ 3 synchrotron periods). The bottom panel shows a zoom-in to the beginning of a burst. Every point is a measured pulse amplitude, the connecting line is a guide to the eye.

7.4 Bursts at Medium Bunch Current

A different bursting regime, at a bunch current of $400\ \mu\text{A}$ is shown in Fig. 7.11. At this current, the spectrogram (cf. Fig. 7.3) shows high intensity at frequencies around $40\ \text{kHz}$ and their harmonics, but no strong lines at direct multiples of the synchrotron frequency. However, there is still a contribution at the low frequencies, which indicates the occurrence of bursts, but with a different shape than in the sawtooth bursting regime. In the top panel of Fig 7.11, an example of the bursts can be seen. The zoom traces reveal the dominant $40\ \text{kHz}$ oscillation. It is approximately at five times the synchrotron frequency and therefore shows five periods during one synchrotron oscillation. Although the frequency is the same at all diode signals, a clear phase offset

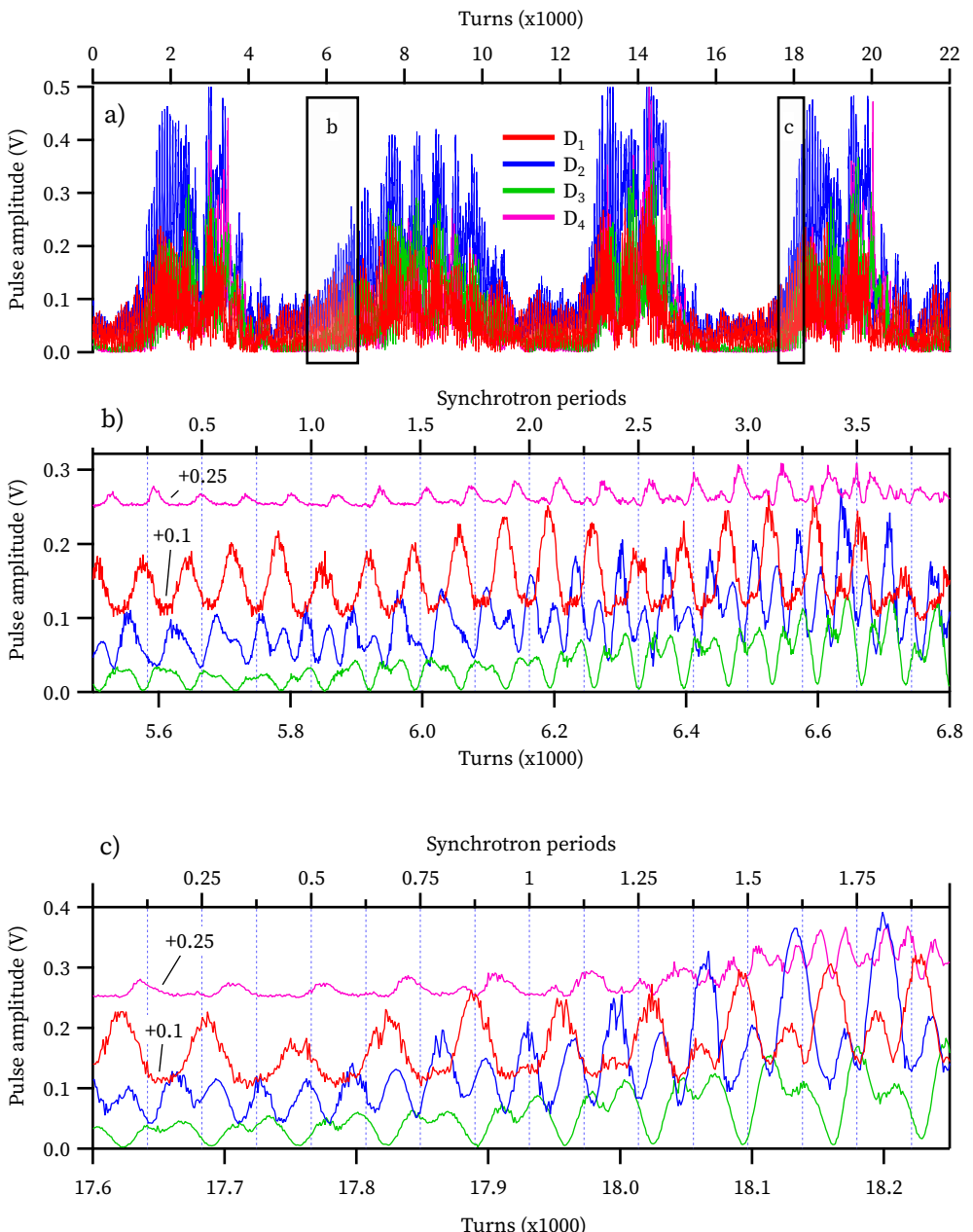


Figure 7.11: Measured turn-by-turn amplitudes of the four different diodes at $400 \mu\text{A}$ ($1000 \text{ turns} \approx 0.368 \text{ ms} \approx 3 \text{ synchrotron periods}$). (b) and (c) are indicated zooms at the beginning of a burst. To increase the visibility at the zoomed traces, the D_1 and D_4 signals are shifted by 0.1 and 0.25 V, respectively. At all diodes, an oscillation with five oscillations per synchrotron period can be identified.

is visible. This is attributed to the rotation of the sub-structures in phase space. A small sub-structure, emitting high frequency components, is enlarging in the projection and thus emitting at lower frequencies.

A direct turn-by-turn comparison on short timescales to the simulation is difficult, as the bursts show a high degree of randomness and are unique. Even though the averaged values are reproducible. However, near the MBI threshold, where no outbursts happen and the amount of white noise is reduced, a direct comparison is possible.

7.5 Regular Bursting Regime

At KARA, the bursting regime slightly above the MBI threshold is referred to as *regular bursting regime* [168]. Here, besides the always visible synchrotron frequency, only a single modulation frequency (the *regular bursting frequency*) and its harmonics are visible. The actual frequency depends on the number of structures in the phase space and on the synchrotron frequency [169].

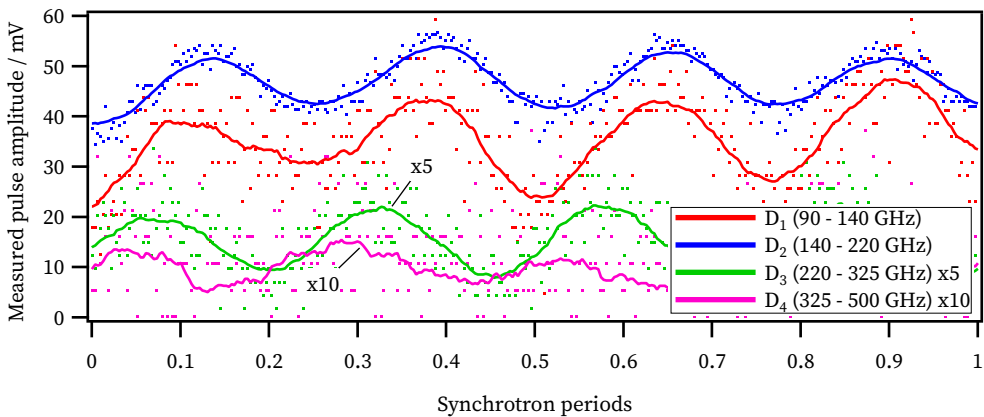


Figure 7.12: Measurement in the regular bursting regime. The pulse amplitudes measured every turn by KAPTURE are shown as dots while the solid lines are smoothed by a box car filter of 30 turns ($11\ \mu\text{s}$). The visible quantization of the D_4 detector signal is due to the low signal strength at the high frequencies in combination with limited ADC resolution. A clear phase shift between the diodes can be seen. Due to the low intensity at high frequencies, the signal of the D_4 detector is limited by the ADC resolution.

Figure 7.12 shows a measurement with the four detectors in that region. Due to the low intensity at high frequencies, the signal of the D_4 detector is limited by the ADC resolution. The same frequency around 32 kHz is observed in all diodes which was

also observed in the spectrograms (cf. Fig. 7.3). In addition to the spectrogram, which only shows the magnitude of the oscillation, a phase shift between the detectors can be seen in the time domain (Fig. 7.12). This is not an artifact but due to a structure which is not rotationally symmetrical. The projection of that structure enlarges and shrinks according to the phase space rotation. Therefore, a different intensity is observed in the distinct spectral ranges. A similar behavior can be observed in the simulation. Fig. 7.13 shows the simulated time-domain data for the same machine settings. Since Inovesa simulates the complete phase space, the source of the observed phase shift can be investigated.

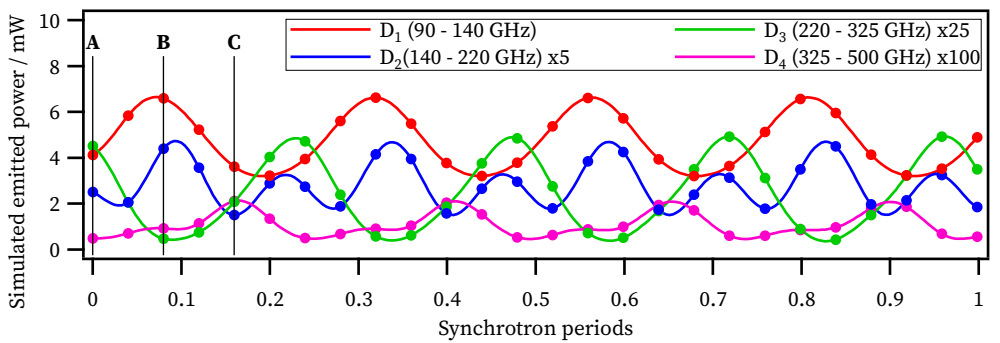


Figure 7.13: Inovesa simulation: Power in observed bands with same conditions as measurement in Fig. 7.12. The phase offsets observed in the simulation are similar to the measured ones. The marked points are shown in more detail in Fig. 7.14

The three marked time steps of Fig. 7.13 are shown in more detail in Fig. 7.14. For better comparison, the average phase space is subtracted from the detailed views [168]. The phase space at that current has permanent sub-structures that rotate counter-clockwise. *Permanent* in this case means that the sub-structures are always present, and the phase space repeats with the observed finger frequency. However, the structures themselves evolve and change in amplitude during their rotation (synchrotron motion) in phase space. At the bunch head, the sub-structures are largest, while they almost vanish on the opposite side. At these machine settings, five minima and maxima in the phase space are seen. The phase space image repeats with the finger frequency, which is approximately four times the synchrotron frequency. The different impact on the spectrum at the three time points explain the different behavior of the narrowband detectors. This effect can not be observed when using a single broadband detector that integrates the whole sensitivity range.

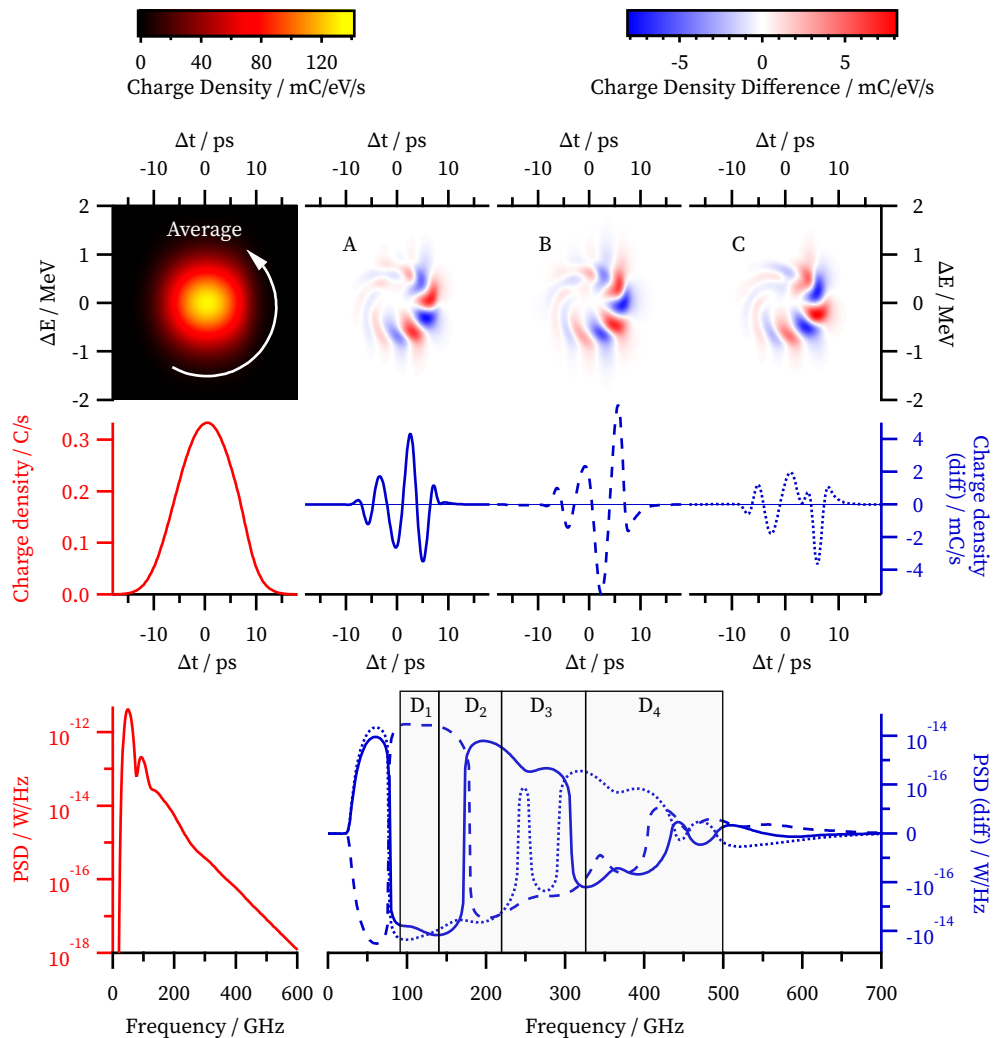


Figure 7.14: Inovesa simulation: The marked time steps of Fig. 7.13. The phase space as simulated by Inovesa (top) is used to calculate the longitudinal charge density (middle) and from that the emitted spectrum (bottom). For better visibility of the sub-structures, the average phase space is subtracted from all time steps. The first column shows the subtracted time-average phase space (first line), time-average charge density profile (second line), and average emitted radiation spectrum (third line).

Note that the spectrum of the average profile is different to the time-average spectrum, shown in the bottom line. In particular, the average profile does not feature any trace of the sub-structures, so its spectrum does not reach the same high frequencies. The three spectra have more or less power than the average, dependent on the individual bunch profile. To account for that and nevertheless present the differences over a wide range, a two sided logarithmic scale is used where differences lower than $1 \times 10^{-18} \text{ W/Hz}$ have been treated as the zero value.

7.6 Summary and Outlook

In fifteen years, more electricity will be sold for automobiles than for light.

— Thomas Alva Edison, 1910

A single-shot four-channel spectrometer prototype, which continuously streams 500 million spectra per second was set up, and first experiments proving the great potential were done. The optical set-up consists of three beam splitters and four individual detectors, which are simultaneously read out in a streaming mode by the KAPTURE acquisition system. This unique setup allowed to resolve single turn dynamics with a repetition rate, orders of magnitude faster than the commercial devices presented in Chapter 5. Accordingly, the micro-bunching instability was observed in four THz frequency bands, with a bunch-by-bunch and turn-by-turn resolution, and first data evaluation was done.

Many of the found features can be reproduced by simulations with the Vlasov-Fokker-Planck (VFP) solver Inovesa. VFP solvers are known to determine the MBI threshold sufficiently well. The comparison of the different diodes at the threshold region demonstrates that a simple model, considering only CSR shielded by parallel plates, does not only reproduce most statistical values, but also the bursting dynamics – at least for KARA. The coincidence at all four frequency ranges is a very good indication that the simulated phase space fits to the real bunch, especially in the regular bursting regime where a clear phase offset between the different frequency ranges could be observed in measurement and simulation. This leads to new insights of the MBI, where the missing parts of the measurements can be completed by the simulations.

Developments are under way to use integrated single-chip detector arrays [Sch17a; Sch16b; Raa16; Raa15b] based on superconducting, electric field-sensitive YBCO detectors [Raa15a] and on room-temperature Schottky detectors [170; Mai18] in combination with the next version of KAPTURE. The array detectors will not only provide more narrowband responses but additionally increase the number of channels and reduce the required setup space. The next KAPTURE version will provide eight readout channels and an improved readout path [Cas17a]. The ability to synchronize multiple KAPTURE boards in principle allows the readout of even more channels.

Moreover, synchronization with other experimental stations at KARA will additionally provide time-resolved information about the energy spread [Keh17] and the longitudinal bunch profile [135], simultaneously [Keh18b], closing the circle of observing all projections of the longitudinal phase space.

8 Heterodyne THz-Spectroscopy

Nature is pleased with simplicity

— Isaac Newton

Heterodyne detection has been an excellent tool for spectral analysis of high frequency analog signals for many decades. The basic principle is that a high frequency signal is converted to a lower frequency where it can be analyzed with outstanding signal-to-noise ratio (SNR) and resolution bandwidth (RBW). It is the basis of all modern spectrum and network analyzers. By feeding the synchrotron radiation into a waveguide with a horn antenna, the electro-magnetic wave can be transformed by a frequency mixer inside the waveguide into an analog signal, whose bandwidth is in the range of common analog signal analyzers. Thereby, the spectrum and electric field of synchrotron radiation can be analyzed by conventional RF equipment, benefiting from the SNR and especially high RBW.

First heterodyne measurements of coherent synchrotron radiation (CSR) have been done by Tammaro et al. [171] at Synchrotron SOLEIL. While they focused on the power and stability of the observed frequency comb, they also demonstrated the use as a tool for ultra-high resolution spectroscopy of samples. Furthermore they managed an increase of the resolution of the measurement from 30 MHz by FTIR to 846 kHz by their heterodyne setup. However, they did not provide theoretical background to the observed frequency comb and the influence of the filling pattern on the spectrum. The fact, that this influence exists had been shown earlier by Billinghamurst et al. [172] at the Canadian Light Source. They demonstrated that the distance between adjacent bunches can be seen in their interferometer spectrum, and they made first theoretical assumptions on how the arrangement of adjacent bunches can be used to change the spectrum. Specific frequencies could be enhanced which they attributed to "superradiance arising from bunch-to-bunch coherence in the terahertz region". They concluded that "these observations demonstrate the potential

for significant advancement in terahertz spectroscopy, particularly if a technique for tuning the frequency of the observed spectral peaks can be developed” [172].

This chapter will actually present an easy-to-use formula on how to tune and influence the enhanced frequencies by modifying the filling pattern. The theory is based on the work of S. Chattpadhyay from 1984 on the beam spectrum observed by electrical pickup devices for accelerator diagnostics [138] and extended for synchrotron radiation in the THz regime. My own heterodyne measurements support these findings and demonstrate a new method to greatly enhance the spectral resolution.

In the following, the heterodyne principle is briefly discussed first along with the signal theory of mixers following Ref. [173]. Afterwards a theory for the expected CSR spectra in single- and multi-bunch operation is derived and backed by my own experimental results. The results presented in this chapter have already been published in parts in [Ste15; Ste16a; Ste16b].

8.1 The Heterodyne Detection Principle

The heterodyne detection technique is the basis of almost all radio frequency receivers and is extensively used in spectrum analyzers. More than a hundred years ago in 1902, the patent for heterodyne detection was granted to R. A. Fessenden [174], a Canadian-born US radio engineer who also used the terms *continuous waves* and *heterodyne* for the first time. The principle of heterodyne technique relays on the fact that the multiplication of two continuous waves at frequencies f_1 and f_2 results in two superimposed output signals, one at the sum $f_1 + f_2$ and the other at the difference $f_1 - f_2$ of the two incoming waves. This enables the conversion of signals to a different frequency range:

$$\sin(2\pi f_1 t) \sin(2\pi f_2 t) = \frac{1}{2} \cos[2\pi(f_1 - f_2)] - \frac{1}{2} \cos[2\pi(f_1 + f_2)], \quad (8.1)$$

where the new frequencies are called *heterodynes*. In signal processing, usually only one of the heterodynes is wanted, and its *mirror frequency* has to be suppressed by filters. If one of the signals is a stable, single frequency (called *local oscillator (LO)*) and the other signal is a broad spectrum, the whole input spectrum is shifted by the local oscillator (LO) frequency. Two configurations are of greater interest: If the LO signal is much higher than the spectrum, an *up-conversion* is done, shifting the

spectrum to the high frequency. This is useful, if a small band signal needs to be sent with a high frequency carrier. In this thesis, a *down-conversion* configuration will be used. In this configuration, a high frequency spectrum is multiplied with a LO of a similar frequency to shift the spectrum down to a very low frequency, where it can be processed more easily. Figure 8.1 graphically summarizes the above description of a perfect down-conversion process where all unwanted frequencies are neglected. The spectral components in the *upper side band (USB)* and the *lower side band (LSB)* of the LO are converted to the same frequency and therefore overlap in the resulting spectrum. This is called *aliasing*.

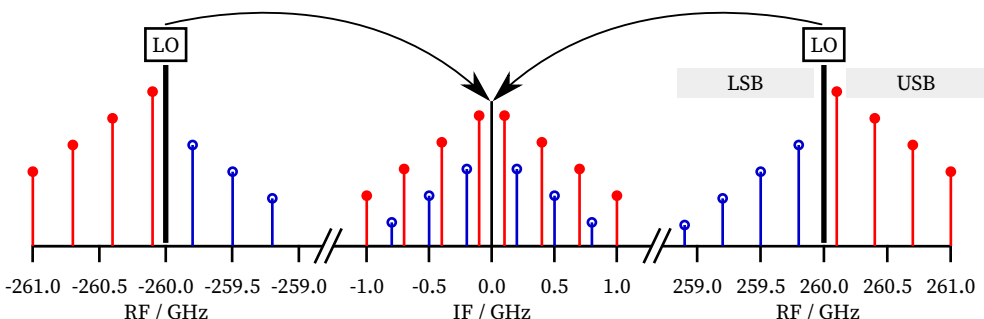


Figure 8.1: Double side band mixing: The upper side band (USB) shown in red and the lower side band (LSB) shown in blue are both being down-converted. This leads to an aliasing and overlapping of frequencies with equal distance to the local oscillator (LO). After the conversion, the high frequency signals can be analyzed easily by low-frequency methods.

An extension of the heterodyne technique has been developed during World War I. The so-called *super heterodyne* detector, often shortened to *superhet*, mixes the wanted frequency to an *intermediate frequency (IF)* instead of directly to the base band. The main advantage of the superhet principle is that the necessary filtering can be done much easier and cheaper by static filters in the IF, whereas before, complex adjustable filters at the RF were needed. In the next step, the processed IF signal is mixed further down and then measured by the base band detector. Today, with the increasing speed and quality of analog to digital converters (ADCs), the IF is often directly digitized and processed digitally. Practically all radio receivers and spectrum analyzers use the super heterodyne principle for detection.

Lucien Levy [175] in France and Edwin Howard Armstrong [176] in the US independently filed a patent for the superhet principle. Since Levy's patent is six months older, he is considered to be the inventor of the superheterodyne method, whereas

Armstrong is recognized as bringing about its commercialization through the “single tuning knob superhet receiver” [177].

The analysis of electrical signals in the base band or very low frequencies provides best performance in terms of noise and RBW. In combination with the heterodyne principle, this performance can be extended to other frequency ranges. This chapter focuses on the analysis of synchrotron radiation in the sub-THz range around 270 GHz with heterodyne detection.

8.2 RF Mixers

Heterodyning is done by a mixer, which just multiplies the two input signals in a perfect mixer circuit. However, such perfectly multiplying circuits do not yet exist for high frequencies like the THz range. Instead, one uses a nonlinearity like a diode characteristic. The nonlinear transfer function F can be expanded to a power series:

$$F(v) = \alpha_1 v + \alpha_2 v^2 + \alpha_3 v^3 + \dots \quad (8.2)$$

Given two waves with amplitudes A as input and using the trigonometric identities, the output voltage can be calculated as

$$v_{out} = F[A_1 \sin(2\pi f_1 t) + A_2 \sin(2\pi f_2 t)] \quad (8.3)$$

$$\begin{aligned} &= \alpha_1 [A_1 \sin(2\pi f_1 t) + A_2 \sin(2\pi f_2 t)] + \alpha_2 [A_1 \sin(2\pi f_1 t) + A_2 \sin(2\pi f_2 t)]^2 + \dots \\ &= \alpha_1 [A_1 \sin(2\pi f_1 t) + A_2 \sin(2\pi f_2 t)] + \alpha_2 \left(\frac{A_1^2}{2} [1 - \cos(4\pi f_1 t)] \right. \\ &\quad \left. + A_1 A_2 [1 - \cos(2\pi f_1 t - 2\pi f_2 t)] + \frac{A_2^2}{2} [1 - \cos(4\pi f_2 t)] \right) + \dots \\ &= \alpha_2 A_1 A_2 \cos[2\pi(f_1 - f_2)t] - \alpha_2 A_1 A_2 \cos[2\pi(f_1 + f_2)t] + \dots, \end{aligned} \quad (8.4)$$

where Eq. (8.4) only shows the difference and sum contributions. The output signal v_{out} consists of the sum and delta of the input frequencies along with a bunch of additional components like multiples (*harmonics*) of the original frequencies ($2f_1, 2f_2, 3f_1, 3f_2, \dots$) and *intermodulation* products ($Mf_1 + Nf_2$), where $M, N \in \mathbb{N}$. If these unwanted frequencies can be filtered out before the output, only the desired heterodyne is left. But there is a negative effect of suppression. The unwanted frequencies carry some

signal power, too, which gets lost, leading to a reduced output power and therefore a reduced SNR.

A mixer in a down-converting configuration typically has three ports: The first as the *RF-input*, the second port is connected to a stable *local oscillator (LO)* and the third port is the IF, the difference between the RF signal and the LO. All other unwanted mixer output products are suppressed as much as possible. The output power depends on the amplitudes of both inputs $A_1 A_2$ and the power lost in unwanted and filtered frequencies. The ratio between the incoming power and the output power is called *conversion loss* and is a quality characteristic of the mixer device. At a certain LO power level, the mixer has the least conversion loss which is considered as the working point. With the constant LO power set for the working point, the conversion loss in dB is a function of the RF input power and the IF output power at their corresponding frequencies:

$$K(f_{\text{RF}}) = -10 \log_{10} \frac{P_{\text{RF}}(f_{\text{RF}})}{P_{\text{IF}}(f_{\text{IF}})}. \quad (8.5)$$

Even a perfect multiplying mixer has a conversion loss of at least 3 dB which is converted to the mirror frequency and is usually removed. Due to technical difficulties, these conversion loss value increases drastically at higher RF frequencies, and complex methods are needed to compensate for that. A selection of commercially available mixers, sold as *spectrum analyzer extender modules* for the WR3.4 waveguide range is listed in Tab. 8.1.

Table 8.1: Selection of commercially available spectrum analyzer extension modules operating between 220 GHz to 325 GHz

Type	Company	Conversion loss	IF bandwidth	Source
M03HWD	OML	60 dB	0.3 GHz	[178]
WHMB-03	Farran Technology	45 dB	1 GHz	[179]
FS-Z325	Radiometer Physics	40 dB	1 GHz	[180]
HM-325	Radiometer Physics	30 dB	3.2 GHz	[181]
WR3.4SAX	Virginia Diodes	14 dB	20 GHz	[182]

This waveguide standard, which has a range of 220 GHz to 325 GHz, has been chosen because the measurements in Chapter 5 showed that the maximum CSR power at the

IR2 beamline is measured above 200 GHz. To be able to observe the radiation emitted by sub-structures, even higher frequencies are needed. The measurements described in this chapter have been carried out with a special spectrum analyzer extension module from Virginia Diodes inc. that has, according to the data sheet, an average conversion loss of only 14 dB [182].

8.3 Frequency Comb by Repeated Emission

Due to the high resolution of the heterodyne measurement setup, all repeating events of the radiation can be resolved. Therefore, a much more sophisticated investigation of the spectrum of synchrotron radiation is needed than has been done in Chapter 3 where only broadband spectra have been considered as they would be observed by a detector moving with the charge. In a storage ring, with a static detector behind a finite aperture, only a short light pulse is detected, but at each turn. Considering, that time domain and frequency domain is equivalent, all signatures of the radiation which occurred during the observation time will be visible. All recurring events, therefore, lead to peaks at the corresponding frequency. This section focuses on the observed spectrum of a single bunch with a very narrowbandwidth. A multi-bunch environment will be discussed in a later section.

Already in 1912, G.A. Schott found in his analysis of the radiation of a single electron circulating an atom, that the observed radiation is discrete and consists of multiples of the revolution frequency [1]. Today, the spectrum of an infinite pulse train with equidistant spacing and a stable phase relation between the pulses is called *frequency comb*, as it looks like a comb in the frequency domain. This has gained much attention when the Nobel price of physics 2005 was awarded to Theodor Hänsch and John Hall “for their contributions to the development of laser-based precision spectroscopy, including the optical frequency comb technique” [183]. Today’s applications for laser based frequency combs comprise atomic clocks, frequency metrology, high resolution spectroscopy and many more. However, the frequency comb emitted by a synchrotron radiation source has not gained much attention in the past. Moreover, synchrotron radiation text books stated [29, p. 807]:

Generally, a real synchrotron radiation beam from say a storage ring will not display this harmonic structure. The distance between the harmonics is extremely small compared to the extracted photon frequencies in the

VUV and X-ray regime while the line width is finite due to the energy spread in a beam of many particles and the spectrum therefore becomes continuous.

In the THz regime, the ratio between observation and revolution frequency is much less and due to CSR, the intensity is comparably large. This chapter will show, that the frequency comb of THz CSR can indeed be observed and its discrete harmonics can well be separated.

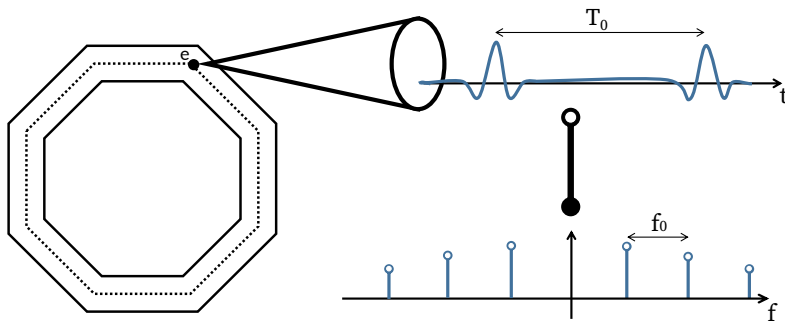


Figure 8.2: A single, circulating electron emits a short light pulse every revolution. The Fourier transformation leads to a frequency comb.

Figure 8.2 sketches a circulating electron emitting a short light pulse every revolution. With the approximation that the signal of every revolution in a storage ring is the same, the time domain signal can be written as the convolution of an infinite train of Dirac impulses, separated by the revolution time of the storage ring T_0 , and the single pulse signal $s_p(t)$:

$$s(t) = \text{III}_{T_0}(t) * s_p(t) \quad (8.6)$$

where $\text{III}_{T_0}(t)$ denotes the Shah distribution [28, pp. 81–83], an infinite train of Dirac delta impulses separated by T_0 :

$$\text{III}_{T_0}(t) = \sum_{n=-\infty}^{\infty} \delta(t - nT_0) \quad (8.7)$$

and $*$ denotes the convolution (see Eq. (2.33)). This approximation implies a single pulse signal $s_p(t)$, identical in phase and amplitude every turn. This is true for a single-cycle CSR pulse of a constant bunch profile. In the following, a constant bunch profile as the origin of $s_p(t)$ will be assumed, and disturbances modelled as an addi-

tional modulation. The transformation into the frequency domain transforms the convolution into a multiplication [28, pp. 115–119], therefore the spectrum reads¹

$$S(f) = \frac{1}{T_0} \text{III}_{f_0}(f) \times S_p(f). \quad (8.8)$$

In the time domain the convolution with the Shah distribution leads to a repeating of the single bunch signal every revolution after a period T_0 , while in the frequency domain a multiplication with the Shah distribution leads to a discretization at multiples of $1/T_0 = f_0$. In the following, this behavior will be illustrated by measurements.

8.4 Heterodyne Measurement Setup

The optical setup is kept rather simple. The synchrotron radiation is coupled out at the diagnostic port and focused by an off-axis paraboloid mirror. A silicon beam splitter divides the beam into two parts while maintaining the polarization.

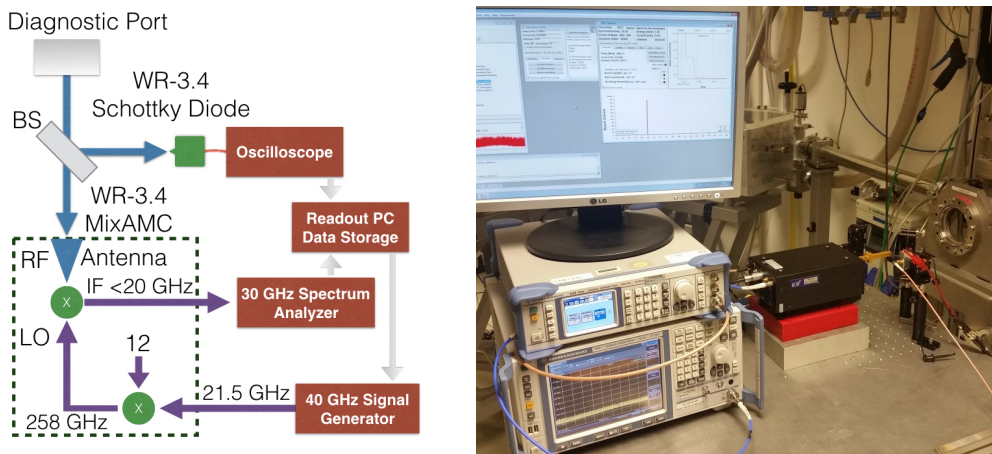


Figure 8.3: Setup of the measurement. The synchrotron light coupled out at the diagnostic port of the IR1 beamline is split by a silicon beam splitter (BS) onto the WR3.4 Schottky diode and to the mixer. The spectrum analyzer measuring the mixer's output, and the oscilloscope capturing the Schottky signal, are read out by a computer which saves and processes the measured data.

¹ See Chapter 1.2 for the convention of the Fourier transform. Uppercase letters refer to the frequency domain and lowercase letters to the time domain.

Then, one beam is being fed by a horn antenna into a waveguide which is the RF input of the mixer. The LO is generated by a signal generator at ≈ 21.5 GHz and then internally multiplied by 12 to 258 GHz. After the mixing process the output signal with an IF frequency of up to 20 GHz is coupled out by a coaxial cable and detected by a 30 GHz spectrum analyzer (cf. App. B.5). The intrinsic conversion loss of around 14 dB is compensated by an IF amplifier resulting in about 2 dB total conversion loss that is not corrected in the following measurements, since absolute power measurements are not needed. However, if the device were used as an absolute power meter, a calibration could be done. By setting the spectrum analyzer's video bandwidth (VBW) to a few Hertz, the bursting instabilities are averaged, leading to a signal being stable in frequency and amplitude.

For comparison, the other beam is measured with a WR3.4 zero bias Schottky detector (see chapter 4.1) sensitive from 220 GHz to 330 GHz with an average responsivity of 2000 V/W. The signal from the Schottky detector is amplified and then read out by an Agilent oscilloscope in peak detect mode (cf. App. B.4). In this mode only the highest and lowest sampling point in a given time interval is saved. As the time interval can only be chosen in given steps, a value of $2.5\ \mu s$ is used so that the maximum ADC count for 6-7 revolutions², is saved. With this setting it's possible to record and read out more than one second of data. Then, the bursts of radiation can be measured and a FFT of the changing intensity reveals characteristic frequencies for given bunch currents (cf. Chapter 6.2).

Both measurement devices, the spectrum analyzer and the oscilloscope, are repeatedly read out by a computer. The setup is sketched in Fig 8.3 together with a photo of the measurement. Figure 8.4 shows a high resolution measurement of a single frequency peak. The measured 3 dB bandwidth of the 96 234th revolution frequency harmonic is 1.1 kHz. This width of the harmonic is due to the phase noise of the system. During the mixing process, the noise of both inputs, the RF and the LO, are overlapped at the output. Both contributions will be shortly investigated in the following.

The phase noise of the LO consists of the initial phase noise of the mixer's frequency generator and the noise added in the up-conversion process. The phase noise added by the RF input is more complicated as it also involves beam physics. It can be seen as the arrival time deviation of the incoming light pulses. In the KARA acceleration

² one revolution in the KARA storage ring is $\approx 386\ ns$

system, a master oscillator creates the 500 MHz RF used for acceleration. This signal is distributed to two Klystrons which amplify the signal to provide the needed RF voltage. It is then fed via waveguides into four cavities which are installed in the storage ring. The deviation of phase and amplitude of each cavity is transferred to the electron beam and consequently to the emitted radiation. Furthermore, the single electrons in phase space change their relative position and lead to different emitted pulse shapes every turn. The combination of these effects is measured in Fig. 8.4.

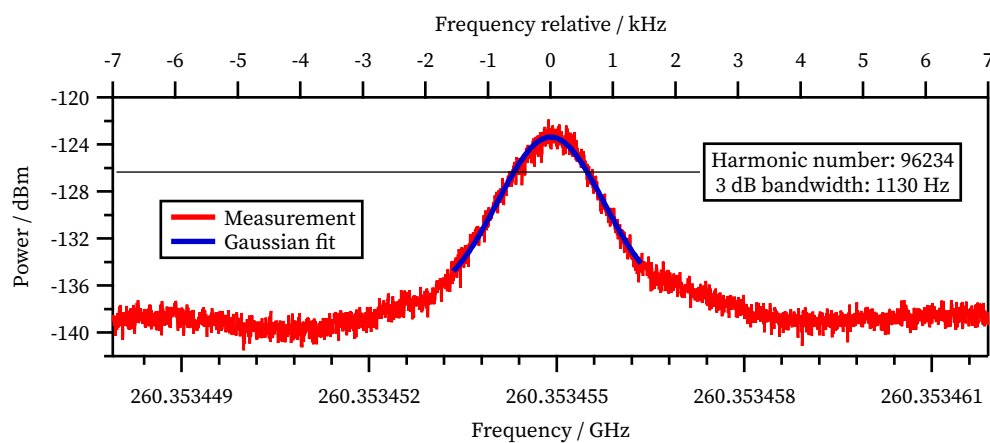


Figure 8.4: High resolution measurement of a single frequency peak. The LO was set to 258 GHz and the measurement was taken at an IF frequency of 2 GHz with a resolution bandwidth (RBW) of 5 Hz and a video bandwidth (VBW) of 1 Hz. The horizontal black line is located at 3 dB below the maximum.

The displayed average noise level is -140 dBm at 5 Hz bandwidth. This corresponds to -147 dBm at 1 Hz, a factor of 2 off from the -150 dBm/Hz specified in the data sheet of the mixer. A measurement with a broader frequency range is shown in Fig. 8.5. It reveals the spectral lines at multiples of the revolution frequency. Due to the double side band mixing, aliased frequencies are observed. They are grayed out in the graph for now, but discussed in more detail in Chapter 8.7.4. Each of the lines consists of additional sidebands due to frequency modulation by the synchrotron motion that will be discussed in the following.

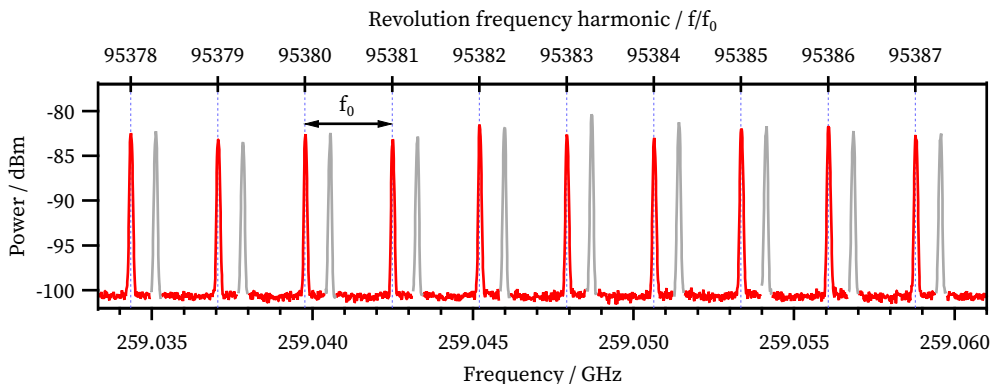


Figure 8.5: Direct spectral measurement of coherent synchrotron radiation by heterodyne spectroscopy. The harmonics of the revolution frequency are down-converted with an 258 GHz LO frequency. The aliased signals from the lower side band are shaded in gray. A modified version was already published in [Ste16b] (©2016 American Physical Society) and has also been used in a recent text book on synchrotron radiation [184, Fig. 4, p. 8].

8.5 Direct Observation of Synchrotron Motion Sidebands in Coherent Synchrotron Radiation

Due to phase focusing from the RF, the electrons are oscillating longitudinally around their reference position (cf. Chapter 1.5.3). This motion can be decomposed into two oscillations: A coherent synchrotron oscillation of the center of mass of the electron bunch and an incoherent synchrotron oscillation of the individual electrons rotating inside the bunch around the center of mass. While the coherent synchrotron oscillation can be excited or damped down by a feedback system, the incoherent synchrotron oscillation, resulting from the stochastically emission of radiation, can not directly be influenced.

Similar to CSR, the coherent signal is orders of magnitude more intense than the incoherent. For a stable electron bunch, with sufficient number of charges, only coherent signals will be detected and the energy spread of the electrons will be hidden. However, it has been shown that for bunched proton beams, this *Schottky noise* could be measured if the coherent signals are sufficiently suppressed [185]. Although this was a necessary step to the invention of stochastic cooling of heavy particles by Simon van der Meer which led to the Nobel prize of physics in 1984 [186], it has not yet resulted in an application in electron storage rings.

The coherent synchrotron motion, where the bunch center of mass is moving, results in an arrival time offset of the detected light pulse. Assuming a sinusoidal oscillation, the bunch arrival time is modulated with frequency f_s and amplitude τ_s

$$s(t) = \sum_{p=-\infty}^{\infty} \delta(t - pT_0 - \tau_s \cos(2\pi f_s t)) * s_p(t), \quad (8.9)$$

where the time in the cosine argument can be substituted by $t = pT_0$, because the amplitude of the synchrotron oscillation is much smaller than the revolution time. The FT is [138; 139], [187, p. 264ff]

$$S(f) = \int_{-\infty}^{\infty} \left[\sum_{p=-\infty}^{\infty} \delta(t - pT_0 - \tau_s \cos(2\pi f_s pT_0)) * s_p(t) \right] e^{-j2\pi ft} dt \quad (8.10)$$

$$= \sum_{p=-\infty}^{\infty} e^{-j2\pi f[pT_0 + t - \tau_s \cos(2\pi f_s pT_0)]} S_p(f) \quad (8.11)$$

$$= f_0 S_p(f) \sum_{p,m=-\infty}^{\infty} j^{-m} J_m(p2\pi f_0 \tau_s) \delta(2\pi \Omega(f)), \quad (8.12)$$

where the fact is used that [188, pp. 8.511, 4]

$$e^{-jx \cos(\theta)} = \sum_m j^{-m} J_m(x) e^{-jm\theta}, \quad (8.13)$$

where J_m are the Bessel functions of m-th order. $\Omega(f) = f - pf_0 + mf_s$ leads to the revolution harmonics known from above. Additionally, every harmonic has satellites spaced by f_s , where the m-th satellite has a spectral amplitude corresponding to the Bessel function of order m: $J_m(p2\pi f_0 \tau_s)$. The Bessel functions up to an order of 5 are shown in the left panel of Fig. 8.6.

By having no coherent synchrotron oscillation ($\tau_s = 0$), for example by damping the oscillation by a bunch-by-bunch feedback (BBB) system, the satellites vanish and only the main harmonic is left. Note that the summed power of all synchrotron sidebands and the main harmonic at a given revolution frequency harmonic is constant [188, pp. 8.512, 1]

$$\sum_{m=-\infty}^{\infty} J_m(p\omega_0 \tau_s) = 1. \quad (8.14)$$

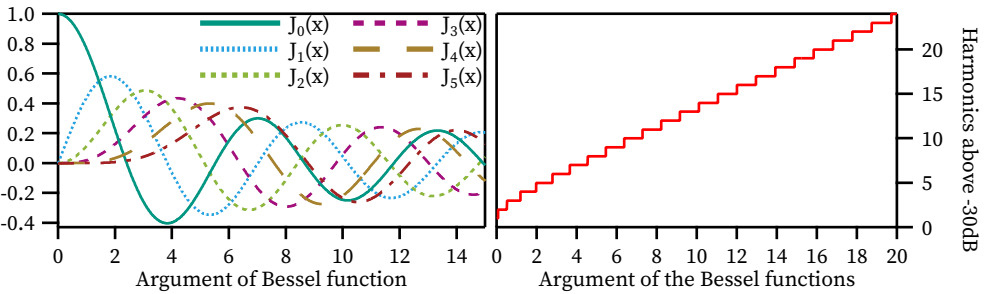


Figure 8.6: Bessel functions up to order 5 (left). The higher the argument, the more sidebands become visible. The argument where the m -th f_s -harmonic is below -30 dB of the total power is shown in the right panel.

Therefore, the more power in the sidebands, the less is in the main harmonic, but the summed power is constant. The higher the argument, the more significant sidebands show up over which the power is distributed. Note that for an argument of 2.4048, the first zero of the Bessel function of 0-th order, the main harmonic vanishes and all power is in the sidebands. The effect of the argument of the Bessel functions in Eq. (8.10) on the number of observable sidebands is depicted in Fig. 8.6 in the right panel. The number of the harmonic, where the power is below a fraction of 1000 (-30 dB) of the total power of the revolution frequency harmonic, increases almost linearly with the Bessel function's argument. Observation in the sub-THz range, with undamped synchrotron oscillations in the range of some picoseconds, will lead to input values of the Bessel functions in the order of 1 to 10 in contrast to measurements by pickup devices at several gigahertz that lead to arguments of two magnitudes less. Therefore, many more sidebands can be observed in the CSR measurements compared to conventional pickup devices.

For measurements that can't resolve the synchrotron frequency, this effectively leads to a broadening of the spectral line of the revolution harmonic. At very high frequencies or high amplitudes of the oscillation, the number of synchrotron sidebands is increased so much, that the sidebands of neighboring main harmonics can be overlapping. Figure 8.7 shows the influence of the argument of the Bessel functions. The magnitude squared of Eq. (8.10) is shown for three different arguments, assuming a constant oscillation amplitude of 1 ps. Around 80 GHz this leads to an argument of 0.5 and at 382 GHz to 2.4048 the first zero of the Bessel function of 0-th order. However, as long as the detector resolution is broader than the synchrotron sidebands, the total measured power will be the same compared to the case without synchrotron

oscillation. This becomes more evident in a time domain picture where, on average, the same number of identical pulses pass the detector, no matter how big or how fast the synchrotron oscillations are.

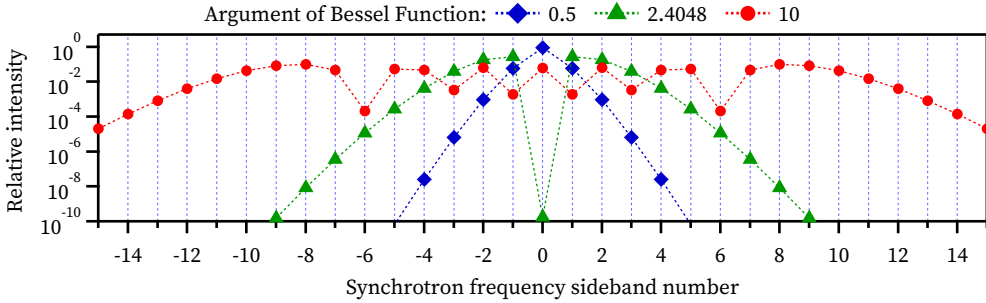


Figure 8.7: Calculated power of the synchrotron oscillation sidebands for a constant oscillation amplitude of 1 ps (0.3 mm). For higher frequencies the intensity and thus visibility of the harmonics increases. Only integer sidebands exist, the dotted lines are to guide the eye.

However, the synchrotron frequency amplitude is not constant, especially during the micro-bunching instability. Due to the outbursts of radiation, which lead to an additional energy loss, the synchronous phase changes (see Chapter 1.5.3), and the synchrotron oscillation amplitude increases. This oscillation is damped due to radiation damping, but overall, the amplitude is not constant and neither is the argument of the Bessel function in Eq. (8.10).

To illustrate this, Fig 8.8 shows the arrival time of a bunch during the micro-bunching instability. It was determined by an EOSD measurement [30]. For the histogram of the arrival time, 100 000 consecutive measurements were analyzed, while a measurement has been taken every 3rd turn. With a Hilbert transformation, the amplitude of the oscillation has been determined and also histogrammed. The frequency of the synchrotron oscillation is stable, while its amplitude changes. Also the zero-crossing of the oscillation, which can be seen as the synchronous phase, changes due to the variation in emitted CSR power. However, the histogram of the 100 000 arrival times shows a Gaussian distribution around an average arrival time. If the synchrotron motion amplitude were constant, the arrival time would oscillate harmonically and one would assume a rectangular histogram with an increase at the turning points. Consequently, the extracted f_s amplitudes vary between 0 ps to 3.3 ps with a maximum around 1.1 ps. Invesa simulations can reproduce this by adding noise to the RF frequency and amplitude [Sch18b].

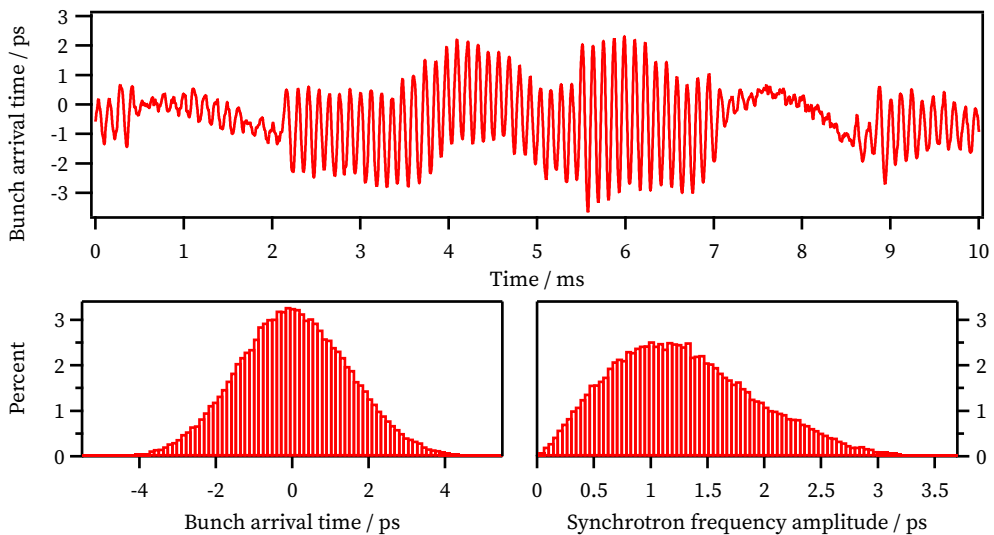


Figure 8.8: Measurement of the bunch arrival time with EOSD (top), histograms of the arrival time (bottom left) and the oscillation amplitude (bottom right). The effective arrival time looks Gaussian around an average phase. The amplitude of the synchrotron motion varies a lot and can not be assumed to be constant. Therefore, the averaged narrowband spectrum (Fig. 8.9) shows an average of all amplitudes. (Data taken by Nicole Hiller [30], arrival times extracted by Stefan Funkner)

At 270 GHz, an oscillation amplitude of ≈ 0.6 ps would lead to an argument of the Bessel function of 1, while an amplitude of ≈ 5 ps already leads to an argument over 8. The corresponding sidebands change accordingly to the synchrotron motion amplitude. It is important to note that an averaged measurement, like presented here, will not measure the spectrum of an average oscillation amplitude, but rather an average of all the different spectra produced by the varying amplitudes.

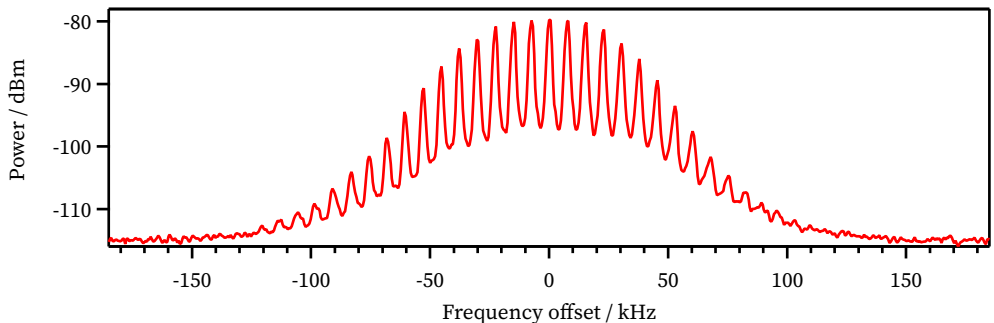


Figure 8.9: Averaged measurement of synchrotron frequency (7.5 kHz) sidebands at the 100 418th revolution frequency harmonic. The signal between the individual peaks does not go down to the baseline because the RBW was set to 1 kHz. To smoothen the data, a VBW of 1 Hz was used.

A measurement of the synchrotron sidebands at the 100 418th revolution frequency harmonic is shown in Fig. 8.9. At the averaged spectrum, approximately 10 harmonics are above noise level with a 30 dB bandwidth of around 150 kHz. Indeed, it has to be taken into account, that especially during the bursting operation the coherent synchrotron oscillation amplitude is not constant; the amplitudes of the sidebands vary but have been averaged by the 1 Hz VBW filter of the spectrum analyzer. Therefore, the sideband power levels have an almost Gaussian shape and not the one that would be expected for a constant amplitude.

8.6 Comparison between Diode and Mixer Power

By tracking the amplitude of the discrete revolution frequency harmonics, the power of the coherent synchrotron radiation can be compared to the signal observed at the same time with the Schottky diode. A spectrogram (see Chapter 6.2) recorded with the Schottky diode is plotted in Fig. 8.10. In this measurement, the RF voltage is 1400 kV and the momentum compaction factor $\alpha_c = 6.1 \times 10^{-4}$. The resulting synchrotron frequency, zero current bunch length and bursting threshold is 12.75 kHz, 3.8 ps and 0.23 mA, respectively. The MBI threshold and the transition to the sawtooth-regime is marked.

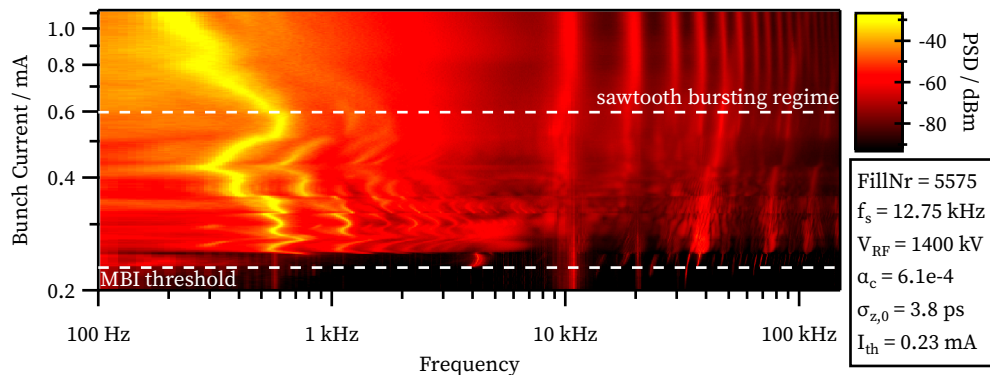


Figure 8.10: Spectrogram measured with a SBD detector sensitive between 220 GHz to 330 GHz simultaneously to the mixer. The horizontal dashed lines denote the bursting threshold and the transition to the sawtooth bursting regime at high currents.

The measured average pulse amplitude of the SBD detector together with the power measured with the mixer is shown in Fig 8.11. A resolution bandwidth (RBW) of 10 kHz

was chosen, in order to be able to scan a broad range in a reasonable amount of time. To increase the statistics for an average detected power, the frequency peaks in a 1 GHz broadband have been analyzed. First, a background spectrum was taken with a closed beamline absorber. After subtracting the background power, the power of each peak was integrated and divided by the RBW. Afterwards, the power is normalized by the 738 harmonics of LSB and USB that lie in the observed range to get the average power per harmonic. The left and right axis of Fig. 8.11 both span two orders of magnitude exactly. While in the linear regime, the measured diode pulse amplitude should be proportional to the optical input power. The discrepancies between the mixer and diode signals can be explained by the different observed bandwidths.

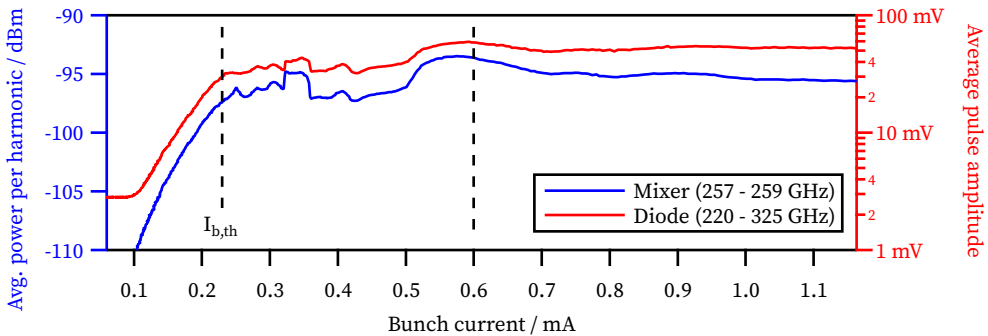


Figure 8.11: Extracted power of an averaged harmonic measured with the mixer in a 2 GHz wide band and the average pulse amplitude measured with the SBD detector. Both scales span two orders of magnitude and while the mixer measurements can directly measure the incoming power, the SBD output voltage is proportional to the incoming power in its linear regime. The vertical dashed lines denote changes in the bursting regime. The lower one belongs to the bursting threshold ($I_{b,\text{th}}$), the upper one to the beginning of the sawtooth bursting. Both are also visible in the spectrogram in Fig. 8.10.

In the average power, the changes in bursting behavior can be seen. Below 1 mA bunch current, the average pulse amplitude of the SBD is dominated by the oscilloscope's noise which in peak detect mode does not recognize peaks below 2 mV. Since the SNR of the detector is still sufficient, an additional amplifier could be used to further observe that range. However, that would lead to a saturation at the high bunch currents. This demonstrates the advantage of the heterodyne measurement in terms of dynamic range.

Up to bursting threshold at $I_{b,\text{th}} = 0.23$ mA, the sub-structures are not significant and the bunch shape is determined by the current-dependent potential-well distortion (cf. Chapter 2.2). The detected power increases according to the bunch current. Above

the threshold, the emitted power is dominated by the size and repetition rate of the sub-structures. Changes in the bursting regime can be seen in the spectrogram as well as the average power. The behavior at high currents is characteristic in the sawtooth bursting regime. With increased current, the repetition rate of the bursts decreases, which leads to almost constant average emitted power observed at 270 GHz between the current range of 0.6 mA to 1.2 mA.

Assuming that the spectral power is constant in the frequency range of the diode and the bandwidth is 220 GHz to 325 GHz, the proportionality factor between average pulse amplitude and input power is around 440. However, this is only a rough estimation of the sensitivity, as the diodes pulse response and the RF coupling losses are not taken into account. Aside from that, the approximation with constant power in the waveguide range is not valid, as the power easily changes by an order of magnitude in that range (cf. measurements in Chapter 5.2).

8.7 Multi Bunch Filling Patterns

Considering the fact that the storage ring is usually operated in a multi-bunch mode, Eqn. (8.6) can be expanded by a convolution of the filling pattern signal $s_F(t)$ [Ste16b]

$$s(t) = \text{III}_{T_0}(t) * s_F(t) * s_p(t). \quad (8.15)$$

The filling pattern signal consists of Dirac delta peaks at the position kT_{RF} of the k -th bunch and area V_k corresponding to the bunch charge

$$s_F(t) = \sum_{k=1}^h V_k \delta(t - kT_{\text{RF}}), \quad (8.16)$$

where h denotes the harmonic number, and is the number of *buckets* ($h = 184$ at KARA) and therefore the maximum number of bunches. As until now, the individual form factors of the bunches in a multi-bunch environment could not be measured; the approximation that all bunches have the same spectrum but individual intensities is used. However, individual form factors of the bunches could be added to Eq. (8.16), if necessary.

8.7.1 Bunch Trains

To investigate the dependence of bunch trains on the spectrum, T_{RF} will be assumed to be constant in this section, which is valid for an accelerator with a fixed accelerating frequency. However, the total number of bunches h and therefore the circumference of the accelerator is varied in this example.

A sketch of a repetitive filling pattern signal is shown in Fig. 8.12. A train with consecutive bunches, separated by T_{RF} , is followed by three empty buckets. After the revolution period time $T_0 = 1/f_0 = hT_{RF}$, the pattern repeats. The signal consists of Dirac delta pulses at the position of the bunches which are scaled by the individual bunch height. One has to keep in mind that the filling pattern signal comprises only one revolution. Only the convolution with the Dirac comb of the revolution signal leads to the infinite repeating which holds the approximation that each turn is identical. This is true if there is no drift and all repeating events like synchrotron oscillations are slower than the measurement can resolve.

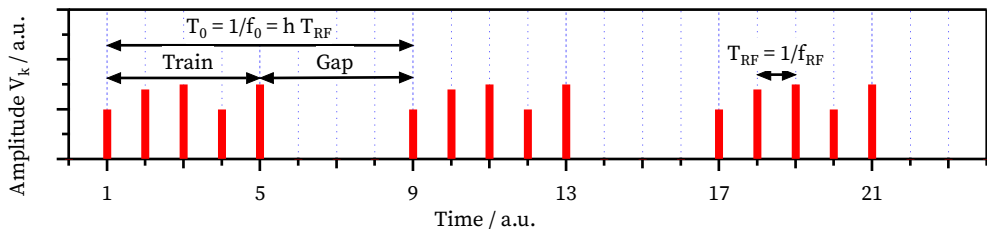


Figure 8.12: Scheme of a repetitive filling pattern signal $s_F(t)$ which repeats after the period time $T_0 = 1/f_0 = hT_{RF}$. T_{RF} denotes the time between consecutive bunches with individual height V_k and h the total number of buckets. Here, the signal consists of a train of 5 bunches and a gap of 3 buckets. The filling pattern signal is the sum of Dirac delta peaks where the height in the graph represents the integral of the infinitesimal short pulse. A modified version was already published in [Ste16b] (©2016 American Physical Society).

As with the single bunch case above, the Fourier transformation reads

$$S(f) = \frac{1}{T_0} \text{III}_{f_0}(f) \times \text{DFT}\{s_F(t), f\} \times S_p(f), \quad (8.17)$$

where the finite sum of the filling pattern signal leads to a discrete Fourier transformation (DFT)

$$\text{DFT}\{s_F(t), f\} \equiv \sum_{k=1}^h V_k e^{-j2\pi fkT_{RF}}. \quad (8.18)$$

Due to the properties of the DFT, the spectrum of the filling pattern signal is continuous and repeats indefinitely with a period length of $f_{\text{RF}} = 1/T_{\text{RF}}$. The complete signal spectrum, however, comprises the DFT multiplied by the Shah-distribution in frequency domain $\text{III}_{f_0}(f)$ and the spectrum of the single pulse signal $S_p(f)$. Note that the resulting power spectrum of the radiation is the magnitude squared of Eq. (8.17).

The influences of the filling pattern on the beam spectrum can be seen by analyzing Eq. (8.18), but keeping in mind that the complete spectrum is sampled at the revolution frequency harmonics and scaled by the single pulse spectrum.

In Fig. 8.13 two scenarios are shown with a train of 5 consecutive pulses. The solid line results from 5 pulses with the same height. In this case the magnitude squared of the DFT has zeroes at multiples of the RF frequency $f_{\text{RF}} = T_{\text{RF}}^{-1}$ divided by the number of consecutive pulses. In the complete spectrum (see Eq. (8.17)), the DFT is sampled only at the discrete harmonics of $f_0 = f_{\text{RF}}/h$. For a total of 8 buckets ($h = 8$), where a gap of 3 follows 5 pulses (positions as in Fig. 8.12, also shown in the inlet), all harmonics have significant power according to the height of the DFT. On the other hand, the special case of $h = 5$ (without gap) leads to discrete harmonics at $f_0 = f_{\text{RF}}/5$, corresponding to the zeros of the DFT. Consequently only harmonics of f_{RF} , the pulse repetition frequency, would be left. This must be the case, as a filling pattern with 5 identical pulses repeating without gap, can, in time domain, not be distinguished from a filling pattern with only a single repeating pulse, and has therefore only contributions to the pulse repetition frequency.

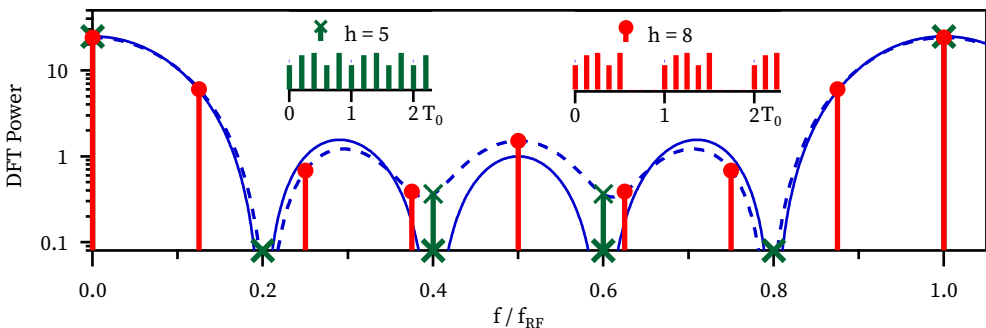


Figure 8.13: $|\text{DFT}|^2$ of five consecutive pulses with distance T_{RF} . According to eq. (8.17), the DFT is sampled at discrete multiples of $f_0 = f_{\text{RF}}/h$. Exemplary two cases are shown: Without a gap ($h = 5$) the DFT is sampled at multiples of $f_0 = f_{\text{RF}}/5$ (green crosses). If a gap of three slots is added ($h = 8$) it is sampled at multiples of $f_0 = f_{\text{RF}}/8$ (red dots). Solid line: all five pulses have the same height; dotted line: filling pattern as in Fig 8.12 and the inset. Note how the uneven filling pattern leads to a sizable contribution at the zeroes of the even filling pattern. Published in [Ste16b] (©2016 American Physical Society).

The case is different if the pulse height differs. Then, a clear repetition frequency can be seen in the time domain, too. The dotted line in Fig. 8.13 depicts the $|DFT|^2$ if the height of the pulses is the one shown in the inlet (or bigger in Fig. 8.12). Then more harmonics of f_0 have significant value while the intensity at the f_{RF} -harmonics decreases accordingly (not visible on log scale).

The trains in a storage ring are usually much longer. At KARA, a train with approximately 33 bunches is injected with every shot from the pre-accelerators, the bunches in the front and back having significantly less charge due to the injection process. Figure 8.14 presents a scenario with a train of 20 bunches, each with the same current. The DFT has the same shape as above: A sinc function with zeroes at $h/20$. Considering that at KARA $h = 184$, many frequency bins showing the sinc envelope become visible.

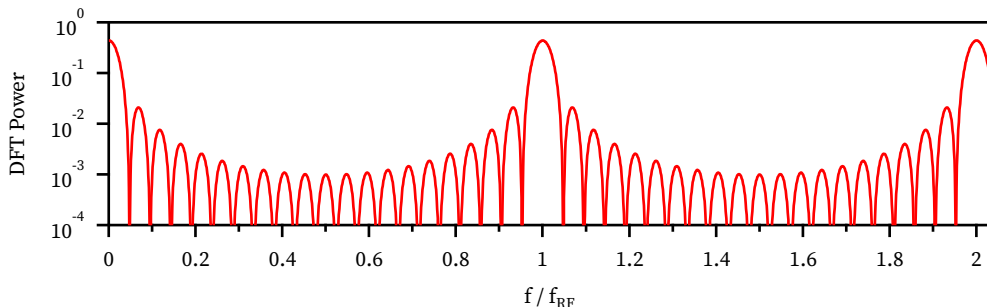


Figure 8.14: Discrete Fourier transformation of 20 consecutive pulses with the same intensity leads to a repeated sinc-function with zero crossings at every $h/20$ harmonic.

Figure 8.15 shows a measurement of the discrete harmonics of the revolution frequency around the 94 944th revolution frequency bin, which is exactly the 516th harmonic of the RF frequency. The aliased signals from the lower sideband are almost below noise level and barely visible. In this case, the storage ring has been filled with one train. Then the first bunches were kicked out, leaving 20 consecutive bunches in the filling pattern, which is shown in the inlet. The blue dots have been calculated according to Eq. (8.17). The single bunch spectrum was assumed to be constant in a limited frequency range.

The calculated intensities also consider the individual heights of the bunches, compared to Fig. 8.14 where equal bunch currents were assumed. However, neither beam-loading nor particle motion effects have been considered, as they were expected to be

negligible at 1.3 GeV beam energy and bunch currents as low as 250 μA . The measured spectrum, the calculated position and amplitude show a good correlation, bearing in mind the approximations used.

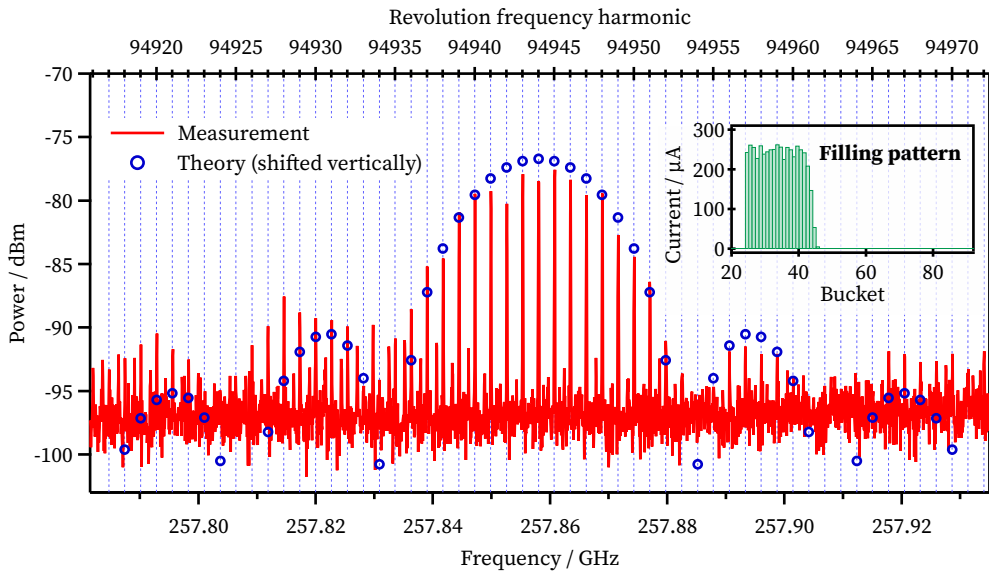


Figure 8.15: Measured and simulated synchrotron radiation spectrum around the 94944th revolution frequency harmonic (516th RF-harmonic) of KARA. The filling pattern consists of 20 consecutive filled bunches (inlet). The calculated intensities have been normalized to the maximum of the measurement. The measured values match the predicted positions and amplitudes of the frequency comb. Visible peaks between revolution frequency harmonics are aliased artefacts from the double sideband mixing process.

8.7.2 Bunch Current Variations

Instabilities lead to differences in the pulse heights in a train. To gain more statistics, the total number of pulses in this section is assumed to be $h = 1000$. Figure 8.16 shows the effect of a uniform filling pattern where all of the 1000 buckets are filled, but with noise added to the intensity. Since there is no gap, only the multiples of the RF frequency would be supposed to show up. However, by adding noise to the pulse intensity, noise is added to the spectrum, too. Again, the intensity can be calculated with Eq. (8.18). Having a RMS noise of 0.1 units on V_k summed over 1000 bunches gives a magnitude squared (power) of 100^2 . Distributed into 1000 frequency harmonics leads to an average “noise floor” of 10 counts that can be seen in the figure.

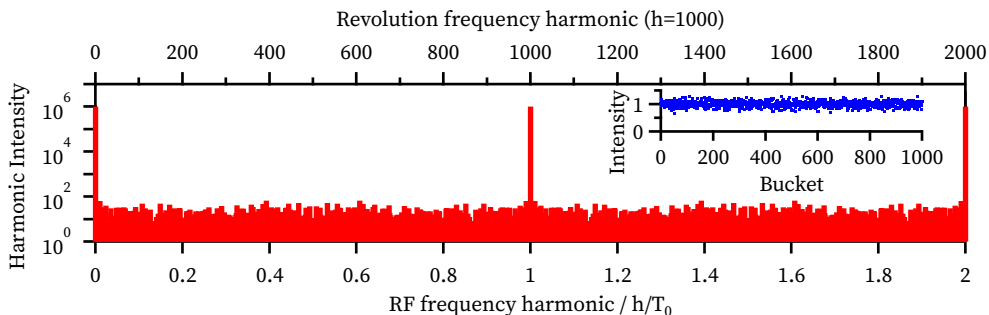


Figure 8.16: Simulation of a spectrum of 1000 buckets that are filled with an intensity of 1 plus Gaussian noise with a mean value of 0.2. The filling pattern is shown in the inlet. Only the sampled revolution frequency harmonic intensities are shown as bars. For a flat homogeneous filling, only the frequency contributions at multiples of the RF frequency f_{RF} would be expected. Due to the intensity noise, contributions at all f_0 harmonics are seen.

A typical multi-bunch fill of a synchrotron light source consists of several trains with consecutively filled bunches that are separated by a gap. Often a bigger gap in the ring is used to damp down instabilities that sum up. The simulation in Fig. 8.17 shows such a filling pattern with additional noise on the bunch intensities.

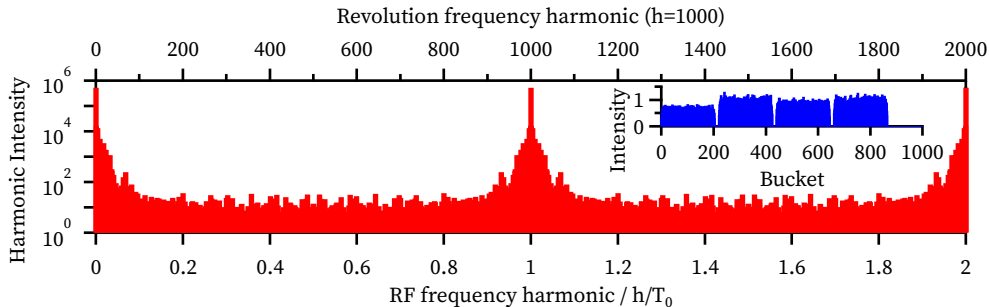


Figure 8.17: Simulation of an uneven multi-bunch fill in a storage ring with trains containing bunches of almost the same intensity and a gap in between. The top right inlay shows the bunch intensity. The overall shape like the gap between the trains and the length thereof leads to power leakage from the RF harmonic to nearby revolution frequency harmonics. Whereas the noise on the individual bunch intensities leads to rise of all harmonics on the cost of the main RF harmonic.

While the gap between the trains and the length of the trains lead to the leakage of power to the harmonics next to the RF frequency multiples, the noise on the bunch intensity is responsible for the overall enhancement of revolution frequency harmonics.

By impinging a modulation onto the bunch currents, a specific frequency bin can be amplified. An example is shown in Fig. 8.18. An even filling pattern of 1000 buckets is modulated with a sinusoidal intensity modulation of 250 periods. The modulation with a period length of 4 buckets can be seen in the left panel where the filling pattern of the first forty buckets is shown. As a result, the DFT has an additional frequency contribution at 250 revolution harmonics next to every RF harmonic. This example shows the potential to enhance specific harmonics by adjusting the filling pattern.

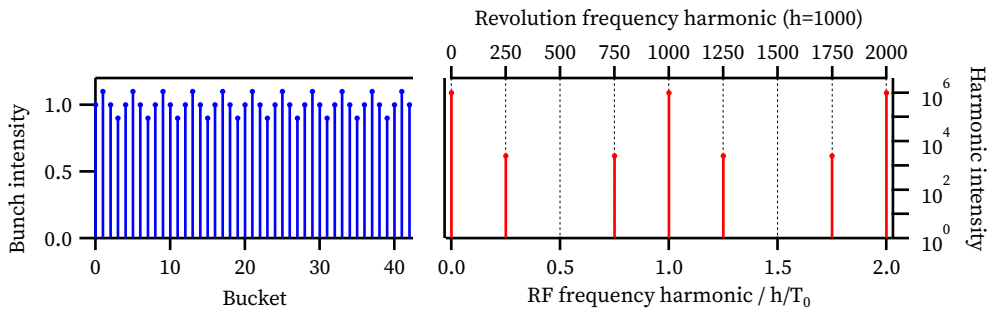


Figure 8.18: Simulation of a filling pattern of 1000 continuous bunches with a sinusoidal intensity modulation of 250 periods. The left panel shows the filling pattern of the first forty buckets. This leads to additional frequency peak at 250 revolution harmonics next to the RF harmonics in the DFT, shown in the right.

8.7.3 Bunch Spacing

This section focuses on the effect of different pulse repetition rates. The distance between the bunches changes the distance between the peaks in the frequency comb, too. In an accelerator, there are two mechanisms that can vary the distance: First, for small variations, the RF frequency can be changed. This increases or decreases the synchronous phase, changing the particles' energy accordingly and thereby leading to a different orbit length. Consequently, the revolution frequency is changed, maintaining the harmonic number. This variation has to be small, otherwise the particles' orbit interferes with the vacuum chamber. At KARA, a change in RF frequency of ± 10 kHz can be done in most accelerator conditions. Accordingly, the revolution frequency changes by $< \pm 54$ Hz. At first glance this seems to be negligible, but this can shift the harmonics above 140 GHz by \pm one revolution frequency. Therefore, above 140 GHz any distinct frequency can be reached and, by adjusting the RF frequency, the frequencies can be scanned. This enables gapless ultra-high resolution spectroscopy.

The second method to change the bunch distance is leaving some buckets empty. In the following, a system of only two pulses, but with different distances while maintaining the revolution frequency, is investigated. Figure 8.19 shows the influence of the distance T_P between two bunches. Shown is the spectral intensity calculated by the magnitude squared of Eq. (8.18). The revolution time is kept constant, only the time between the first and second pulse is altered. Slices at the integer positions are shown on the right.

As expected, the DFT is periodic with the RF frequency f_{RF} that defines the minimum distance between the bunches. The integrated power over all frequencies and the maximum intensity is the same for all integer bunch spacings. However, it can be seen that with increasing distance of the pulses, the individual frequency peaks move closer together while decreasing in width. Detectors which can't resolve the RF frequency will always measure the same power, no matter what the distance between the two bunches is. Only when all particles are packed into a single bunch, coherent enhancement will increase the output power. To see the effect of bunch distances in experiment, a broader range has to be investigated.

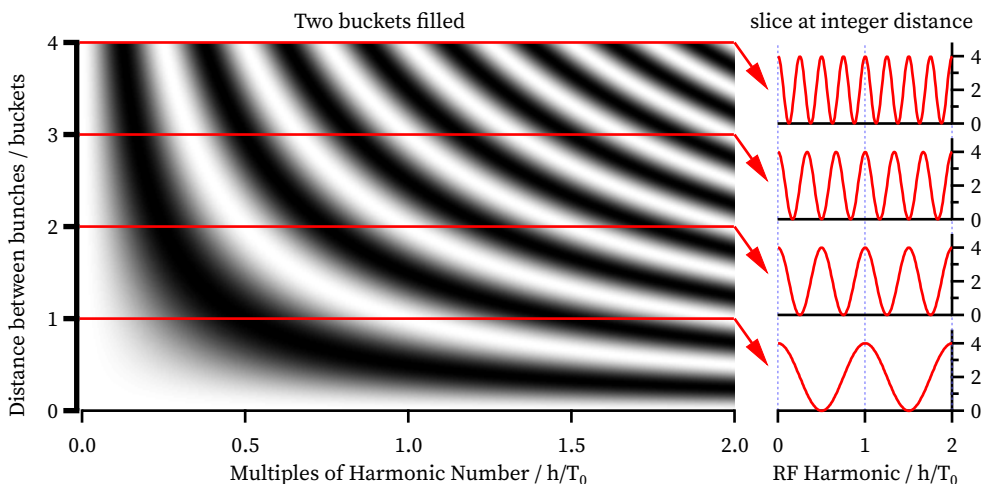


Figure 8.19: Normalized magnitude squared of the discrete-time Fourier transform of a filling pattern with 2 bunches calculated with Eq. (8.18). The pulses have the same amplitude V_k , but different spacing T_P , while T_0 is kept constant. Slices at the integer values are shown on the right. The integrated power is the same at all integer values, while the shape of the spectrum is dependent on the time between the pulses. The complete spectrum by Eq. (8.17) has only contributions at revolution frequency harmonics and is additionally scaled by the single pulse radiation spectrum.

8.7.4 Broadband Data Evaluation

The used double side band (DSB) mixer leads to aliasing of the LSB and USB as described in the beginning of the chapter (cf. Fig. 8.1). However, due to the discrete spectrum of the synchrotron radiation, the folded frequencies of both bands can be separated and thus the effective observable frequency band is doubled. In order to distinguish between both bands, the LO is shifted by an offset of -20 kHz which after the 12 times multiplier leads to a frequency shift of 240 kHz . Frequencies below the LO are shifted to lower frequencies, because their offset to the LO decreases, while components above the LO will shift to higher frequencies. This measurement is shown in Fig. 8.20. To avoid unwanted intermodulation, it has been taken care that the frequency bins from LSB and USB do not overlap.

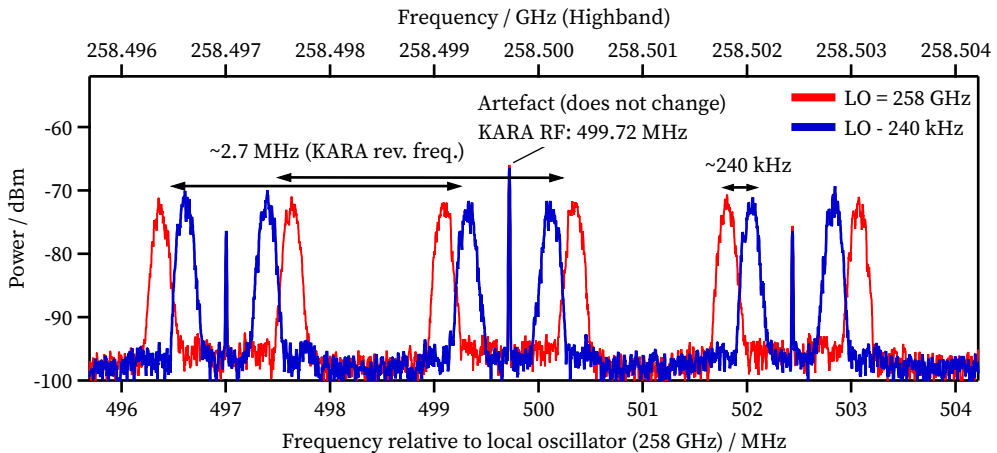


Figure 8.20: By changing the LO frequency, high band and low band can be separated, since the difference from LO to the spectral line changes differently. While the upper side band is shifted to lower frequencies, the lower side band is mixed to higher frequencies. The red, solid curve displays the initial measurement, the blue dashed line is with a shifted LO.

The position of the frequency bands is saved, and in later data analysis the two bands can be separated, because the origin of every frequency peak is known. Artifacts and spurious signals, which do not move, can be identified and masked during data processing. The power of each harmonic is measured and sorted into high and low band. Due to the sorting it is easier to show a broad frequency band, as only the peak amplitudes are shown, neglecting the noise in between so the amplitude change of all harmonics can be tracked easily. Furthermore, this double side band mixing and

sorting allows the analysis of up to 40 GHz bandwidth with 20 GHz IF bandwidth and readout electronics.

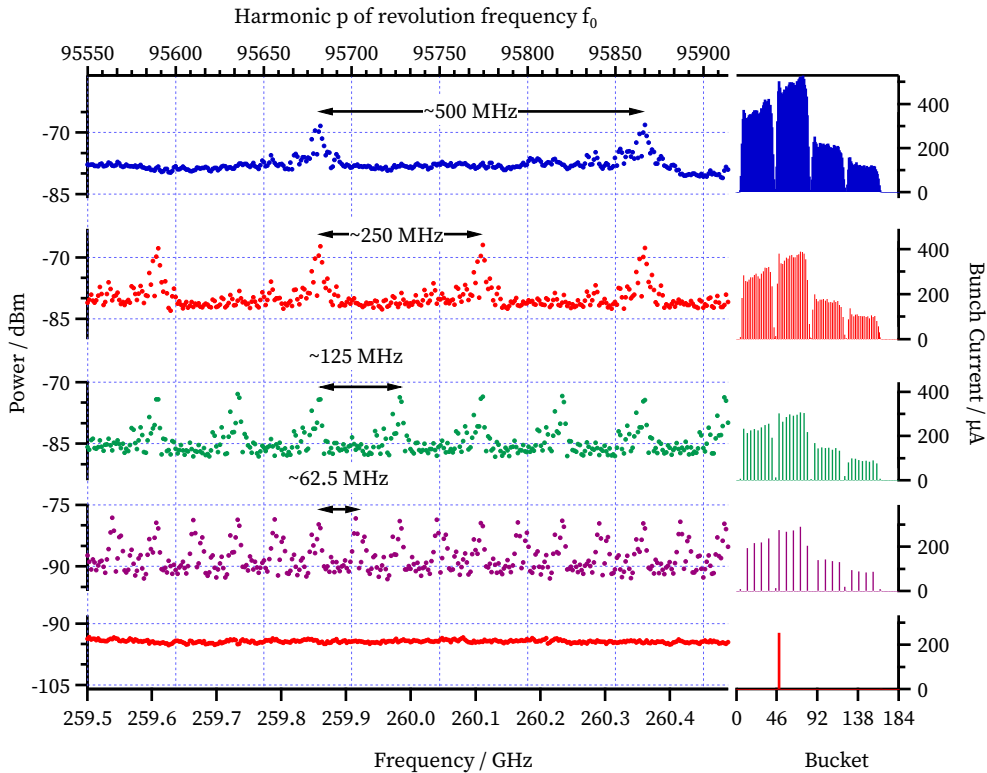


Figure 8.21: Measured THz power spectrum for different filling patterns. On the left, only the power of each harmonic at a given frequency is plotted, discarding the noise in between. The right panel shows the filling pattern. The top plot used the initial filling pattern of 4 trains with 33 bunches each. In the second plot from top every 2nd bunch is kicked out. In the 3rd plot only every 4th bunch is kept and below every 8th. In the bottom panel only a single bunch is left leading to a 2.71 MHz frequency comb with almost equal power. A modified version was already published in [Ste16b] (©2016 American Physical Society).

To analyze the effect of bunch spacing, the storage ring was filled with 4 trains with individual bunch currents. Then with the KARA bunch-by-bunch feedback (BBB) system [140; 141], bunches were kicked out periodically to increase the distance between the ones that were left. The filling pattern was measured by TCSPC in parallel (see Chapter 4.3.4). Figure 8.21 shows measurements for different filling pattern structures. The average displayed noise level is at -115 dBm, therefore all frequency peaks have a significant power level. As described above, only the power of the frequency harmonics is shown, where every dot corresponds to one frequency peak. The corresponding

filling pattern is shown on the right. Initially it consisted of 4 trains with 33 bunches each and different bunch currents (top). Then every second bunch was kicked out by the BBB system. In the second line, additional multiples of 250 MHz separation arise. Even though the total bunch current decayed and half of the electrons were removed, the power at the specific 250 MHz harmonics increased by almost a factor of 10. The same happens when only every 4th respective 8th bunch is kept and all others are kicked out. Last but not least, the bottom panel shows that a single bunch leads to a 2.71 MHz frequency comb whose harmonics have almost identical intensity.

8.8 Summary of Heterodyne Measurements

This chapter described how a heterodyne detection setup was built up, characterized and productively used to observe frequency combs emitted by the circulating electron bunches. Although the discrete nature of the synchrotron radiation was predicted more than 100 years ago by Schott [1], the ability to experimentally resolve it has only recently been attained. In order to perform the measurements, not only low-loss heterodyne mixers were needed, but powerful coherent enhancement of short pulses was essential, too. Tammaro et al. [171] were the first to observe the individual peaks by heterodyne measurements in the sub-THz range and focused on the use for spectroscopy of samples. Whereas in this thesis, the influence of the accelerator parameters on the emitted spectrum was investigated. First, a single bunch in the storage ring was analyzed and the dependency of longitudinal motion demonstrated. Then, the influence of the storage ring filling pattern on the emitted frequency comb spectrum was systematically studied for the first time. An easy-to-use formula to quantify these influences in multi-bunch operation has been developed and supported by the measurements. The influence of the bunch spacing and bunch current differences have been analyzed theoretically and illustrated by measurements.

In a multi-bunch fill with uniform bunch filling, the revolution frequency harmonics are damped down and the energy is concentrated in the RF frequency harmonics. Deviations in the homogeneous filling pattern like gaps or intensity variations lead to noise on all revolution frequency harmonics. It has been shown, how specific frequency bins can be amplified by impinging the corresponding modulation onto the filling pattern signal. Moreover, by changing the revolution frequency, the frequency peaks can be shifted, enabling gapless spectroscopy with a resolution six orders

of magnitude better than the best FTIR currently available at synchrotrons. This can have great potential in ultra-high resolution spectroscopy. In the THz range, this is particularly relevant to the study of rotational states of molecular gases and hyperfine structure lines of e.g. atoms, neutral atoms, molecules and radicals. For example, the line width due to Doppler effects $\Delta\nu_D \equiv \nu_0/c\sqrt{2kT/m}$ in gases scales with the temperature T and inversely with the mass of the molecule m . Therefore, it is now possible to study molecules at low temperatures, e.g. in molecular beams simulating conditions in space, or more complex molecules with higher mass such as biomolecules.

9 Summary and Outlook

Any sufficiently advanced technology is indistinguishable from magic.

— Arthur C. Clarke, Profiles of the Future:
An Inquiry Into the Limits of the Possible

Modern storage-ring light sources produce diffraction-limited synchrotron light by reducing the transverse bunch size below the observed radiation wavelength. A possible next generation could provide coherent radiation with a brilliance many orders of magnitude higher, and, additionally, single cycle pulses. This can be achieved by squeezing the electron bunches longitudinally, until they become smaller than the wavelength of the radiated emission. However, the high intensity radiation which is emitted thereby interacts with its source-bunch inside a bending magnet and distorts the longitudinal bunch profile. Above a charge threshold, the so-called micro-bunching instability does not only limit further compression, but also leads to sub-structures on the bunch profile, additionally disturbing the spectrum of the radiation. Currently, storage rings are limited in bunch length down to around 1 ps at rather low currents, well below the usual operation point, before the instability leads to turbulent bunch-lengthening. The distortions of the bunch profile, and thus the signatures of the instability, can be observed by the emitted coherent synchrotron radiation in the THz range.

The dynamics of the micro-bunching instability are not fully understood and therefore, several techniques to observe the instability in time-domain and frequency-domain were developed, set up, tested, and evaluated. First, state-of-the-art FTIR measurements were carried out. They were performed with a commercial Michelson interferometer and with an in-house-built Martin-Puplett interferometer, specially optimized for THz radiation and capable of balanced detection. The use of ultra-fast detectors, enabling the detection of each bunch in a multi-bunch environment was demonstrated, too. Furthermore, the limitations of these devices were evaluated, and solutions were presented in the following chapters.

Time-domain measurements with ultra-fast THz detectors were used to determine the micro-bunching instability threshold and to create spectrograms which are a finger-print of the machine settings used. Different instability regimes were analyzed and a more stable operation mode at very high bunch currents was identified. In the future, this could be used for better signal-to-noise ratio in spectroscopic measurements. Additionally, first successful experiments of influencing the bursting behavior of the instability by RF phase modulations were performed and further investigations are ongoing.

A single-shot four-channel spectrometer, which continuously streams 500 million spectra per second, was set-up and first experiments proving its great potential were performed. The optical set-up consists of three beam-splitters and four individual detectors, which are simultaneously read out in a streaming mode by the KAPTURE acquisition system. This unique setup allows to resolve single turn dynamics with a repetition rate orders of magnitude faster than the devices commercially available. Accordingly, the micro-bunching instability was observed in four THz frequency bands turn-by-turn in a multi-bunch environment, and first data evaluation was done. Furthermore, the found features agree with performed simulations by the Vlasov-Fokker-Planck solver Inovesa, which opens the door to a better understanding of the instability. This is necessary to benchmark future efforts of controlling the instability, before applying them in the field. The single-shot spectrometer is a valuable tool to verify the feasibility of these efforts in experiments.

Developments improving the single-shot spectrometer are under way to use integrated single-chip detector arrays based on superconducting, electric field-sensitive YBCO detectors and on room-temperature Schottky detectors in combination with the next version of KAPTURE. The latter will provide eight readout channels and an improved readout path. In addition, the synchronization with other experimental stations at KARA will provide time-resolved information about the energy spread and the longitudinal bunch profile, simultaneously.

Ultra-high resolution spectroscopy by heterodyne mixing of the THz radiation was described in the last experimental chapter of this thesis. The setup allowed spectral measurements around 260 GHz with a resolution of down to 1 Hz. By this, the discrete nature of synchrotron radiation in a storage ring, forming a frequency comb, was revealed. The influence of the storage ring filling pattern on the emitted frequency comb was verified for the first time. Additionally, an easy to use formula to quantify

these influences in multi-bunch operation was developed and is supported by the measurements. It was shown, that in a multi-bunch fill with uniform bunch filling, the revolution frequency harmonics are damped down and the energy is concentrated in the RF frequency harmonics. Deviations in the homogeneous filling pattern like gaps or intensity-variations lead to noise on all revolution frequency harmonics. Specific frequency bins can be amplified by impinging the corresponding modulation onto the filling pattern signal. Moreover, by changing the revolution frequency, the harmonics can be shifted accordingly, enabling spectroscopy with a resolution in the Hertz range, at least six orders of magnitude better than the best FTIR currently available at synchrotrons. This heterodyne detection of the synchrotron radiation frequency comb has great potential in ultra-high resolution spectroscopy. In the THz range, this is particularly relevant to the study of rotational states of molecular gases and hyperfine structure lines of e.g. atoms, neutral atoms, molecules and radicals, especially at low temperatures.

In summary, several different techniques for accelerator diagnostics in the THz regime were investigated and put into operation. They have led to a better understanding of the limiting micro-bunching instability and are necessary to quantify future efforts to influence these instabilities. In addition to the beam diagnostics, especially the heterodyne detection setup has great potential in material analysis.

Appendix

The trouble with the world is that the stupid are cocksure and the intelligent full of doubt.
— Bertrand Russell, 1969

A Synchrotron Motion

The momentum compaction factor α_c describes, how a particles' momentum offset leads to an arrival time offset. Due to this arrival time difference ΔT , the particle arrives at a different RF phase at the cavity $\Delta\psi$

$$\Delta\psi = 2\pi f_{\text{RF}}\Delta T = h2\pi f_0\Delta T = 2\pi h \frac{\Delta T}{T_0} = 2\pi h\alpha_c \frac{\Delta E}{E}. \quad (\text{A.1})$$

The average phase shift per turn is

$$\Delta\dot{\psi} = \frac{\Delta\psi}{T_0} = 2\pi f_0 h \alpha_c \frac{\Delta E}{E}. \quad (\text{A.2})$$

A particle, arriving at the cavity at a different phase gains a different amount of energy

$$\delta E = eV_{\text{RF}} \sin(\psi_0 + \Delta\psi) - W. \quad (\text{A.3})$$

Taking into account that off-momentum particles also have a different energy loss per turn

$$W = W_0 + \frac{dW}{dE} \Delta E, \quad (\text{A.4})$$

the different energy, which an off-momentum particle gains, compared to the synchronous particle, can be described by inserting (A.4) and (1.22) into (A.3)

$$\begin{aligned} \delta E &= eV_{\text{RF}} \sin(\psi_0 + \Delta\psi) - eV_{\text{RF}} \sin \psi_0 - \frac{dW}{dE} \Delta E, \\ \delta E &= eV_{\text{RF}} [\sin(\psi_0 + \Delta\psi) - \sin \psi_0] - \frac{dW}{dE} \Delta E. \end{aligned} \quad (\text{A.5})$$

As long as the phase oscillations are small ($\Delta\psi \ll \psi_0$), the phase dependence can be simplified to

$$\begin{aligned}\sin(\psi_0 + \Delta\psi) - \sin\psi_0 &= \sin(\psi_0)\cos\Delta\psi + \cos\psi_0\sin\Delta\psi - \sin\psi_0 \\ &\approx \Delta\psi\cos\psi_0.\end{aligned}\quad (\text{A.6})$$

The average energy change per turn is

$$\Delta\dot{E} = \frac{\delta E}{T_0} = \frac{eV_{\text{RF}}}{T_0}\Delta\psi\cos\psi_0 - \frac{dW}{dE}\frac{\Delta E}{T_0}, \quad (\text{A.7})$$

and the second derivative

$$\Delta\ddot{E} = \frac{eV_{\text{RF}}}{T_0}\Delta\dot{\psi}\cos\psi_0 - \frac{dW}{dE}\frac{\Delta\dot{E}}{T_0}. \quad (\text{A.8})$$

By inserting Eq. (A.2), the longitudinal equation of motion is derived

$$\underbrace{\Delta\ddot{E} + f_0\frac{dW}{dE}\Delta\dot{E}}_{2/\tau_d} - \underbrace{\frac{2\pi f_0^2 h \alpha_c e V_{\text{RF}} \cos\psi_0}{E_0}}_{\omega_s^2} \Delta E = 0, \quad (\text{A.9})$$

where the *synchrotron frequency* f_s

$$f_s = \frac{\omega_s}{2\pi} = f_0 \sqrt{-\frac{\alpha_c h e V_{\text{RF}} \cos\psi_0}{2\pi E}}, \quad (\text{A.10})$$

and the longitudinal *damping time* τ_d

$$\frac{1}{\tau_d} = \frac{f_0}{2} \frac{dW}{dE}, \quad (\text{A.11})$$

is introduced.

With further treatment of the damping time, one arrives at [46, p. 98 ff.]

$$\frac{1}{\tau_d} = \frac{1}{2T_0} \frac{W_0}{E_0} \mathcal{J}_E, \quad (\text{A.12})$$

with \mathcal{J}_E being the damping partition number, which is $\mathcal{J}_E \approx 2$ for most storage rings. As a rule of thumb, the damping time is the time a particle would need to radiate away its total energy [46, p. 102].

B Readout Systems

Ultra-fast detectors need appropriate readout systems to unlock their potential. The readout devices used in this thesis range from commercially available oscilloscopes with analog bandwidths between 4 GHz and 36 GHz, a 30 GHz spectrum analyzer (SA), a 5 MHz dual-channel lock-in amplifier (LIA) and the in-house developed readout system KAPTURE. These will be presented in the following.

B.1 Oscilloscopes

Today, digital oscilloscopes are very complex. In this short introduction, only the main features will be explained. Simplified, the oscilloscope comprises of a trigger, which activates the data taking, and a fast ADC. All used oscilloscopes were equipped with an 8 bit ADC, whose quantizing noise limits the achievable SNR to a maximum of 50 dB [189]. The effective number of bits is slightly less and will be achieved by setting preamplifier in a way that the biggest pulse perfectly fits the ADC range. This not only limits the smallest detectable signal but also the accuracy with which the pulse amplitude can be determined. To avoid aliasing effects during the digitalization process, the analog bandwidth of the oscilloscopes is limited to about 45 % of the ADC sampling rate by an analog anti-aliasing low pass filter. The used oscilloscopes with their main features are summarized in Table B.1.

Table B.1: Oscilloscopes used in this thesis

Model	MSO9404A	DSA-X 93204A	SDA760Zi-A	RTO2064
Manufacturer	Keysight	Keysight	LeCroy	Rohde & Schwarz
BW (GHz)	4	32	6	6
Samplingrate (GSa/s)	20	80	40	20
Memory (MPts)	500	50	64	200
Peak detect mode	✓	✓		✓
Input sensitivity (mV/div)	10-1000	7.5-1000	10-1000	1-1000
Segments	131 072	131 072	5000	200000
Intersegment time (μs)	4.5	2.5	1	0.3
Rise time (ps)	85	12.5	70	76

Note, that memory, number of segments, and peak detect mode limitations are a software rather than hardware limit and depend on the booked options. Details of the different acquisition modes like *peak detect* or *segmented* are explained in more detail in the following. The details of the oscilloscopes vary between manufacturers, therefore, only a simplified version of the working principle is presented.

B.2 Single-Shot Realtime Mode

In the single-shot realtime mode, the oscilloscope's trigger is armed and waiting for an event. After detecting one, the oscilloscope continuously writes the acquired sampling points into the internal memory until the requested acquisition size is reached or the memory is full. All oscilloscopes offer tools to analyze that trace immediately after the recording, i.e. measurements of width and height of pulses or by using statistical methods. After having done the calculations the oscilloscope either waits for a new user command or arms for the next trigger event, depending on the settings. The following acquisition overwrites the trace memory, yet the preceding measurements are saved, so that statistical methods like averaging or standard deviations can be calculated. In this thesis, only the averaging function has been used when setting up the experiments. During the experiment, all the raw data are read out by a computer and saved together with the subsequent analysis which is done at the readout PC.

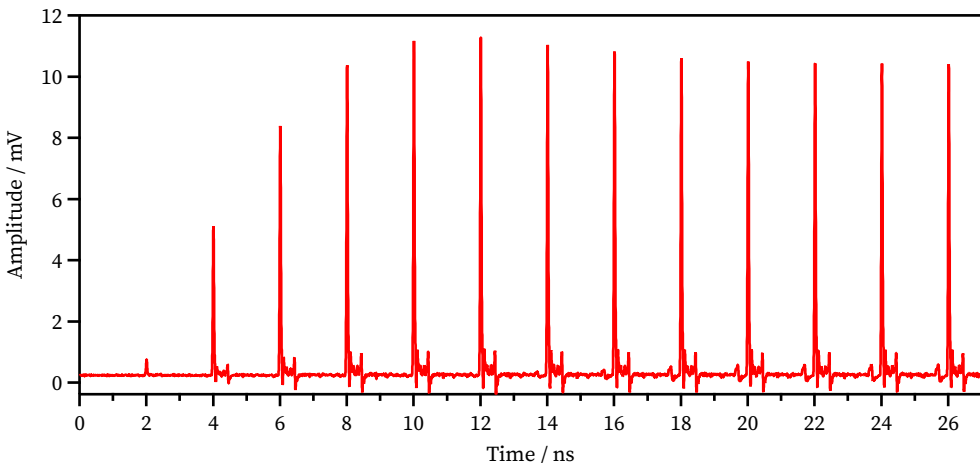


Figure B.1: Oscilloscope trace measured at the beginning of a bunch train. Because of the unstable operation mode, the trace has been averaged by 1024 turns.

Figure B.1 shows an oscilloscope trace of the beginning of an electron bunch train. Due to the unstable short-bunch mode, averaging was done. At the beginning of the train, the bunches have less current and therefore less intensity. The two-nanosecond spaced pulses can be clearly distinguished. The main limitation of the realtime mode is the amount of available memory to store the recorded sampling points. As an example, the LeCroy SDA760Zi-A with 80 GSa/s would have completely filled up its memory of 64 MPts within 0.8 ms. That makes just 2000 turns for every bunch. If, like for the Keysight devices, every point is internally corrected by a calibration curve and therefore has 16 bits accuracy, that would amount to 128 MByte of data to transfer and analyze. For measurements where only the pulse amplitude is important, that would lead to a detection of 368'000 pulse amplitudes or 184 bunches for 2000 turns; or even worse: for a single bunch fill, only 2000 measurement points were confined in 128 MByte of data. Thus, the realtime mode is inappropriate to observe short signals with a long dead time in-between and can not be used for lengthy observation of the bunch signals.

B.3 Segmented Mode

The segmented mode is a way to avoid the limitation described above when observing a sequence of extremely short events and a long pause in-between. Here, only a small number of sampling points are saved into the memory for every trigger event. Without doing any analysis, the oscilloscope arms again, then catches the next trigger and writes the data directly after the previous one instead of overwriting them like in the realtime mode. The minimum time between segments is hardware dependent and ranges from the possibility to catch each turn with the Rohde & Schwarz RTO2064 to every 13th with the Keysight MSO9404A. The maximum number of observable segments is either limited by the maximum memory or by a software option.

A measurement of an optical 4 GHz APD and the determined pulse amplitude of each segment is shown in Fig. B.2. Every 10 turns, a segment with a length of 3 ns was recorded. Then, the complete memory can be transferred to the PC en bloc. There it's split again into the segments and analyzed further. First, the data are interpolated and then the pulse amplitudes and arrival times are determined. Compared to the single-shot realtime mode, the maximum observation time is increased and the amount of data to transfer is drastically reduced. However, the observation time is still limited, first by the memory of the oscilloscopes, and then by the comparably slow transfer

speed of the acquired data to the PC. During the long-term measurements, which will be described later, a measurement is done every 10 or 15 seconds. In that time, the data have to be recorded, transferred to the PC and saved to the hard drive. The transfer to the PC was identified as the bottle neck, especially when using more than one detector simultaneously.

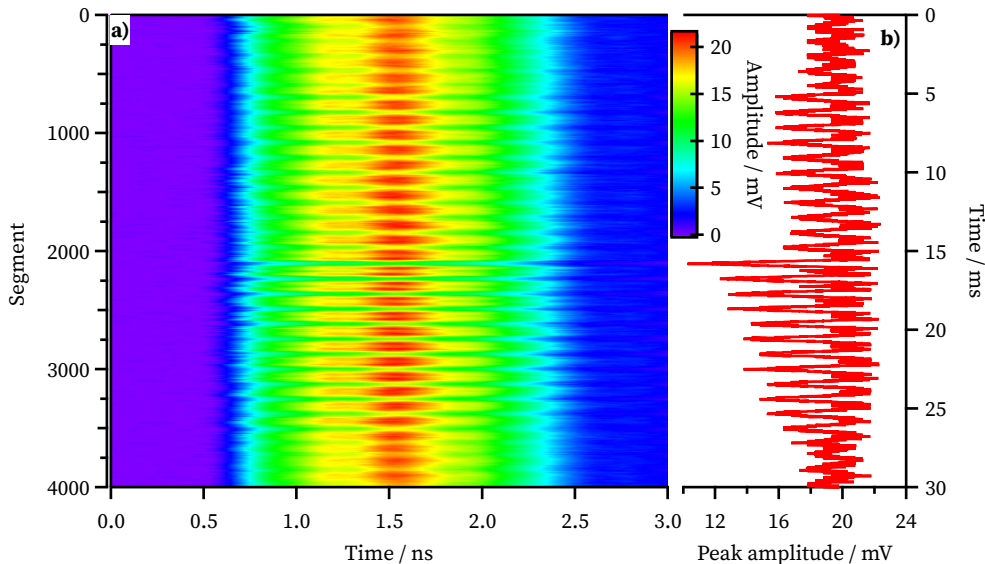


Figure B.2: Example of a measurement in segmented mode of a single bunch detected with an optical APD. The segment length of 3 ns is shown over 4000 segments (a). Every line is the data of one segment. A segment was recorded every 10 turns. In the offline analysis, the amplitude of every pulse in the segment was determined (b). An oscillation with the synchrotron frequency can be observed.

B.4 Peak Detect Mode

A method to further reduce the amount of recorded data is the peak detect mode. The basic principle is that the ADC runs continuously and only remembers the highest and the lowest sampling point. After each changeable interval, these two points are stored to the memory. Therefore, the peak of a pulse can be caught even without triggering and can be observed for a long time. With this method, seconds of data can be recorded easily. The peak detect mode has been used extensively in this thesis with the Keysight MSO9404A. However, this method, too, has a few drawbacks (some of which were explicitly found for the MSO9404A and can differ for another model):

Sampling rate: According to the manual, the MSO9404A reduces the sampling rate to 2 GSa/s when in peak detect mode, thus the maximum of the ultra-fast pulse could be missed, since the analog low-pass filter is still at 4 GHz. Additionally, an interpolation to determine the real height is not being done.

Operation mode: Only makes sense in single bunch mode. While the segmented mode can pick a single bunch in a multi-bunch environment, the peak detect mode only saves the highest and lowest sampling point of the whole interval.

Time accuracy: Only the sampling time of the interval is saved. Information about the exact point of time when the highest point in the interval has occurred is lost.

Interval: The interval can only be set in discrete steps. If the interval is smaller than one turn, there are intervals without a pulse inside. But there exist times where the radiation is below the detection threshold. So, if no pulse is detected, you don't know, if there was no pulse in the interval or if the amplitude was too low. If the interval is chosen to be bigger, there are different numbers of turns in the intervals, due to the discrete interval sizes. Together with the time accuracy limitation, it cannot be found out, to which turn the highest sampling point belongs to.

Noise: The highest and the lowest sampling points are saved, which effectively reduces the signal-to-noise ratio (SNR) as always the highest noise contribution is saved.

Despite these limitations, the peak detect mode is the best compromise to track a single bunch for long observation time. A whole second of data can be recorded easily for each channel, leading to a frequency resolution of the pulse amplitude deviations of 1 Hz. In practice, the interval size is mostly chosen to be 2.5 μ s, resulting in the observation of 6 or 7 turns. Changes in the pulse amplitude faster than 7 turns can therefore not be resolved.

B.5 Spectrum Analyzer

A spectrum analyzer (SA) is extensively used in Chapter 8 which works completely in frequency domain. When the time-domain information is not of interest, a SA can provide a signal-to-noise ratio (SNR) which is many orders of magnitude higher than for an oscilloscope. The working principle relies on the heterodyne detection principle, which is shown in Fig. B.3.

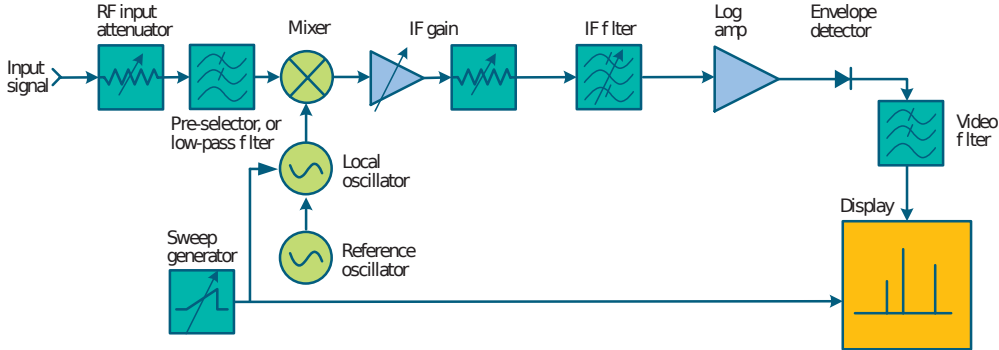


Figure B.3: Block diagram of a classic spectrum analyzer (adapted from [190])

At first, the incoming signal is filtered by an optional attenuator and a coarse low-pass filter for noise reduction. Then the signal is converted to an IF by a *mixer*. The working principle of such a mixer will be discussed in more detail in Chapter 8. An ideal mixer shifts the RF signal by the frequency provided by the LO. Then, the IF is amplified, filtered once more and its power detected, usually by another mixer which transforms the signal into baseband. As a result, the power is measured in a very small bandwidth. This so-called resolution bandwidth (RBW) is determined by the IF filter and usually can be as low as 1 Hz. Since noise power is proportional to the square root of the bandwidth, a SA provides a much higher SNR compared to an oscilloscope. By adjusting the LO frequency with a sweep generator, the frequency range of interest can be scanned.

A disadvantage of the good SNR is that it is not a single-shot method and does not provide time-domain data, because the phase information of the RF input is lost.

B.6 Lock-In Amplifier

The principle of lock-in detection dates back to the 1930s [192; 191]. Like a spectrum analyzer (SA), a lock-in amplifier (LIA) uses a mixer to convert the incoming signal to a lower frequency. Three main differences make the LIA special: First, it is not converting to an intermediate frequency (IF) (heterodyne principle), but directly to the base band (homodyne principle). Second, it uses two phase shifted mixers to get not only the amplitude but also the phase of the incoming signal. Third, it is locked precisely to a reference signal with which the experimental data are modulated. A basic principle is shown in Fig. B.4.

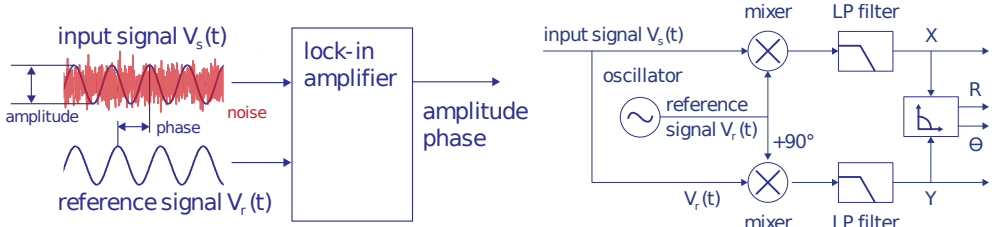


Figure B.4: Block diagram of a lock-in amplifier (adapted from [193])

The noisy input signal needs to be modulated with a reference signal. This can be done by a chopper, or intrinsically by the revolution frequency. The LIA mixes the input by two orthogonal waves of the reference signal. Then, the amplitude and the phase difference between input and reference signal are determined. Only signals with a stable phase contribute to the output, which –compared to the spectrum analyzer– additionally suppresses the noise. At a storage ring, the experimental signals of a bunch are naturally modulated by the revolution clock. The LIA can stream the output signals either electronically to a computer or via an analog output to a subsequent measurement device. A digital eLockIn205/2 from Anfatec Instruments AG with a bandwidth up to 10 MHz is used in this thesis, when signals are observed for a rather long time, like the step-scan FTIR-measurements described in Chapter 5 or when a broad dynamic range is observed like beam profile measurements as shown in Chapter 3.6.

B.7 Data Acquisition

The oscilloscopes and spectrum analyzers described above can be read out by the virtual instrument software architecture (VISA), an industry standard for communicating with test and measurement instruments. The high speed LAN instrument protocol (HiSLIP) is used to communicate via ethernet. The lock-in amplifier can be read out via a web CGI script. An interface to control all devices has been written in IGOR Pro (WaveMetrics Inc., Lake Oswego, OR, USA), a technical graphing and data analysis software. The connected devices are detected by the software and accordingly read out. Depending on the device the data are further processed. For example, oscilloscope data taken in segmented mode are sorted first, then the arrival time and pulse height of the observed pulses are determined. Afterwards, a spectrum of the pulse height data over time is calculated and shown in a spectrogram to get a live feedback

of the current machine status. Additionally, when connected to the KARA network, machine parameters like beam current, filling pattern, synchrotron frequency, or RF voltage are acquired. Then all data are written to an HDF5¹ file container which is the THz-group standard to share and archive measurement data.

Data acquisition can be triggered by three modes. First, the user can manually start a measurement which reads out all devices connected at that time. Second, an automated measurement can be done which reads out the devices after a given time, i.e. performing a 1 s long measurement every 10 s. Third, an external trigger can be used to start the measurement. The software monitors the instruments continuously and reads them out as soon as data taking has been finished. This method is used when synchronized measurements are done and several experimental stations take data at the same time [Keh18b].

B.8 KAPTURE

The analysis of short THz pulses has special readout requirements. The pulse arrival time and amplitude should be tracked for each bunch, separated by 2 ns, for a long time, in the best case continuously. Online analysis should be possible for live evaluation and future projects that could install a feed-back to the accelerator depending on the measurement results. These requirements can not be satisfied by current commercially available instruments. While the segmented mode is already a powerful tool, it is limited not only by the dead time between the segments, the analog bandwidth, the maximum number of segments, the dynamic range of the ADCs but also by the transfer rate to the readout computer.

Therefore, a special readout instrument has been developed at the Institute for Data Processing and Electronics (IPE), the so-called Karlsruhe Pulse Taking Ultra-Fast Readout Electronics (KAPTURE). This chapter is based on the information published in more detail in Refs. [Cas14d; Cas14c; Cas17a]. Information about the first concept was presented in [195].

The design concept is based on the segmented mode of an oscilloscope without dead time and with continuous data streaming to a readout PC. To achieve that, the incoming pulse is split into four channels by a resistive broadband 1:4 power splitter also

¹ Hierarchical Data Format version 5, developed by “The HDF Group”[194]

developed at the IPE. Each channel is connected to a track-and-hold (T/H) chip, whose output is connected to a 12 bit ADC. A common trigger can be set by the FPGA in coarse delays of 150 ps which sets the T/H into hold state. Each T/H trigger signal can be delayed individually by a delay chip, allowing 3 ps steps up to 92 ps. The T/H reset and the following ADC are triggered by 500 MHz, synchronized to the KARA RF clock. As a result, an incoming pulse can be sampled around the peak by four sampling points with a sample distance of down to 3 ps every 2 ns. The described timing scheme is visualized in Fig. B.5.

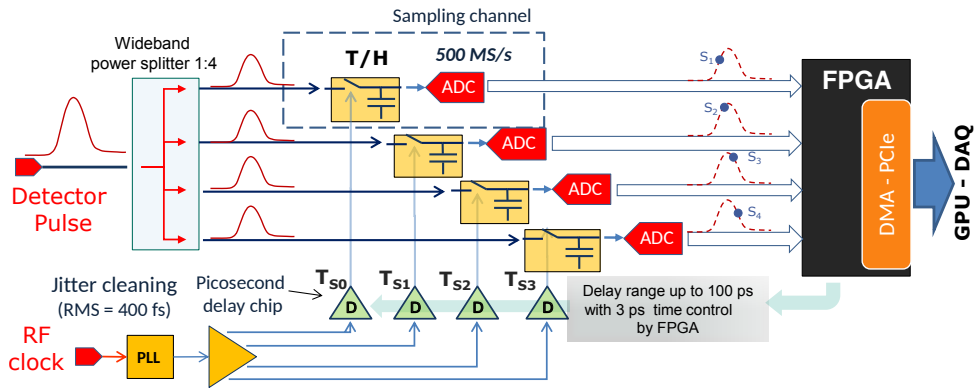


Figure B.5: KAPTURE timing scheme (Courtesy of Michele Caselle, published in [Cas17a])

The four 12 bit ADC are read out by a high throughput board, which was developed at the IPE, too [197; 196]. It uses a new direct memory access (DMA) architecture connected via PCI Express to a readout PC, since a minimum of 24 Gbit/s are needed to transfer all the raw data (12 Bit at 500 MHz for each of the 4 ADC). In our current configuration, the hard disk is too slow to save the measurement data on the fly. Therefore, it is transferred into the PC's 128 GB main memory, analyzed and then written to the computer's hard drive. A continuous streaming and saving of raw data will be possible in the next version of KAPTURE. A view of the finished instrument is shown in Fig. B.6.

KAPTURE can also be operated in a different configuration. Instead of the 1:4 power splitter, four individual detectors are directly connected to the ADCs. Then only one point per pulse is sampled. In this mode, the pulse shape, width and arrival time can not be detected. However, the maximum of the pulse can be sampled for the four detectors in parallel when using proper settings of the sampling time and a stretched

input pulse. This mode is the basis for the four channel single-shot spectrometer which will be presented in Chapter 7. The different operation modes are sketched in Fig. B.7.

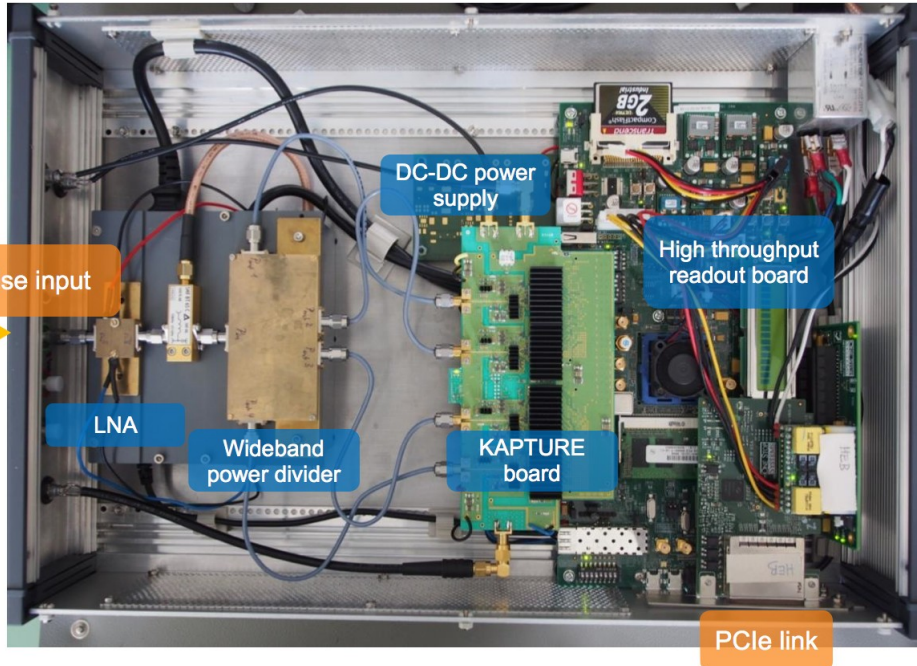


Figure B.6: View inside the KAPTURE system. (Courtesy of Michele Caselle, published in [Cas14d])

As KAPTURE writes its data via DMA directly into the RAM of the connected PC, a special readout is not necessary. The data-consistency-checks, evaluation, sorting, and writing to an easy exchangeable HDF5 format is done via Python scripts of Miriam Brosi [198].

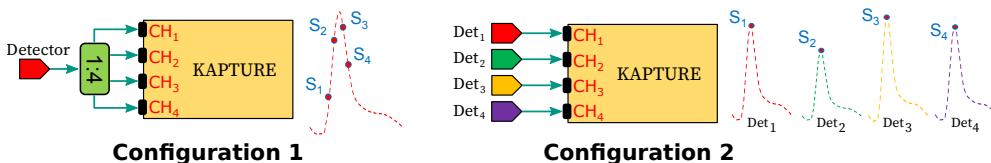


Figure B.7: Two possible KAPTURE configurations: First, a single detector signal is split into four and the pulse is sampled at four different points of time. Second, several detectors are connected to the sampling electronics. Then only one point per pulse is sampled by up to four detectors in parallel. (courtesy Michele Caselle, modified)

C THz Filters

For many measurements in the THz range, quasi-optical filters were used. Highpass filters can block microwave signals from entering the readout circuits. They also prevent the detectors from saturation by lower frequency signals if the focus of the measurement is on the higher frequency components. Bandpass filters are used when a narrowband spectrum is wanted from a broadband source like the synchrotron radiation. Lowpass filters are used to block infrared and visible light. They are important when using thermal detectors like a bolometer as they could be easily saturated by the incoherent synchrotron radiation outside the measurement range.

C.1 Lowpass

Lowpass filters are needed to block the IR radiation but transmit most of the wanted THz range. For that purpose, I have used ZITEX G-108, a 200 μm thick porous polytetrafluorethylen (PTFE) foil produced by Saint-Gobain Performance Plastics. It's usually implemented as a venting material for liquid packaging due to its high chemical resistance, gas permeability and hydrophobicity. However, it turned out that it is a quite good optical filter as it scatters infrared (IR) radiation but is almost transparent in the THz range. Due to the scattering, almost no heat is deposited in the sample, making it a good filter material for cryogenic applications [116, p. 57].

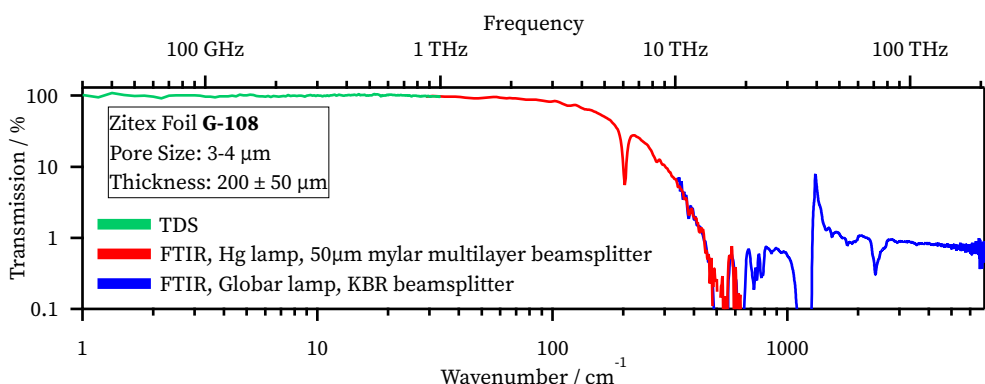


Figure C.1: Transmission spectrum of ZITEX G-108, a 200 μm thick porous PTFE foil. The low frequency spectrum was recorded by time-domain spectrometer (TDS) in ambient air, while the infrared spectra were recorded using an FTIR spectrometer with an HG and Globar source and a 50 μm multilayer mylar and KBR beam splitter, respectively. The foil shows good transmission properties in the THz range while blocking almost 99 % of infrared light.

The transmission property of a Zitex G-108 sample² was measured with TDS in the THz region and FTIR in the IR region. The results in Fig C.1 show a transmission above 90 % for frequencies below 3 THz going down to only 1 % above 13 THz. If more attenuation is needed, the thin foil can be stacked easily.

C.2 Highpass

Highpass filters based on thick grid filters [199] were used. These badges were designed at the Paul Scherrer Institute (PSI), Villigen, Switzerland and consist of 1 mm thick copper sheets with a hexagonal hole pattern of different hole diameters. The holes were drilled through electron beam drilling. Plates with hole sizes between 0.2 mm to 0.6 mm were used, however, the 0.2 mm holes couldn't be cleaned properly and show less transmission. The transmission properties shown in Fig. C.2 were measured using THz-TDS. The transmission in the pass band is around 10 %.

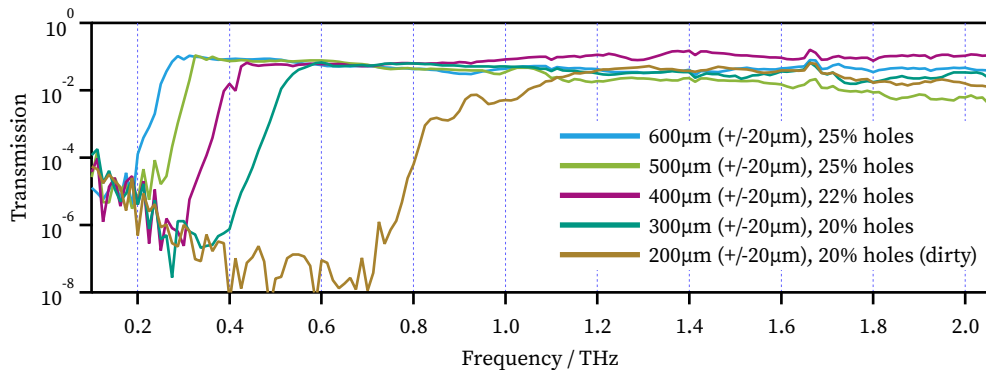


Figure C.2: Measured transmission properties of the highpass filters.

C.3 Bandpass

A series of THz bandpass-filters with different center frequencies from 140 GHz to 3000 GHz can be used, if a more narrowband spectrum is needed. The bandpass filters were produced by the Novosibirsk State University (NSU) and were implemented on

² provided by Saint-Gobain Performance Plastics

the basis of multi-layer frequency selective surfaces produced with electroplating technology [201; 200]. They were designed to provide a filtration bandwidth of around 20 % (FWHM) referred to the center frequency. The transmission behavior of the used filters is shown in Fig. C.3. In the THz region, an out-of-band rejection of 30 dB is achieved while the infrared and visible light is attenuated by roughly 20 dB.

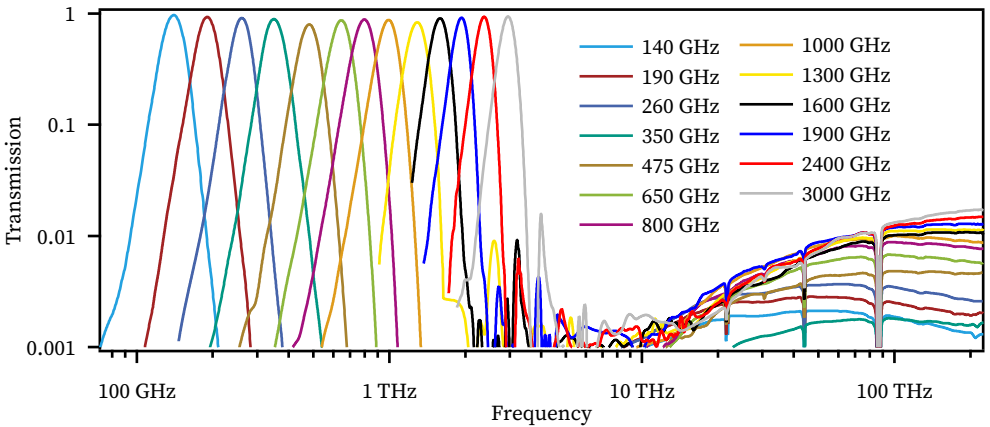


Figure C.3: Transmission properties of the different bandpass filters. FTIR measurement data courtesy of Sergei Kuznetsov, NSU, Novosibirsk, Russian Federation.

C.4 Beam Splitters

The beam splitters used for FTIR are discussed in more detail in Chapter 5. In all other experiments, wire grids are used as beam splitters. Since the synchrotron radiation is mainly linearly polarized (cf. Chapter 3.3 and Fig. (3.6)), wire grids provide a very broadband method with a flat frequency response to split THz beams. Furthermore, by changing the angle of the beam splitters with respect to the incoming light polarization, the power ratio of the reflected and transmitted beams can be adjusted. To achieve equal power in both beams, the light has to see the projection of wires in a 45° angle. Therefore they have to be mounted by 35.3° inside the holder. Two different wire grids are used. First, rotatable grids from Microtech instruments and second, fixed position grids with either 0° or 35.3° angle made by QMC. Their 125 mm clear aperture diameter is big enough to avoid any scattering or absorption of the beam. The grids are made of 20 µm tungsten wire with a separation of 70 µm. The specified working frequency is up to 3 THz.

Publications

- [Bie17] S. Bielawski, E. Blomley, J. Brubach, E. Bründermann, C. Evain, S. Funkner, N. Hiller, M. L. Parquier, L. Manceron, A.-S. Müller, M. J. Nasse, G. Niehues, E. Roussel, P. Roy, M. Schuh, P. Schönfeldt, J. L. Steinmann, C. Szwaj, M.-A. Tordeux, and S. Walter “High Repetition-Rate Electro-optic Sampling: Recent Studies Using Photonic Time-Stretch” in: *Proceedings of the 6th International Beam Instrumentation Conference (IBIC), 20.-24. August, Grand Rapids, MI, USA 2017*
DOI: [10.18429/JACoW-IBIC2017-TU1AB2](https://doi.org/10.18429/JACoW-IBIC2017-TU1AB2) (see p. 84).
- [Bro15] M. Brosi, M. Caselle, E. Hertle, N. Hiller, A. Kopmann, A.-S. Müller, M. Schwarz, P. Schönfeldt, J. L. Steinmann, and M. Weber “Online Studies of THz-radiation in the Bursting Regime at ANKA” in: *Proceedings of the 6th International Particle Accelerator Conference (IPAC), 8.-13. May, Richmond, VA, USA 2015*
DOI: [10.18429/JACoW-IPAC2015-MOPHA042](https://doi.org/10.18429/JACoW-IPAC2015-MOPHA042).
- [Bro16a] M. Brosi, E. Blomley, E. Bründermann, N. Hiller, B. Kehrer, A.-S. Müller, M. Schedler, M. Schuh, P. Schönfeldt, and J. L. Steinmann “Systematic Studies of Short Bunch-Length Bursting at ANKA” in: *Proceedings of the 7th International Particle Accelerator Conference (IPAC), 8.-13. May, Busan, Korea 2016*
DOI: [10.18429/JACoW-IPAC2016-TUPOR006](https://doi.org/10.18429/JACoW-IPAC2016-TUPOR006) (see p. 111).
- [Bro16b] M. Brosi, J. L. Steinmann, E. Blomley, E. Bründermann, M. Caselle, N. Hiller, B. Kehrer, Y.-L. Mathis, M. J. Nasse, L. Rota, M. Schedler, P. Schönfeldt, M. Schuh, M. Schwarz, M. Weber, and A.-S. Müller “Fast mapping of terahertz bursting thresholds and characteristics at synchrotron light sources” in: *Phys. Rev. Accel. Beams* 19 (2016), p. 110701
DOI: [10.1103/PhysRevAccelBeams.19.110701](https://doi.org/10.1103/PhysRevAccelBeams.19.110701) (see p. 110).

- [Bro17] M. Brosi, E. Blomley, E. Bründermann, M. Caselle, B. Kehrer, A. Kopmann, A.-S. Müller, L. Rota, M. Schedler, M. Schuh, M. Schwarz, P. Schönfeldt, J. L. Steinmann, and M. Weber “Studies of the Micro-Bunching Instability in Multi-Bunch Operation at the ANKA Storage Ring” in: *Proceedings of the 8th International Particle Accelerator Conference (IPAC), 14.-19. May, Copenhagen, Denmark 2017*
DOI: 10.18429/JACoW-IPAC2017-THOBA1 (see p. 110).
- [Bro18] M. Brosi, J. Gethmann, A. Bernhard, B. Kehrer, A. Papash, P. Schönfeldt, P. Schreiber, J. L. Steinmann, and A.-S. Müller “Studies of the Micro-Bunching Instability in the Presence of a Damping Wiggler” in: *Journal of Physics: Conference Series* 1067 (2018), p. 062017
DOI: 10.1088/1742-6596/1067/6/062017.
- [Bro19] M. Brosi, J. L. Steinmann, E. Blomley, T. Boltz, E. Bründermann, J. Gethmann, B. Kehrer, Y.-L. Mathis, A. Papash, M. Schedler, P. Schönfeldt, P. Schreiber, M. Schuh, M. Schwarz, A.-S. Müller, M. Caselle, L. Rota, M. Weber, and P. Kuske “Systematic studies of the microbunching instability at very low bunch charges” in: *Phys. Rev. Accel. Beams* 22 (2019), p. 020701
DOI: 10.1103/PhysRevAccelBeams.22.020701 (see p. 111).
- [Brü13] E. Bründermann, D. Schmidt, B. Gasharova, Y.-L. Mathis, D. Moss, J. Steinmann, E. Edengeiser, M. Mischo, and M. Havenith “The ANKA-IR2 nanoscope and micro-and nanospectroscopy applications” in: *38th International Conference on Infrared and Millimeter and Terahertz Waves (IRMMW-THz), 1.-6. September, Mainz, Germany 2013*
DOI: 10.1109/IRMMW-THz.2013.6665734.
- [Cas14b] M. Caselle, M. Brosi, S. Chilingaryan, T. Dritschler, V. Judin, A. Kopmann, A.-S. Mueller, J. Raasch, N. J. Smale, J. Steinmann, M. Vogelgesang, S. Wuensch, M. Siegel, and M. Weber “An ultra-fast digitizer with picosecond sampling time for Coherent Synchrotron Radiation” in: *Real Time Conference (RT), 2014 19th IEEE-NPSS 2014*
DOI: 10.1109/RTC.2014.7097535.
- [Cas14c] M. Caselle, M. Brosi, S. Chilingaryan, T. Dritschler, E. Hertle, V. Judin, A. Kopmann, A.-S. Müller, J. Raasch, M. Schleicher, M. Siegel, N. J. Smale, J. L. Steinmann, M. Vogelgesang, M. Weber, and S. Wuensch “Commissioning of an Ultra-fast Data Acquisition System for Coherent

- Synchrotron Radiation Detection" in: *Proceedings of the 5th International Particle Accelerator Conference (IPAC), 15.-20. June, Dresden, Germany 2014*
 DOI: 10.18429/JACoW-IPAC2014-THPME113 (see p. 182).
- [Cas14d] M. Caselle, M. Brosi, S. Chilingaryan, T. Dritschler, N. Hiller, V. Judin, A. Kopmann, A.-S. Müller, L. Petzold, J. Raasch, L. Rota, M. Siegel, N. J. Smale, J. L. Steinmann, M. Vogelgesang, M. Weber, and S. Wuensch "A Picosecond Sampling Electronic 'KAPTURE' for Terahertz Synchrotron Radiation" in: *Proceedings of the 3rd International Beam Instrumentation Conference (IBIC), 14.-18. September, Monterey, CA, USA 2014* jacow.org/IBIC2014/papers/moczb1.pdf (see pp. 182, 184).
- [Cas17a] M. Caselle, L. E. A. Perez, M. Balzer, A. Kopmann, L. Rota, M. Weber, M. Brosi, J. L. Steinmann, E. Bründermann, and A.-S. Müller "KAPTURE-2. A picosecond sampling system for individual THz pulses with high repetition rate" in: *Journal of Instrumentation* 12.01 (2017), p. C01040
 DOI: 10.1088/1748-0221/12/01/C01040 (see pp. 137, 182, 183).
- [Cas17b] M. Caselle, L. Rota, M. Balzer, M. Brosi, S. Funkner, B. Kehrer, M. J. Nasse, G. Niehues, M. Patil, P. Schönfeldt, M. Schuh, J. L. Steinmann, M. Yan, E. Bründermann, M. Weber, A.-S. Müller, G. Borghi, M. Boscardin, S. Ronchin, and F. B. Kessler "Single-Shot Longitudinal Beam Profile and Terahertz Diagnostics at MHz - Towards GHz-Rates with High-Throughput Electronics" in: *Proceedings of the 6th International Beam Instrumentation Conference (IBIC), 20.-24. August, Grand Rapids, MI, USA 2017*
 DOI: 10.18429/JACoW-IBIC2017-TU2AB3.
- [Cha14] C. Chang, D. Batchelor, E. Hertle, E. Huttel, V. Judin, A.-S. Müller, M. J. Nasse, M. Schuh, and J. L. Steinmann "Design of a Compact Setup to Measure Beam Energy by Detection of Compton Backscattered Photons at ANKA" in: *Proceedings of the 5th International Particle Accelerator Conference (IPAC), 15.-20. June, Dresden, Germany 2014*
 DOI: 10.18429/JACoW-IPAC2014-THPME112 (see p. 79).
- [Cha15] C. Chang, E. Bründermann, E. Hertle, N. Hiller, E. Huttel, A.-S. Müller, M. J. Nasse, M. Schuh, J. L. Steinmann, H.-W. Hübers, and H. Richter "First Results of Energy Measurements with a Compact Compton Backscattering Setup at ANKA" in: *Proceedings of the 6th International*

Particle Accelerator Conference (IPAC), 8.-13. May, Richmond, VA, USA 2015
DOI: 10.18429/JACoW-IPAC2015-MOPHA040 (see p. 79).

- [Fun18a] S. Funkner, E. Bründermann, A.-S. Müller, M. J. Nasse, G. Niehues, T. Schmelzer, J. L. Steinmann, M. Tani, and M. Yan “Implementation of Ultra-Low Frequency Non-Linear Raman Spectroscopy with the Gun Laser at FLUTE” in: *Proceedings of the 9th International Particle Accelerator Conference (IPAC), 29. April - 4. May, Vancouver, BC, Canada 2018*
DOI: 10.18429/JACoW-IPAC2018-THPMF072.
- [Hil14a] N. Hiller, A. Borysenko, E. Hertle, V. Judin, B. Kehrer, S. Marsching, A.-S. Müller, M. J. Nasse, M. Schuh, P. Schönfeldt, N. J. Smale, J. L. Steinmann, P. Peier, B. Steffen, and V. Schlott “Status of Single-shot EOSD Measurement at ANKA” in: *Proceedings of the 5th International Particle Accelerator Conference (IPAC), 15.-20. June, Dresden, Germany 2014*
DOI: 10.18429/JACoW-IPAC2014-WE0BB02 (see p. 84).
- [Hil14b] N. Hiller, A. Borysenko, E. Hertle, V. Judin, B. Kehrer, A.-S. Müller, M. J. Nasse, M. Schuh, P. Schönfeldt, N. J. Smale, J. L. Steinmann, P. Peier, B. Steffen, and V. Schlott “Single-Shot Electro-Optical Diagnostics at the ANKA Storage Ring” in: *Proceedings of the 3rd International Beam Instrumentation Conference (IBIC), 14.-18. September, Monterey, CA, USA 2014*
jacow.org/IBIC2014/papers/mopd17.pdf (see p. 84).
- [Jud14] V. Judin, M. Brosi, M. Caselle, E. Hertle, N. Hiller, A. Kopmann, A.-S. Müller, M. Schuh, N. J. Smale, J. L. Steinmann, and M. Weber “Studies of Bursting CSR in Multi-bunch Operation at the ANKA Storage Ring” in: *Proceedings of the 5th International Particle Accelerator Conference (IPAC), 15.-20. June, Dresden, Germany 2014*
DOI: 10.18429/JACoW-IPAC2014-MOPR0063.
- [Keh16] B. Kehrer, E. Blomley, M. Brosi, E. Bründermann, N. Hiller, A.-S. Müller, M. J. Nasse, M. Schedler, M. Schuh, P. Schönfeldt, P. Schütze, N. J. Smale, and J. L. Steinmann “Simultaneous Detection of Longitudinal and Transverse Bunch Signals at ANKA” in: *Proceedings of the 7th International Particle Accelerator Conference (IPAC), 8.-13. May, Busan, Korea 2016*
DOI: 10.18429/JACoW-IPAC2016-MOPMB014.
- [Keh17] B. Kehrer, E. Blomley, M. Brosi, E. Bründermann, N. Hiller, A.-S. Müller, M. J. Nasse, M. Schedler, M. Schuh, M. Schwarz, P. Schönfeldt, P. Schütze, N. J. Smale, and J. L. Steinmann “Time-Resolved Energy Spread Studies at

- the ANKA Storage Ring” in: *Proceedings of the 8th International Particle Accelerator Conference (IPAC), 14.-19. May, Copenhagen, Denmark 2017*
 DOI: 10.18429/JACoW-IPAC2017-M00CB1 (see pp. 80, 131, 138).
- [Keh18a] B. Kehrer, E. Blomley, M. Brosi, E. Bründermann, A.-S. Müller, M. Schuh, P. Schönfeldt, and J. L. Steinmann “Filling Pattern Measurements Using Dead-Time Corrected Single Photon Counting” in: *Proceedings of the 9th International Particle Accelerator Conference (IPAC), 29. April - 4. May, Vancouver, BC, Canada 2018*
 DOI: 10.18429/JACoW-IPAC2018-WEPAL027 (see p. 82).
- [Keh18b] B. Kehrer, M. Brosi, J. L. Steinmann, E. Blomley, E. Bründermann, M. Caselle, S. Funkner, N. Hiller, M. J. Nasse, G. Niehues, L. Rota, M. Schedler, P. Schönfeldt, M. Schuh, P. Schütze, M. Weber, and A.-S. Müller “Synchronous detection of longitudinal and transverse bunch signals at a storage ring” in: *Phys. Rev. Accel. Beams* 21 (2018), p. 102803
 DOI: 10.1103/PhysRevAccelBeams.21.102803 (see pp. 138, 182).
- [Mai18] C. Mai, B. Büsing, S. Khan, A. M. auf der Heide, B. Riemann, B. Sawadski, P. Ungelenk, M. Brosi, J. L. Steinmann, F. Frei, C. Gerth, M. Laabs, N. Neumann, and N. Lockmann “A Tunable Narrowband Source in the Sub-THz and THz Range at DELTA” in: *Proceedings of the 9th International Particle Accelerator Conference (IPAC), 29. April - 4. May, Vancouver, BC, Canada 2018*
 DOI: 10.18429/JACoW-IPAC2018-THPMK098 (see pp. 76, 137).
- [Mül13] A.-S. Müller, B. M. Balzer, M. Caselle, N. Hiller, M. Hofherr, K. Ilin, V. Judin, B. Kehrer, S. Marsching, S. Naknaimueang, M. J. Nasse, J. Raasch, A. Scheuring, M. Schuh, M. Schwarz, M. Siegel, N. J. Smale, J. L. Steinmann, P. Thoma, M. Weber, and S. Wuensch “Studies of Bunch-bunch Interactions in the ANKA Storage Ring with Coherent Synchrotron Radiation using an Ultra-fast Terahertz Detection System” in: *Proceedings of 4th International Particle Accelerator Conference (IPAC), 12.-17. Mai, Shanghai, China 2013*
jacow.org/IPAC2013/papers/mopea019.pdf.
- [Nie18] G. Niehues, M. Brosi, E. Bründermann, M. Caselle, S. Funkner, B. Kehrer, M. J. Nasse, M. Patil, L. Rota, J. L. Steinmann, M. Weber, and A.-S. Müller “Towards Single-Pulse Spectral Analysis of MHz-Repetition Rate Sources” in: *43rd International Conference on Infrared, Millimeter, and*

Terahertz Waves (IRMMW-THz) 2018

DOI: [10.1109/IRMMW-THz.2018.8510133](https://doi.org/10.1109/IRMMW-THz.2018.8510133).

- [Pap18] A. Papash, E. Blomley, M. Brosi, J. Gethmann, B. Kehrer, A.-S. Müller, M. Schuh, P. Schönenfeldt, and J. L. Steinmann “Non-Linear Optics and Low Alpha Operation at the Storage Ring KARA at KIT” in: *Proceedings of the 9th International Particle Accelerator Conference (IPAC), 29. April - 4. May, Vancouver, BC, Canada 2018*
DOI: [10.18429/JACoW-IPAC2018-THPMF070](https://doi.org/10.18429/JACoW-IPAC2018-THPMF070) (see p. 22).
- [Raa15a] J. Raasch, A. Kuzmin, P. Thoma, K. Ilin, M. Arndt, S. Wuensch, M. Siegel, J. Steinmann, A.-S. Müller, E. Roussel, C. Evain, C. Szwaj, S. Bielawski, T. Konomi, S.-I. Kimura, K. Katoh, M. Hosaka, N. Yamamoto, H. Zen, K. Iida, and B. Holzapfel “Investigation of the Electrical Field Sensitivity of Sub- μm Y-Ba-Cu-O Detectors” in: *IEEE Transactions on Applied Superconductivity* 25.3 (2015)
DOI: [10.1109/TASC.2014.2365138](https://doi.org/10.1109/TASC.2014.2365138) (see pp. 77, 137).
- [Raa15b] J. Raasch, A. Schmid, A. Kuzmin, K. Ilin, A. Arndt, S. Wünsch, M. Siegel, J. Steinmann, A.-S. Müller, K. Iida, and B. Holzapfel “Single-Shot Terahertz Spectroscopy with Picosecond Time Resolution” in: *8th Workshop on Infrared Microscopy and Spectroscopy using Accelerator-based Sources (WIRMS), 11.-15. Oktober, Long Island, NY, USA 2015* (see pp. 120, 137).
- [Raa16] J. Raasch, M. Arndt, G. Cinque, M. Frogley, B. Holzapfel, J. Hänisch, K. Ilin, K. Kuzmin, A.-S. Müller, A. Schmid, M. Siegel, J. L. Steinmann, and S. Wuensch “Single-Shot THz Spectroscopy for the Characterization of Single-Bunch Bursting CSR” in: *Proceedings of the 5th International Beam Instrumentation Conference (IBIC), 13.-18. September, Barcelona, Spain 2016*
DOI: [10.18429/JACoW-IBIC2016-WEPG56](https://doi.org/10.18429/JACoW-IBIC2016-WEPG56) (see pp. 120, 137).
- [Rou15a] E. Roussel, S. Bielawski, C. Evain, C. Szwaj, A. Borysenko, N. Hiller, A.-S. Müller, P. Schönenfeldt, and J. L. Steinmann “Electro-Optical Measurements of the Longitudinal Bunch Profile in the Near-Field on a Turn-by-Turn Basis at the Anka Storage Ring” in: *Proceedings of the 4th International Beam Instrumentation Conference (IBIC), 13.-17. September, Melbourne, Australia 2015*
DOI: [10.18429/JACoW-IBIC2015-MOPB006](https://doi.org/10.18429/JACoW-IBIC2015-MOPB006) (see p. 84).

- [Sch13] P. Schönfeldt, N. Hiller, V. Judin, A.-S. Müller, M. Schwarz, and J. L. Steinmann “Comparison of Different Approaches to Determine the Bursting Threshold at ANKA” in: *Proceedings of 4th International Particle Accelerator Conference (IPAC), 12.-17. Mai, Shanghai, China 2013* jacow.org/IPAC2013/papers/mopea020.pdf.
- [Sch14a] P. Schönfeldt, A. Borysenko, E. Hertle, N. Hiller, V. Judin, A.-S. Müller, S. Naknaimueang, M. Schuh, M. Schwarz, and J. L. Steinmann “Fluctuation of Bunch Length in Bursting CSR: Measurement and Simulation” in: *Proceedings of the 5th International Particle Accelerator Conference (IPAC), 15.-20. June, Dresden, Germany 2014* DOI: [10.18429/JACoW-IPAC2014-MOPRO068](https://doi.org/10.18429/JACoW-IPAC2014-MOPRO068).
- [Sch14c] J. Schwarzkopf, M. Brosi, C. Chang, E. Hertle, V. Judin, B. Kehrer, A.-S. Müller, M. Schuh, M. Schwarz, P. Schönfeldt, P. Schütze, J. L. Steinmann, and F. Caspers “Investigating Polarisation and Shape of Beam Microwave Signals at the ANKA Storage Ring” in: *Proceedings of the 5th International Particle Accelerator Conference (IPAC), 15.-20. June, Dresden, Germany 2014* DOI: [10.18429/JACoW-IPAC2014-MOPRO062](https://doi.org/10.18429/JACoW-IPAC2014-MOPRO062).
- [Sch16b] A. Schmid, M. Brosi, E. Bründermann, K. Ilin, B. Kehrer, K. Kuzmin, A.-S. Müller, J. Raasch, M. Schuh, P. Schönfeldt, M. Siegel, J. L. Steinmann, S. Wuensch, and S. Kuznetsov “Single-Shot Spectral Analysis of Synchrotron Radiation in THz Regime at ANKA” in: *Proceedings of the 7th International Particle Accelerator Conference (IPAC), 8.-13. May, Busan, Korea 2016* DOI: [10.18429/JACoW-IPAC2016-MOPMB016](https://doi.org/10.18429/JACoW-IPAC2016-MOPMB016) (see pp. 120, 137).
- [Sch16c] P. Schönfeldt, M. Brosi, A.-S. Müller, and J. L. Steinmann “A Parallelized Vlasov-Fokker-Planck-Solver for Desktop PCs” in: *Proceedings of the 7th International Particle Accelerator Conference (IPAC), 8.-13. May, Busan, Korea 2016* DOI: [10.18429/JACoW-IPAC2016-TUPOR005](https://doi.org/10.18429/JACoW-IPAC2016-TUPOR005).
- [Sch17a] A. Schmid, J. Raasch, A. Kuzmin, J. L. Steinmann, S. Wuensch, M. Arndt, M. Siegel, A. S. Mueller, G. Cinque, and M. Frogley “An Integrated Planar Array of Ultra-fast Y-Ba-Cu-O Detectors for Spectroscopic Measurements” in: *IEEE Transactions on Applied Superconductivity* 27.4 (2017), pp. 1–5 DOI: [10.1109/TASC.2016.2625763](https://doi.org/10.1109/TASC.2016.2625763) (see pp. 120, 137).

- [Sch17c] P. Schönfeldt, M. Brosi, M. Schwarz, J. L. Steinmann, and A.-S. Müller “Parallelized Vlasov-Fokker-Planck solver for desktop personal computers” in: *Phys. Rev. Accel. Beams* 20 (2017), p. 030704
DOI: [10.1103/PhysRevAccelBeams.20.030704](https://doi.org/10.1103/PhysRevAccelBeams.20.030704) (see p. 49).
- [Sch18b] P. Schönfeldt, T. Boltz, A. Mochihashi, A.-S. Müller, and J. L. Steinmann “Elaborated Modeling of Synchrotron Motion in Vlasov-Fokker-Planck Solvers” in: *Proceedings of the 9th International Particle Accelerator Conference (IPAC), 29. April - 4. May, Vancouver, BC, Canada 2018*
DOI: [10.18429/JACoW-IPAC2018-THPAK032](https://doi.org/10.18429/JACoW-IPAC2018-THPAK032) (see p. 152).
- [Sch18d] P. Schönfeldt, T. Boltz, A. Mochihashi, J. L. Steinmann, and A.-S. Müller “Elaborated Modeling of Synchrotron Motion in Vlasov-Fokker-Planck Solvers” in: *Journal of Physics: Conference Series* 1067.6 (2018), p. 062025
DOI: [10.1088/1742-6596/1067/6/062025](https://doi.org/10.1088/1742-6596/1067/6/062025).
- [Ste14] J. L. Steinmann, E. Hertle, N. Hiller, V. Judin, A.-S. Müller, M. Schuh, P. Schönfeldt, P. Schütze, and E. Bründermann “Spectral Analysis of Micro-Bunching Instabilities using Fast THz Detectors” in: *Proceedings of the 5th International Particle Accelerator Conference (IPAC), 15.-20. June, Dresden, Germany 2014*
DOI: [10.18429/JACoW-IPAC2014-THPME124](https://doi.org/10.18429/JACoW-IPAC2014-THPME124).
- [Ste15] J. L. Steinmann, M. Brosi, E. Bründermann, C. Caselle, E. Hertle, N. Hiller, B. Kehrer, A.-S. Müller, M. Schuh, M. Schwarz, P. Schönfeldt, P. Schütze, and J. L. Hesler “Non-interferometric Spectral Analysis of Synchrotron Radiation in the THz regime at ANKA” in: *Proceedings of the 6th International Particle Accelerator Conference (IPAC), 8.-13. May, Richmond, VA, USA 2015*
DOI: [10.18429/JACoW-IPAC2015-TUPWA043](https://doi.org/10.18429/JACoW-IPAC2015-TUPWA043) (see p. 140).
- [Ste16a] J. L. Steinmann, E. Blomley, M. Brosi, E. Bründermann, M. Caselle, N. Hiller, B. Kehrer, A.-S. Müller, M. Schedler, M. Schuh, M. Schwarz, P. Schönfeldt, and M. Siegel “Influence of Filling Pattern Structure on Synchrotron Radiation Spectrum at ANKA” in: *Proceedings of the 7th International Particle Accelerator Conference (IPAC), 8.-13. May, Busan, Korea 2016*
DOI: [10.18429/JACoW-IPAC2016-WEPOW015](https://doi.org/10.18429/JACoW-IPAC2016-WEPOW015) (see p. 140).

- [Ste16b] J. L. Steinmann, E. Blomley, M. Brosi, E. Bründermann, M. Caselle, J. L. Hesler, N. Hiller, B. Kehrer, Y.-L. Mathis, M. J. Nasse, J. Raasch, M. Schedler, P. Schönfeldt, M. Schuh, M. Schwarz, M. Siegel, N. Smale, M. Weber, and A.-S. Müller “Frequency-Comb Spectrum of Periodic-Patterned Signals” in: *Phys. Rev. Lett.* 117 (2016), p. 174802
DOI: [10.1103/PhysRevLett.117.174802](https://doi.org/10.1103/PhysRevLett.117.174802) (see pp. 140, 149, 156–158, 165).
- [Ste17] J. L. Steinmann, E. Blomley, M. Brosi, E. Bründermann, M. Caselle, B. Kehrer, A.-S. Müller, L. Rota, M. Schuh, P. Schönfeldt, M. Siegel, and M. Weber “4-Channel Single Shot and Turn-by-Turn Spectral Measurements of Bursting CSR” in: *Proceedings of the 8th International Particle Accelerator Conference (IPAC), 14.-19. May, Copenhagen, Denmark 2017*
DOI: [10.18429/JACoW-IPAC2017-MOPAB056](https://doi.org/10.18429/JACoW-IPAC2017-MOPAB056) (see p. 120).
- [Stel18a] J. L. Steinmann, M. Brosi, E. Bründermann, M. Caselle, S. Funkner, B. Kehrer, A.-S. Müller, M. J. Nasse, G. Niehues, L. Rota, M. Schuh, P. Schönfeldt, M. Siegel, and M. Weber “Turn-by-Turn Measurements for Systematic Investigations of the Micro-Bunching Instability” in: *Proceedings of the 60th ICFA Advanced Beam Dynamics Workshop (FLS'18), Shanghai, China 2018*
DOI: [10.18429/JACoW-FLS2018-TUP2WD03](https://doi.org/10.18429/JACoW-FLS2018-TUP2WD03).
- [Stel18b] J. L. Steinmann, T. Boltz, M. Brosi, E. Bründermann, M. Caselle, B. Kehrer, L. Rota, P. Schönfeldt, M. Schuh, M. Siegel, M. Weber, and A.-S. Müller “Continuous bunch-by-bunch spectroscopic investigation of the microbunching instability” in: *Phys. Rev. Accel. Beams* 21 (2018), p. 110705
DOI: [10.1103/PhysRevAccelBeams.21.110705](https://doi.org/10.1103/PhysRevAccelBeams.21.110705) (see p. 120).
- [Szw16] C. Szwaj, C. Evain, M. L. Parquier, S. Bielawski, E. Roussel, L. Manceron, J. B. Brubach, M. A. Tordeux, J. P. Ricaud, L. Cassinari, M. Labat, M. E. Couprie, P. Roy, A. Borysenko, N. Hiller, A. S. Müller, P. Schönfeldt, and J. L. Steinmann “Unveiling the complex shapes of relativistic electrons bunches, using photonic time-stretch electro-optic sampling” in: *2016 IEEE Photonics Society Summer Topical Meeting Series (SUM) 2016*
DOI: [10.1109/PHOSST.2016.7548779](https://doi.org/10.1109/PHOSST.2016.7548779).
- [Szw17] C. Szwaj, C. Evain, M. Le Parquier, S. Bielawski, E. Roussel, L. Manceron, J.-B. Brubach, M.-A. Tordeux, J.-P. Ricaud, L. Cassinari, M. Labat,

M.-E. Couprie, P. Roy, A. Borysenko, N. Hiller, A.-S. Müller, P. Schönfeld, and J. L. Steinmann “Unveiling relativistic electron bunch microstructures and their dynamical evolutions, using photonic time-stretch” in: *Proc. SPIE 10089: Real-time Measurements, Rogue Phenomena, and Single-Shot Applications II* 2017
DOI: 10.1117/12.2255723 (see p. 84).

Supervised Student Theses

- [Geg15] M. Geggus “Aufbau eines Teststandes für THz-Optiken mithilfe eines vakuumfähigen Martin-Puplett-Interferometers” Bachelor thesis Karlsruhe Institute of Technology, 2015 (see p. 94).
- [Mal15] L. Mall “Programmierung und Charakterisierung eines portablen Martin-Puplett-Interferometers zum Einsatz an ANKA” Bachelor thesis Karlsruhe Institute of Technology, 2015 (see p. 94).
- [Mar15] M. Martin “Untersuchung der Polarisationsabhängigkeit der Mikrowellenstrahlung am ANKA Speicherring” Bachelor thesis Karlsruhe Institute of Technology, 2015.
- [Sax17] C. Sax “Aufbau einer Messeinrichtung zur 2-D Charakterisierung von THz-Strahlprofilen” Bachelor thesis Karlsruhe Institute of Technology, 2017 (see pp. 69, 70, 82).

Bibliography

- [1] G. A. Schott “Electromagnetic Radiation” in: *Cambridge University Press* (1912) (see pp. 1, 57, 144, 166).
- [2] J. P. Blewett “Radiation Losses in the Induction Electron Accelerator” in: *Phys. Rev.* 69 (1946), pp. 87–95
DOI: [10.1103/PhysRev.69.87](https://doi.org/10.1103/PhysRev.69.87) (see p. 1).
- [3] F. R. Elder, A. M. Gurewitsch, R. V. Langmuir, and H. C. Pollock “Radiation from Electrons in a Synchrotron” in: *Phys. Rev.* 71 (1947), pp. 829–830
DOI: [10.1103/PhysRev.71.829.5](https://doi.org/10.1103/PhysRev.71.829.5) (see p. 1).
- [4] H. Winick “Fourth generation light sources” in: *Proceedings of the 1997 Particle Accelerator Conference* vol. 1 1997, pp. 37–41
DOI: [10.1109/PAC.1997.749539](https://doi.org/10.1109/PAC.1997.749539) (see p. 1).
- [5] G. Stupakov and S. Heifets “Beam instability and microbunching due to coherent synchrotron radiation” in: *Phys. Rev. ST Accel. Beams* 5 (2002), p. 054402
DOI: [10.1103/PhysRevSTAB.5.054402](https://doi.org/10.1103/PhysRevSTAB.5.054402) (see p. 2).
- [6] M. Venturini and R. Warnock “Bursts of Coherent Synchrotron Radiation in Electron Storage Rings: A Dynamical Model” in: *Phys. Rev. Lett.* 89 (2002), p. 224802
DOI: [10.1103/PhysRevLett.89.224802](https://doi.org/10.1103/PhysRevLett.89.224802) (see pp. 2, 49).
- [7] J. M. Byrd, W. P. Leemans, A. Loftsdottir, B. Marcelis, M. C. Martin, W. R. McKinney, F. Sannibale, T. Scarvie, and C. Steier “Observation of Broadband Self-Amplified Spontaneous Coherent Terahertz Synchrotron Radiation in a Storage Ring” in: *Phys. Rev. Lett.* 89 (2002), p. 224801
DOI: [10.1103/PhysRevLett.89.224801](https://doi.org/10.1103/PhysRevLett.89.224801) (see pp. 2, 49).

- [8] M. Abo-Bakr, J. Feikes, K. Holldack, P. Kuske, W. B. Peatman, U. Schade, G. Wüstefeld, and H.-W. Hübers “Brilliant, Coherent Far-Infrared (THz) Synchrotron Radiation” in: *Phys. Rev. Lett.* 90 (2003), p. 094801
DOI: [10.1103/PhysRevLett.90.094801](https://doi.org/10.1103/PhysRevLett.90.094801) (see p. 2).
- [9] M. Abo-Bakr, J. Feikes, K. Holldack, G. Wüstefeld, and H.-W. Hübers “Steady-State Far-Infrared Coherent Synchrotron Radiation detected at BESSY II” in: *Phys. Rev. Lett.* 88 (2002), p. 254801
DOI: [10.1103/PhysRevLett.88.254801](https://doi.org/10.1103/PhysRevLett.88.254801) (see p. 2).
- [10] M. Abo-Bakr, J. Feikes, K. Holldack, D. Ponwitz, G. Wuestefeld, and H.-W. Hübers “Coherent mm-Radiation Experiments at the BESSY II Storage Ring” in: *Proc. of the European Particle Accelerator Conference (EPAC2000)*, Wien 2000, pp. 720–722
epaper.kek.jp/e00/PAPERS/WEP3A11.pdf (see p. 2).
- [11] A. Hight Walker, U. Arp, G. Fraser, T. B. Lucatorto, and J. Wen “New infrared beamline at the NIST SURF II storage ring” in: *Proc SPIE* 3153 (1997), p. 42
DOI: [10.1117/12.290261](https://doi.org/10.1117/12.290261) (see pp. 2, 16).
- [12] U. Arp, G. T. Fraser, A. R. Hight Walker, T. B. Lucatorto, K. K. Lehmann, K. Harkay, N. Sereno, and K.-J. Kim “Spontaneous coherent microwave emission and the sawtooth instability in a compact storage ring” in: *Phys. Rev. ST Accel. Beams* 4 (2001), p. 054401
DOI: [10.1103/PhysRevSTAB.4.054401](https://doi.org/10.1103/PhysRevSTAB.4.054401) (see pp. 2, 49).
- [13] A.-S. Müller, Y.-L. Mathis, I. Birkel, B. Gasharova, C. Hirschmugl, E. Huttel, D. Moss, R. Rossmanith, and P. Wesolowski “Far Infrared Coherent Synchrotron Edge Radiation at ANKA” in: *Synchrotron Radiation News* 19.3 (2006), pp. 18–24
DOI: [10.1080/08940880600755202](https://doi.org/10.1080/08940880600755202) (see pp. 2, 62).
- [14] G. Carr, S. Kramer, J. Murphy, R. Lobo, and D. Tanner “Observation of coherent synchrotron radiation from the NSLS VUV ring” in: *Nuclear Instruments and Methods in Physics Research Section A: Accelerators, Spectrometers, Detectors and Associated Equipment* 463.1 (2001), pp. 387–392
DOI: [10.1016/S0168-9002\(01\)00521-6](https://doi.org/10.1016/S0168-9002(01)00521-6) (see p. 2).
- [15] G. Carr, S. Kramer, J. Murphy, J. LaVeigne, R. Lobo, D. Reitze, and D. Tanner “Investigation of Coherent Emission from the NSLS VUV Ring” in: *Proceedings*

- of the 1999 Particle Accelerator Conference, New York* (1999)
jacow.org/p99/PAPERS/TUBL4.PDF (see p. 2).
- [16] A. Mochihashi, M. Hosaka, M. Katoh, S. Kimura, M. Shimada, T. Takahashi, and Y. Takashima “Observation of THz Synchrotron Radiation Burst in UVSOR-II Electron Storage Ring” in: *10th European Particle Accelerator Conference, Edinburgh, UK, 26 - 30 Jun 2006* (2006)
jacow.org/e06/PAPERS/THPLS042.PDF (see p. 2).
- [17] E. Roussel, C. Evain, C. Szwaj, S. Bielawski, J. Raasch, P. Thoma, A. Scheuring, M. Hofherr, K. Ilin, S. Wünsch, M. Siegel, M. Hosaka, N. Yamamoto, Y. Takashima, H. Zen, T. Konomi, M. Adachi, S. Kimura, and M. Katoh “Microbunching Instability in Relativistic Electron Bunches: Direct Observations of the Microstructures Using Ultrafast YBCO Detectors” in: *Phys. Rev. Lett.* 113 (2014), p. 094801
DOI: [10.1103/PhysRevLett.113.094801](https://doi.org/10.1103/PhysRevLett.113.094801) (see p. 2).
- [18] Åke Andersson, M. S. Johnson, and B. Nelander “Coherent synchrotron radiation in the far-infrared from a 1 mm electron bunch” in: *Optical Engineering* 39 (2000)
DOI: [10.1117/1.1327498](https://doi.org/10.1117/1.1327498) (see p. 2).
- [19] G. Rehm, A. Morgan, R. Bartolini, I. Martin, and P. Karataev “Ultra-fast mm-wave Detectors for Observation of Microbunching Instabilities in the Diamond Storage Ring” in: *Proc. 9th European Workshop on Beam Diagnostics and Instrumentation for Particle Accelerators (DIPAC 09)* (2009)
jacow.org/d09/papers/tupd32.pdf (see p. 2).
- [20] W. Shields, R. Bartolini, G. Boorman, P. Karataev, A. Lyapin, J. Puntree, and G. Rehm “Microbunch Instability Observations from a THz Detector at Diamond Light Source” in: *Journal of Physics: Conference Series* 357.1 (2012), p. 012037
DOI: [10.1088/1742-6596/357/1/012037](https://doi.org/10.1088/1742-6596/357/1/012037) (see pp. 2, 103).
- [21] J. Feikes, M. von Hartrott, M. Ries, P. Schmid, G. Wüstefeld, A. Hoehl, R. Klein, R. Müller, and G. Ulm “Metrology Light Source: The first electron storage ring optimized for generating coherent THz radiation” in: *Phys. Rev. ST Accel. Beams* 14 (2011), p. 030705
DOI: [10.1103/PhysRevSTAB.14.030705](https://doi.org/10.1103/PhysRevSTAB.14.030705) (see pp. 2, 103).

- [22] C. Evain, J. Barros, A. Loulergue, M. A. Tordeux, R. Nagaoka, M. Labat, L. Cassinari, G. Creff, L. Manceron, J. B. Brubach, P. Roy, and M. E. Couprie “Spatio-temporal dynamics of relativistic electron bunches during the micro-bunching instability in storage rings” in: *EPL (Europhysics Letters)* 98.4 (2012), p. 40006
DOI: 10.1209/0295-5075/98/40006 (see pp. 2, 103).
- [23] F. Wang, D. Cheever, M. Farkhondeh, W. Franklin, E. Ihloff, J. van der Laan, B. McAllister, R. Milner, C. Tschalaer, D. Wang, D. F. Wang, A. Zolfaghari, T. Zwart, G. L. Carr, B. Podobedov, and F. Sannibale “Coherent THz Synchrotron Radiation from a Storage Ring with High-Frequency RF System” in: *Phys. Rev. Lett.* 96 (2006), p. 064801
DOI: 10.1103/PhysRevLett.96.064801 (see p. 2).
- [24] E. Karantzoulis, G. Penco, A. Perucchi, and S. Lupi “Characterization of coherent THz radiation bursting regime at Elettra” in: *Infrared Physics & Technology* 53.4 (2010), pp. 300–303
DOI: 10.1016/j.infrared.2010.04.006 (see p. 2).
- [25] B. E. Billingshurst, J. C. Bergstrom, C. Baribeau, T. Batten, T. E. May, J. M. Vogt, and W. A. Wurtz “Longitudinal bunch dynamics study with coherent synchrotron radiation” in: *Phys. Rev. Accel. Beams* 19 (2016), p. 020704
DOI: 10.1103/PhysRevAccelBeams.19.020704 (see p. 2).
- [26] N. G. Lehtinen *Conversion of formulae and quantities between unit systems* http 2010
n1pc.stanford.edu/nleht/Science/reference/conversion.pdf (see p. 5).
- [27] E. W. Weisstein *Fourier Transform* MathWorld—A Wolfram Web Resource. <http://mathworld.wolfram.com/FourierTransform.html> (visited on 10/01/2018) (see p. 5).
- [28] R. N. Bracewell *The Fourier Transform and Its Applications* 3rd ed. McGraw-Hill New York, 2000 ISBN: 978-0073039381 (see pp. 6, 145, 146).
- [29] H. Wiedemann *Particle Accelerator Physics* 3rd ed. Springer, Berlin, 2007
DOI: 10.1007/978-3-319-18317-6 (see pp. 6, 18, 80, 144).
- [30] N. Hiller “Electro-Optical Bunch Length Measurements at the ANKA Storage Ring” PhD thesis Karlsruhe Institute of Technology (KIT), 2013
publikationen.bibliothek.kit.edu/1000041159/3096634 (see pp. 7, 53, 84, 152, 153).

-
- [31] M. S. Livingston “Early History of Particle Accelerators” in: ed. by L. Marton and C. Marton vol. 50 Advances in Electronics and Electron Physics Academic Press, 1980, pp. 1–88
DOI: 10.1016/S0065-2539(08)61061-6 (see p. 9).
 - [32] J. D. Cockcroft and E. T. S. Walton “Disintegration of lithium by swift protons” in: *Nature* 129.3261 (1932), pp. 649–649
DOI: 10.1038/129649a0 (see p. 9).
 - [33] Nobel Media AB, 2014 *The Nobel Prize in Physics 1951*
www.nobelprize.org/prizes/physics/1951 (visited on 12/01/2018) (see p. 9).
 - [34] R. Widerøe “Über ein neues Prinzip zur Herstellung hoher Spannungen” in: *Archiv für Elektrotechnik* 21.4 (1928), pp. 387–406 ISSN: 1432-0487
DOI: 10.1007/BF01656341 (see p. 10).
 - [35] R. Widerøe *The Infancy of particle accelerators: Life and work of Rolf Widerøe* ed. by P. Waloschek Braunschweig, Germany: Vieweg, 1994
DOI: 10.1007/978-3-663-05244-9 (see p. 10).
 - [36] E. O. Lawrence and M. S. Livingston “The Production of High Speed Light Ions Without the Use of High Voltages” in: *Phys. Rev.* 40 (1932), pp. 19–35
DOI: 10.1103/PhysRev.40.19 (see p. 11).
 - [37] V. I. Veksler “A New Method of Accelerating Relativistic Particles.” in: *Doklady Akad. Nauk SSSR (Proceedings of the USSR Academy of Sciences) (in Russian)* 43 (1944) <http://lhe.jinr.ru/rus/veksler/wv0/publikacii/1944Veksler.pdf> (see p. 11).
 - [38] V. I. Veksler “About the New Method of Accelerating Relativistic Particles” in: *Doklady Akad. Nauk SSSR (Proceedings of the USSR Academy of Sciences) (in Russian)* 44 (1944) <http://www1.jinr.ru/Books/veksler/13.pdf> (see p. 11).
 - [39] V. I. Veksler “A new method of acceleration of relativistic particles” in: *J. Phys.* 9 (1945), pp. 153–158
cds.cern.ch/record/109364 (see p. 11).
 - [40] J. D. Jackson “Classical Electrodynamics, 3rd ed.” in: *American Journal of Physics* 67.9 (1999), pp. 841–842
DOI: 10.1119/1.19136 (see p. 11).

- [41] A. Hofmann *The Physics of Synchrotron Radiation*: Cambridge Monographs on Particle Physics, Nuclear Physics and Cosmology Cambridge University Press, 2004
DOI: 10.1017/CBO9780511534973 (see p. 11).
- [42] A. Liénard “Champ électrique et Magnétique” in: *Champ électrique et magnétique produit par une charge électrique concentrée en un point et animée d'un mouvement quelconque* 16.27-29 (1898), pp. 5–14, 53–59, 106–112
documents.epfl.ch/users/v/ve/velo/www/ALienard-Champ_electrique_et_magnetique.pdf (see pp. 11, 12).
- [43] E. Wiechert “Elektrodynamische Elementargesetze” in: *Archives Néerlandaises des Sciences Exactes et Naturelles* vol. 5 2 1900, p. 549
archive.org/details/archivesnerlan0205holl (see p. 11).
- [44] J. Larmor “LXIII. On the theory of the magnetic influence on spectra; and on the radiation from moving ions” in: *Philosophical Magazine Series 5* 44.271 (1897), pp. 503–512
DOI: 10.1080/14786449708621095 (see p. 11).
- [45] K. Wille *Physik der Teilchenbeschleuniger und Synchrotronstrahlungsquellen* 1st ed. Vieweg+Teubner Verlag, Wiesbaden, 1996
DOI: 10.1007/978-3-663-11850-3 (see pp. 12, 13, 60).
- [46] M. Sands “The Physics of Electron Storage Rings: An Introduction” in: *Conf. Proc. C6906161* (1969), pp. 257–411
slac.stanford.edu/pubs/slacreports/reports02/slac-r-121.pdf (see pp. 14, 174).
- [47] K. Y. Ng “Physics of Intensity Dependent Beam Instabilities” in: *U.S. Particle Accelerator School (USPAS 2002) Long Beach, California, January 14-25, 2002* 2002
DOI: 10.1142/5835 (see p. 15).
- [48] F. Perez, I. Birkel, E. Huttel, A. S. Moller, and M. Pont “Beam size and bunch length measurements at the Anka storage ring” in: *Proceedings of the 2003 Particle Accelerator Conference* vol. 5 2003, pp. 3276–3278
DOI: 10.1109/PAC.2003.1289886 (see p. 21).
- [49] V. G. Vaccaro *Longitudinal instability of a coasting beam above transition, due to the action of lumped discontinuities* tech. rep. CERN-ISR-RF-66-35. ISR-RF-66-35 Geneva: CERN, 1966
cds.cern.ch/record/1216806 (see p. 23).

-
- [50] A. W. Chao *Physics of collective beam instabilities in high-energy accelerators* 1993 www.slac.stanford.edu/~achao/wileybook.html (see p. 24).
 - [51] Y. S. Derbenev, J. Rossbach, E. L. Saldin, and V. D. Shiltsev *Microbunch radiative tail-head interaction* tech. rep. 1995 cds.cern.ch/record/291102 (see pp. 25, 28).
 - [52] J. B. Murphy, S. Krinsky, and R. L. Gluckstern “Longitudinal wake field for an electron moving on a circular orbit” in: *Part. Accel.* 57 (1997), pp. 9–64 cds.cern.ch/record/1120287 (see pp. 25, 30).
 - [53] R. L. Warnock and P. L. Morton “Fields Excited by a Beam in a Smooth Toroidal Chamber: Pt. 1. Longitudinal Coupling Impedance” in: *Part. Accel.* 25 (1990), p. 113 slac.stanford.edu/pubs/slacpubs/4500/slac-pub-4562.pdf (see pp. 25, 29).
 - [54] K.-Y. Ng “Resonant Impedance in a Toroidal Beam Pipe” in: *Part. Accel.* 25 (1990), p. 153 lib-extopc.kek.jp/preprints/PDF/1988/8808/8808025.pdf (see p. 25).
 - [55] E. Saldin, E. Schneidmiller, and M. Yurkov “On the coherent radiation of an electron bunch moving in an arc of a circle” in: *Nuclear Instruments and Methods in Physics Research Section A: Accelerators, Spectrometers, Detectors and Associated Equipment* 398.2 (1997), pp. 373–394 ISSN: 0168-9002 DOI: 10.1016/S0168-9002(97)00822-X (see p. 25).
 - [56] M. Dohlus and T. Limberg “Emittance growth due to wake fields on curved bunch trajectories” in: *Nuclear Instruments and Methods in Physics Research Section A: Accelerators, Spectrometers, Detectors and Associated Equipment* 393.1 (1997), pp. 494–499 ISSN: 0168-9002 DOI: 10.1016/S0168-9002(97)00552-4 (see p. 25).
 - [57] G. Stupakov and D. Zhou “Analytical theory of coherent synchrotron radiation wakefield of short bunches shielded by conducting parallel plates” in: *Phys. Rev. Accel. Beams* 19 (2016), p. 044402 DOI: 10.1103/PhysRevAccelBeams.19.044402 (see p. 25).
 - [58] T. Agoh “Dynamics of coherent synchrotron radiation by paraxial approximation” http PhD thesis University of Tokyo, 2004 acc-physics.kek.jp/Ago/Agoh_thesis.pdf (see pp. 25, 28).

- [59] T. Agoh “Steady fields of coherent synchrotron radiation in a rectangular pipe” in: *Phys. Rev. ST Accel. Beams* 12 (2009), p. 094402
DOI: [10.1103/PhysRevSTAB.12.094402](https://doi.org/10.1103/PhysRevSTAB.12.094402) (see pp. 25–30).
- [60] G. V. Stupakov and I. A. Kotelnikov “Calculation of coherent synchrotron radiation impedance using the mode expansion method” in: *Phys. Rev. ST Accel. Beams* 12 (2009), p. 104401
DOI: [10.1103/PhysRevSTAB.12.104401](https://doi.org/10.1103/PhysRevSTAB.12.104401) (see p. 28).
- [61] D. Zhou “Coherent Synchrotron Radiation and Microwave Instability in Electron Storage Rings” PhD thesis Sokendai, Tsukuba, 2011
inspirehep.net/record/1313669/files/thesis_dmzhou_final.pdf (see p. 28).
- [62] R. Warnock, R. Ruth, M. Venturini, and J. A. Ellison “Impedance description of coherent synchrotron radiation with account of bunch deformation” in: *Phys. Rev. ST Accel. Beams* 8 (2005), p. 014402
DOI: [10.1103/PhysRevSTAB.8.014402](https://doi.org/10.1103/PhysRevSTAB.8.014402) (see p. 29).
- [63] A. Faltens and L. J. Laslett “The Longitudinal Electric Field Of A Modulated Straight Relativistic Beam Moving Parallel To A Perfectly Conducting Infinite Plane” in: *UCRL-ERAN-188* (1972) (see p. 29).
- [64] S. A. Kheifets and B. W. Zotter “Shielding effects on coherent synchrotron radiation” in: CERN-SL-95-92-AP (1995), 11 p
cds.cern.ch/record/292013 (see p. 29).
- [65] S. Heifets and A. Michailichenko “On the impedance due to synchrotron radiation” in: *Conference Record of the 1991 IEEE Particle Accelerator Conference 1991*, 458–460 vol.1
DOI: [10.1109/PAC.1991.164333](https://doi.org/10.1109/PAC.1991.164333) (see p. 30).
- [66] D. Sagan, G. Hoffstaetter, C. Mayes, and U. Sae-Ueng “Extended one-dimensional method for coherent synchrotron radiation including shielding” in: *Phys. Rev. ST Accel. Beams* 12 (2009), p. 040703
DOI: [10.1103/PhysRevSTAB.12.040703](https://doi.org/10.1103/PhysRevSTAB.12.040703) (see p. 30).
- [67] D. J. Wingham “Electron synchrotron radiation in the far infrared” in: *Phys. Rev. D* 35 (1987), pp. 2584–2594
DOI: [10.1103/PhysRevD.35.2584](https://doi.org/10.1103/PhysRevD.35.2584) (see p. 30).

- [68] J. Schwinger “On the Classical Radiation of Accelerated Electrons” in: *Phys. Rev.* 75 (1949), pp. 1912–1925
DOI: 10.1103/PhysRev.75.1912 (see pp. 31, 57).
- [69] R. Li and C.-Y. Tsai “CSR Impedance for Non-Ultrarelativistic Beams” in: *Proceedings of the 6th International Particle Accelerator Conference (IPAC)*, 8.-13. May, 2015, Richmond, VA, USA 2015, MOPMN004
DOI: 10.18429/JACoW-IPAC2015-MOPMN004 (see p. 31).
- [70] R. A. Bosch “Edge radiation in an electron storage ring” in: *Il Nuovo Cimento D* 20.4 (1998), pp. 483–493 ISSN: 1826-9893
DOI: 10.1007/BF03185543 (see pp. 33, 60, 61).
- [71] E. Saldin, E. Schneidmiller, and M. Yurkov “Klystron instability of a relativistic electron beam in a bunch compressor” in: *Nuclear Instruments and Methods in Physics Research Section A: Accelerators, Spectrometers, Detectors and Associated Equipment* 490.1 (2002), pp. 1–8 ISSN: 0168-9002
DOI: 10.1016/S0168-9002(02)00905-1 (see p. 33).
- [72] R. A. Bosch, K. J. Kleman, and J. Wu “Modeling two-stage bunch compression with wakefields: Macroscopic properties and microbunching instability” in: *Phys. Rev. ST Accel. Beams* 11 (2008), p. 090702
DOI: 10.1103/PhysRevSTAB.11.090702 (see p. 34).
- [73] R. A. Bosch “Longitudinal wake of a bunch of suddenly accelerated electrons within the radiation formation zone” in: *Phys. Rev. ST Accel. Beams* 10 (2007), p. 050701
DOI: 10.1103/PhysRevSTAB.10.050701 (see p. 34).
- [74] L. Wang and Y. Li “Analysis of the longitudinal space charge impedance of a round uniform beam inside parallel plates and rectangular chambers” in: *Phys. Rev. ST Accel. Beams* 18 (2015), p. 024201
DOI: 10.1103/PhysRevSTAB.18.024201 (see p. 34).
- [75] Z. Huang, M. Borland, P. Emma, J. Wu, C. Limborg, G. Stupakov, and J. Welch “Suppression of microbunching instability in the linac coherent light source” in: *Phys. Rev. ST Accel. Beams* 7 (2004), p. 074401
DOI: 10.1103/PhysRevSTAB.7.074401 (see p. 34).
- [76] K. L. F. Bane and M. Sands “The Short-Range Resistive Wall Wakefields” in: *AIP Conf. Proc.* 367 (1996), pp. 131–149
DOI: 10.1063/1.50300 (see p. 35).

- [77] R. Li and S. Benson “Studies of resistive wall heating at JLAB FEL” in: *Proceedings of the 4th International Particle Accelerator Conference (IPAC) 12.-17. May, 2013, Shanghai, China* 2013, pp. 1868–1870 jacow.org/ipac2013/papers/tupwa071.pdf (see p. 35).
- [78] H. Schlarb “Resistive Wall Wake Fields” http://tesla.desy.de/~schlarb/diplom_h.ps Universitat Hamburg, 1997 (see p. 35).
- [79] R. L. Gluckstern “Longitudinal impedance of a periodic structure at high frequency” in: *Phys. Rev. D* 39 (1989), pp. 2780–2783 DOI: [10.1103/PhysRevD.39.2780](https://doi.org/10.1103/PhysRevD.39.2780) (see p. 38).
- [80] K. Bane “The Impedance of Flat Metallic Plates with Small Corrugations” in: *CERN Yellow Reports: Conference Proceedings* 1.0 (2018) ISSN: 2519-8092 DOI: [10.23732/CYRCP-2018-001.5](https://doi.org/10.23732/CYRCP-2018-001.5) (see p. 38).
- [81] K. Bane, G. Stupakov, and E. Gjonaj “Joule heating in a flat dechirper” in: *Phys. Rev. Accel. Beams* 20 (2017), p. 054403 DOI: [10.1103/PhysRevAccelBeams.20.054403](https://doi.org/10.1103/PhysRevAccelBeams.20.054403) (see p. 38).
- [82] K. L. F. Bane and P. B. Wilson “Bunch lengthening due to potential well distortion from cylindrical cavities with beam ports” in: *IEEE Transactions on Nuclear Science* 24.3 (1977), pp. 1485–1486 DOI: [10.1109/TNS.1977.4328986](https://doi.org/10.1109/TNS.1977.4328986) (see p. 39).
- [83] J. Haissinski “Exact longitudinal equilibrium distribution of stored electrons in the presence of self-fields” in: *Il Nuovo Cimento B (1971-1996)* 18.1 (1973), pp. 72–82 ISSN: 1826-9877 DOI: [10.1007/BF02832640](https://doi.org/10.1007/BF02832640) (see pp. 39, 43).
- [84] P. Schonfeldt “Simulation and measurement of the dynamics of ultra-short electron bunch profiles for the generation of coherent THz radiation” PhD thesis Karlsruhe Institute of Technology (KIT), 2018 DOI: [10.5445/IR/1000084466](https://doi.org/10.5445/IR/1000084466) (see pp. 41, 49).
- [85] R. L. Warnock and J. A. Ellison “A General method for propagation of the phase space distribution, with application to the sawtooth instability” in: *The physics of high brightness beams. Proceedings, 2nd ICFA Advanced Accelerator Workshop, Los Angeles, USA, November 9-12, 1999* <http://slac.stanford.edu/pubs/slacpubs/8250/slac-pub-8404.pdf> (see pp. 41, 43, 47).

- [86] A. A. Vlasov “The vibrational properties of an electron gas” in: *Phys. Usp.* 10.6 (1968), pp. 721–733
DOI: 10.1070/PU1968v010n06ABEH003709 (see p. 41).
- [87] K. Y. Ng *Physics of intensity dependent beam instabilities* 2006
www.worldscibooks.com/physics/5835.html (see p. 41).
- [88] K. L. F. Bane, Y. Cai, and G. Stupakov “Threshold studies of the microwave instability in electron storage rings” in: *Phys. Rev. ST Accel. Beams* 13 (2010), p. 104402
DOI: 10.1103/PhysRevSTAB.13.104402 (see pp. 42, 46, 47).
- [89] K. Bane, S. Krinsky, and J. B. Murphy “Longitudinal potential well distortion due to the synchrotron radiation wakefield” in: *AIP Conference Proceedings* 367.1 (1996), pp. 191–198
DOI: 10.1063/1.50304 (see p. 43).
- [90] R. Warnock and K. Bane “Numerical solution of the Haïssinski equation for the equilibrium state of a stored electron beam” in: *Phys. Rev. Accel. Beams* 21 (2018), p. 124401
DOI: 10.1103/PhysRevAccelBeams.21.124401 (see p. 43).
- [91] A. Chao, B. Chen, and K. Oide “A weak microwave instability with potential well distortion and radial mode coupling” in: *Proceedings Particle Accelerator Conference* vol. 5 1995, 3040–3042 vol.5
DOI: 10.1109/PAC.1995.505777 (see p. 45).
- [92] E. Keil and W. Schnell *Concerning Longitudinal Stability in the ISR* tech. rep. CERN-ISR-TH-RF-69-48, 1969
cds.cern.ch/record/1229157 (see p. 46).
- [93] D. Boussard *Observation of microwave longitudinal instabilities in the CPS* tech. rep. CERN-LabII-RF-INT-75-2 CERN, 1975
cds.cern.ch/record/872559 (see p. 46).
- [94] F. J. Sacherer “A longitudinal stability criterion for bunched beams” in: CERN-MPS-INT-BR-73-3 (1973)
cds.cern.ch/record/322639 (see p. 46).
- [95] A. W. Chao and J. Gareyte “Scaling law for bunch lengthening in SPEAR II” in: *Part. Accel.* 25 (1990), pp. 229–234
cds.cern.ch/record/210836 (see p. 46).

- [96] N. Hiller, S. Hillenbrand, A. Hofmann, E. Huttel, V. Judin, B. Kehrer, M. Klein, S. Marsching, A.-S. Müller, A. Plech, N. Smale, K. Sonnad, and P. Tavares “Observation of Bunch Deformation at the ANKA Storage Ring” in: *Proceedings of the 1st International Particle Accelerator Conference (IPAC)*, 23.-28. May, 2010, Kyoto, Japan 2010
jacow.org/IPAC10/papers/wepea020.pdf (see p. 46).
- [97] S. Krinsky and J. M. Wang “Longitudinal Instabilities with a Non-Harmonic rf Potential” in: *IEEE Trans. Nucl. Sci.* 30 (1983), pp. 2492–2494
DOI: [10.1109/TNS.1983.4332858](https://doi.org/10.1109/TNS.1983.4332858) (see p. 46).
- [98] K. Oide and K. Yokoya “Longitudinal single bunch instability in electron storage rings” in: *KEK-Preprint* (1990)
cds.cern.ch/record/208816 (see p. 47).
- [99] S. Heifets “Tracking code for microwave instability” in: *ILC DAMPING RINGS R&D WORKSHOP - ILCDR06* vol. 25 1990, p. 113
slac.stanford.edu/pubs/slacpubs/12000/slac-pub-12122.pdf (see p. 47).
- [100] Y. Cai “Scaling law of coherent synchrotron radiation in a rectangular chamber” in: *Phys. Rev. ST Accel. Beams* 17 (2014), p. 020702
DOI: [10.1103/PhysRevSTAB.17.020702](https://doi.org/10.1103/PhysRevSTAB.17.020702) (see p. 48).
- [101] C. J. Hirschmugl, M. Sagurton, and G. P. Williams “Multiparticle coherence calculations for synchrotron-radiation emission” in: *Phys. Rev. A* 44 (1991), pp. 1316–1320
DOI: [10.1103/PhysRevA.44.1316](https://doi.org/10.1103/PhysRevA.44.1316) (see p. 52).
- [102] M. Clemens, M. Dohlus, S. Lange, G. Pöplau, T. Limberg, and U. van Rienen “Microbunch Amplification in the European XFEL.” in: *TESLA-FEL Reports* (2009)
bib-pubdb1.desy.de/record/87933 (see p. 52).
- [103] J. S. Nodwick and D. S. Saxon “Suppression of Coherent Radiation by Electrons in a Synchrotron” in: *Phys. Rev.* 96 (1954), pp. 180–184
DOI: [10.1103/PhysRev.96.180](https://doi.org/10.1103/PhysRev.96.180) (see pp. 52, 57).
- [104] T. Nakazato, M. Oyamada, N. Niimura, S. Urasawa, O. Konno, A. Kagaya, R. Kato, T. Kamiyama, Y. Torizuka, T. Nanba, Y. Kondo, Y. Shibata, K. Ishi, T. Ohsaka, and M. Ikezawa “Observation of coherent synchrotron radiation”

- in: *Phys. Rev. Lett.* 63 (1989), pp. 1245–1248
DOI: 10.1103/PhysRevLett.63.1245 (see p. 54).
- [105] L. I. Schiff “Production of Particle Energies beyond 200 Mev” in: *Review of Scientific Instruments* 17.1 (1946), pp. 6–14
DOI: 10.1063/1.1770395 (see p. 57).
- [106] F. C. Michel “Intense Coherent Submillimeter Radiation in Electron Storage Rings” in: *Phys. Rev. Lett.* 48 (1982), pp. 580–583
DOI: 10.1103/PhysRevLett.48.580 (see p. 57).
- [107] R. Lai and A. Sievers “On using the coherent far IR radiation produced by a charged-particle bunch to determine its shape: I Analysis” in: *Nuclear Instruments and Methods in Physics Research Section A: Accelerators, Spectrometers, Detectors and Associated Equipment* 397.2–3 (1997), pp. 221–231 ISSN: 0168-9002
DOI: 10.1016/S0168-9002(97)00690-6 (see p. 57).
- [108] R. Kato, T. Nakazato, M. Oyamada, S. Urasawa, T. Yamakawa, M. Yoshioka, M. Ikezawa, K. Ishi, T. Kanai, Y. Shibata, and T. Takahashi “Suppression of coherent synchrotron radiation in conducting boundaries” in: *Proceedings of International Conference on Particle Accelerators* 1993, 1617–1619 vol.2
DOI: 10.1109/PAC.1993.308543 (see p. 58).
- [109] R. Kato, T. Nakazato, M. Oyamada, S. Urasawa, T. Yamakawa, M. Yoshioka, M. Ikezawa, K. Ishi, T. Kanai, Y. Shibata, and T. Takahashi “Suppression and enhancement of coherent synchrotron radiation in the presence of two parallel conducting plates” in: *Phys. Rev. E* 57 (1998), pp. 3454–3460
DOI: 10.1103/PhysRevE.57.3454 (see p. 58).
- [110] W. D. Duncan and G. P. Williams “Infrared synchrotron radiation from electron storage rings” in: *Appl. Opt.* 22.18 (1983), pp. 2914–2923
DOI: 10.1364/AO.22.002914 (see p. 60).
- [111] G. Geloni, V. Kocharyan, E. Saldin, E. Schneidmiller, and M. Yurkov “Theory of edge radiation. Part I: Foundations and basic applications” in: *Nuclear Instruments and Methods in Physics Research Section A: Accelerators, Spectrometers, Detectors and Associated Equipment* 605.3 (2009), pp. 409–429 ISSN: 0168-9002
DOI: 10.1016/j.nima.2009.03.240 (see p. 61).
- [112] O. Chubar “Simulation of emission and propagation of coherent synchrotron radiation wave fronts using the methods of wave optics” in: *Infrared Physics & Technology* 49.1–2 (2006) International Workshop on Infrared Microscopy and

- Spectroscopy with Accelerator-Based Sources., pp. 96–103 ISSN: 1350-4495
DOI: [10.1016/j.infrared.2006.01.010](https://doi.org/10.1016/j.infrared.2006.01.010) (see p. 61).
- [113] O. V. Chubar and N. V. Smolyakov “Generation of intensive long-wavelength edge radiation in high-energy electron storage rings” in: *Proceedings of International Conference on Particle Accelerators* 1993, 1626–1628 vol.2
DOI: [10.1109/PAC.1993.308540](https://doi.org/10.1109/PAC.1993.308540) (see p. 61).
- [114] Y.-L. Mathis, B. Gasharova, and D. Moss “Terahertz Radiation at ANKA, the New Synchrotron Light Source in Karlsruhe” English in: *Journal of Biological Physics* 29.2-3 (2003), pp. 313–318 ISSN: 0092-0606
DOI: [10.1023/A:1024429801191](https://doi.org/10.1023/A:1024429801191) (see p. 62).
- [115] P. Rieger, Y.-L. Mathis, B. Gasharova, and D. Moss “Simulation of photon intensity distributions to facilitate the design of beamlines at accelerator-based IR/THz sources” in: *Vibrational Spectroscopy* 75. Supplement C (2014), pp. 196–202 ISSN: 0924-2031
DOI: [10.1016/j.vibspec.2014.06.005](https://doi.org/10.1016/j.vibspec.2014.06.005) (see p. 68).
- [116] E. Bründermann, H.-W. Hübers, and M. F. Kimmitt *Terahertz Techniques* 1st ed. Springer Series in Optical Sciences 151 Springer-Verlag Berlin Heidelberg, 2012
ISBN: 978-3-642-02591-4
DOI: [10.1007/978-3-642-02592-1](https://doi.org/10.1007/978-3-642-02592-1) (see pp. 73, 185).
- [117] C. Sydlo, O. Cojocari, D. Schçnherr, T. Goebel, P. Meissner, and H. Hartnagel “Fast THz detectors based on InGaAs Schottky Diodes” in: *Frequenz* 62.5-6 (2008), pp. 107–110
DOI: [10.1515/FREQ.2008.62.5-6.107](https://doi.org/10.1515/FREQ.2008.62.5-6.107) (see p. 74).
- [118] J. L. Hesler and T. W. Crowe “NEP and responsivity of THz zero-bias Schottky diode detectors” in: *Joint 32nd International Conference on Infrared and Millimeter Waves and the 15th International Conference on Terahertz Electronics* 2007, pp. 844–845
DOI: [10.1109/ICIMW.2007.4516758](https://doi.org/10.1109/ICIMW.2007.4516758) (see p. 74).
- [119] W. L. Bishop, E. R. Meiburg, R. J. Mattauch, T. W. Crowe, and L. Poli “A micron-thickness, planar Schottky diode chip for terahertz applications with theoretical minimum parasitic capacitance” in: *IEEE International Digest on Microwave Symposium* vol. 3 1990, pp. 1305–1308
DOI: [10.1109/MWSYM.1990.99818](https://doi.org/10.1109/MWSYM.1990.99818) (see p. 74).

- [120] J. L. Hesler and T. W. Crowe “Responsivity and Noise Measurements of Zero-Bias Schottky Diode Detectors” in: *18th International Symposium on Space Terahertz Technology 2007*, pp. 89–92
www.nrao.edu/meetings/isstt/papers/2007/2007089092.pdf (see p. 74).
- [121] J. L. Hesler, L. Liu, H. Xu, Y. Duan, and R. M. Weikle “The development of quasi-optical THz detectors” in: *33rd International Conference on Infrared, Millimeter and Terahertz Waves 2008*, pp. 1–2
DOI: [10.1109/ICIMW.2008.4665521](https://doi.org/10.1109/ICIMW.2008.4665521) (see p. 74).
- [122] A. Semenov, O. Cojocari, H. W. Hubers, F. Song, A. Klushin, and A. S. Muller “Application of Zero-Bias Quasi-Optical Schottky-Diode Detectors for Monitoring Short-Pulse and Weak Terahertz Radiation” in: *IEEE Electron Device Letters* 31.7 (2010), pp. 674–676
DOI: [10.1109/LED.2010.2048192](https://doi.org/10.1109/LED.2010.2048192) (see p. 74).
- [123] J. Raasch “Electrical-field sensitive $\text{YBa}_2\text{Cu}_3\text{O}_7$ detectors for real-time monitoring of picosecond THz pulses” PhD thesis Karlsruhe Institute of Technology (KIT), 2017
DOI: [10.5445/IR/1000073798](https://doi.org/10.5445/IR/1000073798) (see p. 77).
- [124] P. Goldsmith *Quasioptical Systems: Gaussian Beam Quasioptical Propogation and Applications* IEEE Press Series on RF and Microwave Technology Wiley, 1998
DOI: [10.1109/9780470546291](https://doi.org/10.1109/9780470546291) (see p. 78).
- [125] A. Siegman *Lasers* University Science Books, 1986 ISBN: 9780935702118 (see p. 78).
- [126] A.-S. Müller, I. Birkel, E. Huttel, F. Perez, M. Pont, and R. Rossmanith “Energy Calibration of the ANKA Storage Ring” in: *9th European Particle Accelerator Conference (EPAC 2004) Lucerne, Switzerland, July 5-9 2004*
jacow.org/e04/PAPERS/THPKF022.PDF (see p. 79).
- [127] C. Chang “Precise determination of the electron beam energy with Compton backscattered laser photons at ANKA” PhD thesis Karlsruhe Institute of Technology (KIT), 2016
DOI: [10.5445/IR/1000051914](https://doi.org/10.5445/IR/1000051914) (see pp. 79, 80).
- [128] B. Kehrer, A. Borysenko, E. Hertle, N. Hiller, M. Holz, A. Müller, P. Schönfeldt, and P. Schütze “Visible light diagnostics at the ANKA storage ring” in: *Proceedings of the 6th International Particle Accelerator Conference*

- (IPAC), 8.-13. May, 2015, Richmond, VA, USA 2015
jacow.org/IPAC2015/papers/mopha037.pdf (see p. 80).
- [129] P. Schütze, A. Borysenko, E. Hertle, N. Hiller, B. Kehrer, A. Müller, and P. Schönfeldt “A fast gated intensified camera setup for transversal beam diagnostics at the ANKA storage ring” in: *Proceedings of the 6th International Particle Accelerator Conference (IPAC)*, 8.-13. May, 2015, Richmond, VA, USA 2015
DOI: [10.18429/JACoW-IPAC2015-MOPHA039](https://doi.org/10.18429/JACoW-IPAC2015-MOPHA039) (see p. 80).
- [130] P. Schütze *Transversale Strahldynamik bei der Erzeugung kohärenter Synchrotronstrahlung* Springer Fachmedien Wiesbaden, 2018
DOI: [10.1007/978-3-658-20386-3](https://doi.org/10.1007/978-3-658-20386-3) (see p. 80).
- [131] P. Forck *Lecture notes on Beam Instrumentation and Diagnostics* 2012
www-bd.gsi.de/conf/juas/juas_script.pdf (see p. 81).
- [132] B. Kehrer, A. Borysenko, E. Hertle, N. Hiller, M. Holz, A.-S. Müller, P. Schönfeldt, and P. Schütze “Visible Light Diagnostics at the ANKA Storage Ring” in: *Proceedings of the 6th International Particle Accelerator Conference (IPAC)*, 8.-13. May, 2015, Richmond, VA, USA 2015
DOI: [10.18429/JACoW-IPAC2015-MOPHA037](https://doi.org/10.18429/JACoW-IPAC2015-MOPHA037) (see p. 82).
- [133] P. Schönfeldt “Systematische Untersuchungen der Bestimmung von Burstingschwellen” Diploma thesis Karlsruhe Institute of Technology, 2014 (see p. 83).
- [134] X. Yan, A. M. MacLeod, W. A. Gillespie, G. M. H. Knippels, D. Oepts, A. F. G. van der Meer, and W. Seidel “Subpicosecond Electro-optic Measurement of Relativistic Electron Pulses” in: *Phys. Rev. Lett.* 85 (2000), pp. 3404–3407
DOI: [10.1103/PhysRevLett.85.3404](https://doi.org/10.1103/PhysRevLett.85.3404) (see p. 83).
- [135] P. Schönfeldt, E. Blomley, E. Bründermann, M. Caselle, S. Funkner, N. Hiller, B. Kehrer, A.-S. Müller, M. Nasse, G. Niehues, L. Rota, M. Schedler, M. Schuh, and M. Weber “Towards Near-Field Electro-Optical Bunch Profile Monitoring in a Multi-Bunch Environment” in: *Proceedings of the 8th International Particle Accelerator Conference (IPAC)*, 14.-19. May, 2017, Copenhagen, Denmark (Copenhagen, Denmark) International Particle Accelerator Conference 8 Geneva, Switzerland: JACoW, 2017, pp. 227–230 ISBN: 978-3-95450-182-3
DOI: [10.18429/JACoW-IPAC2017-MOPAB055](https://doi.org/10.18429/JACoW-IPAC2017-MOPAB055) (see pp. 84, 138).

- [136] C. Evain, E. Roussel, M. Le Parquier, C. Szwaj, M.-A. Tordeux, J.-B. Brubach, L. Manceron, P. Roy, and S. Bielawski “Direct Observation of Spatiotemporal Dynamics of Short Electron Bunches in Storage Rings” in: *Phys. Rev. Lett.* 118 (2017), p. 054801
DOI: [10.1103/PhysRevLett.118.054801](https://doi.org/10.1103/PhysRevLett.118.054801) (see p. 84).
- [137] E. Roussel, C. Evain, M. Le Parquier, C. Szwaj, S. Bielawski, L. Manceron, J.-B. Brubach, M.-A. Tordeux, J.-P. Ricaud, L. Cassinari, M. Labat, M.-E. Couprie, and P. Roy “Observing microscopic structures of a relativistic object using a time-stretch strategy” in: *Scientific Reports* 5 (2015)
DOI: [10.1038/srep10330](https://doi.org/10.1038/srep10330) (see p. 84).
- [138] S. Chattopadhyay “Some Fundamental Aspects of Fluctuations and Coherence in Charged-Particle Beams in Storage Rings” in: *CERN 84-11* (1984)
cds.cern.ch/record/155458 (see pp. 84, 140, 150).
- [139] J. M. Byrd “Bunched Beam Signals in Time and Frequency Domain” in: *Particle accelerators; Beam measurement*, 1998, pp. 233–262
DOI: [10.1142/9789812818003_0010](https://doi.org/10.1142/9789812818003_0010) (see pp. 84, 150).
- [140] E. Hertle, N. Hiller, E. Huttel, M. Höner, B. Kehrer, A.-S. Müller, N. Smale, and D. Teytelman “First Results of the New Bunch-by-bunch Feedback System at ANKA” in: *Proceedings of the 5th International Particle Accelerator Conference (IPAC)*, 15.-20. June, 2014, Dresden, Germany (Dresden, Germany) International Particle Accelerator Conference 5 Geneva, Switzerland: JACoW, 2014, pp. 1739–1741
DOI: [10.18429/JACoW-IPAC2014-TUPRI074](https://doi.org/10.18429/JACoW-IPAC2014-TUPRI074) (see pp. 85, 165).
- [141] E. Blomley, A.-S. Müller, and M. Schedler “Beam Studies with a New Longitudinal Feedback System at the ANKA Storage Ring” in: *Proceedings of the 7th International Particle Accelerator Conference (IPAC)*, 8.-13. May, 2016, Busan, Korea (Busan, Korea) International Particle Accelerator Conference 7 2016, pp. 2658–2660
DOI: [10.18429/JACoW-IPAC2016-WEPOR001](https://doi.org/10.18429/JACoW-IPAC2016-WEPOR001) (see pp. 85, 165).
- [142] P. R. Griffiths and J. A. de Haseth *Fourier transform infrared spectrometry* 2nd ed. John Wiley & Sons, 2007
DOI: [10.1002/047010631X](https://doi.org/10.1002/047010631X) (see p. 87).

- [143] Bruker Optik GmbH *Guide for Infrared Spectroscopy* 2011
www.bruker.com/fileadmin/user_upload/8-PDF-Docs/OpticalSpectroscopy/SW_downloads/GuideIFS.zip (see p. 89).
- [144] R. Klein, R. Thornagel, and G. Ulm “The Electron Storage Rings MLS and BESSY II as Primary Source Standards” in: *Metrology with Synchrotron Radiation* vol. 124 3-4 Physikalisch-Technische Bundesanstalt Braunschweig and Berlin, 2014
www.ptb.de/cms/fileadmin/internet/fachabteilungen/abteilung_7/7.1_radiometrie/PTB-Mitt_2015_Primaernormale_ENG.pdf (see p. 89).
- [145] J. C. Heip “Design and Characterisation of THz Beam Transport Systems” Diplomarbeit Karlsruhe Institute of Technology, 2013 (see p. 90).
- [146] D. Martin and E. Puplett “Polarised interferometric spectrometry for the millimetre and submillimetre spectrum” in: *Infrared Physics* 10.2 (1970), pp. 105–109
DOI: [10.1016/0020-0891\(70\)90006-0](https://doi.org/10.1016/0020-0891(70)90006-0) (see p. 94).
- [147] L. Fröhlich “Bunch Length Measurements Using a Martin-Puplett Interferometer at the VUV-FEL” PhD thesis University of Hamburg, 2005
www-library.desy.de/preparch/desy/thesis/desy-thesis-05-011.pdf (see p. 95).
- [148] M. L. Reback, C. W. Roske, T. E. Bitterwolf, P. R. Griffiths, and C. J. Manning “Stopped-Flow Ultra-Rapid-Scanning Fourier Transform Infrared Spectroscopy on the Millisecond Time Scale” in: *Applied Spectroscopy* 64.8 (2010), pp. 907–911
DOI: [10.1366/000370210792081019](https://doi.org/10.1366/000370210792081019) (see p. 98).
- [149] T. N. Buican and H. C. Carrieri “Ultra-high speed solid-state FTIR spectroscopy and applications for chemical defense” in: *24th Army Science Conference, Orlando, FL* http 2004
www.dtic.mil/get-tr-doc/pdf?AD=ADA431953 (see p. 98).
- [150] S. P. Heussler, H. O. Moser, S. M. P. Kalaiselvi, C. Quan, C. J. Tay, S. P. Turaga, and M. Breese “Pulsed and high-speed FTIR spectroscopy” in: vol. 8374 2012, p. 10
DOI: [10.1117/12.919533](https://doi.org/10.1117/12.919533) (see p. 98).
- [151] J. Thangaraj, G. Andonian, R. Thurman-Keup, J. Ruan, A. S. Johnson, A. Lumpkin, J. Santucci, T. Maxwell, A. Murokh, M. Ruelas, and A. Ovodenko “Demonstration of a real-time interferometer as a bunch-length monitor in a

- high-current electron beam accelerator” in: *Review of Scientific Instruments* 83.4 (2012), p. 043302
DOI: 10.1063/1.3698388 (see p. 98).
- [152] P. Kuske “Investigation of the Temporal Structure of CSR-Bursts at BESSY II” in: *Particle accelerator. Proceedings, 23rd Conference, PAC’09, Vancouver, Canada, May 4-8, 2009* 2010, FR5RFP063
jacow.org/PAC2009/papers/fr5rfp063.pdf (see p. 103).
- [153] D. Li, M. Ball, B. Brabson, J. Budnick, D. D. Caussyn, A. W. Chao, G. East, M. Ellison, D. Friesel, B. Hamilton, H. Huang, W. P. Jones, S. Y. Lee, M. G. Minty, S. Nagaitsev, K. Y. Ng, X. Pei, T. Sloan, M. Syphers, L. Teng, Y. Wang, Y. T. Yan, and P. L. Zhang “Experimental measurement of resonance islands induced by rf voltage modulation” in: *Phys. Rev. E* 48 (1993), R1638–R1641
DOI: 10.1103/PhysRevE.48.R1638 (see p. 111).
- [154] H. Huang, M. Ball, B. Brabson, J. Budnick, D. D. Caussyn, A. W. Chao, J. Collins, V. Derenchuk, S. Dutt, G. East, M. Ellison, D. Friesel, B. Hamilton, W. P. Jones, S. Y. Lee, D. Li, M. G. Minty, S. Nagaitsev, K. Y. Ng, X. Pei, A. Riabko, T. Sloan, M. Syphers, L. Teng, Y. Wang, Y. T. Yan, and P. L. Zhang “Experimental determination of the Hamiltonian for synchrotron motion with rf phase modulation” in: *Phys. Rev. E* 48 (1993), pp. 4678–4688
DOI: 10.1103/PhysRevE.48.4678 (see p. 111).
- [155] M. Syphers, M. Ball, B. Brabson, J. Budnick, D. D. Caussyn, A. W. Chao, J. Collins, V. Derenchuk, S. Dutt, G. East, M. Ellison, T. Ellison, D. Friesel, W. Gabella, B. Hamilton, H. Huang, W. P. Jones, S. Y. Lee, D. Li, M. G. Minty, S. Nagaitsev, K. Y. Ng, X. Pei, G. Rondeau, T. Sloan, L. Teng, S. Tepikian, Y. Wang, Y. T. Yan, and P. L. Zhang “Experimental study of synchro-betatron coupling induced by dipole modulation” in: *Phys. Rev. Lett.* 71 (1993), pp. 719–722
DOI: 10.1103/PhysRevLett.71.719 (see p. 111).
- [156] M. Ellison, M. Ball, B. Brabson, J. Budnick, D. D. Caussyn, A. W. Chao, J. Collins, S. A. Curtis, V. Derenchuk, S. Dutt, G. East, T. Ellison, D. Friesel, W. Gabella, B. Hamilton, H. Huang, W. P. Jones, W. Lamble, S. Y. Lee, D. Li, M. G. Minty, S. Nagaitsev, K. Y. Ng, X. Pei, G. Rondeau, T. Sloan, M. Syphers, S. Tepikian, Y. Yan, and P. L. Zhang “Driven response of the synchrotron

- motion of a beam” in: *Phys. Rev. Lett.* 70 (1993), pp. 591–594
DOI: [10.1103/PhysRevLett.70.591](https://doi.org/10.1103/PhysRevLett.70.591) (see p. 111).
- [157] D. Li, M. Ball, B. Brabson, J. Budnick, D. Caussyn, A. Chao, V. Derenchuk, S. Dutt, G. East, M. Ellison, D. Friesel, B. Hamilton, H. Huang, W. Jones, S. Lee, J. Liu, M. Minty, K. Ng, X. Pei, A. Riabko, T. Sloan, M. Syphers, Y. Wang, Y. Yan, and P. Zhang “Effects of rf voltage modulation on particle motion” in: *Nuclear Instruments and Methods in Physics Research Section A: Accelerators, Spectrometers, Detectors and Associated Equipment* 364.2 (1995), pp. 205–223 ISSN: 0168-9002
DOI: [10.1016/0168-9002\(95\)00440-8](https://doi.org/10.1016/0168-9002(95)00440-8) (see p. 111).
- [158] F. Orsini and A. Mosnier “Effectiveness of rf phase modulation for increasing bunch length in electron storage rings” in: *Phys. Rev. E* 61 (2000), pp. 4431–4440
DOI: [10.1103/PhysRevE.61.4431](https://doi.org/10.1103/PhysRevE.61.4431) (see p. 111).
- [159] S. Sakanaka, M. Izawa, T. Mitsuhashi, and T. Takahashi “Improvement in the beam lifetime by means of an rf phase modulation at the KEK Photon Factory storage ring” in: *Phys. Rev. ST Accel. Beams* 3 (2000), p. 050701
DOI: [10.1103/PhysRevSTAB.3.050701](https://doi.org/10.1103/PhysRevSTAB.3.050701) (see p. 111).
- [160] J. M. Byrd, W.-H. Cheng, and F. Zimmermann “Nonlinear effects of phase modulation in an electron storage ring” in: *Phys. Rev. E* 57 (1998), pp. 4706–4712
DOI: [10.1103/PhysRevE.57.4706](https://doi.org/10.1103/PhysRevE.57.4706) (see p. 111).
- [161] M. H. Wang and S. Y. Lee “RF voltage modulations and the coupled bunch instabilities” in: *Journal of Applied Physics* 92.1 (2002), pp. 555–563
DOI: [10.1063/1.1482426](https://doi.org/10.1063/1.1482426) (see p. 111).
- [162] N. P. Abreu, R. H. A. Farias, and P. F. Tavares “Longitudinal dynamics with rf phase modulation in the Brazilian electron storage ring” in: *Phys. Rev. ST Accel. Beams* 9 (2006), p. 124401
DOI: [10.1103/PhysRevSTAB.9.124401](https://doi.org/10.1103/PhysRevSTAB.9.124401) (see pp. 111, 112).
- [163] E. J. Akutowicz “On the Determination of the Phase of a Fourier Integral, I” in: *Transactions of the American Mathematical Society* 83.1 (1956), pp. 179–192
DOI: [10.2307/1992910](https://doi.org/10.2307/1992910) (see p. 119).
- [164] B. Schmidt, S. Wesch, T. Kövener, C. Behrens, E. Hass, S. Casalbuoni, and P. Schmüser *Longitudinal Bunch Diagnostics using Coherent Transition Radiation Spectroscopy* tech. rep. DESY-18-027; arXiv:1803.00608 2018, p. 60
DOI: [10.3204/PUBDB-2018-01372](https://doi.org/10.3204/PUBDB-2018-01372) (see p. 119).

- [165] A. Finn, P. Karataev, and G. Rehm “A Multi-band Single Shot Spectrometer for Observation of mm-Wave Bursts at Diamond Light Source” in: *Proceedings of the 6th International Particle Accelerator Conference (IPAC), 8.-13. May, 2015, Richmond, VA, USA* 2015, MOPTY080
jacow.org/IPAC2015/papers/mopty080.pdf (see p. 120).
- [166] A. Finn “Design and development of a turn-by-turn spectrometer in order to investigate micro-bunching instabilities at the Diamond Light Source Ltd.”
PhD thesis 2017
pure.royalholloway.ac.uk/portal/files/29197530/thesis_AiveenFinn.pdf (see p. 120).
- [167] *Virginia Diodes, Inc., Charlottesville, VA*
vadiodes.com (visited on 2017) (see p. 121).
- [168] T. Boltz “Comprehensive Analysis of Micro-Structure Dynamics in Longitudinal Electron Bunch Profiles” Master Thesis Karlsruhe Institute of Technology, 2017
DOI: 10.5445/IR/1000068253 (see pp. 134, 135).
- [169] E. Roussel, C. Evain, C. Szwaj, and S. Bielawski “Microbunching instability in storage rings: Link between phase-space structure and terahertz coherent synchrotron radiation radio-frequency spectra” in: *Phys. Rev. ST Accel. Beams* 17 (2014), p. 010701
DOI: 10.1103/PhysRevSTAB.17.010701 (see p. 134).
- [170] M. Schiselski, M. Laabs, N. Neumann, S. Kovalev, B. Green, M. Gensch, and D. Plettemeier “A planar Schottky diode based integrated THz detector for fast electron pulse diagnostics” in: *2016 IEEE MTT-S International Microwave Symposium (IMS) 2016*, pp. 1–4
DOI: 10.1109/MWSYM.2016.7540173 (see p. 137).
- [171] S. Tammaro, O. Pirali, P. Roy, J.-F. Lampin, G. Ducournau, A. Cuisset, F. Hindle, and G. Mouret “High density terahertz frequency comb produced by coherent synchrotron radiation” in: *Nat Commun* 6.7733 (2015)
DOI: 10.1038/ncomms8733 (see pp. 139, 166).
- [172] B. E. Billinghurst, J. C. Bergstrom, L. Dallin, M. de Jong, T. E. May, J. M. Vogt, and W. A. Wurtz “Observation of superradiant synchrotron radiation in the terahertz region” in: *Phys. Rev. ST Accel. Beams* 16 (2013), p. 060702
DOI: 10.1103/PhysRevSTAB.16.060702 (see pp. 139, 140).

- [173] K. M. Gier, C. Heckel, J. Reutter, W. Schmid, S. Schmoll, and H. Tschieche “Modulation and demodulation” in: *Taschenbuch der Hochfrequenztechnik* ed. by K. Lange and K.-H. Löcherer Berlin, Heidelberg: Springer Berlin Heidelberg, 1986, pp. 577–640 ISBN: 978-3-642-96894-5
DOI: 10.1007/978-3-642-96894-5_14 (see p. 140).
- [174] R. Fessenden *Wireless signaling*. US Patent 706,742 1902 www.google.com/patents/US706742 (see p. 140).
- [175] L. Lévy *Système de transmission électrique à distance, applicable particulièrement à la télégraphie et téléphonie sans fil* FR493660 1919 worldwide.espacenet.com/publicationDetails/originalDocument?CC=FR&NR=493660A&KC=A&FT=D&date=19190819# (see p. 141).
- [176] E. H. Armstrong “A New System of Short Wave Amplification” in: *Proceedings of the Institute of Radio Engineers* 9.1 (1921), pp. 3–11 ISSN: 0731-5996
DOI: 10.1109/JRPROC.1921.220092 (see p. 141).
- [177] A. S. Douglas “The Legacies of Edwin Howard Armstrong.” in: *Proceedings of the Radio Club of America, Inc.* vol. 64 3 1990, pp. 123–142 antiqueradios.com/superhet/ (see p. 142).
- [178] *Datasheet: M03HWD* OML, Inc. 2017 (see p. 143).
- [179] *Datasheet: WHMB-03* Farran Technology 2017 (see p. 143).
- [180] *Datasheet: FS-Z325* Radiometer Physics GmbH 2017 (see p. 143).
- [181] *Datasheet: HM325* Radiometer Physics GmbH 2017 (see p. 143).
- [182] *Datasheet: WR3.4SAX* Virginia Diodes Inc. 2017 (see pp. 143, 144).
- [183] T. Udem, R. Holzwarth, and T. W. Hansch “Optical frequency metrology” in: *Nature* 416.6877 (2002), pp. 233–237
DOI: 10.1038/416233a (see p. 144).
- [184] A.-S. Müller and M. Schwarz “Accelerator-Based THz Radiation Sources” in: *Synchrotron Light Sources and Free-Electron Lasers: Accelerator Physics, Instrumentation and Science Applications* ed. by E. Jaeschke, S. Khan, J. R. Schneider, and J. B. Hastings Springer International Publishing, 2014, pp. 1–31 ISBN: 978-3-319-04507-8
DOI: 10.1007/978-3-319-04507-8_6-1 (see p. 149).

- [185] T. P. R. Linnecar and W. Scandale “A transverse Schottky noise detector for bunched proton beams” in: *IEEE Trans. Nucl. Sci.* 28.CERN-SPS-81-5-DI (1981), pp. 2147–2149
cds.cern.ch/record/134310 (see p. 149).
- [186] C. Rubbia “Simon van der Meer (1925-2011)” in: *Nature* 472.7342 (2011), pp. 170–170
DOI: 10.1038/472170a (see p. 149).
- [187] J. L. Laclare “Bunched beam coherent instabilities” in: *CERN* 87-03 (1987)
DOI: 10.5170/CERN-1987-003-V-1.264 (see p. 150).
- [188] I. S. Gradshteyn and I. M. Ryžik *Table of integrals, series, and products* ed. by A. Jeffrey and D. Zwillinger 7. ed. Amsterdam: Elsevier/Academic Press, 2007
DOI: 10.1016/C2009-0-22516-5 (see p. 150).
- [189] R. Kuc *Introduction to Digital Signal Processing* 1st New York, NY, USA: McGraw-Hill, Inc., 1988 ISBN: 0070355703 (see p. 175).
- [190] Keysight (formerly Agilent) *Spectrum Analysis Basics* Application Note 150 2016 www.keysight.com/find/appnote150 (see p. 180).
- [191] W. C. Michels and N. L. Curtis “A Pentode Lock-In Amplifier of High Frequency Selectivity” in: *Review of Scientific Instruments* 12.9 (1941), pp. 444–447
DOI: 10.1063/1.1769919 (see p. 180).
- [192] C. R. Cossens “A balance-detector for alternating-current bridges” in: *Proceedings of the Physical Society* 46.6 (1934), p. 818
DOI: 10.1088/0959-5309/46/6/310 (see p. 180).
- [193] Zurich Instruments *Principles of lock-in detection and the state of the art* online Whitepaper 2016 www.zhinst.com/sites/default/files/li_primer/zi_whitepaper_principles_of_lock-in_detection.pdf (see p. 181).
- [194] The HDF Group *Hierarchical Data Format, version 5* 1997-2018 www.hdfgroup.org/HDF5/ (see p. 182).
- [195] M. Caselle, M. Balzer, S. Chilingaryan, M. Hofherr, V. Judin, A. Kopmann, N. J. Smale, P. Thoma, S. Wuensch, A.-S. Müller, M. Siegel, and M. Weber “An ultra-fast data acquisition system for coherent synchrotron radiation with terahertz detectors” in: *Journal of Instrumentation* 9.01 (2014), p. C01024
DOI: 10.1088/1748-0221/9/01/c01024 (see p. 182).

- [196] L. Rota, M. Vogelgesang, L. A. Perez, M. Caselle, S. Chilingaryan, T. Dritschler, N. Zilio, A. Kopmann, M. Balzer, and M. Weber “A High-throughput Readout Architecture Based on PCI-Express Gen3 and DirectGMA Technology” in: *Journal of Instrumentation* 11.02 (2016), P02007 DOI: 10.1088/1748-0221/11/02/P02007 (see p. 183).
- [197] L. Rota, M. Caselle, S. Chilingaryan, A. Kopmann, and M. Weber “A PCIe DMA Architecture for Multi-Gigabyte per Second Data Transmission” in: *IEEE Transactions on Nuclear Science* 62.3 (2015), pp. 972–976 DOI: 10.1109/TNS.2015.2426877 (see p. 183).
- [198] M. Brosi “Untersuchung des Burstingverhaltens von Synchrotronstrahlung im THz-Bereich” Master Thesis Karlsruhe Institute of Technology, 2014 (see p. 184).
- [199] K. Hanke, V. Schlott, K. Aulenbacher, H. Braun, and F. Chautard *Beam diagnostics using coherent transition radiation at the CLIC test facility* tech. rep. CLIC-Note-298 Geneva: CERN, 1996 cds.cern.ch/record/302736 (see p. 186).
- [200] S. A. Kuznetsov, M. A. Astafyev, A. V. Gelfand, and A. V. Arzhannikov “Microstructured frequency selective quasi-optical components for submillimeter-wave applications” in: *44th European Microwave Conference* 2014, pp. 881–884 DOI: 10.1109/EuMC.2014.6986576 (see p. 187).
- [201] M. Thumm, A. V. Arzhannikov, V. Astrelin, A. Burdakov, N. Ginzburg, I. Ivanov, P. Kalinin, S. A. Kuznetsov, M. Makarov, K. I. Mekler, A. Paulish, N. Y. Peskov, S. V. Polosatkin, S. Popov, V. V. Postupaev, A. F. Rovenskikh, A. Sergeev, S. L. Sinitsky, V. F. Sklyarov, V. Stepanov, L. N. Vyacheslavov, and V. Y. Zaslavsky “Generation of High Power THz Waves in Relativistic Electron Beam Plasma and Two-Sheet-Beam FEM” in: *International Journal of Terahertz Science and Technology* 5.1 (2012), pp. 18–39 DOI: 10.11906/TST.018-039.2012.03.03 (see p. 187).
- [202] S. Funkner et al. “High throughput data streaming of individual longitudinal electron bunch profiles in a storage ring with single-shot electro-optical sampling” in: (2018) arXiv: 1809.07530 [physics.acc-ph].

- [203] V. Judin “Untersuchung von Bunch-Bunch-Wechselwirkungen und des Einflusses der geometrischen Impedanz bei der Erzeugung kohärenter THz-Strahlung” PhD thesis Karlsruhe Institute of Technology (KIT), 2013
nbn-resolving.org/urn:nbn:de:swb:90-395281.
- [204] A.-S. Müller, N. H. A. Hofmann, E. Huttel, K. Il'in, V. Judin, B. Kehrer, M. Klein, S. Marsching, C. Meuter, S. Naknaimueang, M. Nasse, A. Plech, P. Probst, A. Scheuring, M. Schuh, M. Schwarz, M. Siegel, N. Smale, M. Streichert, F. Caspers, A. Semenov, H.-W. Hübers, and E. Bründermann “Experimental Aspects of CSR in the ANKA Storage Ring” in: *ICFA Beam Dynamic Newsletter* vol. 57 2012
icfa-usa.jlab.org/archive/newsletter/icfa_bd_nl_57.pdf.

Acknowledgements

Physics is, hopefully, simple. Physicists are not.

— Edward Teller, Conversations on the Dark Secrets of Physics (1991)

I am deeply grateful to Prof. Michael Siegel and Prof. Anke-Susanne Müller for giving me the opportunity to write this thesis. Special thanks to Anke-Susanne for introducing me to the beauty of accelerator physics and supervising me for the past years. Additionally, I want to thank Erik Bründermann for his support in my academic career and the sharing of his invaluable knowledge and experience in THz technologies. Without Anke-Susanne and Erik I wouldn't even have started my PhD. I want to thank the BMBF for financing so many wonderful projects I have been part of and the Helmholtz International Research School for Tertronics (HIRST) for broadening my horizon in technical and management training modules.

The fun and productive working environment I have enjoyed would not have been possible without all the wonderful colleagues I have been working with. In particular, I want to thank my "predecessors" Vitali Judin and Nicole Hiller for the experience and equipment I could take on and especially for the collaborations they already started. All the room mates I had during the years, especially Benjamin Kehrer my personal travel agent who knows literally every train station.

Miriam Brosi for numerous common beamtimes and nightshifts, the operation of KAPTURE and the Terabytes of raw data she recorded and the prepared HDF5 data she provided me. Michele Caselle, the mastermind behind KAPTURE, for the creation of that nice sampling hardware and endless discussions on sampling, RF circuits, timing and FPGA programming. Markus Schwarz, my esteemed theorist on duty, for endless discussions on synchrotron radiation, dispersion relation and Fourier transforms.

Advice and comments given by Tobias Boltz, Stefan Funkner, Michael Nasse and Nigel Smale have been a great help in writing this thesis.

Edmund Blomley, Marcel Schuh, Manuel Schedler, Akira Mochihashi and Erhard Huttel for many fruitful discussions on all topics of accelerators and operating the

KARA machine. Manuel helped with the phase modulation, Eddy realized all (physically possible) special requests like custom filling patterns, unusual α_c and RF values, triggered phase jumps and many more.

I have greatly benefited from external beam times at DELTA, HZDR, PSI and DIAMOND. Not only from the captured data and gained experience but also many discussions with the colleagues there. For this common beam times I want to thank Franziska Frei, Christopher Gerth, Carsten Mai, Shaukath Khan, Peter Kuske, Markus Ries, Michael Gensch, Günther Rehm. Especially the friends from the KIT-IMS THz-detector group for many common beam times at KARA and the one at DIAMOND: Juliane Raasch, Artem Kuzmin and Alexander Schmid.

My Bachelor and Master students Matthias Martin, Manuel Geggus, Lukas Mall and Carl Sax for their contributions and pleasant cooperation.

I want to thank Virginia Diodes and especially Jeffrey Hesler for providing the RF-Mixer used in Chapter 9. Jeffrey participated in two beamtimes, helping on set up and alignment of the device, even on night shifts.

Last but not least, I want to thank my family for their unconditional support during these years of privations, especially my wife Eva and my mother Barbara (who also proofread the complete thesis).

Wenn man einen Freund hat, ... braucht man sich vor nichts zu fürchten.

— Janosch, Oh, wie schön ist Panama (1978)

Several novel diagnostic systems based on the detection of coherent THz radiation are presented. Among others, a heterodyne setup for highest spectral resolution at 270 GHz and the fastest THz single-shot spectrometer with 500 MHz repetition rate with continuous, FPGA based readout were developed and commissioned. The investigation of the photon beam properties allow for bunch-by-bunch and turn-by-turn diagnostics of the emitting electron bunches in the accelerator. It is used for time-resolved studies of the micro-bunching instability, for example in the vicinity of an RF phase modulation. The accompanying simulations were performed with the Vlasov-Fokker-Planck solver Invesa and show a good agreement of simulation and measurement which enhances the knowledge of the physics behind the micro-bunching instability.



ISBN 978-3-7315-0889-2



9 783731 508892 >

Gedruckt auf FSC-zertifiziertem Papier